博士論文

# Petrogenesis of Triassic gabbros and associated basalts from Chukotka (NE Russia): implications for eastern margin of Siberian LIP

(極東ロシア Chukotka、三畳紀はんれい岩および玄武岩の起源～シベリア・トラッ プ東縁としての意義)

DESTA Minyahl Teferi

平成２７年

## SUMMARY

The PhD thesis consists of two parts and describes the comparative geochemical and petrological study of the Siberian LIP (~250 Ma) and Ethiopian LIP (~30 Ma) to consider their mantle and crustal processes in view of magmatic diversity among those LIPs. These two LIPs display contrasting high field strength elements (HFSEs) and petrographic features. The majority of the erupted low-Ti basalts of Siberian LIP are characterized by HFSE depleted trace element distribution patterns similar to island-arc-basalt, whereas the Ethiopian LIP basalts are HFSE-enriched and closly resemble OIB. Moreover, the hydrous nature of the mantle source for the Siberian LIP is evident from the presence of primary hydrous minerals such as in the gabbro, meimechite and ferropicrite rocks; however, the Ethiopian LIP is originated from anhydrous source.

The first chapter of this thesis studies the petrogenesis of Triassic gabbros and associated basalts of Chukotka, NE Russia, aming to find the eastern marginal extension of Siberian LIP. Our findings also provide additional constraints for the much debated origin of the Arctic Alaska-Chukotka microplate (AACM). We have identified two types of mafic rocks in this study, i.e. island-arc basalt (IAB)-type amphibole bearing gabbros (such as pyroxene-hornblende gabbro, hornblende gabbro, hornblende-pyroxene gabbro) and basalts (with ankaramites, pyroxene-phyric basalt, lamprophyre, and basaltic andesites sub-type) and OIB-type gabbros (include rare to no amphiboles). These gabbroic and associated basaltic rocks are mainly thoiliitic with both intra-plate and island-arc basalt geochemical features. In the primitive mantle normalized trace element patterns, IAB-type gabbroic and basaltic rocks are characterized by depletion in HFSE (Nb, Ta, Zr and Hf) and enrichment in LILE, and

resemble arc-type igneous rocks. OIB-type gabbroic rocks can be distinguished from the rest of the studied samples by the absence of HFSE depletion, but show strong negative Sr anomalies. The positive Ti anomaly in the OIB-type gabbros can be attributed to high content of ilmenite in these rocks. Geochemical data suggest partial melting of the subduction-modified, metasomatized enriched mantle wedge of garnet lherzolite to produce the parental melt of the IAB-type gabbroic and basaltic rocks of Chukotka. The composition of the mantle source and degree of partial melting that produced the parental magmas of these rocks, determined by using REE abundance and ratios, indicate that IAB-type gabbroic and basaltic melts were generated at about 10-30% partial melting of hydrous garnet lherzolite. The geochemical similarity of the studied IAB-type gabbroic and basaltic rocks of Chukotka with Bel'kov Island dolerite and low-Ti Nadezhdinsky suit (Noril'sk region) in terms of the presence of dominant hydrous minerals and negative HFSE anomalies, it is possible that the eastern Chukotka was placed closer to the Siberian LIP in Triassic, and the Triassic mafic magmatism in Chukotka represents a marginal part of the Siberian LIP. Therefore, our finding gives an additional evidence for the recently suggested subduction related origin of the Siberian LIP.

The second chapter of this thesis presents the first finding of ferropicrite lava from the Ethiopian LIP (~30 Ma) in association with ultratitaniferous transitional basalt and picrites of the second high-Ti (HT2) series. The major and trace element data of the Ethiopian ferropicrite is compatible with the eclogitic source that has possibly represents the recycled oceanic crust components in the upwelling Afar plume head. The occurrence of this ferropicrite further supports the involvement of deep plume sources during Ethiopian LIP magmatism.

**TABLE OF CONTENTS**

## LIST OF FIGURES

## LIST OF TABLES

**ACKNOWLEDGMENTS**

First and foremost I am greatly indebted to my supervisor Prof. Akira Ishiwatari for his permission to study his rock samples which are collected from outcrops in the course of his Japanese-Russian joint field work for ophiolite in the Chukotka area, northeast Russia, during 2009. I would like to express him my sincere gratitude for his guidance and encouragement throughout the research, for his valuable comments and suggestions, and friendly support in every step of my study, patience and comprehension even in the most difficult times. Without his guidance and constant thoughtful feedback this PhD would not have been achievable. Dr. Sumaki Machi also highly acknowledged for his sample collection during this field work and for providing me the GPS record for each samples.

Another special thank you goes to Dr. Dereje Ayalew from Addis Ababa University for his kindly permission to study his ferropicrite rock samples collected from Ethiopian large igneous province and for his valuable comments and suggestions on my study during his short visit to Tohoku University.

I am grateful to all my members of the geology and petrology research group in earth science department. I would especially like to thank Dr. Tsuyoshi Miyamoto for his guidance during sample preparation, EPMA analysis and for his X-ray fluorescence analyses of bulk-rock. I thank Dr. Naoto Hirano for his valuable suggestions and comments on my research during the laboratory seminar. Also I like to thank Dr. Akio Goto for his car service from Kawauchi to Aobayama when I needed and for his kindly approach.

I am very much indebted to Prof. Shoji Arai and all his staff members of earth science department in

Kanazawa University for their comments and assistance with LA-ICP-MS trace element determinations.

I want also to thank to Prof. Yildrim Dilek for his comments and suggestions in the latest version of the manuscript.

I would like to acknowledge the Grant-in-Aid for Scientific research (C)-23540554 provided by the Ministry of Education, Culture, Sports, Science and Technology (MEXT) during my research in Tohoku University.

Finally, heartfelt thanks goes to my parents, especially my mum, Tirunesh, my father, Mezgeb, my young brother Dagem and sisters, Betselot and Yabsera for their constant and unconditional support, encouragement and prayer. Thank you very much for your love and care!

Above all, I owe it all to Almighty God for granting me the wisdom, health and strength to undertake this research work and enabling me to its completion.

.

.

# CHAPTER 1

# Petrogenesis of Triassic gabbros and associated basalts from Chukotka (NE Russia): implications for eastern margin of Siberian LIP


## 1.1. ABSTRACT

The Triassic gabbroic intrusions and associated basaltic lavas from Chukotka contain abundant hornblende, and are mainly tholeiitic with both OIB-type and island-arc basalt (IAB)-type geochemical signatures. Mg-number (Mg#=100×Mg/ ($Mg+Fe^{2+}$)) ranges from 48 to 66 for IAB-type gabbros, around 40 for OIB-type gabbros, 63-65 for ankaramites (IAB-type), 57 for pyroxene phyric basalt (IAB-type), 51-54 for lamprophyres (IAB-type) and 43-50 for basaltic andesite (IAB-type). $TiO_2$ contents of the studied samples are low (<2 wt. %) except for OIB-type gabbros (4.3-5.3 wt. %). Gabbroic rocks generally have lower $K_2O$ and $Na_2O$ than the volcanic rocks. OIB-type gabbros are typically enriched in $FeO^*$ (16-18 wt. %) as compared to IAB-type gabbros (10-14 wt. %), and IAB-type basaltic rocks (ankaramites ~10 wt. %, lamprophyres ~14, pyroxene-phyric basalt 11 wt. %, and basaltic andesite 9-10 wt. %). In the primitive mantle normalized trace element patterns, IAB-type gabbroic and basaltic rocks are characterized by depletion in HFSE (Nb, Ta, Zr and Hf) and enrichment in LILE, and resemble arc-type igneous rocks. OIB-type gabbroic rocks can be distinguished from the rest of the studied samples by the absence of HFSE depletion, but show strong negative Sr anomalies. The positive Ti anomaly in

the OIB-type gabbros can be attributed to high content of ilmenite in these rocks. The composition of the mantle source and degree of partial melting that produced the parental magmas of these rocks, determined by using REE abundance and ratios, indicate that IAB-type gabbroic and basaltic melts were generated at about 10-30% partial melting of hydrous garnet lherzolite. Trace element characteristics of IAB-type gabbroic rocks and basalts are compatible with their magmas derived from subduction influenced melts, whereas OIB-type gabbros show within-plate geochemical characteristics. IAB-type gabbroic and basaltic rocks display similar geochemical features with the low-Ti Nadezhdinsky suit (Noril'sk region) and Bel'kov dolerite (New Siberian Islands) of Siberian LIP in view of HFSE depletion and high $H_2O$ content of the magma to crystallize abundant hornblende not only in gabbros but also as phenocrysts in basalts.

**Keywords:** Island-arc geochemistry, intra-plate geochemistry, ankaramite, hornblende basalt, HFSE

## 1.2. GENERAL INTRODUCTION

The Arctic Alaska-Chukotka microplate (AACM) is the key element in the tectonic evolution of Amerasian Basin (Miller et al., 2006). In the north it is bounded by the Arctic Alaskan and Russian outer shelf edges. Its southern boundary is defined by a belt of arc and an ophiolitic rocks that includes the Angayucham terrane of the southern Brooks Range (Moore et al., 1994) and South Anyui zone of western Chukotka (Sokolov et al., 2002). Eastern Chukotka is interpreted as a part of this microplate which is formed during the Cretaceous opening of the Amerasian basin. Geophysical data sets and seismic reflection based stratigraphic correlations support to the suggested rifting model or "rotational model" for the formation of Amerasian basin (Grantz et al. 1998; Lawver

et al. 2002). This model proposes that early Cretaceous rifting rotated a continental mass, now it is known as Arctic Alaska-Chukotka microplate, southward from the Arctic margin of Canada. On the other hand, Miller et al. (2006) proposed that AACM is rifted from the Siberian craton, which is supported by U–Pb dates of detrital zircons from the Triassic terrigenous sedimentary rocks of eastern Chukotka, Wrangel Island, and the Lisburne Hills in the Arctic Alaska region indicating that the youngest detrital zircon population has a Permo-Triassic age similar to the basaltic rocks of the eastern Urals, Tunguska and Taimyr provinces of the Siberian large igneous province (LIP). Kuz'michov and Pease (2007) also reported that the hypabyssal mafic rocks (dolerites) of the New Siberian Archipelago (Bel'kov Island) have similar age (252±2 Ma, U-Pb TIMS ages of igneous zircons), petrographic features and geochemical signatures with the moderately alkaline basalts in the Noril'sk district, Siberia. As a result, Miller et al., (2006) and Kuz'michov and Pease (2007) concluded that the eastern Chukotka along with other parts of AACM, was closer to the Siberian craton than to Arctic Canada, or that it may even have constituted a part of the Siberian platform, respectively. Recent investigations have shown that hypabyssal mafic rocks and basalts with inter-pillow cherts and terrigenous sedimentary rocks spacially associated with them occur in the vicinity of the Kolyuchinskaya Bay in eastern Chukotka, and that the trace element patterns and Sr- and Nd-isotope compositions of these sedimentary and volcanic associations are similar to the tholeiitic flood basalts of the main plateau stage of the Siberian LIP (Ledneva et al., 2011). Moreover, the gabbroic rocks of western Chukotka (such as in the area of Keperveem, Malyi Anyui and Raucha Uplifts; Fig. 1.1B) and the Siberian trap basalts are highly similar in terms of the geochemistry of their major oxides (Gel'man, 1963;

Degtyaryov, 1975). Small bodies of gabbroic intrusions (dikes and sills) are also widespread in the Permian-lower Triassic and lower-middle Triassic shelf and continental slope sedimentary sequences (Ledneva et al., 2014).

### 1.2.1. Objectives

The mafic intrusive and extrusive rocks occur in the eastern Chukotka and are assumed to be of Permo-Triassic to Early-Middle Triassic age. This study is primarily aiming to find the possible eastern marginal extension of Siberian large igneous province (Permo-Triassic, ~250 Ma) and compared its petrology and geochemistry with the central Siberian plateau. Here, we present XRF whole rock geochemical analyses, electron microprobe analyses of hornblende, clinopyroxene, plagioclase and Fe-Ti oxide, LA-ICP-MS analyses of bulk-rock, hornblende and clinopyroxene for the Triassic gabbros and associated basaltic rocks of Chukotka in order to place constraints on the origin of their parental magmas, and to fingerprint their geochemical signatures. We compared our results with the previously published data from Siberian LIP in search for genetic relationships between these igneous provinces. Our findings also provide additional constraints for the much debated origin of the AACM.

### 1.2.2. Analytical Techniques

The samples were collected by the Prof. Akira Ishiwatari from outcrops in the course of his Japanese-Russian joint field work for ophiolite in 2009 in the Chukotka area, northeast Russia. Electron microprobe analyses were conducted on hornblende, clinopyroxene, plagioclase and Fe±Ti oxide minerals in polished thin section, using

an energy dispersive X-ray spectrometer Oxford Link ISIS equipped on the JEOL JSM-5410 Scanning electron microscope (SEM) at the Earth Science department, Tohoku University. The reader is referred to Erdenesaihan et al. (2013) and Desta et al. (2014) for analytical details about electron microprobe technique. Major and some trace elements (V, Cr, Ni, Rb, Sr, Ba, Y, Zr, Nb) were obtained using X-ray fluorescence spectrometer (XRF-RIX 2100) on fused glass discs at the aforementioned department, Tohoku University. The loss on ignition (LOI) was determined following the procedure described by Desta et al. (2014). The trace element analysis of whole rock and mafic minerals (i.e. clinopyroxene and amphibole) have been carried out by a laser ablation (193 nm ArF exciemer: MicroLas GeoLas Q-plus)-inductively coupled plasma spectrometer Agilent 7500S (LA-ICPMS) at Kanazawa University (Ishida et al., 2004). Detailed LA-ICPMS analytical procedures have been reported by Erdenesaihan et al. (2013) and Desta et al. (2014).

### 1.3. GEOLOGICAL SETTING

The study area (Fig. 2.1B) is situated within the Arctic Alaska-Chukotka microplate (AACM) or Chukotka microcontinent (Parfenov et al., 1993). The AACM is composed of a Neoprotrozoic crystalline basement (Natal'in et al., 1999, Amato, et al., 2009), and overlain by Carboniferous and Permian platform strata (P'yankov, 1981; Natal'in et al., 1999). These units are, in turn, overlain by a Permo-Triassic to upper Triassic terrigenous continental shelf sedimentary sequence (Tuchkova et al., 2009) and a Jurassic volcanic-terrigenous foreland sedimentary package (Vatrushkina and Tuchkova, 2014).

To the south, the AACM is bounded by the South Anyui Suture (SAS) zone, which was formed by the closure

of a late Jurassic-early Cretaceous oceanic basin and the collision of the North Asian craton with AACM (Seslavinsky, 1979; Parfenov, 1984). This suture zone is buried under the Cretaceous Okhotsk-Chukotka volcanic belt (Tikhomirov et al., 2012).

In the western part of Chukotka it is marked by Mesozoic terrigenous turbidite and fragments of ophiolite sequences (Sokolov et al., 2002). In the eastern Chukotka the position of SAS attributed to the Velmai terrane (Parfenov et al., 1993; Nokleberg et al., 1998; Sokolov et al., 2009).

In the study area the gabbroic intrusions occur as flat-lying tabular bodies ranging in thickness from a few meters to few hundred meters, and are mainly confined to the upper Permian-lower Triassic and lower-middle Triassic strata of the AACM cover (Fig. 1.1). However, the upper Triassic sedimentary units overlying these older sequences are devoid of tabular bodies of gabbroic intrusions (Til'man and Sosunov, 1960; Gel'man, 1963; Degtyaryov, 1975). In the western Chukotka these intrusions extend for ~350 km (the Keperveem and Raucha Uplifts); in central and eastern Chukotka they are traced to a distance of ~ 900 km (the vicinity of Cape Schmidt and the interfluves of the Amguema and Vel'may rivers and the Kolyuchinskaya Bay area) (Fig. 1.1B; Ledneva et al., 2014). These gabbroic rocks were recognized as parts of a large regional complex (Til'man and Sosunov, 1960; Gel'man, 1963) named as the Amguema-Anyui Igneous Province (Degtyaryov, 1975). The Permo-Triassic to early-middle Triassic age of these intrusion is proven by: (1) their stratigraphic position within the Permian-lower Triassic and lower-middle Triassic terrigenous sediments, contemporaneous joint deformation of gabbroic bodies and their country rocks (Til'man and Sosunov, 1960; Gel'man, 1963); (2) bulk-rock K-Ar determinations

of 250, 231 and 223 Ma (Ivanov and Milov, 1975; Degtyaryov, 1975) and (3) and the U-Pb TIMS igneous zircon age of 252±4 Ma obtained for the Kolyuchinskaya Bay gabbro (Sokolov, et al., 2009). The gabbroic intrusions described by Ledneva et al. (2014) are characterized by intra-plate basaltic geochemical features.

However, our mineralogical and geochemical data confirm the presence of both island-arc basalt (IAB)-type and OIB-type mafic intrusions in the Triassic system of Chukotka. These two gabbro types were likely derived from two different mantle sources. Our OIB-type gabbros are analogous to those described by Ledneva et al. (2014) in terms of petrography and geochemistry. In the study area, these OIB-type and IAB-type gabbroic rocks and associated IAB-type basaltic units (i.e. ankaramites, pyroxene-phyric basalts, lamprophyres and basaltic andesites) are commonly occurring together and are exposed as platformal edifice (Fig. 1.3A). The basaltic lavas rarely exhibit pillow structure (at S4 of Fig. 1.2, See Fig. 1.3E). They are commonly interbedded with sandstone, siltstone, and mudstone and bedded tuff. The most magnesian samples (i.e. ankaramites, Sample#69, #70, and #71) of this study come from the sampling locality 4 (Fig.1.2; Tables 1.1 and 1.2; N66˚45′26″ , W177˚17′31″).

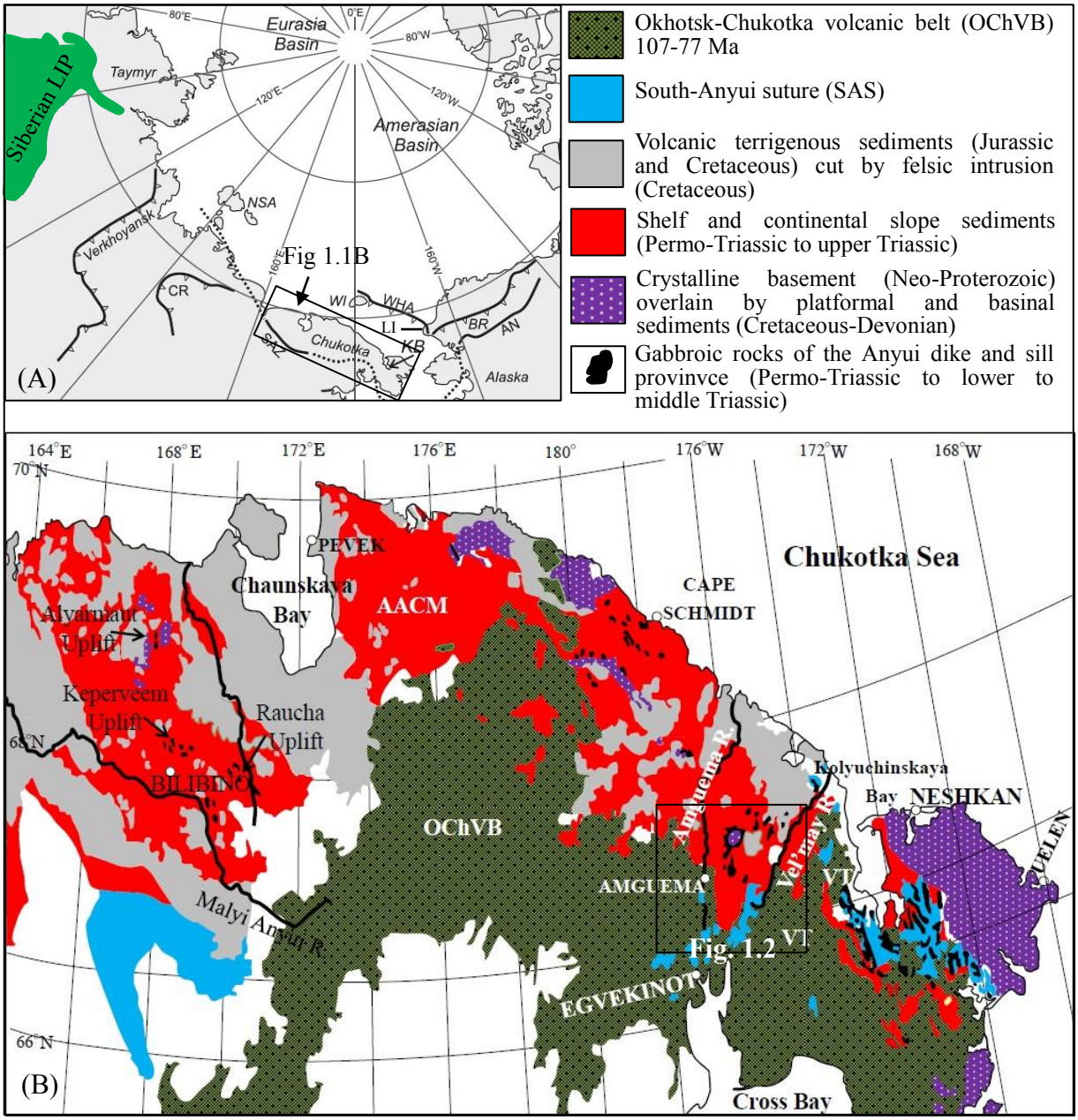


**Figure 1.1:** (A) A position of the AACM among major geological structures of Arctic region (modified after Miller et al., 2006). Abbreviations: SAS, South Anyui suture; LI, Lisburn Hills; WI, Wrangel Island; WHA, Wrangel, Herald Arch; KB, Kolyuchinskaya Bay; NSA, New Siberian Archipelago; CR, Chersky Range; BR, Brooks Range; AN, Angayucham belt. (B) General geology of Chukotka microplate after Ledneva et al. (2014) and position of study area. Abbreviations: AACM, Arctic Alaska-Chukotka microplate; OChVB, Okhotsk-Chukotka volcanic belt; VT, Vel'may terrane.

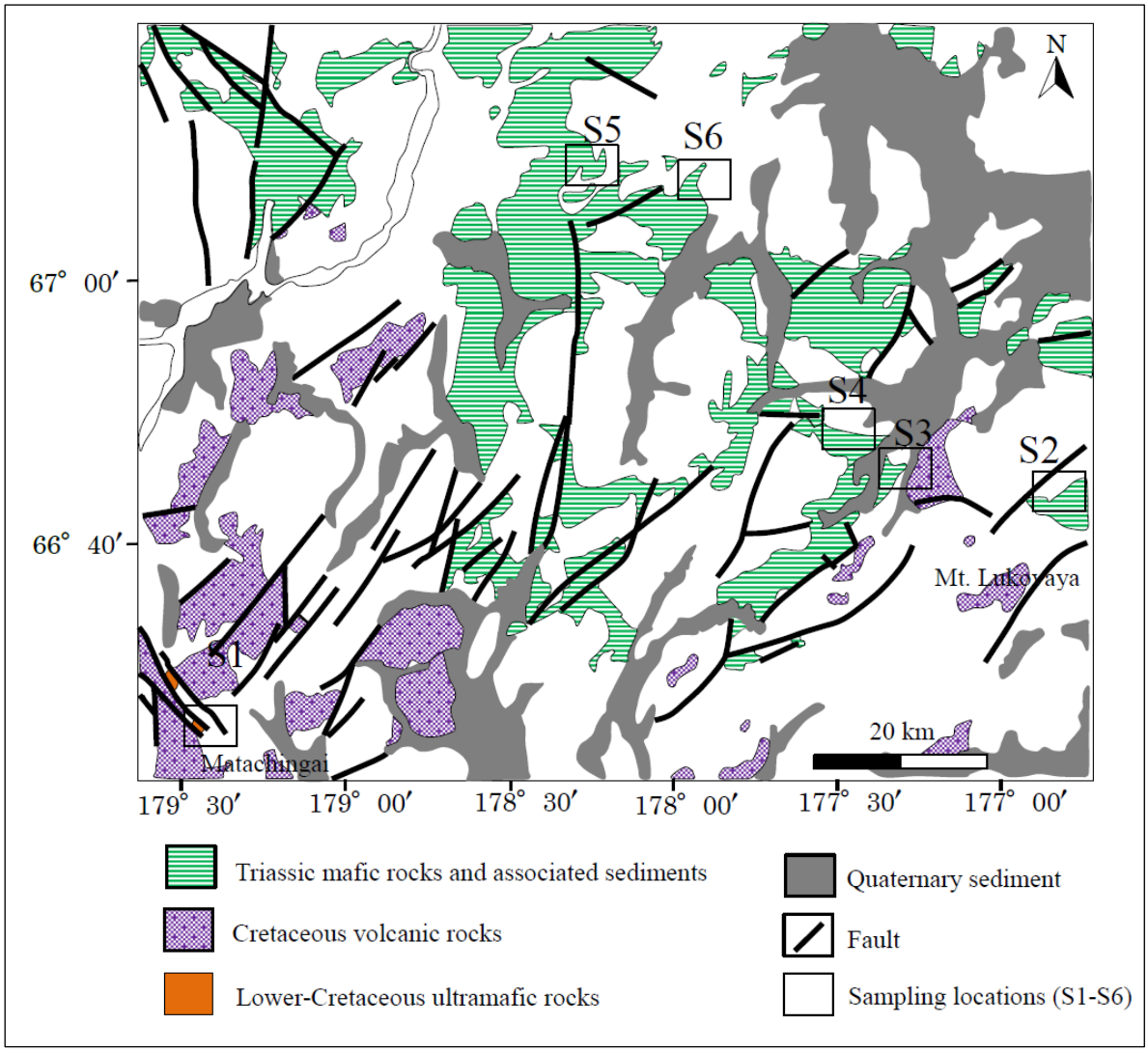


**Figure 1.2:** Sketch geological map of the Chukotka peninsula showing the sampling location of the Triassic basaltic and gabbroic rocks.


**Figure 1.3:** (A) Field photographs showing the occurrence of the studied gabbros as plat formal edifice tabular hills behind the field vehicle. (B) Fine grained gabbroic dike occurring within coarse grained melanocratic gabbro. (C) Details showing coarse grained IAB-type hornblende gabbro. (D) OIB-type gabbro cut by felsic veins. (E) Pillow lava of basalt that is closely associated with dolerite and gabbro in the S4 area. (F) Hand specimen of hornblende basaltic andesite showing large brown amphibole phenocrysts with a size as large as 1 cm (the coin is 22 mm in diameter).

## 1.4. PETROGRAPHY

### 1.4.1. Gabbroic rocks

We have identified two types of gabbroic bodies in this study, i.e. IAB-type amphibole bearing gabbroic rocks such as pyroxene-hornblende gabbro, hornblende gabbro, hornblende-pyroxene gabbro and OIB-type gabbros (include rare to no amphiboles).

IAB-type gabbros display a notable grain size variation; from medium grained (subordinately fine grained) to coarse crystals with size reaching about 20 mm (Fig. 1.4). They have a granular texture with hornblende, pyroxene and plagioclase. However, in some samples plagioclase minerals are altered to chlorite, epidote and probably sericite. Magnetite mineral occurs dominantly with variable size and shape (Fig. 1.4A-D). Rare apatite grains are also observed as accessory minerals in IAB-type pyroxene-hornblende gabbro.

OIB-type gabbros consist mainly of clinopyroxene, plagioclase (locally transformed to sericite) and ilmenite (Fig. 1.4E and F). They are massive fine- to medium grained rocks and are mainly display hypidiomorphic-granular texture. In general, olivine and orthopyroxene crystals are absent in both types of gabbros.

#### 1.4.1.1. Clinopyroxene

Clinopyroxene shows a characteristic subhederal to irregular shape and enclosed within the calcic amphibole oikocrysts in IAB-type gabbros. Their color varies from light-yellow, colorless, pale green to pinkish. Clinopyroxene in OIB-type gabbros forms elongated, subhedral to anhedral shape.

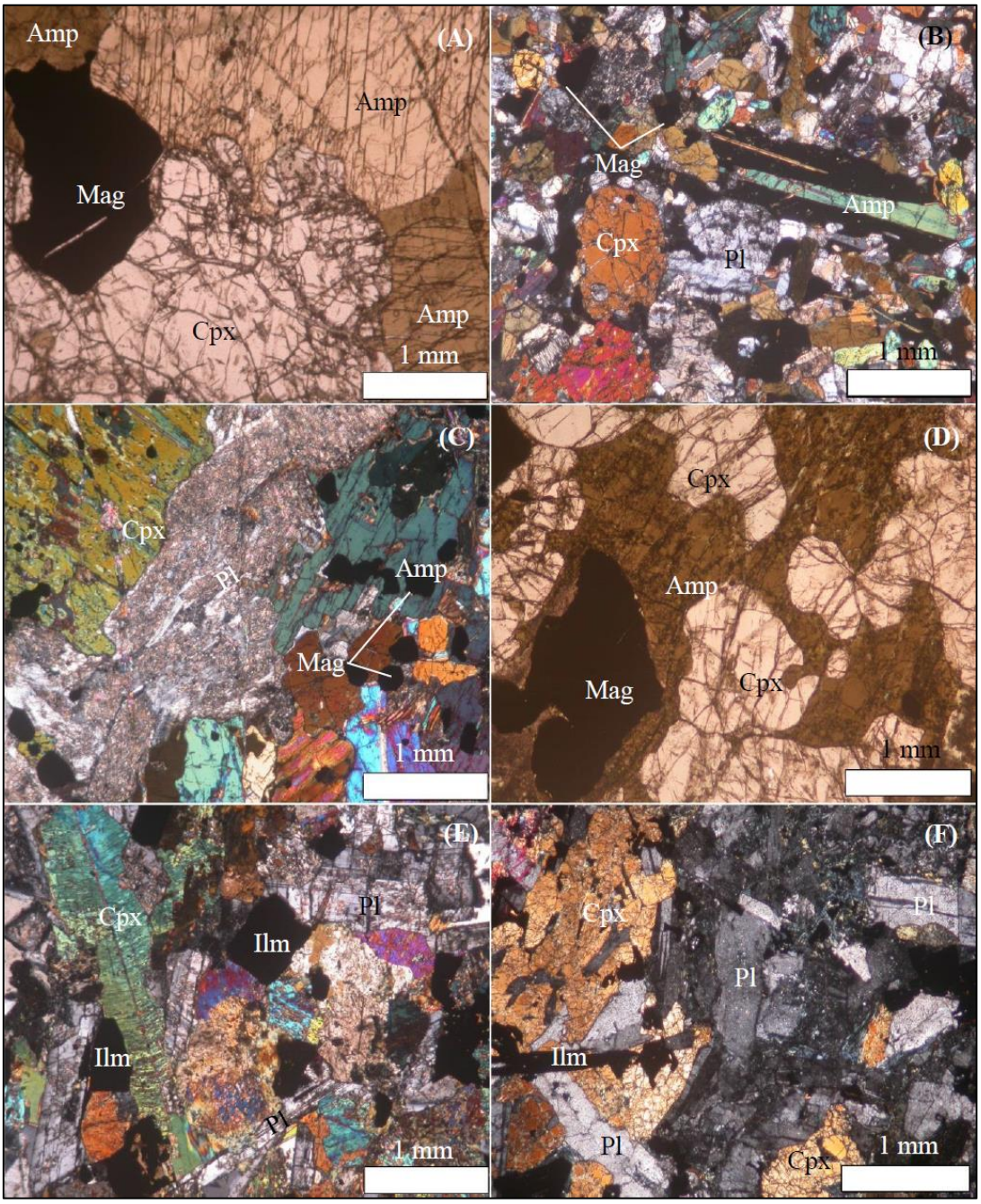


**Figure 1.4:** Photomicrographs of the Triassic gabbroic rocks of Chukotka (Crossed-nicols). (A) coarse grained hornblende-gabbro (IAB-type) showing euhedral crystals of amphibole in contact with altered plagioclase, (B) fine grained hornblende gabbros (IAB-type), (C) and (D) poikilitic texure in IAB-type gabbros, (E) and (F) OIB-type gabbros showing ophitic texture and ilmenite grains. Cpx, clinoopyroxene; Amp, amphibole; Pl, plagioclase; Mag, magnetite; Ilm, ilmenite.

#### 1.4.1.2. Amphibole

Amphiboles are the dominant ferromagnesian minerals in the IAB-type gabbroic rocks. The colour of hornblende minerals varies from light brown to green. They generally display sub-hedral to anhedral shape, but shows good cleavage (Fig. 1.4A). They usually occur as oikocrysts and enclose relatively small sized pyroxenes, plagioclase, opaque minerals and rarely apatite. Their grain size varies from 1 to 20 mm.

#### 1.4.1.3. Plagioclase

Plagioclase is not well preserved (partly to completely altered) in gabbros and is replaced by sericite minerals. However, few relict plagioclases from IAB-type gabbros are analyzed. They are usually twinned, but zoned plagioclase is rare. Plagioclase in OIB-type gabbros forms euhedral and sub-hedral tabular crystals and display ploysynthetic twinning where they are fresh.

#### 1.4.1.4. Biotite

Biotite is rarely present in IAB-type gabbros (mainly found in pyroxene-hornblende gabbro). They occur as a minor phase and inter-layered with chlorite minerals. Their grain size varies from 1.4 mm to 2 mm.

#### 1.4.1.5. Opaque

Opaque minerals such as magnetite and titano-magnetite are predominant in IAB-type gabbroic rocks, whereas ilmenite is common in the OIB-type gabbroic rocks (Fig. 1.4E and F). The size of titano-magnetite in the coarse grained hornblende gabbro (Sample #60; IAB-type) reaches as large as 2 mm. Opaque minerals are also occurring as inclusion within the amphibole minerals.

### 1.4.2. Basaltic rocks

Two groups of volcanic rocks are recognized based on their texture and whole-rock chemical analysis: (1) basaltic rocks such as ankaramites (Sample #69, #70 and #71) and pyroxene-phyric basalt (Sample #67) with clinopyroxene as a main phenocryst phase, and (2) basaltic andesites (Sample #55 and #56) containing hornblende and few clinopyroxene phenocryts (Fig. 1.5). We have also identified two lamprophyre samples based on their high modal abundance of amphibole phenocryst (Sample #74 and #77) (hereafter we explained these samples as basaltic rocks for the sake of simplicity). Basaltic rocks show sub-ophitic, porphyritic, glomeroporphyritic and glassy textures. The most common texture is porphyritic with phenocrysts of amphibole (mainly in lamprophyres), clinopyroxene and plagioclase minerals (Fig. 1.5). Rapid crystallization is indicated by the occurrence of glass (altered) in the groundmass of pyroxene-phyric basalt. The modal abundances of phenocrysts are in the range of 5-40%. Plagioclase phenocrysts occur in the hornblende basaltic andesite (~5%). Clinopyroxenes are the main phenocrysts in ankaramite (~40 vol. %) and pyroxene phyric basaltic rocks (~25 vol. %). The most common groundmass minerals include plagioclase, amphibole, Fe-Ti oxide, rare biotite, quartz and pyroxene. All these basaltic rocks display island-arc basalt type trace element patterns.

#### 1.4.2.1. Clinopyroxene

Clinopyroxene occur as elongated and prismatic crystals in basaltic rocks. Its shape varies from euhedral to anhedral (irregular). Clinopyroxene phenocrysts varies in size and reaches as large as 4.5 mm in basaltic andesite, 2.5 mm in pyroxene-phyric basalt and 3.5 mm in ankaramites, and 2.5 mm in lamprophyres (Fig. 1.5).

The color in a thinsection varies from light green, pinkish, to light yellow and pale brown. Some of these crystals show normal or oscillatory zoning and resorbed texture. They also occur as broken pieces in the pyroxene-phyric basalt and they exhibits well developed zoning (Fig. 1.5C and D). Clinopyroxene phenocrysts in basaltic andesite also display oscillatory zoning and locally contain plagioclase and ilmenite inclusion. Clinopyroxene phenocrysts in basaltic andesite are ubiquitously resorbed and are commonly twinned (e.g. in Sample #56).

#### 1.4.2.2. Plagioclase

Plagioclase in most basalt is not well preserved, but some in basaltic andesite and lamprophyre have survived. They occur as phenocrysts and groundmass in basaltic andesite and as only groundmass in ankaramites and lamprophyres. Albite-rich plagioclase occurs as fresh phenocryst in the basaltic andesite, where as anorthite-rich plagioclase likely more affected by alteration.

#### 1.4.2.3. Amphibole

Amphibole minerals occur in the ankaramite rocks only as groundmass, and as phenocrysts in the basaltic andesites and lamprophyres. They occur as elongated anhedral (rounded) and euhedral phenocrysts in basaltic andesite, but as they occur as subhedral and needle-like crystals in the lamprophyres. Amphibole phenocrysts are commonly glomerocrystic in lamprophyre samples. Their size reaches as large as 1cm in hornblende basaltic andesite (Fig. 1.3F). Some of the amphiboles from basaltic andesite (Sample #56; Fig. 1.5B) display resorption both in the core and along their margins. Their colour ranges from pale brown to dark brown. The euhedral amphibole phenocrysts in the basaltic andesite show clear oscillatory zoning (e.g. in Sample #55). In hornblende

basaltic andesite they occur in association with alkali feldspar and clinopyroxene phenocrysts. Amphibole phenocryts in the basaltic andesite locally exhibit twinning.

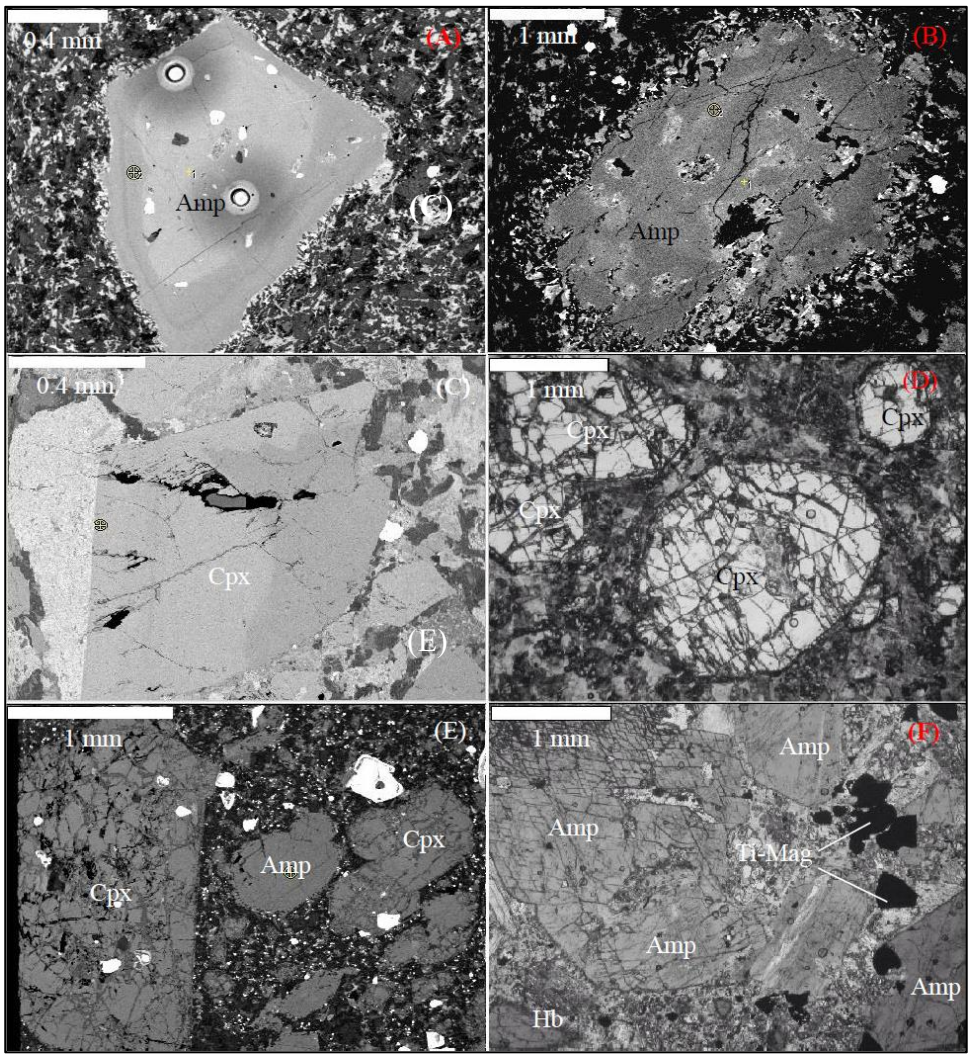


**Figure 1.5:** Backscatter electron (BSE) images illustrating the petrographic characteristics of the basaltic rocks. (A-B) Brown hornblende phenocrysts in basaltic andesites (Sample #55 and #56 respectively) displaying oscillatory zoning (A) and resorbed texture (B). (C) Fragment of clinopyroxene phenocryst with broken side in pyroxene-phyric basalt (Sample #67), showing evidence of incipient melting. (D) Open nicol view of ankaramite (Sample #69) showing porphyritic texture. (E-F) Lampropyre (Sample #77) exhibiting a cluster of euhedral to sub-hedral phenocrysts of clinopyroxene and hornblende (BSE image, E; open nicol view, F). Amp, amphibole; Cpx, clinopyroxene; Plg, plagioclase; Ti-Mag, Ti-Magnetite.

#### 1.4.2.4. Opaque

Opaque minerals such as iron-sulfide and magnetite are investigated from the pyroxene-phyric basalt and ankaramites and lamprophyres, respectively. They are irregular shaped or subhedral and occur as interstitial grains in hornblende and clinopyroxene phenocryst. They have variable crystal size, but mostly as large as 0.5 mm in lamprophyre, 0.2 mm in ankaramite and 0.065mm in pyroxene-phyric basalt. Ilmenite is present as an inclusion in amphibole and clinopyroxene phenocrysts and groundmass in basaltic andesite samples.

## 1.5. RESULTS

### 1.5.1. Whole-rock major and trace element composition

Representative, major element chemical data for the Triassic gabbroic and basaltic rocks of Chukotka are presented in Table 1.1. All the analyzed samples are tholeiitic in composition, although, one basaltic and one basaltic andesite samples plot on the dividing line between the calc-alkaline and tholeiitic fields on the $SiO_2$-$FeO_{Total}$/MgO diagram of Miyashiro (1974) (Fig. 1.6A). In the AFM diagram of Irvine and Baragar (1971), the studied samples plot above and on the demarcating line, showing a tholeiitic affinity, and following an iron enrichment trend (Fig. 1.6B). These rocks have Nb/Y ratios of 0.09-0.59, plotting in the sub-alkaline basalt field on the Nb/Y versus Zr/Ti diagram of Winchester and Floyd (1977) and Pearce (1996) (Fig. 1.6C), except one sample of OIB-type gabbro falling in the alkaline field. Variation diagrams for major element oxides against MgO wt. % are presented in Fig. 1.7A-F. Mg-number ($Mg\#=100\times Mg/(Mg+Fe^{2+})$) range from 48 to 66 for IAB-

type gabbros, around 40 for OIB-type gabbros, 63-65 for ankaramites (IAB-type), 57 for pyroxene phyric basalt (IAB-type), 51-54 for lamprophyres (IAB-type), and 43-50 for basaltic andesite (IAB-type) rocks (Table 1.1).

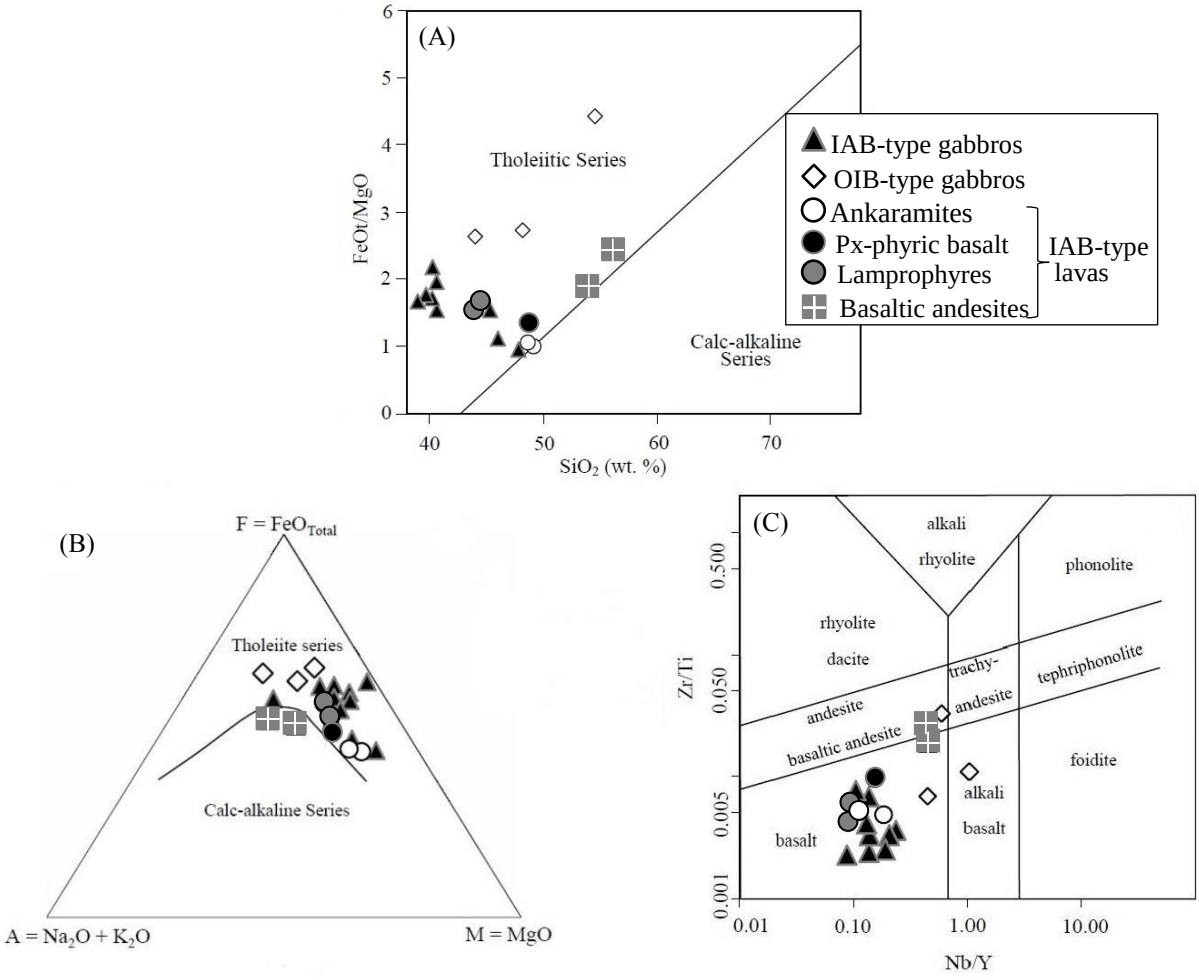


**Figure 1.6:** Classification diagrams for the mafic rocks of Chukotka: (A) FeOt/MgO versues $SiO_2$ (wt. %) diagram (after Miyashiro, 1974). (B) AFM ($Na_2O$+$K_2O$-$FeO_{Total}$-MgO) triangle diagram; (C) immobile element ratios such as Nb/Y vs Zr/Ti distinguishing subalkaline and alkaline basalts (Winchester and Floyd 1977, modified by Pearce, 1996).

The low to intermediate Mg-number of the studied samples suggests that these rocks do not represent primary, mantle-derived melts. This is consistent to the low concentrations of compatible trace element (such as Cr and Ni) in the studied samples.

The $TiO_2$ contents of all the studied samples are low (<2 wt. %) except OIB-type gabbros (4.3-5.3 wt. %). IAB-type gabbros have higher CaO contents (13-19 wt. %) (Except Sample #78, ~7 wt. %) compared to OIB-type gabbros (5-9 wt. %). OIB-type gabbros typically enriched in $FeO^*$ (16-18 wt. %) as compared to IAB-type gabbros (10-14 wt. %), and IAB-type basaltic rocks (~10 wt. %, ankaramites; 11 wt. %, pyroxene-phyric basalt; ~14 wt. %, lamprophyres and basaltic andesite samples 9-10 wt. %). Ankaramites have higher $CaO/Al_2O_3$ (0.99-1.04) ratios compared to pyroxene-phyric basalt, lamprophyres and basaltic andesites (0.83, 0.82-0.86 and 0.43-0.44, respectively). Moreover, ankaramite samples have high Cr/Ni (6.5-7.6), and Sc/Ni (~0.9) ratios, characteristic of arc ankaramites (Bardsell and Berry, 1990). Considering the above points Sample #75 (IAB-type gabbros) show similar characteristics to ankaramite samples, thus it may represent the intrusive equivalent of ankaramite lava. Gabbroic rocks generally have lower $K_2O$ and $Na_2O$ than the volcanic rocks. The $Na_2O$ concentrations in the studied samples increases with deceasing MgO content, whereas the $K_2O$ content of gabbroic rocks (except basaltic rocks) show more scattered trend (Fig. 1.7E and F).

Trace element compositions of the analysed samples are provided in Tables 1.1 and 1.2. Variation diagrams (Fig. 1.8A-F) show that the compatible elements (Ni and Cr) decrease with decreasing MgO. The Ni content of the studied samples are low, and even the most mafic ankaramite have low Ni (~81 ppm) at high Cr (>500 ppm).

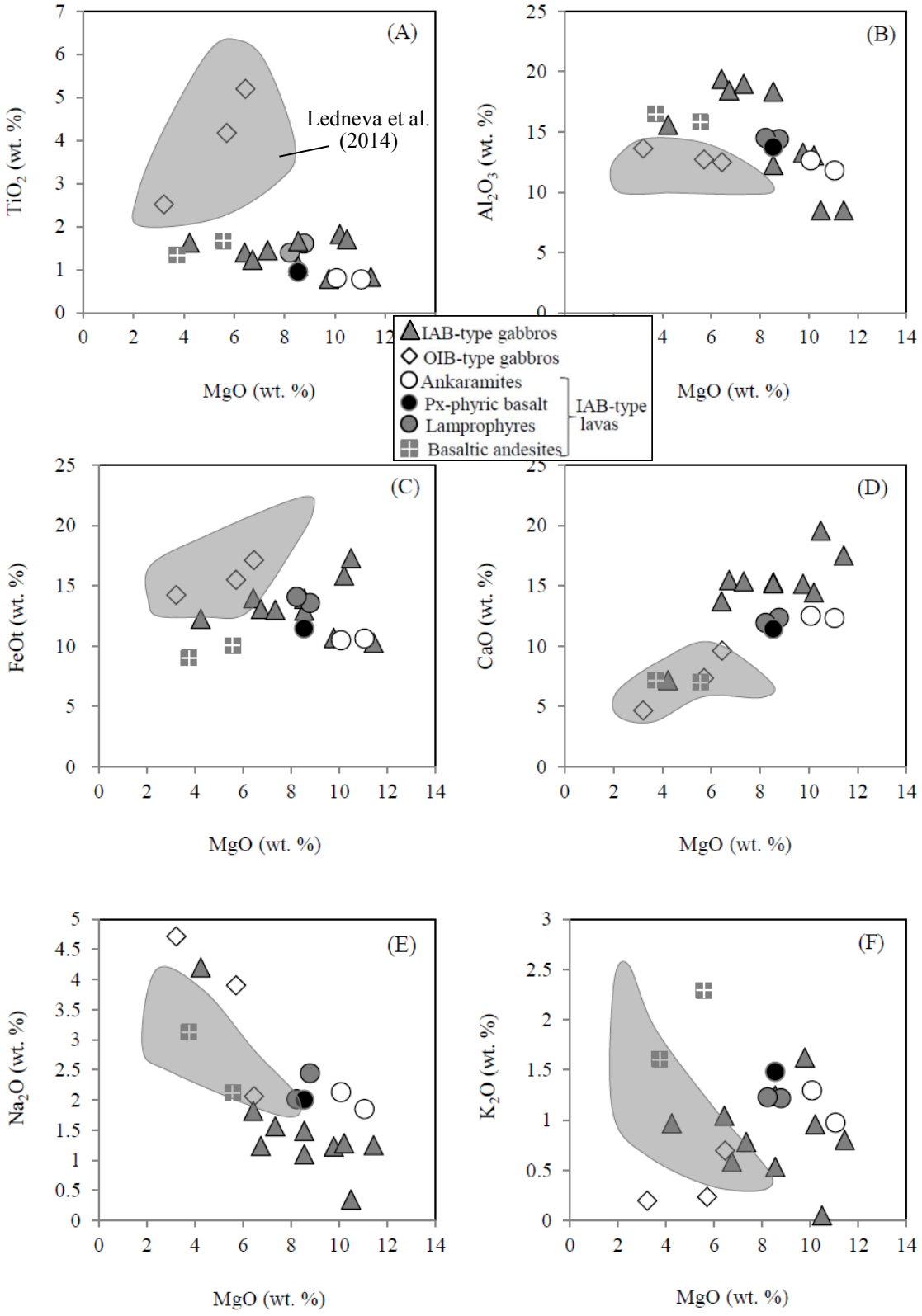


**Figure 1.7:** Plots of MgO (wt. %) vs $TiO_2$ (wt. %), $Al_2O_3$ (wt. %), FeOt (wt. %), CaO (wt. %), $Na_2O$ (wt. %) and $K_2O$ (wt. %) for Triassic mafic rocks of Chukotka, NE Russia. The shaded area displays the bulk-rock composition of gabbroic rocks reported by Ledneva et al. (2014).

Incompatible elements (Such as Zr and Nb) are very low in abundance for IAB-type gabbros and basalts but are high in OIB-type gabbros and basaltic andesite and increase with decreasing MgO. ΣREE is low in IAB-type gabbroic rocks (32-72 ppm), ankaramite (~38 ppm), pyroxene-pyric basalt (~63 ppm), and lamprophyres (52-56 ppm) but is high in basaltic andesites (~174 ppm) and OIB-type gabbros (138-175 ppm).

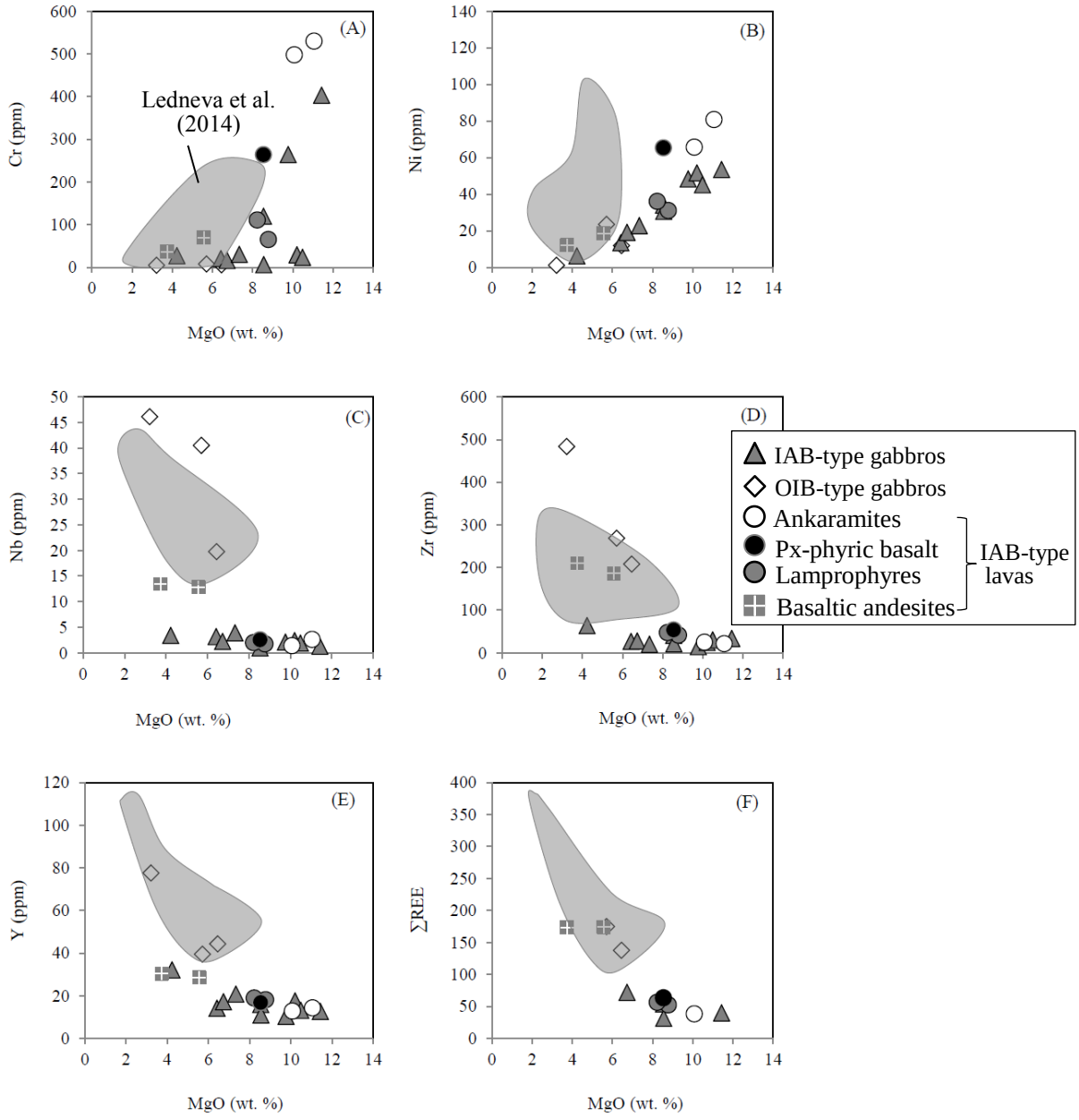


**Figure 1.8:** Variation diagrams of trace elements (ppm) vs. MgO (wt. %) for the Triassic mafic rocks of Chukotka.

In the primitive mantle normalized multi-trace elements plot normalized to the primitive mantle (Fig. 1.9), analysed IAB-type gabbroic and basaltic rocks are characterized by depletion of high field strength elements (HFSE) such as Nb, Ta, Zr and Hf relative to the neighbouring elements, similar to those of arc-type igneous rocks (Rudnick, 1995; Taylor and McLennan, 1995). They are depleted in HREE compared with N-MORB. In addition, these rocks exhibit depletion in Rb and Th relative to Ba and U, respectively, and show positive anomalies of Ba and K (and Pb in one IAB-type gabbro sample). However, the concentrations of Th and U in IAB-type gabbros are variable. All the analyzed IAB-type gabbroic and basaltic rocks have $Th_N/La_N$ <1, and two samples (Sample #75 of IAB-type gabbro and Sample #69 of basaltic rocks) have $Th_N/La_N$ ~1.2. The most basic intrusive rock (Sample #75 of IAB-type gabbros) is depleted in LREE compared to MREE similar to NMORB, but the former is more depleted in HREE (Fig. 1.9B). We see strong positive Sr anomalies in IAB-type gabbroic and basaltic rocks, whereas negative Sr anomalies in OIB-type gabbros. On the primitive mantle normalized REE plot (Fig. 1.9D), the hornblende basaltic andesites display elevated trace element and total REE concentration compared to the basaltic rocks. Basaltic andesites share similar patterns of depletion in HFSE (Nb, Ta) to those displayed by basaltic rocks. However, they do not show negative Zr and Hf anomalies (Fig. 1.9C). Basaltic andesite rocks show enrichment in Th ($(Th/La)_N$ >1.5) and U relative to HFSE (Nb/U=7.8-9.3). Moreover, they exhibit strong LREE enrichment ($(La/Yb)_N$= 7.38-7.74), with a slightly concave-upward heavy REE (HREE) distribution and have slight negative Eu anomalies (Eu/Eu* ~0.85) (Fig. 1.9D).

OIB-type gabbroic rocks can be distinguished from the rest of the studied samples based on the absence of

HFSE depletion, but show strong negative Sr anomalies. Moreover, their HFSE are slightly enriched relative to LREE ($(La/Nb)_N$ =0.69-1.01) (Fig. 1.9C) and Nb/U=33-58. The positive Ti anomaly in the OIB-type gabbros can be attributed to their high content of ilmenite.

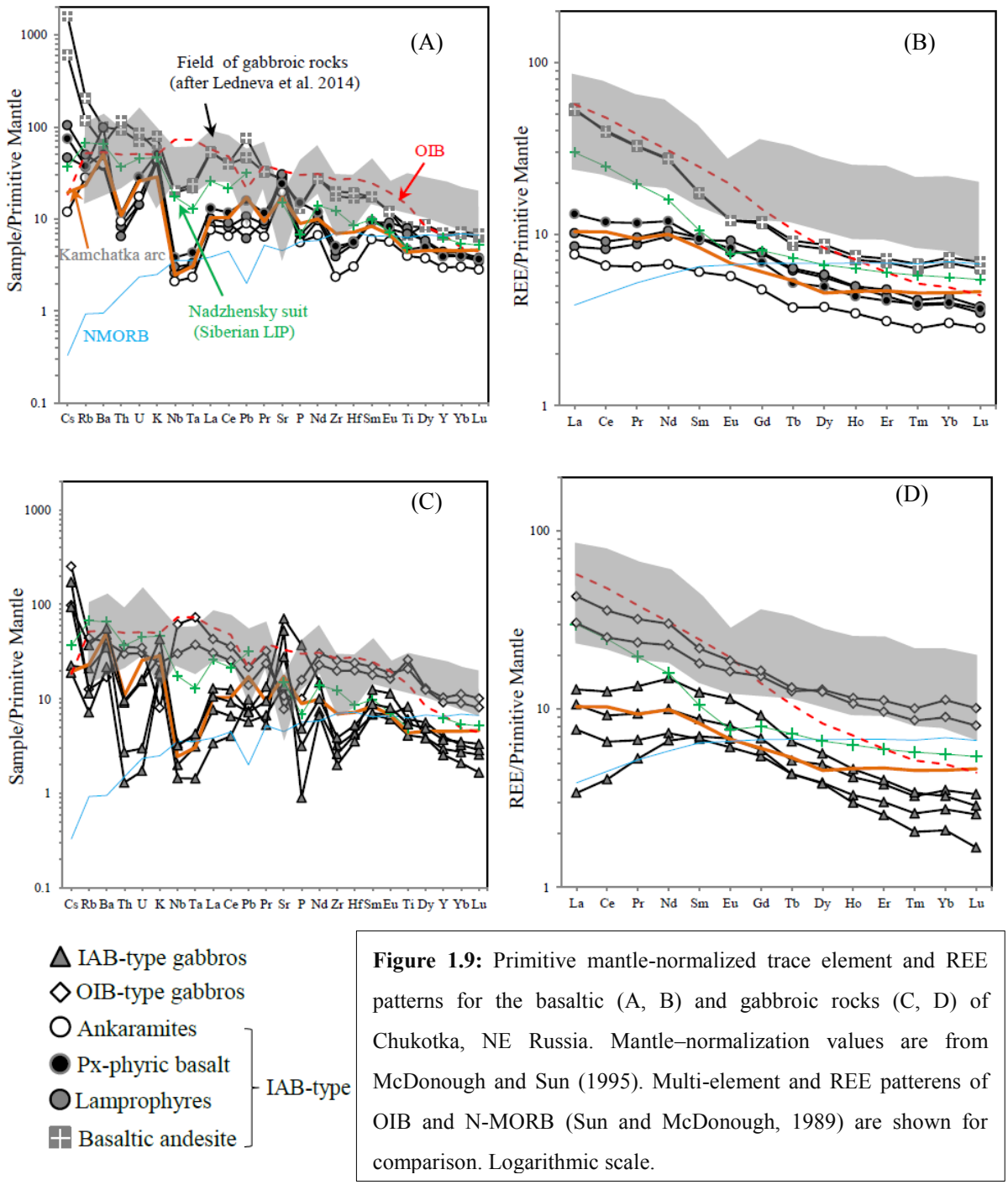


**Figure 1.9:** Primitive mantle-normalized trace element and REE patterns for the basaltic (A, B) and gabbroic rocks (C, D) of Chukotka, NE Russia. Mantle–normalization values are from McDonough and Sun (1995). Multi-element and REE patterens of OIB and N-MORB (Sun and McDonough, 1989) are shown for comparison. Logarithmic scale.

**Table 1.1:** Major and trace element compositions for the basaltic and gabbroic rocks of Chukotka, NE, Russia.

| Rock | Ankaramites | | Px-phyric basalt | Lamprophyres | | Basaltic andesites | | IAB-type gabbros | | | | | | | | | | OIB-type gabbros | | |
|---|---|---|---|---|---|---|---|---|---|---|---|---|---|---|---|---|---|---|---|---|
| Sample | #69 | #71 | #67 | #74 | #77 | 55 | #56 | #57 | #58 | #62 | #63 | #66 | #72 | #73 | #75 | #76 | #78 | #81 | #84 | #85 |
| Lat.(N) | 66˚ 45′26″ | 66˚ 45′26″ | 66˚ 45′40″ | 66˚ 45′13″ | 66˚ 45′10″ | 66˚ 43′22″ | 66˚ 43′22″ | 66˚ 44′24″ | 66˚ 44′22″ | 66˚ 44′10″ | 66˚ 44′10″ | 66˚ 45′0″ | 66˚ 45′17″ | 66˚ 45′13″ | 66˚ 45′10″ | 66˚ 45′10″ | 66˚ 45′10″ | 66˚ 46′52″ | 66˚ 47′17″ | 66˚ 56′37″ |
| Lon.(W) | 177˚ 17′31″ | 177˚ 17′31″ | 177˚ 17′45″ | 177˚ 17′30″ | 177˚ 17′15″ | 177˚ 17′42″ | 177˚ 17′42″ | 177˚ 23′47″ | 177˚ 23′46″ | 177˚ 24′4″ | 177˚ 24′4″ | 177˚ 20′51″ | 177˚ 17′28″ | 177˚ 17′30″ | 177˚ 17′15″ | 177˚ 17′15″ | 177˚ 17′26″ | 177˚ 21′37″ | 177˚ 22′7″ | 177˚ 40′25″ |
| Major oxides (wt.%; determined by XRF) | | | | | | | | | | | | | | | | | | | | |
| $SiO_2$ | 47.92 | 47.64 | 47.61 | 43.79 | 43.74 | 54.12 | 54.23 | 39.97 | 39.18 | 38.62 | 40.70 | 39.27 | 44.58 | 38.88 | 47.64 | 45.26 | 50.97 | 53.71 | 49.74 | 45.20 |
| $TiO_2$ | 0.79 | 0.74 | 0.92 | 1.36 | 1.60 | 1.67 | 1.29 | 1.70 | 1.67 | 1.41 | 1.22 | 1.35 | 1.06 | 1.75 | 0.82 | 0.77 | 1.58 | 2.47 | 4.31 | 5.32 |
| $Al_2O_3$ | 12.43 | 11.40 | 13.43 | 14.18 | 14.35 | 15.83 | 15.92 | 18.80 | 8.31 | 18.46 | 18.36 | 18.76 | 12.00 | 12.54 | 8.41 | 13.02 | 15.16 | 13.40 | 13.11 | 12.77 |
| $FeO^*$ | 10.30 | 10.27 | 11.21 | 13.78 | 13.54 | 10.04 | 8.68 | 14.27 | 16.94 | 12.65 | 13.01 | 13.51 | 12.69 | 15.23 | 10.17 | 10.48 | 11.93 | 14.00 | 15.99 | 17.54 |
| CaO | 12.31 | 11.90 | 11.17 | 11.67 | 12.32 | 6.99 | 6.92 | 15.58 | 19.18 | 14.94 | 15.39 | 13.27 | 14.99 | 13.88 | 17.36 | 14.85 | 6.96 | 4.57 | 7.60 | 9.84 |
| MgO | 9.94 | 10.70 | 8.37 | 8.06 | 8.78 | 5.58 | 3.61 | 8.77 | 10.28 | 7.14 | 6.71 | 6.22 | 8.38 | 9.82 | 11.34 | 9.59 | 4.12 | 3.17 | 5.90 | 6.61 |
| MnO | 0.22 | 0.20 | 0.22 | 0.27 | 0.31 | 0.15 | 0.11 | 0.15 | 0.16 | 0.17 | 0.18 | 0.17 | 0.19 | 0.22 | 0.19 | 0.17 | 0.21 | 0.21 | 0.27 | 0.21 |
| $K_2O$ | 1.27 | 0.94 | 1.45 | 1.20 | 1.21 | 2.29 | 1.55 | 0.55 | 0.05 | 0.76 | 0.58 | 1.01 | 1.22 | 0.92 | 0.80 | 1.59 | 0.94 | 0.19 | 0.24 | 0.71 |
| $Na_2O$ | 2.09 | 1.79 | 1.96 | 1.97 | 2.44 | 2.12 | 3.01 | 1.12 | 0.34 | 1.52 | 1.23 | 1.76 | 1.46 | 1.23 | 1.24 | 1.20 | 4.09 | 4.64 | 4.03 | 2.11 |
| $P_2O_5$ | 0.11 | 0.05 | 0.30 | 0.14 | 0.12 | 0.28 | 0.26 | 0.02 | 0.01 | 0.21 | 0.76 | 0.03 | 0.10 | 0.03 | 0.07 | 0.02 | 0.10 | 0.52 | 0.34 | 0.21 |
| Total | 98.53 | 95.63 | 97.88 | 97.95 | 99.92 | 100.17 | 96.54 | 102.52 | 96.12 | 95.55 | 99.59 | 95.35 | 98.07 | 94.50 | 99.14 | 96.95 | 96.06 | 97.41 | 103.31 | 102.48 |
| Mg# | 63.2 | 65.0 | 57.1 | 51.1 | 53.6 | 49.8 | 42.6 | 52.3 | 51.9 | 50.2 | 47.9 | 45.1 | 54.1 | 53.5 | 66.5 | 61.9 | 38.1 | 28.7 | 39.7 | 40.2 |
| LOI | 3.56 | | 3.18 | 1.53 | 3.10 | 0.94 | 1.00 | | | | 1.01 | | 1.18 | | 0.98 | | | | 1.60 | 1.19 |
| Trace elements (ppm; determined by XRF) | | | | | | | | | | | | | | | | | | | | |
| V | 316 | 296 | 325 | 522 | 580 | 224 | 159 | 578 | 622 | 434 | 426 | 468 | 464 | 669 | 334 | 327 | 404 | 189 | 517 | 731 |
| Cr | 466 | 530 | 286 | 102 | 62 | 59 | 35 | 18 | 23 | 30 | 24 | 20 | 109 | 29 | 358 | 364 | 27 | 4. | 5.2 | 1.7 |
| Ni | 67 | 81 | 72 | 32 | 27 | 18 | 6.5 | 26 | 45 | 23 | 14 | 13 | 28 | 52 | 56 | 48 | 6. | 1. | 15 | n.d |
| Rb | 20 | 14 | 28 | 36 | 27 | 156 | 88 | 6.7 | 0.9 | 8. | 8. | 13 | 28 | 12 | 16 | 39 | 219 | 5. | 11 | 33 |
| Sr | 380 | 312 | 460 | 534 | 524 | 547 | 521 | 969 | 203 | 1077 | 1188 | 839 | 481 | 449 | 259 | 628 | 615 | 111 | 161 | 215 |
| Ba | 243 | 177 | 324 | 246 | 605 | 691 | 455 | 149 | 56. | 306 | 276 | 375 | 311 | 159 | 220 | 533 | 416 | 98 | 165 | 309 |
| Y | 16 | 14 | 18 | 20 | 20 | 35 | 32 | 13 | 14 | 21 | 19 | 14 | 16 | 18 | 14 | 10 | 32 | 78 | 43 | 47 |
| Zr | 34 | 21 | 63 | 54 | 52 | 208 | 212 | 40 | 30 | 20 | 46 | 27 | 48 | 24 | 40 | 15 | 64 | 483 | 282 | 216 |
| Nb | 2.4 | 2.6 | 3.7 | 2.9 | 2.9 | 10.5 | 10.4 | 2.5 | 1.9 | 3.9 | 3.2 | 3.2 | 3.1 | 2.4 | 2.6 | 2.1 | 3.4 | 46 | 26 | 13.6 |

*Total Fe as FeO; n.d., not determined; LOI, loss on ignition.

**Table 1.2:** Bulk-rock trace element analyses of mafic rocks of Chukotka, NE Russia.

| Rock | Ankara-mite | Px-phyric basalt | Lamprophyres | | Basaltic andesites | | IAB-type gabbros | | | | OIB-type gabbros | |
|---|---|---|---|---|---|---|---|---|---|---|---|---|
| Sample | #69 | #67 | #74 | #77 | #55 | #56 | #57 | #72 | #75 | #6 | #84 | #85 |
| Lat. (N) | 66°45′26″ | 66°45′40″ | 66°45′13″ | 66°45′10″ | 66°43′22″ | 66°43′22″ | 66°44′24″ | 66°45′17″ | 66°45′10″ | 66°44′10″ | 66°47′17″ | 66°56′37″ |
| Lon. (W) | 177°17′31″ | 177°17′45″ | 177°17′30″ | 177°17′15″ | 177°17′42″ | 177° 17′42″ | 177°23′47″ | 177°17′28″ | 177°17′15″ | 177°24′4″ | 177°22′7″ | 177°40′25″ |
| Determined by LA-ICP-MS | | | | | | | | | | | | |
| Sc | 58.4 | 48.9 | 92.3 | 92.3 | 25.5 | 20.4 | 62.7 | 82.7 | 103.2 | 33.7 | 34.9 | 49.4 |
| Ti | 8200 | 9200 | 12200 | 13000 | 13400 | 11400 | 14000 | 10400 | 8400 | 11700 | 27800 | 34200 |
| V | 390 | 395 | 552 | 624 | 273 | 213 | 602 | 543 | 401 | 505 | 468 | 614 |
| Cr | 498 | 264 | 110 | 64.9 | 69.5 | 36.4 | 6.0 | 119 | 403 | 16.2 | 7.3 | 5.5 |
| Co | 38.6 | 38.7 | 30.4 | 41.9 | 18.2 | 14.1 | 48.0 | 46. | 41.8 | 32.2 | 41.4 | 47.9 |
| Ni | 65.6 | 65.3 | 36.0 | 30.9 | 18.5 | 12.1 | 30.6 | 33.9 | 53.4 | 19.1 | 23.4 | 11.9 |
| Rb | 16.9 | 22.5 | 29.9 | 22.2 | 123.5 | 70.5 | 4.3 | 22.3 | 12.6 | 6.9 | 7.6 | 26.4 |
| Sr | 388 | 482 | 608 | 553 | 536 | 540 | 1045 | 549 | 274 | 1403 | 155 | 213 |
| Y | 12.7 | 16.8 | 18.9 | 18.1 | 28.5 | 30.4 | 11.0 | 15.9 | 12.7 | 17.2 | 39.5 | 44.3 |
| Zr | 25 | 53 | 47 | 41 | 186 | 210 | 21 | 41 | 34 | 27 | 269 | 208 |
| Nb | 1.4 | 2.5 | 2.0 | 1.7 | 12.8 | 13.4 | 1.0 | 2.1 | 1.3 | 2.2 | 40.5 | 19.8 |
| Cs | 0.25 | 1.57 | 2.19 | 0.97 | 33.4 | 12.59 | 0.40 | 1.97 | 0.47 | 3.61 | 2.05 | 5.30 |
| Ba | 261 | 345 | 250 | 653 | 661 | 423 | 143 | 367 | 231 | 316 | 112 | 264 |
| La | 4.9 | 8.5 | 6.5 | 5.5 | 34.1 | 34.9 | 2.2 | 6.9 | 5.0 | 8.4 | 27.8 | 19.7 |
| Ce | 10.9 | 19.7 | 15.2 | 13.7 | 67.2 | 65.9 | 6.8 | 15.5 | 11.0 | 21.0 | 59.9 | 42.4 |
| Pr | 1.6 | 2.9 | 2.4 | 2.2 | 8.3 | 8.2 | 1.3 | 2.4 | 1.7 | 3.4 | 8.1 | 6.0 |
| Nd | 8.3 | 14.9 | 13.1 | 12.1 | 34.6 | 34.1 | 8.3 | 12.5 | 9.2 | 18.6 | 37.7 | 28.6 |
| Sm | 2.4 | 3.8 | 3.9 | 3.8 | 7.0 | 7.1 | 2.9 | 3.6 | 2.8 | 5.0 | 8.9 | 7.3 |
| Eu | 0.9 | 1.3 | 1.2 | 1.4 | 1.8 | 1.9 | 1.1 | 1.2 | 0.9 | 1.8 | 2.9 | 2.5 |
| Gd | 2.6 | 3.7 | 4.3 | 4.2 | 6.3 | 6.4 | 3.2 | 3.7 | 3.0 | 5.0 | 8.9 | 8.3 |
| Tb | 0.4 | 0.5 | 0.6 | 0.6 | 0.9 | 0.9 | 0.4 | 0.5 | 0.4 | 0.7 | 1.3 | 1.2 |
| Dy | 2.5 | 3.3 | 3.9 | 3.8 | 5.5 | 5.8 | 2.6 | 3.3 | 2.6 | 3.8 | 8.4 | 8.7 |
| Ho | 0.5 | 0.6 | 0.7 | 0.7 | 1.1 | 1.1 | 0.4 | 0.6 | 0.5 | 0.7 | 1.6 | 1.7 |
| Er | 1.4 | 1.8 | 2.1 | 1.9 | 3.0 | 3.2 | 1.1 | 1.7 | 1.3 | 1.8 | 4.2 | 4.9 |
| Tm | 0.2 | 0.3 | 0.3 | 0.3 | 0.4 | 0.5 | 0.1 | 0.2 | 0.2 | 0.2 | 0.6 | 0.7 |
| Yb | 1.3 | 1.8 | 1.9 | 1.7 | 3.0 | 3.2 | 0.9 | 1.5 | 1.2 | 1.4 | 4.0 | 5.0 |
| Lu | 0.2 | 0.2 | 0.3 | 0.2 | 0.4 | 0.5 | 0.1 | 0.2 | 0.2 | 0.2 | 0.5 | 0.7 |
| Hf | 0.86 | 1.58 | 1.60 | 1.52 | 4.77 | 5.43 | 1.00 | 1.49 | 1.24 | 1.19 | 6.77 | 5.65 |
| Ta | 0.09 | 0.16 | 0.12 | 0.12 | 0.81 | 0.89 | 0.05 | 0.16 | 0.12 | 0.15 | 2.69 | 1.38 |
| Pb | 1.34 | 2.37 | 0.93 | 1.60 | 11.33 | 7.01 | 1.48 | 1.08 | 0.86 | 1.12 | 3.25 | 2.10 |
| Th | 0.75 | 0.93 | 0.66 | 0.52 | 7.44 | 9.38 | 0.10 | 0.77 | 0.74 | 0.22 | 2.84 | 2.40 |
| U | 0.35 | 0.57 | 0.29 | 0.28 | 1.38 | 1.72 | 0.03 | 0.32 | 0.31 | 0.06 | 0.69 | 0.61 |
| Eu/Eu* | 1.07 | 1.03 | 0.91 | 1.08 | 0.85 | 0.84 | 1.06 | 1.04 | 1.00 | 1.07 | 0.99 | 0.98 |
| ΣREE | 38.1 | 63.3 | 56.4 | 52.1 | 174 | 174 | 31.4 | 53.8 | 40.0 | 72.0 | 175 | 138 |
| La/Sm | 2.04 | 2.24 | 1.67 | 1.45 | 4.87 | 4.92 | 0.76 | 1.92 | 1.79 | 1.68 | 3.12 | 2.69 |
| Sm/Yb | 1.85 | 2.11 | 2.05 | 2.24 | 2.33 | 2.22 | 3.22 | 2.40 | 2.33 | 3.57 | 2.23 | 1.46 |
| Dy/Yb | 1.92 | 1.83 | 2.05 | 2.24 | 1.83 | 1.81 | 2.89 | 2.20 | 2.17 | 2.71 | 2.10 | 1.74 |
| (La/Nb) | 3.62 | 3.42 | 3.35 | 3.24 | 2.71 | 2.64 | 2.33 | 3.32 | 3.84 | 3.82 | 0.69 | 1.01 |
| (Th/Ta) | 4.03 | 2.69 | 2.57 | 1.97 | 4.25 | 4.89 | 0.90 | 2.25 | 2.94 | 0.69 | 0.45 | 0.80 |

Note: Eu/Eu*= $EuN/\sqrt{SmN \times GdN}$; subscript N denotes normalized to Primitive mantle (McDonough and Sun, 1995).

## 1.5.2. MINERAL CHEMISTRY

### 1.5.2.1. Major element chemistry of minerals in gabbroic rocks

#### 1.5.2.1.1. Clinopyroxene

The chemical composition of clinopyroxene grains from IAB-type and OIB-type gabbroic rocks are listed in Table 1.3. In the conventional classification diagram (Morimoto et al. 1988), clinopyroxenes of IAB-type gabbros ranges from augite to diopside, but some compositions plot above the 50% Ca line, whereas those in OIB-type gabbros mainly ploted in the augite field (Fig. 1.10). Generally, on a pyroxene quadrilateral diagram the clinopyroxene compositions of IAB-type gabbros exhibit an alkaline trend (Wo increase with Fs) whereas clinopyroxenes from OIB-type gabbros follow a tholeiitic trend (Wo decrease with En). Clinopyroxenes in IAB-type gabbroic rocks show lower $TiO_2$ (0.17-1.25 wt. %, average 0.70 wt. %) and higher CaO (22.0-25.1 wt. %, average 22.9 wt. %) and Mg# (76.9-90.2, average 78.3) than those in OIB-type gabbros (0.7-2.7, average 1.0 wt. %; 18.3-21.1, average 20.1 wt.% and 53.2-70.6, average, 63.6, respectively; Fig. 1.11). Clinopyroxene in one IAB-type gabbro sample (Sample #78) has lower CaO (16.9-19.5 wt. %) than other clinopyroxene. The clinopyroxenes from both IAB-type and OIB-type gabbroic rocks are characterized by Ti contents decreasing with Al (Fig. not shown). However, the Ti/Al ratios in clinopyroxenes of the IAB-type gabbros clinopyroxenes are lower than those in the OIB-type gabbros.

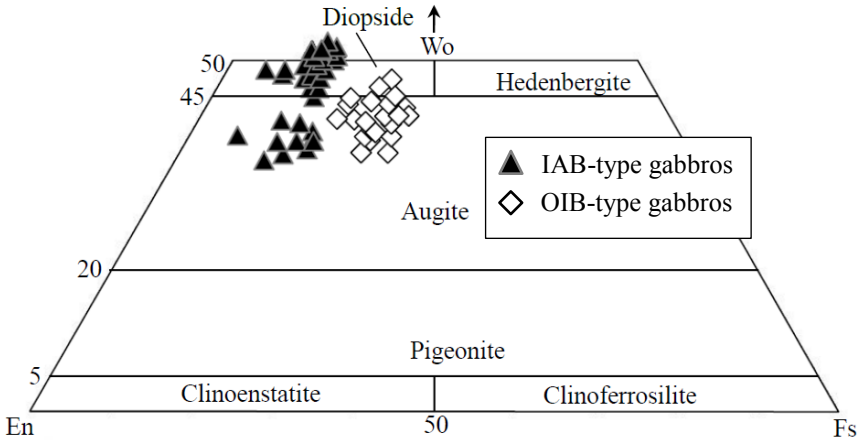


**Figure 1.10:** Pyroxene quadrilateral diagram showing the composition of pyroxene from the gabbroic rocks in the Chukotka area, NE, Russia. Nomenclature (after Morimoto et al. 1988).

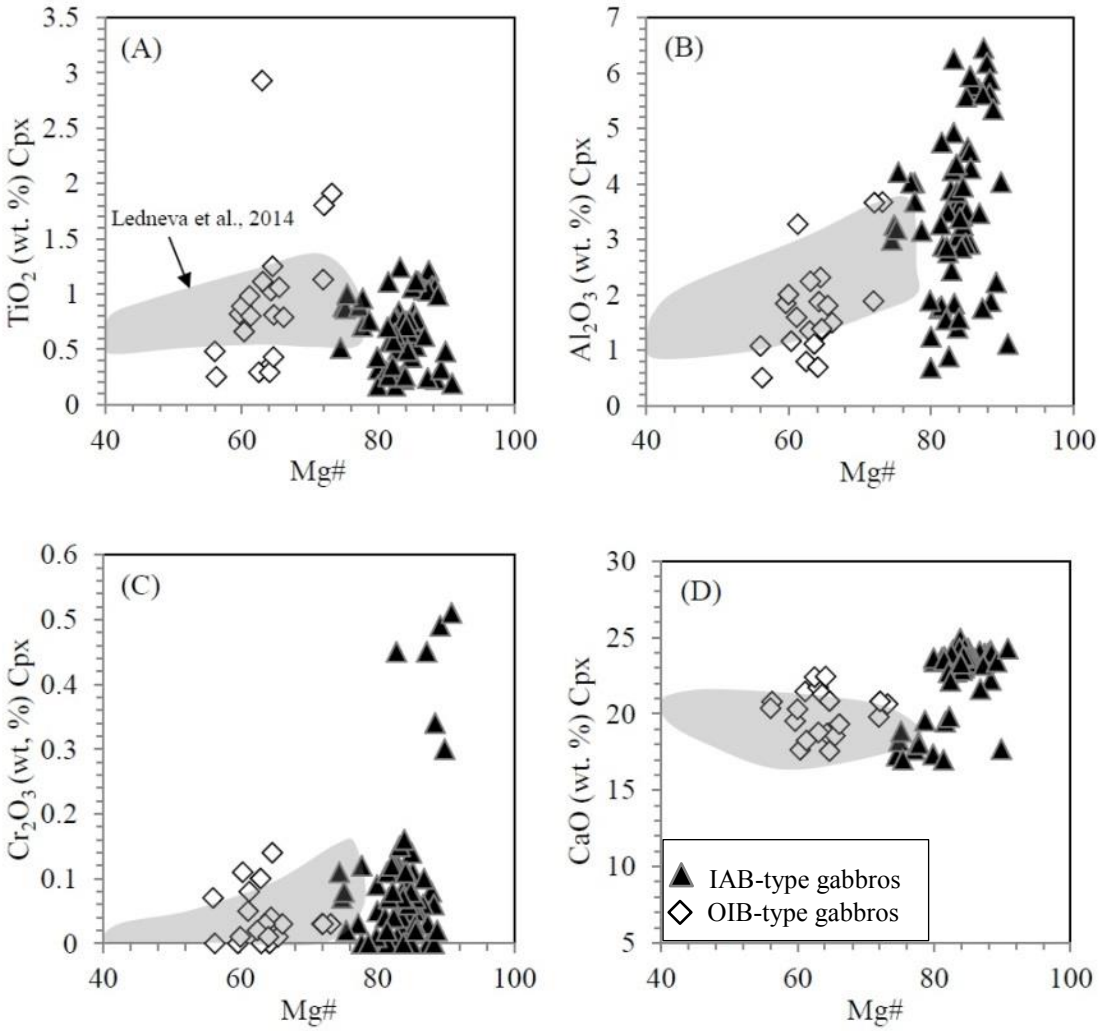


**Figure 1.11**: Major element chemistry of clinopyroxene crystals from the gabbroic rocks of Chukotka. The shaded circle showing clinopyroxene composition of gabbroic rocks reported by Ledneva et al. (2014).

**Table 1.3:** Representative electron-microprobe analyses of clinopyroxene crystals in gabbroic rocks of Chukotka, NE Russia.

| Rock | IAB-type gabbros | | | | | | | | | | | | | | | | |
|---|---|---|---|---|---|---|---|---|---|---|---|---|---|---|---|---|---|
| Sample | #57 | | | | | | #58 | | | | #60 | | | #62 | | | |
| Mineral | Cpx1 | Cpx2 | Cpx3 | Cpx4 | Cpx5 | Cpx6 | Cpx1 | Cpx2 | Cpx3 | Cpx4 | Cpx1 | Cpx2 | Cpx3 | Cpx1 | Cpx4 | Cpx5 | Cpx6 |
| | core | core | core | core | core | core | core | core | core | core | core | core | core | core | core | core | core |
| $SiO_2$ | 46.88 | 47.11 | 44.14 | 47.71 | 48.47 | 49.01 | 48.07 | 47.15 | 49.44 | 49.54 | 47.83 | 47.97 | 48.8 | 48.89 | 50.24 | 51.87 | 49.81 |
| $TiO_2$ | 1.21 | 1.07 | 1.06 | 1.06 | 1.04 | 0.83 | 1.24 | 1.11 | 1.06 | 0.75 | 1.03 | 0.99 | 0.78 | 0.84 | 0.62 | 0.66 | 0.77 |
| $Al_2O_3$ | 6.45 | 6.18 | 5.88 | 5.62 | 5.71 | 4.65 | 6.25 | 5.78 | 5.57 | 4.92 | 5.61 | 5.34 | 4.58 | 4.24 | 3.6 | 3.89 | 3.62 |
| $Cr_2O_3$ | 0 | 0.08 | | 0.06 | 0.06 | 0.11 | 0.05 | 0.05 | | 0.04 | 0.03 | 0.02 | 0.05 | 0.12 | 0.07 | 0.45 | 0.11 |
| FeO | 6.65 | 6.8 | 6.06 | 6.49 | 6.94 | 6.76 | 7.76 | 7.5 | 7.77 | 6.79 | 6.83 | 6.61 | 6.59 | 6.91 | 6.79 | 6.75 | 6.83 |
| Mno | 0.17 | 0.06 | 0.12 | 0.11 | 0.09 | 0.15 | 0.03 | 0.08 | 0.11 | 0.12 | 0.17 | 0.06 | 0.14 | | | | |
| MgO | 12.45 | 12.71 | 12 | 12.85 | 13.19 | 13.25 | 12.69 | 12.5 | 13.25 | 13.6 | 13.02 | 13.17 | 13.16 | 12.88 | 13.45 | 13.93 | 13.32 |
| CaO | 23.93 | 23.94 | 22.22 | 24.14 | 24.08 | 23.84 | 23.88 | 23.58 | 24.28 | 22.88 | 23.37 | 23.44 | 23.3 | 23.23 | 23.68 | 24.17 | 23.3 |
| $Na_2O$ | 0.2 | 0.17 | 0.2 | 0.22 | 0.18 | 0.2 | 0.17 | 0.25 | 0.23 | 0.29 | 0.31 | 0.37 | 0.35 | 0.39 | 0.34 | 0.36 | 0.37 |
| Total | 97.94 | 98.12 | 91.68 | 98.26 | 99.76 | 98.8 | 100.14 | 98 | 101.71 | 98.93 | 98.2 | 97.97 | 97.75 | 97.5 | 98.79 | 102.08 | 98.13 |
| Cations (O=6) | | | | | | | | | | | | | | | | | |
| Si | 1.791 | 1.796 | 1.798 | 1.814 | 1.816 | 1.851 | 1.799 | 1.805 | 1.822 | 1.86 | 1.819 | 1.826 | 1.859 | 1.869 | 1.892 | 1.888 | 1.889 |
| Al | 0.29 | 0.278 | 0.282 | 0.252 | 0.252 | 0.207 | 0.276 | 0.261 | 0.242 | 0.218 | 0.251 | 0.24 | 0.206 | 0.191 | 0.16 | 0.167 | 0.162 |
| Ti | 0.035 | 0.031 | 0.033 | 0.03 | 0.029 | 0.023 | 0.035 | 0.032 | 0.029 | 0.021 | 0.03 | 0.028 | 0.022 | 0.024 | 0.017 | 0.018 | 0.022 |
| Al | 0.29 | 0.278 | 0.282 | 0.252 | 0.252 | 0.207 | 0.276 | 0.261 | 0.242 | 0.218 | 0.251 | 0.24 | 0.206 | 0.191 | 0.16 | 0.167 | 0.162 |
| $Cr^{3+}$ | 0 | 0.002 | | 0.002 | 0.002 | 0.003 | 0.001 | 0.002 | | 0.001 | 0.001 | 0.001 | 0.001 | 0.004 | 0.002 | 0.013 | 0.003 |
| $Fe^{2+}$ | 0.213 | 0.217 | 0.206 | 0.207 | 0.217 | 0.213 | 0.243 | 0.24 | 0.239 | 0.213 | 0.217 | 0.211 | 0.21 | 0.221 | 0.214 | 0.206 | 0.217 |
| Mn | 0.005 | 0.002 | 0.004 | 0.003 | 0.003 | 0.005 | 0.001 | 0.003 | 0.003 | 0.004 | 0.005 | 0.002 | 0.004 | | | | |
| Mg | 0.709 | 0.722 | 0.729 | 0.728 | 0.736 | 0.746 | 0.708 | 0.713 | 0.728 | 0.761 | 0.738 | 0.747 | 0.747 | 0.734 | 0.755 | 0.756 | 0.753 |
| Ca | 0.979 | 0.978 | 0.97 | 0.984 | 0.967 | 0.965 | 0.958 | 0.967 | 0.959 | 0.92 | 0.952 | 0.956 | 0.951 | 0.952 | 0.956 | 0.943 | 0.947 |
| Na | 0.015 | 0.013 | 0.016 | 0.016 | 0.013 | 0.015 | 0.013 | 0.018 | 0.017 | 0.021 | 0.023 | 0.027 | 0.026 | 0.029 | 0.025 | 0.025 | 0.028 |
| Total | 4.037 | 4.039 | 4.038 | 4.036 | 4.035 | 4.028 | 4.034 | 4.041 | 4.039 | 4.019 | 4.036 | 4.038 | 4.026 | 4.024 | 4.021 | 4.016 | 4.021 |
| Mg# | 76.89 | 76.89 | 77.97 | 77.86 | 77.23 | 77.79 | 74.45 | 74.82 | 75.28 | 78.13 | 77.28 | 77.97 | 78.06 | 76.86 | 77.92 | 78.58 | 77.63 |
| Wo | 51.49 | 51.02 | 50.92 | 51.28 | 50.36 | 50.16 | 50.18 | 50.36 | 49.79 | 48.57 | 49.92 | 49.95 | 49.84 | 49.92 | 49.66 | 49.50 | 49.40 |
| En | 37.29 | 37.66 | 38.28 | 37.93 | 38.33 | 38.77 | 37.09 | 37.14 | 37.79 | 40.18 | 38.69 | 39.03 | 39.15 | 38.49 | 39.22 | 39.68 | 39.28 |
| Fs | 11.22 | 11.32 | 10.81 | 10.79 | 11.30 | 11.07 | 12.73 | 12.50 | 12.41 | 11.25 | 11.38 | 11.02 | 11.01 | 11.59 | 11.12 | 10.81 | 11.32 |

*Total Fe expressed as FeO; Mg#= 100×Mg ($Mg+Fe^{2+}$).
Abbreviations: Wo, wollastonite; En, enstatite; Fs, ferrosilite.

**Table 1.3:** (*Continued*)

| Rock | IAB-type gabbros | | | | | | | | | | | | | | | | |
|---|---|---|---|---|---|---|---|---|---|---|---|---|---|---|---|---|---|
| Sample | #63 | | | | | | #64 | | | | #72 | | | | | | |
| Mineral | Cpx1 | Cpx2 | Cpx3 | Cpx4 | Cpx6 | Cpx7 | Cpx2 | Cpx3 | Cpx4 | Cpx5 | Cpx1 | Cpx2 | Cpx3 | | Cpx4 | Cpx5 | Cpx6 |
| | core | core | core | core | core | core | core | core | core | core | core | core | core | rim | core | core | core |
| $SiO_2$ | 49.25 | 50.55 | 50.52 | 51.18 | 51.67 | 53.67 | 50.92 | 50.3 | 50.92 | 49.91 | 49.68 | 53.16 | 49.99 | 53.25 | 53.32 | 50.93 | 52.3 |
| $TiO_2$ | 0.71 | 0.67 | 0.74 | 0.75 | 0.53 | 0.5 | 0.75 | 0.71 | 0.65 | 0.76 | 0.59 | 0.32 | 0.43 | 0.3 | 0.17 | 0.23 | 0.17 |
| $Al_2O_3$ | 3.42 | 3.03 | 3.64 | 3.61 | 2.92 | 2.44 | 3.05 | 3.5 | 3.25 | 3.85 | 4.35 | 1.24 | 2.92 | 1.75 | 0.68 | 1.4 | 0.88 |
| $Cr_2O_3$ | 0.09 | 0.02 | 0.04 | 0.07 | 0.03 | 0.01 | | 0.14 | 0.09 | 0.08 | 0.08 | 0.05 | 0.08 | 0.04 | 0.09 | 0.07 | 0.12 |
| FeO | 6.78 | 6.85 | 6.62 | 7.43 | 6.51 | 7.37 | 5.76 | 6.4 | 6.52 | 6.34 | 7.72 | 7.42 | 6.61 | 7.7 | 7.92 | 7.72 | 6.4 |
| Mno | 0.26 | 0.24 | 0.37 | 0.28 | 0.27 | 0.42 | 0.18 | 0.25 | 0.29 | 0.2 | 0.09 | 0.37 | 0.25 | 0.12 | 0.27 | 0.34 | 0.17 |
| MgO | 13.25 | 13.77 | 13.5 | 13.79 | 14.28 | 14.59 | 13.86 | 13.69 | 13.89 | 13.39 | 13.51 | 14.01 | 14 | 14.58 | 14.07 | 13.28 | 14.04 |
| CaO | 23.02 | 23.08 | 23.56 | 23.75 | 23.64 | 24.11 | 24.91 | 23.9 | 23.77 | 23.78 | 23.25 | 23.42 | 23.68 | 23.67 | 23.64 | 24.28 | 23.94 |
| $Na_2O$ | 0.39 | 0.41 | 0.37 | 0.42 | 0.42 | 0.36 | | 0.26 | 0.31 | 0.25 | 0.27 | 0.49 | 0.04 | 0.32 | 0.43 | 0.3 | 0.33 |
| Total | 97.17 | 98.62 | 99.36 | 101.28 | 100.27 | 103.47 | 99.43 | 99.15 | 99.69 | 98.56 | 99.54 | 100.48 | 98 | 101.73 | 100.59 | 98.55 | 98.35 |
| Cations (O=6) | | | | | | | | | | | | | | | | | |
| Si | 1.889 | 1.907 | 1.892 | 1.886 | 1.914 | 1.93 | 1.902 | 1.888 | 1.899 | 1.883 | 1.865 | 1.969 | 1.9 | 1.947 | 1.977 | 1.939 | 1.975 |
| Al | 0.155 | 0.135 | 0.161 | 0.157 | 0.127 | 0.103 | 0.134 | 0.155 | 0.143 | 0.171 | 0.192 | 0.054 | 0.131 | 0.076 | 0.03 | 0.063 | 0.039 |
| Ti | 0.02 | 0.019 | 0.021 | 0.021 | 0.015 | 0.013 | 0.021 | 0.02 | 0.018 | 0.021 | 0.017 | 0.009 | 0.012 | 0.008 | 0.005 | 0.007 | 0.005 |
| Al | 0.155 | 0.135 | 0.161 | 0.157 | 0.127 | 0.103 | 0.134 | 0.155 | 0.143 | 0.171 | 0.192 | 0.054 | 0.131 | 0.076 | 0.03 | 0.063 | 0.039 |
| $Cr^{3+}$ | 0.003 | 0.001 | 0.001 | 0.002 | | | | 0.004 | 0.003 | 0.002 | 0.002 | 0.001 | 0.002 | 0.001 | 0.003 | 0.002 | 0.004 |
| $Fe^{2+}$ | 0.218 | 0.216 | 0.207 | 0.229 | 0.202 | 0.222 | 0.18 | 0.201 | 0.203 | 0.2 | 0.242 | 0.23 | 0.21 | 0.235 | 0.246 | 0.246 | 0.202 |
| Mn | 0.009 | 0.008 | 0.012 | 0.009 | 0.008 | 0.013 | 0.006 | 0.008 | 0.009 | 0.006 | 0.003 | 0.012 | 0.008 | 0.004 | 0.008 | 0.011 | 0.006 |
| Mg | 0.758 | 0.774 | 0.753 | 0.758 | 0.788 | 0.782 | 0.772 | 0.766 | 0.772 | 0.753 | 0.756 | 0.773 | 0.793 | 0.795 | 0.778 | 0.753 | 0.79 |
| Ca | 0.946 | 0.933 | 0.946 | 0.938 | 0.938 | 0.929 | 0.997 | 0.961 | 0.95 | 0.961 | 0.935 | 0.929 | 0.964 | 0.927 | 0.939 | 0.99 | 0.968 |
| Na | 0.029 | 0.03 | 0.027 | 0.03 | 0.03 | 0.025 | | 0.019 | 0.023 | 0.019 | 0.019 | 0.035 | 0.003 | 0.023 | 0.031 | 0.022 | 0.024 |
| Total | 4.027 | 4.023 | 4.02 | 4.03 | 4.022 | 4.017 | 4.012 | 4.022 | 4.02 | 4.016 | 4.029 | 4.011 | 4.021 | 4.015 | 4.014 | 4.031 | 4.009 |
| Mg# | 77.66 | 78.18 | 78.44 | 76.80 | 79.60 | 77.89 | 81.09 | 79.21 | 79.18 | 79.01 | 75.75 | 77.07 | 79.06 | 77.18 | 75.97 | 75.37 | 79.64 |
| Wo | 49.22 | 48.52 | 49.63 | 48.73 | 48.65 | 48.06 | 51.15 | 49.84 | 49.35 | 50.21 | 48.37 | 48.08 | 49.01 | 47.37 | 47.83 | 49.77 | 49.39 |
| En | 39.44 | 40.25 | 39.51 | 39.38 | 40.87 | 40.45 | 39.61 | 39.73 | 40.10 | 39.34 | 39.11 | 40.01 | 40.31 | 40.62 | 39.63 | 37.86 | 40.31 |
| Fs | 11.34 | 11.23 | 10.86 | 11.89 | 10.48 | 11.48 | 9.24 | 10.43 | 10.55 | 10.45 | 12.52 | 11.90 | 10.68 | 12.01 | 12.53 | 12.37 | 10.31 |

**Table 1.3:** (*Continued*)

| Rock | IAB-type gabbros | | | | | | | | | | | | | | | |
|---|---|---|---|---|---|---|---|---|---|---|---|---|---|---|---|---|
| Sample | #75 | | | #76 | | | | | | | #78 | | | | | |
| Mineral | Cpx1 | | Cpx3 | Cpx1 | Cpx2 | Cpx3 | Cpx4 | Cpx5 | Cpx6 | Cpx8 | Cpx1 | Cpx2 | | Cpx4 | Cpx5 | |
| | core | rim | core | core | core | core | Core | core | core | core | core | core | rim | core | core | rim |
| $SiO_2$ | 52.69 | 51.87 | 52.83 | 51.19 | 52 | 51.92 | 49.99 | 53.11 | 51.12 | 53.66 | 51.01 | 52.46 | 52.23 | 52.94 | 53.98 | 52.76 |
| $TiO_2$ | 0.23 | 0.25 | 0.26 | 0.49 | 0.24 | 0.35 | 0.71 | 0.26 | 0.32 | 0.19 | 0.51 | 0.89 | 0.87 | 0.76 | 0.48 | 0.7 |
| $Al_2O_3$ | 1.88 | 1.84 | 1.79 | 2.84 | 1.75 | 1.55 | 3.38 | 1.57 | 2.22 | 1.11 | 2.99 | 3.25 | 3.18 | 3.15 | 4.03 | 3.27 |
| $Cr_2O_3$ | 0.34 | 0.15 | 0.11 | 0.11 | 0.45 | 0.12 | 0.11 | 0.16 | 0.49 | 0.51 | 0.11 | 0.07 | 0.08 | | 0.3 | 0.02 |
| FeO | 4.59 | 7.32 | 6.74 | 6.02 | 4.71 | 6.74 | 6.81 | 6.53 | 4.38 | 3.27 | 9.54 | 9.52 | 9.12 | 7.79 | 3.61 | 6.65 |
| Mno | 0.11 | 0.23 | 0.19 | 0.2 | 0.08 | 0.25 | 0.18 | 0.16 | 0.12 | 0.03 | 0.12 | 0.2 | 0.22 | 0.24 | 0.07 | 0.28 |
| MgO | 15.99 | 14.71 | 14.92 | 14.42 | 15.73 | 14.64 | 13.69 | 15.16 | 15.67 | 16.92 | 15.64 | 15.91 | 15.5 | 16.16 | 17.95 | 16.35 |
| CaO | 23.99 | 22.75 | 23.54 | 23.81 | 23.19 | 22.73 | 22.85 | 23.31 | 23.4 | 24.28 | 17.26 | 18.21 | 18.85 | 19.54 | 17.69 | 16.99 |
| $Na_2O$ | 0.03 | 0.3 | 0.09 | 0.1 | 0.1 | 0.27 | 0.42 | 0.33 | | | 0.36 | 0.28 | 0.24 | 0.2 | 0.23 | 0.25 |
| Total | 99.85 | 99.42 | 100.47 | 99.18 | 98.25 | 98.57 | 98.14 | 100.59 | 97.72 | 99.97 | 97.54 | 100.79 | 100.29 | 100.78 | 98.35 | 97.29 |
| Cations (O=6) | | | | | | | | | | | | | | | | |
| Si | 1.94 | 1.94 | 1.948 | 1.913 | 1.945 | 1.953 | 1.895 | 1.954 | 1.924 | 1.961 | 1.932 | 1.923 | 1.925 | 1.931 | 1.961 | 1.966 |
| Al | 0.082 | 0.081 | 0.078 | 0.125 | 0.077 | 0.069 | 0.151 | 0.068 | 0.098 | 0.048 | 0.133 | 0.14 | 0.138 | 0.135 | 0.172 | 0.143 |
| Ti | 0.006 | 0.007 | 0.007 | 0.014 | 0.007 | 0.01 | 0.02 | 0.007 | 0.009 | 0.005 | 0.014 | 0.025 | 0.024 | 0.021 | 0.013 | 0.02 |
| Al | 0.082 | 0.081 | 0.078 | 0.125 | 0.077 | 0.069 | 0.151 | 0.068 | 0.098 | 0.048 | 0.133 | 0.14 | 0.138 | 0.135 | 0.172 | 0.143 |
| $Cr^{3+}$ | 0.01 | 0.004 | 0.003 | 0.003 | 0.013 | 0.004 | 0.003 | 0.005 | 0.015 | 0.015 | 0.003 | 0.002 | 0.002 | | 0.009 | 0.001 |
| $Fe^{2+}$ | 0.141 | 0.229 | 0.208 | 0.188 | 0.148 | 0.212 | 0.216 | 0.201 | 0.138 | 0.1 | 0.302 | 0.292 | 0.281 | 0.238 | 0.11 | 0.207 |
| Mn | 0.004 | 0.007 | 0.006 | 0.006 | 0.002 | 0.008 | 0.006 | 0.005 | 0.004 | 0.001 | 0.004 | 0.006 | 0.007 | 0.007 | 0.002 | 0.009 |
| Mg | 0.878 | 0.82 | 0.82 | 0.803 | 0.877 | 0.821 | 0.774 | 0.832 | 0.879 | 0.922 | 0.883 | 0.869 | 0.851 | 0.879 | 0.972 | 0.908 |
| Ca | 0.946 | 0.911 | 0.93 | 0.953 | 0.929 | 0.916 | 0.928 | 0.919 | 0.944 | 0.951 | 0.7 | 0.715 | 0.744 | 0.764 | 0.689 | 0.678 |
| Na | 0.002 | 0.022 | 0.007 | 0.007 | 0.007 | 0.019 | 0.031 | 0.024 | | | 0.026 | 0.02 | 0.017 | 0.014 | 0.016 | 0.018 |
| Total | 4.009 | 4.021 | 4.007 | 4.012 | 4.005 | 4.012 | 4.024 | 4.015 | 4.011 | 4.003 | 3.997 | 3.992 | 3.989 | 3.989 | 3.945 | 3.951 |
| Mg# | 86.16 | 78.17 | 79.77 | 81.03 | 85.56 | 79.48 | 78.18 | 80.54 | 86.43 | 90.22 | 74.51 | 74.85 | 75.18 | 78.69 | 89.83 | 81.43 |
| Wo | 48.14 | 46.48 | 47.50 | 49.02 | 47.54 | 47.00 | 48.38 | 47.08 | 48.14 | 48.20 | 37.14 | 38.11 | 39.66 | 40.62 | 38.90 | 37.81 |
| En | 44.68 | 41.84 | 41.88 | 41.31 | 44.88 | 42.12 | 40.35 | 42.62 | 44.82 | 46.73 | 46.84 | 46.32 | 45.36 | 46.73 | 54.88 | 50.64 |
| Fs | 7.18 | 11.68 | 10.62 | 9.67 | 7.57 | 10.88 | 11.26 | 10.30 | 7.04 | 5.07 | 16.02 | 15.57 | 14.98 | 12.65 | 6.21 | 11.54 |

**Table 1.3:** (*Continued*)

| Rock | OIB-type gabbros | | | | | | | | | | | | | | | | | |
|---|---|---|---|---|---|---|---|---|---|---|---|---|---|---|---|---|---|---|
| Sample | #81 | | | | #84 | | | #85 | | | | | | #86 | | | | |
| Mineral | Cpx1 | Cpx2 | Cpx3 | Cpx4 | Cpx7 | Cpx8 | Cpx9 | Cpx1 | Cpx2 | Cpx3 | Cpx4 | Cpx6 | Cpx7 | Cpx1 | Cpx2 | Cpx3 | Cpx4 | Cpx5 |
| | core | core | core | core | core | core | core | core | core | core | core | core | core | core | core | core | core | core |
| $SiO_2$ | 50.17 | 51.4 | 50.98 | 51.43 | 50.83 | 48.49 | 48.92 | 51.96 | 53.36 | 51.72 | 52.47 | 51.83 | 49.55 | 48.79 | 50.53 | 52.56 | 50.09 | 51.81 |
| $TiO_2$ | 1.25 | 0.66 | 1.03 | 0.81 | 1.13 | 1.91 | 1.8 | 0.79 | 0.25 | 0.82 | 0.89 | 0.98 | 0.8 | 2.93 | 0.32 | 0.29 | 0.29 | 0.43 |
| $Al_2O_3$ | 2.31 | 1.16 | 1.87 | 1.36 | 1.88 | 3.67 | 3.66 | 1.49 | 0.5 | 1.84 | 2 | 1.59 | 3.27 | 1.34 | 1.11 | 0.79 | 0.69 | 1.38 |
| $Cr_2O_3$ | 0.1 | 0.04 | 0.11 | | | 0.03 | 0.03 | 0.03 | 0.03 | | | 0.07 | 0.05 | 0.08 | 0.1 | 0.03 | 0.02 | 0.01 |
| FeO | 13.17 | 15.83 | 13.43 | 13.63 | 10.39 | 10.61 | 10.26 | 12.12 | 15.33 | 14.67 | 14.41 | 13.19 | 15.08 | 12.15 | 12.5 | 12.66 | 12.69 | 12.13 |
| Mno | 0.28 | 0.43 | 0.4 | 0.28 | 0.23 | 0.18 | 0.15 | 0.35 | 0.37 | 0.37 | 0.48 | 0.56 | 0.29 | 0.33 | 0.22 | 0.48 | 0.32 | 0.41 |
| MgO | 12.94 | 12.96 | 13.22 | 13.91 | 14.02 | 12.85 | 12.78 | 13.3 | 11.08 | 12.17 | 12.14 | 11.65 | 12.03 | 11.31 | 11.32 | 11.68 | 10.94 | 12.27 |
| CaO | 18.71 | 17.62 | 18.69 | 17.54 | 19.78 | 20.62 | 20.8 | 19.32 | 20.78 | 19.51 | 20.29 | 21.44 | 18.24 | 21.71 | 21.27 | 22.38 | 22.42 | 20.82 |
| $Na_2O$ | 0.24 | 0.17 | 0.19 | 0.25 | 0.32 | 0.39 | 0.37 | 0.17 | 0.16 | 0.16 | 0.08 | 0.16 | 0.29 | 0.18 | 0.33 | 0.14 | 0.15 | 0.31 |
| Total | 99.17 | 100.27 | 99.92 | 99.21 | 98.58 | 98.75 | 98.77 | 99.53 | 101.86 | 101.26 | 102.76 | 101.47 | 99.6 | 98.82 | 97.7 | 101.01 | 97.61 | 99.57 |
| Cations (O=6) | | | | | | | | | | | | | | | | | | |
| Si | 1.914 | 1.954 | 1.931 | 1.955 | 1.931 | 1.853 | 1.864 | 1.962 | 2 | 1.943 | 1.941 | 1.943 | 1.897 | 1.886 | 1.966 | 1.977 | 1.961 | 1.966 |
| Al | 0.104 | 0.052 | 0.084 | 0.061 | 0.084 | 0.165 | 0.165 | 0.066 | 0.022 | 0.081 | 0.087 | 0.07 | 0.147 | 0.061 | 0.051 | 0.035 | 0.032 | 0.062 |
| Ti | 0.036 | 0.019 | 0.029 | 0.023 | 0.032 | 0.055 | 0.052 | 0.022 | 0.007 | 0.023 | 0.025 | 0.028 | 0.023 | 0.085 | 0.009 | 0.008 | 0.009 | 0.012 |
| Al | 0.104 | 0.052 | 0.084 | 0.061 | 0.084 | 0.165 | 0.165 | 0.066 | 0.022 | 0.081 | 0.087 | 0.07 | 0.147 | 0.061 | 0.051 | 0.035 | 0.032 | 0.062 |
| $Cr^{3+}$ | 0.003 | 0.001 | 0.003 | 0 | | 0.001 | 0.001 | 0.001 | 0.001 | | | 0.002 | 0.002 | 0.002 | 0.003 | 0.001 | 0.001 | 0 |
| $Fe^{2+}$ | 0.42 | 0.503 | 0.425 | 0.433 | 0.33 | 0.339 | 0.327 | 0.383 | 0.481 | 0.461 | 0.446 | 0.414 | 0.483 | 0.393 | 0.406 | 0.398 | 0.416 | 0.385 |
| Mn | 0.009 | 0.014 | 0.013 | 0.009 | 0.007 | 0.006 | 0.005 | 0.011 | 0.012 | 0.012 | 0.015 | 0.018 | 0.01 | 0.011 | 0.007 | 0.015 | 0.01 | 0.013 |
| Mg | 0.736 | 0.734 | 0.746 | 0.788 | 0.794 | 0.732 | 0.726 | 0.749 | 0.619 | 0.682 | 0.669 | 0.651 | 0.686 | 0.652 | 0.656 | 0.655 | 0.639 | 0.694 |
| Ca | 0.765 | 0.717 | 0.758 | 0.714 | 0.805 | 0.844 | 0.849 | 0.781 | 0.834 | 0.785 | 0.804 | 0.861 | 0.748 | 0.899 | 0.887 | 0.902 | 0.94 | 0.846 |
| Na | 0.018 | 0.013 | 0.014 | 0.018 | 0.023 | 0.029 | 0.027 | 0.012 | 0.012 | 0.011 | 0.006 | 0.011 | 0.022 | 0.014 | 0.025 | 0.01 | 0.012 | 0.023 |
| Total | 4.005 | 4.007 | 4.003 | 4.001 | 4.006 | 4.024 | 4.016 | 3.987 | 3.988 | 3.998 | 3.993 | 3.998 | 4.018 | 4.003 | 4.01 | 4.001 | 4.02 | 4.001 |
| Mg# | 63.67 | 59.34 | 63.71 | 64.54 | 70.64 | 68.35 | 68.95 | 66.17 | 56.27 | 59.67 | 60.00 | 61.13 | 58.68 | 62.39 | 61.77 | 62.20 | 60.57 | 64.32 |
| Wo | 39.82 | 36.69 | 39.29 | 36.90 | 41.73 | 44.07 | 44.64 | 40.83 | 43.12 | 40.72 | 41.90 | 44.70 | 39.02 | 46.24 | 45.51 | 46.14 | 47.12 | 43.95 |
| En | 38.31 | 37.56 | 38.67 | 40.72 | 41.16 | 38.22 | 38.17 | 39.15 | 32.01 | 35.37 | 34.86 | 33.80 | 35.79 | 33.54 | 33.66 | 33.50 | 32.03 | 36.05 |
| Fs | 21.86 | 25.74 | 22.03 | 22.38 | 17.11 | 17.70 | 17.19 | 20.02 | 24.87 | 23.91 | 23.24 | 21.50 | 25.20 | 20.22 | 20.83 | 20.36 | 20.85 | 20.00 |

#### 1.5.2.1.2. Amphiboles

Amphiboles are the dominant ferro-magnesian minerals in the IAB-type gabbroic rocks of Chukotka. Most of the amphiboles from IAB-type gabbros are plotted in the pargasite compositional field whereas from OIB-type gabbros plotted in the magnesio-hornblende, actinolitic hornblende and edenite field (Fig. 1.12).

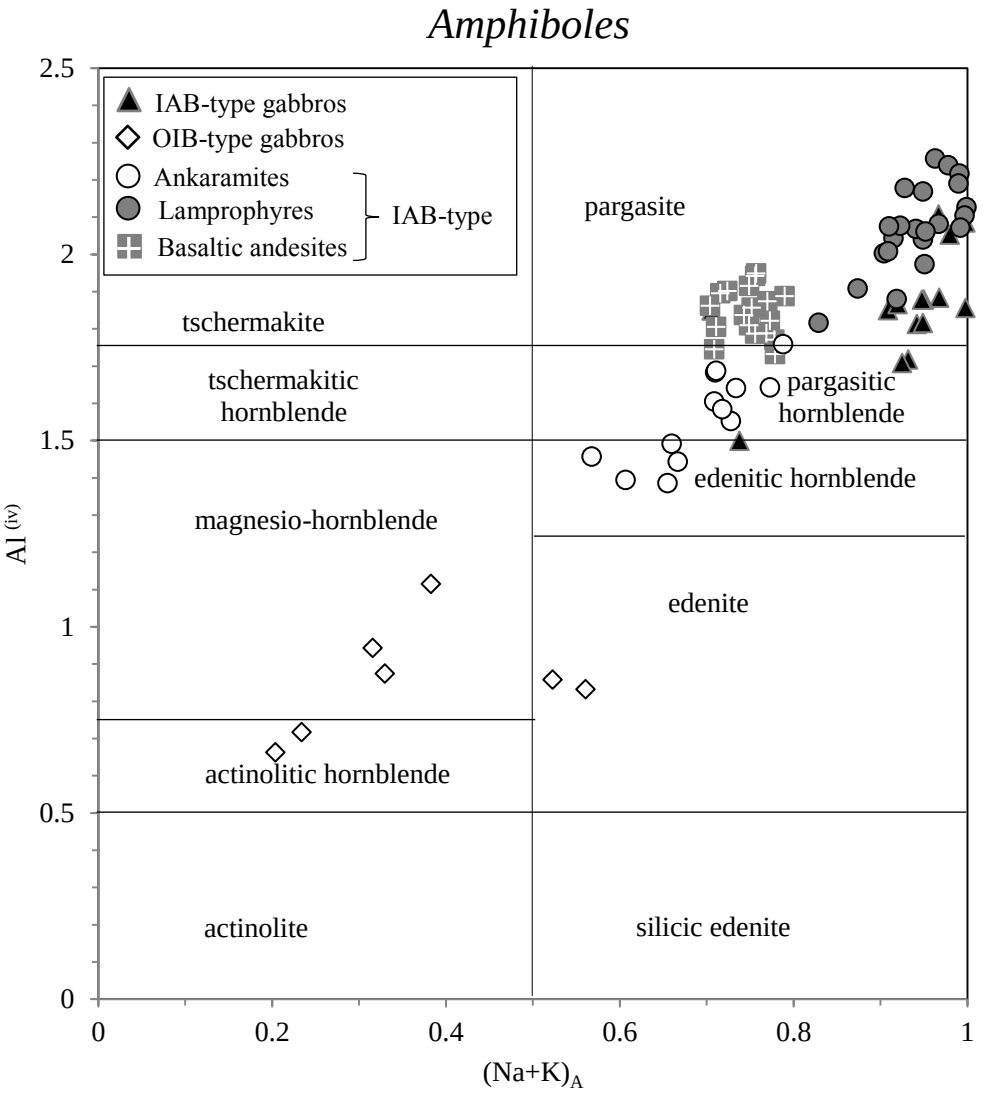


**Figure 1.12:** Plot of $Al^{(IV)}$ versus cations in A-site for hornblende in the studied rocks (nomenclature from Leake, 1978).

In the $Al_{total}$ versus $Al^{iv}$ variation diagram (Fig. not shown), amphibole minerals from IAB-type gabbroic rocks have higher content of $Al_{total}$ than those from OIB-type gabbroic rocks. It is important to note that amphiboles from the most magesian IAB-type gabbro (i.e. Sample #75) are higher in MgO (14.5-16.3 wt. %) compared to the rest of the studied samples, but it is similar to those in ankaramitic volcanic rocks (14.6-16.4 wt. %). Amphibole crystal from IAB-type gabbroic rocks have higher $TiO_2$ (2.3-3.1 wt. %) and $Al_2O_3$ (11.1-14.8) content compared to those in OIB-type gabbros (0.5-0.9 wt. %, 4.9-6.6 wt. %; respectively; Fig. 1.13A and B). Mg-numbers in amphibole are mostly lower than those of clinopyroxene from the basaltic and gabbroic rocks and is interpreted as a late magmatic mineral.

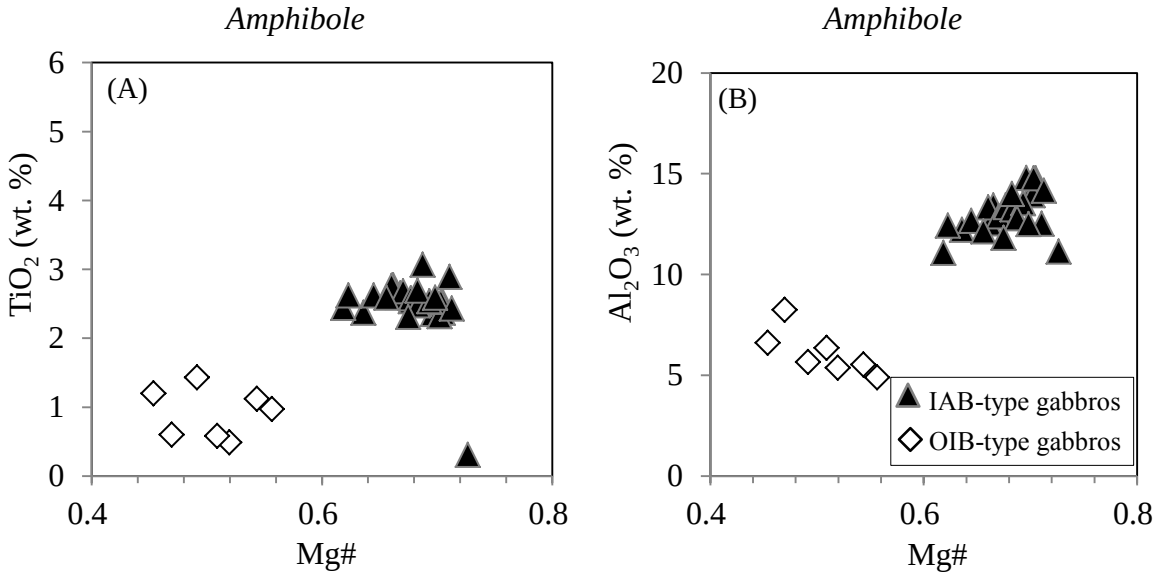


**Figure 1.13:** Major element chemistry of amphibole from gabbroic rocks of Chukotka, NE Russia.

**Table 1.4:** Representative electron-microprobe analyses of hornblende crystals in gabbroic rocks of Chukotka, NE Russia

| Rock | IAB-type gabbros | | | | | | | | | | | | | | | | |
|---|---|---|---|---|---|---|---|---|---|---|---|---|---|---|---|---|---|
| Sample | #57 | | | | | | #63 | | | | | | #64 | | | | |
| Minera | Hb1 | Hb2 | Hb3 | Hb4 | Hb5 | Hb6 | Hb2 | Hb3 | Hb4 | Hb5 | Hb6 | Hb7 | Hb1 | Hb2 | Hb3 | Hb4 | Hb5 |
| Positio | core | core | core | core | core | core | core | core | core | core | core | core | core | core | core | core | core |
| $SiO_2$ | 38.71 | 39.24 | 39.94 | 38.7 | 40.19 | 40.37 | 40.96 | 41.71 | 42.12 | 42.08 | 41.13 | 41.21 | 39.57 | 40.65 | 41.24 | 40.99 | 42.76 |
| $TiO_2$ | 2.37 | 2.35 | 2.52 | 2.32 | 2.53 | 2.43 | 2.65 | 2.77 | 2.62 | 2.5 | 2.6 | 2.76 | 2.54 | 2.58 | 2.48 | 2.54 | 2.69 |
| $Al_2O_3$ | 14.47 | 14.79 | 14.77 | 13.93 | 14.78 | 14.15 | 12.99 | 12.53 | 12.92 | 13.15 | 13.43 | 13.33 | 13.44 | 13.35 | 13.23 | 13.54 | 14 |
| $Cr_2O_3$ | | | | 0.004 | | | 0.04 | 0.1 | 0.06 | | 0.1 | 0.02 | 0.02 | 0.05 | 0.03 | 0.01 | 0.07 |
| FeO | 9.81 | 10.33 | 10.41 | 10.06 | 10.44 | 10.11 | 11.64 | 12.14 | 12.04 | 11.37 | 11.77 | 12.02 | 10.99 | 11.29 | 11.22 | 10.71 | 11.58 |
| MnO | 0.07 | 0.15 | 0.19 | 0.02 | 0.06 | 0.17 | 0.29 | 0.25 | 0.26 | 0.27 | 0.18 | 0.31 | 0.14 | 0.15 | 0.14 | 0.18 | 0.22 |
| MgO | 13.15 | 13.29 | 13.97 | 13.3 | 13.88 | 14.07 | 13.16 | 13.34 | 13.49 | 13.84 | 13.14 | 13.12 | 12.93 | 13.29 | 13.6 | 13.58 | 14 |
| CaO | 12.59 | 12.5 | 12.89 | 12.48 | 13 | 12.95 | 12.4 | 12.34 | 12.30 | 12.09 | 12.63 | 12.72 | 12.16 | 12.53 | 12.51 | 12.47 | 12.72 |
| $Na_2O$ | 2.56 | 2.83 | 2.72 | 2.6 | 2.76 | 2.65 | 3.02 | 3.07 | 3.12 | 3.4 | 3.06 | 3.03 | 2.9 | 3.06 | 2.95 | 3.01 | 3.23 |
| $K_2O$ | 1.08 | 1.18 | 1.25 | 1.16 | 1.21 | 1.18 | 0.95 | 0.83 | 0.84 | 0.98 | 0.96 | 0.99 | 0.95 | 0.92 | 1.04 | 1.03 | 1.08 |
| Total | 94.81 | 96.66 | 98.66 | 94.574 | 98.85 | 98.08 | 98.1 | 99.08 | 99.77 | 99.68 | 99 | 99.51 | 95.64 | 97.87 | 98.44 | 98.06 | 102.35 |
| Cations (O=23) | | | | | | | | | | | | | | | | | |
| Si | 5.893 | 5.877 | 5.862 | 5.915 | 5.882 | 5.947 | 6.065 | 6.117 | 6.122 | 6.11 | 6.036 | 6.028 | 5.997 | 6.024 | 6.068 | 6.043 | 6.049 |
| Ti | 0.271 | 0.265 | 0.278 | 0.267 | 0.278 | 0.269 | 0.295 | 0.305 | 0.287 | 0.273 | 0.287 | 0.304 | 0.29 | 0.287 | 0.274 | 0.281 | 0.286 |
| Al | 2.595 | 2.61 | 2.556 | 2.51 | 2.55 | 2.458 | 2.267 | 2.165 | 2.214 | 2.251 | 2.323 | 2.298 | 2.401 | 2.332 | 2.294 | 2.352 | 2.334 |
| $Cr^{3+}$ | | | | 0.005 | | | 0.005 | 0.011 | 0.007 | | 0.011 | 0.002 | 0.002 | 0.006 | 0.004 | 0.001 | 0.008 |
| $Fe^{2+}$ | 1.249 | 1.294 | 1.278 | 1.285 | 1.278 | 1.245 | 1.442 | 1.489 | 1.464 | 1.381 | 1.445 | 1.47 | 1.392 | 1.399 | 1.381 | 1.32 | 1.37 |
| Mn | 0.009 | 0.019 | 0.024 | 0.002 | 0.008 | 0.022 | 0.037 | 0.032 | 0.032 | 0.033 | 0.022 | 0.039 | 0.017 | 0.019 | 0.017 | 0.023 | 0.027 |
| Mg | 2.984 | 2.967 | 3.057 | 3.031 | 3.029 | 3.089 | 2.903 | 2.916 | 2.923 | 2.994 | 2.875 | 2.861 | 2.921 | 2.935 | 2.982 | 2.983 | 2.952 |
| Ca | 2.054 | 2.006 | 2.027 | 2.045 | 2.038 | 2.044 | 1.967 | 1.94 | 1.915 | 1.882 | 1.985 | 1.993 | 1.975 | 1.99 | 1.972 | 1.97 | 1.928 |
| Na | 0.757 | 0.822 | 0.775 | 0.771 | 0.784 | 0.758 | 0.867 | 0.873 | 0.88 | 0.956 | 0.871 | 0.86 | 0.852 | 0.879 | 0.841 | 0.86 | 0.887 |
| K | 0.21 | 0.225 | 0.234 | 0.227 | 0.227 | 0.222 | 0.18 | 0.155 | 0.155 | 0.181 | 0.179 | 0.185 | 0.183 | 0.174 | 0.196 | 0.193 | 0.195 |
| Total | 16.022 | 16.085 | 16.091 | 16.058 | 16.074 | 16.054 | 16.028 | 16.003 | 15.999 | 16.061 | 16.034 | 16.04 | 16.03 | 16.045 | 16.029 | 16.026 | 16.036 |
| Mg# | 70.49 | 69.63 | 70.52 | 70.23 | 70.33 | 71.27 | 66.81 | 66.20 | 66.63 | 68.43 | 66.55 | 66.06 | 67.73 | 67.72 | 68.35 | 69.32 | 68.30 |

**Table 1.4:** (*Continued*)

| Rock | IAB-type gabbros | | | | | | | | | | OIB-type gabbros | | | | | | |
|---|---|---|---|---|---|---|---|---|---|---|---|---|---|---|---|---|---|
| Sample | #72 | | | | #75 | | | | #76 | | #85 | | | #86 | | | |
| Minera | Hb1 | Hb2 | Hb3 | Hb4 | Hb1 | Hb2 | Hb3 | Hb4 | Hb1 | Hb3 | Hb2 | Hb3 | Hb4 | Hb1 | Hb2 | Hb3 | Hb4 |
| Positio | core | core | core | core | core | core | core | core | core | core | core | core | core | core | core | core | core |
| $SiO_2$ | 42.38 | 42.41 | 41.65 | 42.42 | 42.22 | 45.54 | 42.52 | 42.51 | 41.3 | 42.62 | 49.08 | 47.72 | 49.32 | 46.19 | 49.98 | 48.13 | 49.61 |
| $TiO_2$ | 2.37 | 2.44 | 2.62 | 2.62 | 2.89 | 0.31 | 3.07 | 2.59 | 2.59 | 2.31 | 1.43 | 1.2 | 1.12 | 0.6 | 0.49 | 0.58 | 0.97 |
| $Al_2O_3$ | 12.22 | 11.08 | 12.42 | 12.67 | 12.52 | 11.14 | 12.79 | 12.51 | 12.14 | 11.82 | 5.66 | 6.61 | 5.53 | 8.24 | 5.38 | 6.36 | 4.89 |
| $Cr_2O_3$ | 0.08 | 0.08 | 0.05 | 0.03 | 0.06 | 0.02 | | 0.09 | 0.07 | 0.02 | | 0.03 | 0.03 | | 0.12 | 0.08 | 0.03 |
| FeO | 13.43 | 13.91 | 13.79 | 12.98 | 10.53 | 10.95 | 11.34 | 11.2 | 11.94 | 11.55 | 19.85 | 21.46 | 17.79 | 20.34 | 19.06 | 19.09 | 17.13 |
| MnO | 0.14 | 0.13 | 0.11 | 0.09 | 0.2 | 0.17 | 0.15 | 0.16 | 0.2 | | 0.16 | 0.15 | 0.27 | 0.13 | 0.23 | 0.2 | 0.17 |
| MgO | 13.17 | 12.66 | 12.78 | 13.22 | 14.53 | 16.34 | 14 | 14.55 | 12.78 | 13.46 | 10.77 | 10.01 | 11.9 | 10.11 | 11.57 | 11.11 | 12.07 |
| CaO | 12.09 | 12.27 | 12.18 | 12.28 | 11.7 | 12.33 | 12.34 | 12.29 | 12.14 | 12.19 | 11.76 | 10.73 | 12.08 | 11.71 | 12.05 | 11.77 | 11.66 |
| $Na_2O$ | 2.97 | 2.65 | 2.87 | 3.12 | 3.14 | 2.48 | 2.92 | 2.86 | 2.73 | 2.8 | 2 | 1.73 | 1.91 | 1.41 | 0.99 | 1.3 | 1 |
| $K_2O$ | 1.13 | 1.18 | 1.13 | 1.17 | 1.06 | 0.91 | 1.07 | 1.06 | 1.09 | 1.02 | 0.66 | 0.63 | 0.76 | 0.56 | 0.39 | 0.47 | 0.38 |
| Total | 99.98 | 98.81 | 99.6 | 100.6 | 98.85 | 100.19 | 100.2 | 99.82 | 96.98 | 97.79 | 101.37 | 100.27 | 100.71 | 99.29 | 100.26 | 99.09 | 97.91 |
| Cations (O=23) | | | | | | | | | | | | | | | | | |
| Si | 6.187 | 6.283 | 6.122 | 6.144 | 6.15 | 6.501 | 6.134 | 6.151 | 6.185 | 6.292 | 7.142 | 7.057 | 7.168 | 6.885 | 7.283 | 7.126 | 7.337 |
| Ti | 0.26 | 0.272 | 0.289 | 0.286 | 0.317 | 0.033 | 0.333 | 0.282 | 0.292 | 0.256 | 0.156 | 0.134 | 0.122 | 0.067 | 0.053 | 0.065 | 0.108 |
| Al | 2.102 | 1.935 | 2.152 | 2.163 | 2.15 | 1.874 | 2.175 | 2.134 | 2.143 | 2.056 | 0.97 | 1.152 | 0.947 | 1.448 | 0.924 | 1.11 | 0.852 |
| $Cr^{3+}$ | 0.009 | 0.009 | 0.006 | 0.004 | 0.007 | 0.002 | | 0.01 | 0.008 | 0.002 | | 0.003 | 0.003 | | 0.014 | 0.009 | 0.004 |
| $Fe^{2+}$ | 1.639 | 1.723 | 1.695 | 1.572 | 1.283 | 1.307 | 1.368 | 1.355 | 1.495 | 1.426 | 2.415 | 2.654 | 2.163 | 2.536 | 2.323 | 2.364 | 2.119 |
| Mn | 0.017 | 0.017 | 0.013 | 0.012 | 0.025 | 0.02 | 0.018 | 0.02 | 0.025 | | 0.019 | 0.019 | 0.033 | 0.017 | 0.028 | 0.026 | 0.021 |
| Mg | 2.866 | 2.795 | 2.8 | 2.855 | 3.154 | 3.477 | 3.011 | 3.138 | 2.853 | 2.962 | 2.336 | 2.206 | 2.577 | 2.247 | 2.513 | 2.452 | 2.661 |
| Ca | 1.891 | 1.947 | 1.918 | 1.905 | 1.825 | 1.886 | 1.907 | 1.905 | 1.948 | 1.932 | 1.834 | 1.701 | 1.881 | 1.869 | 1.881 | 1.868 | 1.847 |
| Na | 0.841 | 0.762 | 0.818 | 0.877 | 0.887 | 0.686 | 0.816 | 0.801 | 0.794 | 0.801 | 0.566 | 0.496 | 0.539 | 0.407 | 0.281 | 0.373 | 0.286 |
| K | 0.21 | 0.223 | 0.212 | 0.216 | 0.197 | 0.166 | 0.197 | | 0.207 | 0.192 | 0.123 | 0.119 | 0.141 | 0.107 | 0.072 | 0.089 | 0.071 |
| Total | 16.022 | 15.966 | 16.025 | 16.034 | 15.995 | 15.952 | 15.959 | 15.796 | 15.95 | 15.919 | 15.561 | 15.541 | 15.574 | 15.583 | 15.372 | 15.482 | 15.306 |
| Mg# | 63.62 | 61.86 | 62.29 | 64.49 | 71.08 | 72.68 | 68.76 | 69.84 | 65.62 | 67.50 | 49.17 | 45.39 | 54.37 | 46.98 | 51.96 | 50.91 | 55.67 |

#### 1.5.2.1.3. Plagioclase

*Plagioclase* crystals composition in the IAB-type gabbroic rock varying from $An_{100-46}$ $Ab_{0-54}$ (i.e. anorthite to andesine), whereas in OIB-type gabbroic rocks $An_{1-57}Ab_{99-42}Or_{0-25}$ (i.e. labradorite to alkali-feldspars) (Fig. 1.14). However, rare orthoclase crystals are also present in IAB-type gabbros (Sample #75). Representative plagioclase compositions are given in Table 1.5.

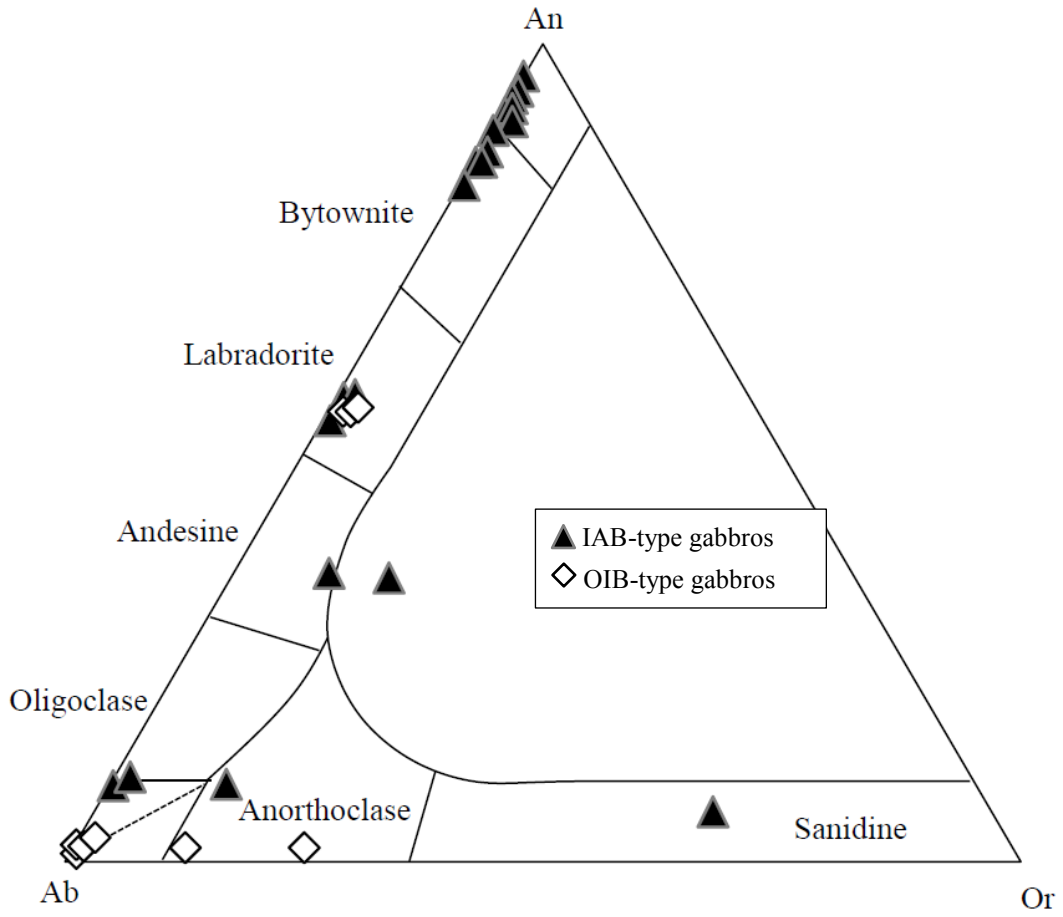


**Figure 1.14:** An-Ab-Or triangular diagram showing the compositions of plagioclase from gabbroic rocks of Chukotka. An, Anorthite; Ab, Albite; Or, Orthoclase.

**Table 1.5:** Average electron microprobe analyses of plagioclase and alkali feldspar from the basaltic and gabbroic rocks of Chukotka, NE Russia.

| Rock Type | Lamprophyres | | Basaltic andesites | | IAB-type gabbros | | | | | | OIB-type gabbro |
|---|---|---|---|---|---|---|---|---|---|---|---|
| Sample | #74 | #77 | #55 | #56 | #62 | #63 | #64 | #72 | #75 | #76 | #85 |
| n: | 4 | 4 | 6 | 3 | 5 | 5 | 5 | 3 | 4 | 3 | 3 |
| $SiO_2$ | 56.89 | 59.38 | 52.58 | 51.17 | 46.04 | 46.58 | 44.79 | 57.13 | 53.92 | 51.44 | 54.98 |
| $Al_2O_3$ | 26.71 | 28.34 | 30.26 | 30.50 | 33.02 | 34.30 | 34.54 | 27.09 | 32.66 | 29.99 | 27.68 |
| FeO | 0.70 | 1.05 | 0.21 | 0.47 | 0.55 | 0.60 | 0.51 | 0.40 | 0.93 | 0.44 | 1.02 |
| CaO | 8.60 | 1.12 | 13.08 | 13.57 | 17.26 | 18.19 | 18.89 | 9.46 | 2.40 | 13.36 | 10.88 |
| $Na_2O$ | 4.85 | 6.75 | 3.79 | 3.03 | 1.27 | 1.02 | 0.50 | 5.41 | 3.68 | 3.53 | 4.83 |
| $K_2O$ | 1.98 | 5.65 | 0.31 | 0.47 | 0.03 | 0.02 | 0.02 | 0.68 | 8.56 | 0.16 | 0.37 |
| Total | 99.81 | 100.59 | 100.22 | 99.21 | 98.24 | 100.78 | 99.30 | 100.17 | 99.71 | 98.97 | 99.89 |
| Cations (O=8) | | | | | | | | | | | |
| Si | 2.566 | 2.643 | 2.376 | 2.347 | 2.155 | 2.129 | 2.083 | 2.562 | 2.460 | 2.359 | 2.489 |
| Al | 1.427 | 1.496 | 1.616 | 1.648 | 1.822 | 1.847 | 1.893 | 1.434 | 1.758 | 1.624 | 1.476 |
| Fe | 0.027 | 0.039 | 0.007 | 0.018 | 0.022 | 0.023 | 0.020 | 0.015 | 0.035 | 0.017 | 0.039 |
| Ca | 0.421 | 0.053 | 0.637 | 0.667 | 0.866 | 0.890 | 0.941 | 0.456 | 0.116 | 0.659 | 0.528 |
| Na | 0.422 | 0.575 | 0.330 | 0.270 | 0.116 | 0.091 | 0.045 | 0.470 | 0.324 | 0.313 | 0.424 |
| K | 0.113 | 0.326 | 0.018 | 0.028 | 0.002 | 0.001 | 0.003 | 0.038 | 0.500 | 0.009 | 0.021 |
| Total | 4.975 | 4.988 | 4.983 | 4.978 | 4.981 | 4.982 | 4.983 | 4.975 | 5.002 | 4.981 | 4.977 |
| An | 44.08 | 5.94 | 64.92 | 69.10 | 88.07 | 90.62 | 95.36 | 47.24 | 10.06 | 67.05 | 54.23 |
| Ab | 44.55 | 48.90 | 33.30 | 28.00 | 11.76 | 9.24 | 4.54 | 48.75 | 19.42 | 32.03 | 43.61 |
| Or | 11.37 | 45.16 | 1.78 | 2.89 | 0.16 | 0.14 | 0.10 | 4.01 | 70.53 | 0.92 | 2.16 |

Abbreviations: An, Anorthite; Ab, Albite; Or, orthoclase; n, number of analyses used for the average; n, number of analyses used for the average.

#### 1.5.2.1.4. Biotite

Biotite from IAB-type gabbroic rocks have Mg# [= 100*Mg/ (Mg+$Fe^{2+}$)] between 64-66 whereas biotite from OIB-type gabbros has Mg# about 30. In the Mg# [= 100*Mg/ (Mg+$Fe^{2+}$)] vs Al classification diagram biotite from IAB-type gabbro fall in the phlogopite compositional field, but those from OIB-type gabbro plotted in annite (Fig. not shown). Biotite crystals lie in the magmatic biotite domain of the FeO* (=$FeO^{total}$+MnO)-10×$TiO_2$-MgO diagram (Fig. not shown; Nachit et al., 2005).

**Table 1.6:** Electron-microprobe analyses of biotite from the basaltic and gabbroic rocks of Chukotka, NE Russia.

| Rock | IAB-type gabbro | | OIB-type gabbro | Basaltic andesite | | | | |
|---|---|---|---|---|---|---|---|---|
| Sample | #72 | | #85 | #56 | | | | |
| Mineral | Bi1 | Bi2 | Bi1 | Bi1 | Bi2 | Bi3 | Bi4 gm | Bi5 |
| $SiO_2$ | 39.78 | 39.54 | 37.63 | 44.34 | 43.15 | 41.57 | 43.27 | 40.33 |
| $TiO_2$ | 4.89 | 4.79 | 4.95 | 0.66 | 0.59 | 0.62 | 0.84 | 0.43 |
| $Al_2O_3$ | 15.5 | 15.27 | 13.39 | 15.49 | 12.94 | 14.24 | 13.26 | 15.49 |
| $Cr_2O_3$ | 0.08 | 0.07 | 0.06 | 0.02 | 0.07 | 0.02 | 0.01 | 0.08 |
| FeO | 14.99 | 14.65 | 28.13 | 19.02 | 20.93 | 21.85 | 20.34 | 22.83 |
| MnO | | | 0.12 | 0.00 | 0.00 | 0.00 | 0.00 | 0.00 |
| MgO | 15.16 | 15.95 | 6.65 | 10.93 | 12.21 | 12.45 | 12.45 | 13.50 |
| CaO | 0.03 | | 0.00 | 0.10 | 1.34 | 0.25 | 1.01 | 0.29 |
| $Na_2O$ | 0.2 | 0.17 | 0.06 | 0.05 | 0.06 | 0.04 | 0.03 | 0.08 |
| $K_2O$ | 9.37 | 9.56 | 9.00 | 9.38 | 8.71 | 8.95 | 8.78 | 6.97 |
| Total | 100 | 100 | 100 | 100 | 100 | 100 | 100 | 100 |
| Si | 5.619 | 5.588 | 5.678 | 6.276 | 6.208 | 6.012 | 6.199 | 5.805 |
| Ti | 0.52 | 0.509 | 0.562 | 0.071 | 0.064 | 0.068 | 0.091 | 0.047 |
| Al | 2.58 | 2.544 | 2.382 | 2.584 | 2.194 | 2.427 | 2.239 | 2.628 |
| Cr | 0.009 | 0.008 | 0.007 | 0.002 | 0.008 | 0.002 | 0.002 | 0.01 |
| Fe | 1.771 | 1.732 | 3.55 | 2.251 | 2.518 | 2.643 | 2.437 | 2.748 |
| Mn | | | 0.016 | | | | | |
| Mg | 3.192 | 3.361 | 1.496 | 2.306 | 2.62 | 2.684 | 2.659 | 2.896 |
| Ca | 0.005 | | | 0.015 | 0.207 | 0.039 | 0.155 | 0.043 |
| Na | 0.055 | 0.047 | 0.018 | 0.015 | 0.016 | 0.011 | 0.01 | 0.023 |
| K | 1.688 | 1.724 | 1.732 | 1.694 | 1.598 | 1.65 | 1.604 | 1.28 |
| Total | 15.439 | 15.513 | 15.441 | 15.214 | 15.433 | 15.536 | 15.396 | 15.48 |
| Mg# | 0.64 | 0.66 | 0.30 | 0.51 | 0.51 | 0.50 | 0.52 | 0.51 |

#### 1.5.2.1.5. Opaque minerals

Opaque phases in the IAB-type gabbroic rocks include magnetite and titano-magnetite. The $TiO_2$ content of magnetite varies from 0.17 to 0.43 wt. %. Titano-magnetite contains $TiO_2$ ranging from 3.39 to 5.09 wt. %. Opaque minerals in OIB-type gabbros are mainly ilmenite with $TiO_2$ content ranging from 49.3 to 51.1 wt. %.

### 1.5.2.2. Major element chemistry of minerals in basaltic rocks

On the basis of petrography and mineral chemistry two distinct groups of lava are identified i.e. basaltic rocks (phyroxene-phyric basalt, ankaramites and lamprophyres) and hornblende bearing basaltic andesites. Both groups of lava are characterized by island-arc basalt (IAB)-type geochemical features. Orthopyroxene and olivine grains are not observed in the studied samples.

#### 1.5.2.2.1. Clinopyroxene

In the conventional classification diagram (Morimoto et al., 1988), clinopyroxene from basaltic rocks is diopsidic in composition ($Wo_{45-50}En_{36-50}Fs_{4-14}$; Fig. 1.15), with the averaged $TiO_2$ contents ranging from 0.23 to 0.85 wt. % and $Al_2O_3$ from 1.83 to 4.84 wt. %, whereas clinopyroxene in basaltic andesite is augite ($Wo_{29-42}En_{31-40}Fs_{17-37}$) with 0.59-0.77 wt. % $TiO_2$ and 2.22-2.71 wt. % $Al_2O_3$ (Table 1.7).

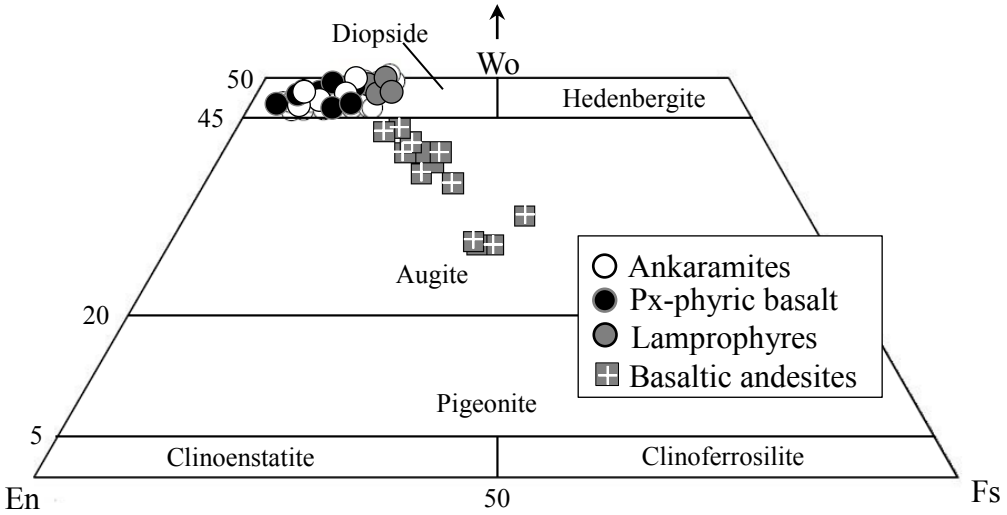


**Figure 1.15:** Pyroxene quadrilateral diagram showing the composition of pyroxene (after Morimoto et al., 1988) from the basaltic rocks in the Chukotka area, NE, Russia.

Clinopyroxene in basalts is higher in CaO than those of basaltic andesite. The Mg# [= 100×Mg/ (Mg+$Fe^{2+}$)] of clinopyroxene in ankaramites ranges from 85.3 to 92.4 (average 87.1), pyroxene-phyric basalt from 72.4 to 91.2 (average 84.5), lamprophyres from 80.5 to 93.1 (average 86.6) and basaltic andesites ranges from 45.5 to 70.6 (average 57.9) (Table 1.7; Fig. 1.16). Clinopyroxene crystals have high $Al^{VI}/Al^{IV}$ ratios (generally >0.25). $TiO_2$ and $Al_2O_3$ content of clinopyroxene in basalts displays a negative correlation with Mg#, whereas those in basaltic andesites have positive correlation (Fig. 1.16). Clinopyroxene in basaltic andesites has higher content of $FeO^*$ (10.7-16.4 wt. %) than that in basalts (4.6-7.7 wt. %). Clinopyroxene of ankaramites have relatively high $Cr_2O_3$ (as high as 0.79 wt. %) compared to the other clinopyroxenes. In general, the $Cr_2O_3$ content of clinopyroxene in basalts is high and decreases with deceasing Mg#, but is low and constant for basaltic andesite (Fig. 1.16C). The clinopyroxene phenocrysts of basalts (mainly in pyroxene-phyric basalt) show strong normal zoning with a general ferrosilite (Fs) increase from core to rim. However, few clinopyroxene phenocrysts from pyroxene-

phyric basalt shows reverse Fe enrichment from core to rim. Sometimes oscillatory-zoned clinopyroxene is observerd in ankaramites (e.g. Sample #70; Fig. 1.17). In general, the compositional difference between core and rim of clinopyroxenes follows the normal pyroxene fractionation trend: the cores are richer in Mg, Si and Cr and poorer in Fe, Ti and Al.

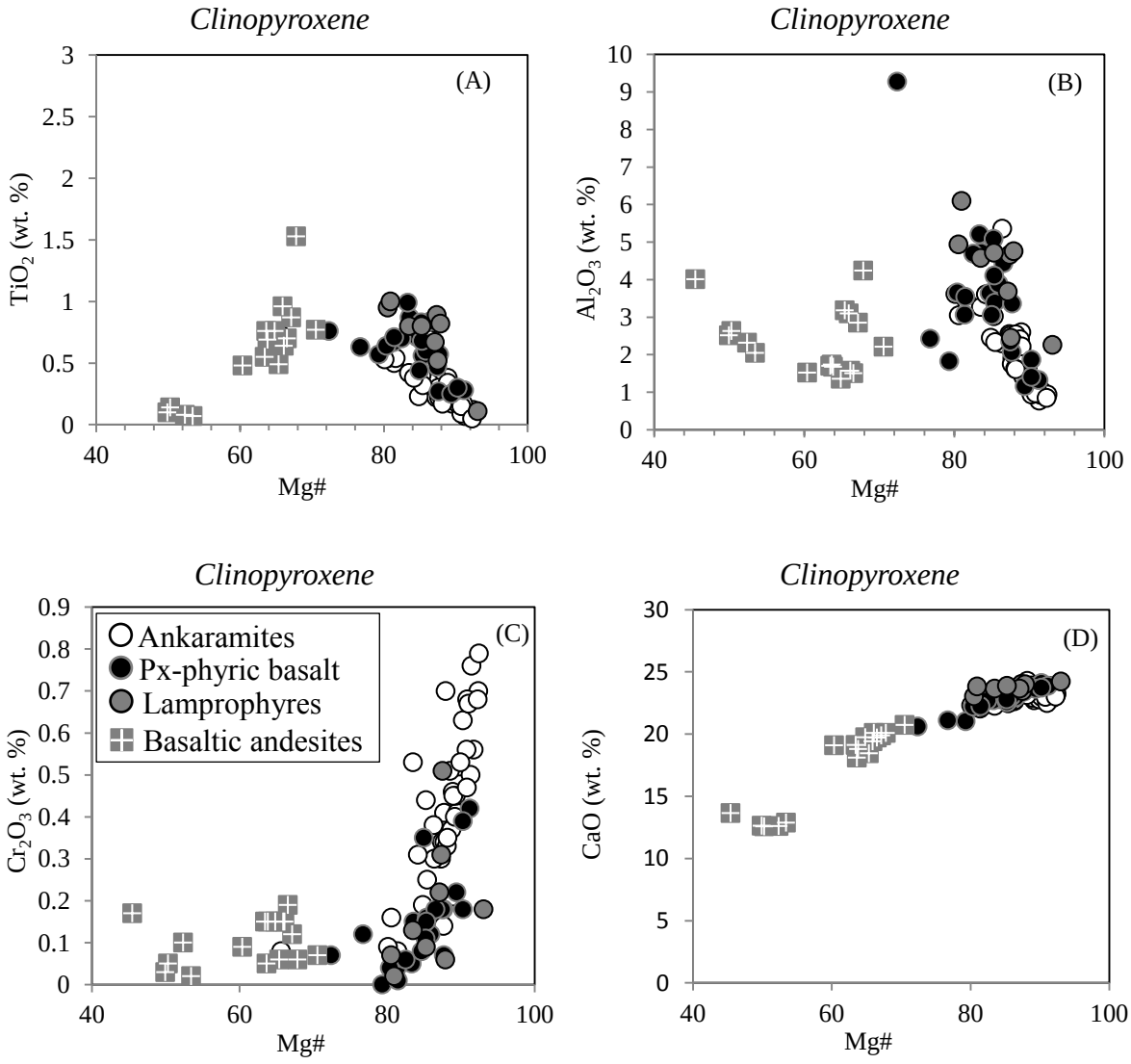


**Figure 1.16**: Major element chemistry of clinopyroxene phenocrysts from the basaltic rocks of Chukotka.

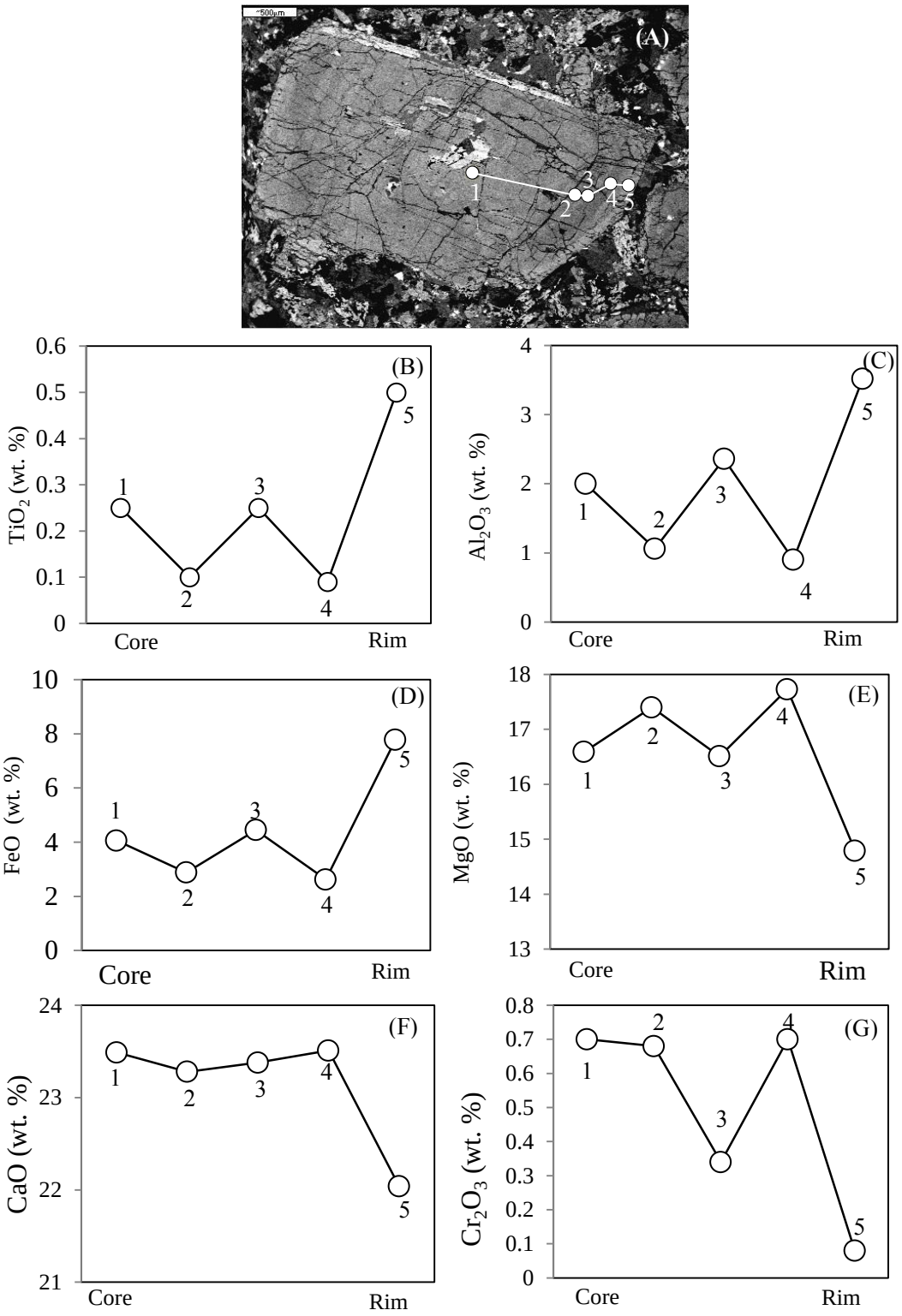


**Figure 1.17:** (A) BSE-image of clinopyroxene phenocryst. (B-G) Compositional variations ($TiO_2$, $Al_2O_3$, FeO, MgO, CaO and $Cr_2O3$) from core to rim traverse for oscillatory zoned clinopyroxene phenocryst of ankaramite rock (Cpx2, Sample #70; Table 1.7).

**Table 1.7:** Representative electron-microprobe analyses of clinopyroxene phenocrysts and microphenocrysts in basaltic rocks of Chukotka, NE Russia.

| Rock | Basaltic andesites | | | | | | | | | | | | | | | | |
|---|---|---|---|---|---|---|---|---|---|---|---|---|---|---|---|---|---|
| Sample | #55 | | | | | #56 | | | | | | | | | | | |
| Mineral | Px1gm | Px2 | Px3 | Px5 | Px6 | Px1 | Px1 | Px1 | Px2 | Px2 | Px2 | Px2 | Px2 | Px2 | Px2 | Px3 | Px4gm |
| | | | | core | rim | core | rim1 | rim2 | core | rim1 | rim2 | rim3 | rim4 | rim5 | rim6 | | |
| $SiO_2$ | 49.39 | 53.97 | 52.69 | 53.19 | 53.16 | 52.36 | 51.5 | 52.5 | 51.96 | 51.93 | 52.26 | 52.46 | 50.71 | 49.84 | 50.56 | 50.47 | 52.16 |
| $TiO_2$ | 2.55 | 0.07 | 0.1 | 0.14 | 0.08 | 0.48 | 0.87 | 0.64 | 0.77 | 0.69 | 0.7 | 0.76 | 0.96 | 1.53 | 0.76 | 0.49 | 0.55 |
| $Al_2O_3$ | 4.01 | 2.05 | 2.52 | 2.63 | 2.32 | 1.52 | 2.85 | 1.57 | 2.21 | 1.68 | 1.51 | 1.36 | 3.1 | 4.24 | 1.74 | 3.18 | 1.7 |
| $Cr_2O_3$ | 0.17 | 0.02 | 0.03 | 0.05 | 0.1 | 0.09 | 0.12 | 0.15 | 0.07 | 0.15 | 0.19 | 0.15 | 0.15 | 0.06 | 0.05 | 0.06 | 0.15 |
| FeO | 20.03 | 19.03 | 20.48 | 19.94 | 19.13 | 14.83 | 12.21 | 12.42 | 10.43 | 13.59 | 12.84 | 13.23 | 12.18 | 11.04 | 13.66 | 13.53 | 13.96 |
| MnO | | | | 0.39 | 0.33 | 0.26 | 0.25 | 0.42 | 0.25 | 0.39 | 0.31 | 0.38 | 0.27 | 0.24 | 0.24 | 0.33 | 0.34 |
| MgO | 9.37 | 12.25 | 11.46 | 11.32 | 11.8 | 12.56 | 13.2 | 13.53 | 14.02 | 13.38 | 13.69 | 13.47 | 13.23 | 13.04 | 13.2 | 12.96 | 13.09 |
| CaO | 13.64 | 12.88 | 12.63 | 12.59 | 12.61 | 19.11 | 19.9 | 20.1 | 20.74 | 18.8 | 19.71 | 19.75 | 19.43 | 20.08 | 18.11 | 18.45 | 19.13 |
| $Na_2O$ | 0.58 | 0.28 | 0.26 | | | 0.26 | 0.34 | 0.15 | 0.1 | 0.19 | 0.19 | 0.15 | 0.11 | 0.16 | 0.16 | 0.32 | 0.27 |
| Total | 99.74 | 100.55 | 100.17 | 100.25 | 99.53 | 101.47 | 101.24 | 101.48 | 100.55 | 100.8 | 101.4 | 101.71 | 100.14 | 100.23 | 98.48 | 99.79 | 101.35 |
| Cations (O=6) | | | | | | | | | | | | | | | | | |
| Si | 1.902 | 2.024 | 2.001 | 2.011 | 2.019 | 1.96 | 1.917 | 1.95 | 1.934 | 1.947 | 1.945 | 1.95 | 1.906 | 1.868 | 1.941 | 1.912 | 1.949 |
| Ti | 0.074 | 0.003 | 0.003 | 0.004 | 0.002 | 0.013 | 0.024 | 0.018 | 0.022 | 0.019 | 0.02 | 0.021 | 0.027 | 0.043 | 0.022 | 0.014 | 0.016 |
| Al | 0.182 | 0.091 | 0.113 | 0.117 | 0.104 | 0.067 | 0.125 | 0.069 | 0.097 | 0.074 | 0.066 | 0.06 | 0.137 | 0.187 | 0.079 | 0.142 | 0.075 |
| $Cr^{3+}$ | 0.005 | 0.001 | 0.001 | 0.001 | 0.003 | 0.003 | 0.004 | 0.005 | 0.002 | 0.004 | 0.006 | 0.004 | 0.005 | 0.002 | 0.002 | 0.002 | 0.004 |
| $Fe^{2+}$ | 0.645 | 0.597 | 0.65 | 0.631 | 0.608 | 0.464 | 0.38 | 0.386 | 0.325 | 0.426 | 0.4 | 0.411 | 0.383 | 0.346 | 0.439 | 0.429 | 0.436 |
| Mn | | | | | 0.011 | 0.008 | 0.008 | 0.013 | 0.008 | 0.012 | 0.01 | 0.012 | 0.009 | 0.008 | 0.008 | 0.011 | 0.011 |
| Mg | 0.538 | 0.685 | 0.648 | 0.638 | 0.668 | 0.701 | 0.732 | 0.749 | 0.778 | 0.748 | 0.76 | 0.746 | 0.741 | 0.729 | 0.756 | 0.732 | 0.729 |
| Ca | 0.563 | 0.518 | 0.514 | 0.51 | 0.513 | 0.766 | 0.793 | 0.8 | 0.827 | 0.755 | 0.786 | 0.787 | 0.783 | 0.806 | 0.745 | 0.749 | 0.766 |
| Na | 0.043 | 0.02 | 0.019 | | | 0.019 | 0.024 | 0.011 | 0.007 | 0.014 | 0.014 | 0.011 | 0.008 | 0.012 | 0.012 | 0.024 | 0.02 |
| Total | 3.952 | 3.939 | 3.949 | 3.912 | 3.928 | 4.001 | 4.007 | 4.001 | 4 | 3.999 | 4.007 | 4.002 | 3.999 | 4.001 | 4.004 | 4.015 | 4.006 |
| Mg# | 45.48 | 53.43 | 49.92 | 50.28 | 52.35 | 60.17 | 65.83 | 65.99 | 70.53 | 63.71 | 65.51 | 64.48 | 65.92 | 67.81 | 63.26 | 63.05 | 62.58 |
| Wo | 32.25 | 28.78 | 28.37 | 28.67 | 28.68 | 39.67 | 41.63 | 41.34 | 42.85 | 39.14 | 40.39 | 40.48 | 41.06 | 42.85 | 38.40 | 39.21 | 39.67 |
| En | 30.81 | 38.06 | 35.76 | 35.86 | 37.34 | 36.30 | 38.43 | 38.71 | 40.31 | 38.78 | 39.05 | 38.37 | 38.86 | 38.76 | 38.97 | 38.32 | 37.75 |
| Fs | 36.94 | 33.17 | 35.87 | 35.47 | 33.99 | 24.03 | 19.95 | 19.95 | 16.84 | 22.08 | 20.55 | 21.14 | 20.08 | 18.39 | 22.63 | 22.46 | 22.58 |

*Total Fe expressed as FeO; Mg#= 100×Mg (Mg+$Fe^{2+}$). Abbreviations: Wo, wollastonite; En, enstatite; Fs, ferrosilite; n, number of analyses used for average.

**Table 1.7:** (*Continued*)

| Rock | Pyroxene-phyric basalt | | | | | | | | | | | | | | | | |
|---|---|---|---|---|---|---|---|---|---|---|---|---|---|---|---|---|---|
| Sample | #67 | | | | | | | | | | | | | | | | |
| Minral | Cpx1 | | Cpx2 | Cpx3 | | Cpx4 | | Cpx5 | | Cpx6 | | Cpx8 | | Cpx9 | | Cpx10 | |
| | core | rim | | core | rim | core | rim | core | rim | core | rim | core | rim | core | rim | core | rim |
| $SiO_2$ | 52.92 | 53.26 | 50.63 | 52.11 | 52.82 | 52.77 | 49.94 | 50.68 | 48.88 | 50.88 | 50.8 | 49.51 | 47.91 | 51.34 | 48.71 | 53.22 | 48.88 |
| $TiO_2$ | 0.28 | 0.3 | 0.71 | 0.27 | 0.47 | 0.28 | 0.67 | 0.56 | 0.7 | 0.57 | 0.57 | 0.6 | 0.76 | 0.44 | 0.68 | 0.25 | 0.83 |
| $Al_2O_3$ | 1.33 | 1.41 | 3.64 | 2.07 | 2.35 | 1.87 | 3.07 | 3.39 | 4.69 | 3.36 | 1.83 | 3.89 | 9.28 | 3.06 | 4.11 | 1.16 | 5.09 |
| $Cr_2O_3$ | 0.42 | 0.39 | 0.08 | 0.18 | 0.18 | 0.18 | 0.04 | 0.16 | 0.06 | 0.07 | | 0.12 | 0.07 | 0.35 | 0.15 | 0.22 | 0.11 |
| FeO | 3.64 | 3.52 | 6.52 | 4.61 | 4.67 | 4.34 | 7.27 | 5.89 | 7.74 | 5.28 | 7.55 | 6.41 | 7.44 | 5.49 | 6.6 | 3.52 | 6.16 |
| MnO | 0.05 | 0.13 | 0.11 | 0.09 | 0.04 | 0.11 | 0.13 | 0.13 | 0.11 | 0.16 | 0.38 | 0.14 | 0.15 | 0.12 | 0.1 | 0.09 | 0.12 |
| MgO | 16.73 | 16.9 | 14.57 | 15.8 | 16.11 | 16.27 | 13.86 | 14.88 | 13.54 | 15.07 | 14.39 | 14.31 | 10.94 | 15.22 | 13.9 | 16.63 | 14.06 |
| CaO | 23.88 | 23.73 | 23.22 | 23.49 | 23.96 | 24.1 | 22.37 | 23.09 | 22.72 | 23.42 | 21.04 | 23.01 | 20.61 | 23.06 | 22.57 | 23.63 | 22.79 |
| $Na_2O$ | 0.04 | 0.01 | 0.14 | 0.05 | | 0.05 | 0.25 | 0.07 | 0.13 | 0.12 | 0.34 | 0.09 | 0.81 | 0.04 | 0.17 | | 0.1 |
| Total | 99.29 | 99.65 | 99.62 | 98.67 | 100.6 | 99.97 | 97.6 | 98.85 | 98.57 | 98.93 | 96.9 | 98.08 | 97.97 | 99.12 | 96.99 | 98.72 | 98.14 |
| Cations (O=6) | | | | | | | | | | | | | | | | | |
| Si | 1.951 | 1.953 | 1.885 | 1.94 | 1.928 | 1.939 | 1.903 | 1.896 | 1.852 | 1.898 | 1.946 | 1.874 | 1.808 | 1.91 | 1.867 | 1.968 | 1.846 |
| Ti | 0.008 | 0.008 | 0.02 | 0.007 | 0.013 | 0.008 | 0.019 | 0.016 | 0.02 | 0.016 | 0.016 | 0.017 | 0.022 | 0.012 | 0.019 | 0.007 | 0.023 |
| Al | 0.058 | 0.061 | 0.16 | 0.091 | 0.101 | 0.081 | 0.138 | 0.149 | 0.209 | 0.148 | 0.083 | 0.173 | 0.413 | 0.134 | 0.186 | 0.051 | 0.227 |
| $Cr^{3+}$ | 0.012 | 0.011 | 0.002 | 0.005 | 0.005 | 0.005 | 0.001 | 0.005 | 0.002 | 0.002 | | 0.004 | 0.002 | 0.01 | 0.005 | 0.007 | 0.003 |
| $Fe^{2+}$ | 0.112 | 0.108 | 0.203 | 0.144 | 0.143 | 0.133 | 0.232 | 0.184 | 0.245 | 0.165 | 0.242 | 0.203 | 0.235 | 0.171 | 0.212 | 0.109 | 0.195 |
| Mn | 0.002 | 0.004 | 0.003 | 0.003 | 0.001 | 0.004 | 0.004 | 0.004 | 0.004 | 0.005 | 0.012 | 0.004 | 0.005 | 0.004 | 0.003 | 0.003 | 0.004 |
| Mg | 0.919 | 0.924 | 0.809 | 0.876 | 0.877 | 0.891 | 0.788 | 0.83 | 0.764 | 0.838 | 0.822 | 0.807 | 0.615 | 0.844 | 0.794 | 0.917 | 0.792 |
| Ca | 0.943 | 0.932 | 0.927 | 0.937 | 0.937 | 0.949 | 0.914 | 0.925 | 0.922 | 0.936 | 0.864 | 0.934 | 0.833 | 0.919 | 0.927 | 0.936 | 0.922 |
| Na | 0.003 | 0.001 | 0.01 | 0.003 | | 0.004 | 0.018 | 0.005 | 0.01 | 0.009 | 0.025 | 0.007 | 0.06 | 0.003 | 0.013 | | 0.007 |
| Total | 4.008 | 4.002 | 4.019 | 4.006 | 4.005 | 4.014 | 4.017 | 4.014 | 4.028 | 4.017 | 4.01 | 4.023 | 3.993 | 4.007 | 4.026 | 3.998 | 4.019 |
| Mg# | 89.14 | 89.54 | 79.94 | 85.88 | 85.98 | 87.01 | 77.25 | 81.85 | 75.72 | 83.55 | 77.26 | 79.90 | 72.35 | 83.15 | 78.93 | 89.38 | 80.24 |
| Wo | 47.77 | 47.45 | 47.81 | 47.88 | 47.88 | 48.10 | 47.26 | 47.71 | 47.75 | 48.27 | 44.81 | 48.05 | 49.49 | 47.52 | 47.96 | 47.71 | 48.30 |
| En | 46.56 | 47.05 | 41.72 | 44.76 | 44.81 | 45.16 | 40.74 | 42.81 | 39.56 | 43.22 | 42.63 | 41.51 | 36.54 | 43.64 | 41.08 | 46.74 | 41.49 |
| Fs | 5.67 | 5.50 | 10.47 | 7.36 | 7.31 | 6.74 | 12.00 | 9.49 | 12.69 | 8.51 | 12.55 | 10.44 | 13.96 | 8.84 | 10.97 | 5.56 | 10.21 |

**Table 1.7:** (*Continued*)

| Rock | Ankaramites | | | | | | | | | | | | | | | | |
|---|---|---|---|---|---|---|---|---|---|---|---|---|---|---|---|---|---|
| Sampl | #69 | | | | | | #70 | | | | | #71 | | | | | |
| Minera | Cpx1 | Cpx 2 | | Cpx4 | | Cpx5 | Cpx2 | | | | | Cpx2 | | | | | |
| | core | core | rim | core | rim | core | core | inner | inner | inner | outer | core | inner | inner | inner | inner | outer |
| $SiO_2$ | 52.82 | 53.31 | 52.63 | 54.28 | 52.55 | 54.88 | 53.53 | 53.88 | 52.96 | 54.49 | 50.6 | 52.4 | 53.44 | 52.22 | 53.55 | 51.59 | 53.8 |
| $TiO_2$ | 0.22 | 0.26 | 0.38 | 0.07 | 0.27 | 0.73 | 0.25 | 0.1 | 0.25 | 0.09 | 0.5 | 0.21 | 0.09 | 0.22 | 0.1 | 0.23 | 0.09 |
| $Al_2O_3$ | 1.91 | 1.66 | 2.51 | 0.78 | 2.54 | 2.25 | 2 | 1.06 | 2.36 | 0.9 | 3.52 | 1.42 | 0.92 | 1.93 | 1.15 | 2.22 | 1.08 |
| $Cr_2O_3$ | 0.41 | 0.52 | 0.34 | 0.5 | 0.36 | 0.08 | 0.7 | 0.68 | 0.34 | 0.7 | 0.08 | 0.4 | 0.56 | 0.45 | 0.68 | 0.45 | 0.56 |
| FeO | 4.79 | 4.14 | 5.13 | 2.96 | 5.23 | 14.6 | 4.06 | 2.88 | 4.45 | 2.62 | 7.78 | 3.62 | 2.79 | 4.39 | 3.07 | 4.45 | 3.13 |
| MnO | 0.1 | 0.11 | 0.05 | 0.19 | 0.09 | 0.66 | 0.16 | 0.04 | 0.07 | 0.03 | 0.09 | 0.07 | 0.07 | | 0.05 | 0.05 | 0.03 |
| MgO | 16.33 | 16.74 | 16.35 | 17.45 | 15.78 | 15.64 | 16.59 | 17.4 | 16.51 | 17.73 | 14.7 | 16.7 | 17.4 | 16.29 | 17.15 | 16.15 | 17.29 |
| CaO | 23.47 | 23.91 | 23.33 | 23.88 | 24.27 | 11.29 | 23.49 | 23.28 | 23.38 | 23.51 | 22.0 | 22.7 | 22.86 | 23.26 | 23.15 | 22.91 | 23.1 |
| $Na_2O$ | | | | | | 0.41 | | | | | 0.07 | | 0.07 | 0.07 | | 0.03 | |
| Total | 100.0 | 100.6 | 100.7 | 100.1 | 101.0 | 100.54 | 100.7 | 99.32 | 100.3 | 100.07 | 99.5 | 97.6 | 98.2 | 98.83 | 98.9 | 98.08 | 99.08 |
| Cations (O=6) | | | | | | | | | | | | | | | | | |
| Si | 1.939 | 1.942 | 1.921 | 1.975 | 1.918 | 2.014 | 1.944 | 1.972 | 1.934 | 1.977 | 1.89 | 1.96 | 1.977 | 1.938 | 1.97 | 1.93 | 1.975 |
| Ti | 0.006 | 0.007 | 0.01 | 0.002 | 0.008 | 0.02 | 0.007 | 0.003 | 0.007 | 0.002 | 0.01 | 0.00 | 0.003 | 0.006 | 0.003 | 0.006 | 0.002 |
| Al | 0.083 | 0.071 | 0.108 | 0.034 | 0.109 | 0.097 | 0.086 | 0.046 | 0.102 | 0.039 | 0.15 | 0.06 | 0.04 | 0.084 | 0.05 | 0.098 | 0.047 |
| $Cr^{3+}$ | 0.012 | 0.015 | 0.01 | 0.014 | 0.01 | 0.002 | 0.02 | 0.02 | 0.01 | 0.02 | 0.00 | 0.01 | 0.016 | 0.013 | 0.02 | 0.013 | 0.016 |
| $Fe^{2+}$ | 0.147 | 0.126 | 0.157 | 0.09 | 0.16 | 0.448 | 0.123 | 0.088 | 0.136 | 0.079 | 0.24 | 0.11 | 0.086 | 0.136 | 0.094 | 0.139 | 0.096 |
| Mn | 0.003 | 0.003 | 0.002 | 0.006 | 0.003 | 0.021 | 0.005 | 0.001 | 0.002 | 0.001 | 0.00 | 0.00 | 0.002 | | 0.002 | 0.002 | 0.001 |
| Mg | 0.894 | 0.909 | 0.889 | 0.947 | 0.859 | 0.856 | 0.898 | 0.949 | 0.899 | 0.959 | 0.82 | 0.93 | 0.959 | 0.901 | 0.941 | 0.901 | 0.946 |
| Ca | 0.923 | 0.933 | 0.912 | 0.931 | 0.949 | 0.444 | 0.914 | 0.913 | 0.915 | 0.914 | 0.88 | 0.90 | 0.906 | 0.925 | 0.913 | 0.918 | 0.908 |
| Na | | | | | | 0.029 | | | | | 0.00 | | 0.005 | 0.005 | | 0.002 | |
| Total | 4.007 | 4.006 | 4.009 | 3.999 | 4.016 | 3.931 | 3.997 | 3.992 | 4.005 | 3.991 | 4.01 | 3.99 | 3.994 | 4.008 | 3.993 | 4.009 | 3.991 |
| Mg# | 85.88 | 87.83 | 84.99 | 91.32 | 84.30 | 65.64 | 87.95 | 91.51 | 86.86 | 92.39 | 77.2 | 89.1 | 91.77 | 86.88 | 90.92 | 86.63 | 90.79 |
| Wo | 46.99 | 47.41 | 46.58 | 47.31 | 48.22 | 25.40 | 47.23 | 46.82 | 46.92 | 46.82 | 45.2 | 46.5 | 46.44 | 47.15 | 46.87 | 46.88 | 46.56 |
| En | 45.52 | 46.19 | 45.40 | 48.12 | 43.65 | 48.97 | 46.41 | 48.67 | 46.10 | 49.13 | 42.2 | 47.6 | 49.15 | 45.92 | 48.31 | 46.02 | 48.51 |
| Fs | 7.49 | 6.40 | 8.02 | 4.57 | 8.13 | 25.63 | 6.36 | 4.51 | 6.97 | 4.05 | 12.4 | 5.79 | 4.41 | 6.93 | 4.83 | 7.10 | 4.93 |

**Table 1.7:** (*Continued*)

| Rock | Lamprophyres | | | | | | | | |
|---|---|---|---|---|---|---|---|---|---|
| Sample | #59 | | #74 | | #77 | | | | |
| Mineral | Cpx1 | Cpx5 | Cpx1 | Cpx2 | Cpx1 | | Cpx2 | Cpx3 | Cpx4 |
| | core | core | core | core | core | rim | core | core | core |
| $SiO_2$ | 52.04 | 50.68 | 49.9 | 46.87 | 49.18 | 50.02 | 48.45 | 49.88 | 48.79 |
| $TiO_2$ | 0.52 | 0.89 | 0.8 | 0.11 | 0.82 | 0.67 | | 0.80 | 1.00 |
| $Al_2O_3$ | 2.45 | 4.66 | 4.58 | 2.26 | 4.76 | 3.68 | 4.94 | 4.72 | 6.10 |
| $Cr_2O_3$ | 0.51 | 0.31 | 0.13 | 0.18 | 0.06 | 0.22 | 0.07 | 0.09 | 0.02 |
| FeO | 4.39 | 5.8 | 6.3 | 8.42 | 6.80 | 6.09 | 8.58 | 7.02 | 8.82 |
| MnO | 0.03 | 0.14 | 0.14 | 0.45 | 0.19 | 0.02 | 0.15 | 0.11 | 0.16 |
| MgO | 15.91 | 14.69 | 13.77 | 12.8 | 13.80 | 14.51 | 12.66 | 14.03 | 12.67 |
| CaO | 23.47 | 24.02 | 23.65 | 24.22 | 24.01 | 23.67 | 23.03 | 23.88 | 23.83 |
| $Na_2O$ | 0.04 | 0.11 | 0.12 | 0.03 | 0.130 | 0.080 | 0.240 | 0.070 | 0.140 |
| Total | 99.36 | 101.3 | 99.39 | 95.34 | 99.750 | 98.960 | 99.070 | 100.600 | 101.530 |
| Cations (O=6) | | | | | | | | | |
| Si | 1.923 | 1.854 | 1.864 | 1.867 | 1.840 | 1.876 | 1.837 | 1.848 | 1.808 |
| Ti | 0.015 | 0.024 | 0.022 | 0.003 | 0.023 | 0.019 | 0.027 | 0.022 | 0.028 |
| Al | 0.107 | 0.201 | 0.201 | 0.106 | 0.210 | 0.163 | 0.221 | 0.206 | 0.266 |
| $Cr^{3}+$ | 0.015 | 0.009 | 0.004 | 0.006 | 0.002 | 0.006 | 0.002 | 0.003 | 0.001 |
| $Fe^{2+}$ | 0.136 | 0.177 | 0.197 | 0.281 | 0.213 | 0.191 | 0.272 | 0.218 | 0.273 |
| Mn | 0.001 | 0.004 | 0.004 | 0.015 | 0.006 | 0.001 | 0.005 | 0.003 | 0.005 |
| Mg | 0.876 | 0.801 | 0.767 | 0.76 | 0.77 | 0.811 | 0.716 | 0.775 | 0.699 |
| Ca | 0.929 | 0.942 | 0.947 | 1.034 | 0.963 | 0.951 | 0.936 | 0.948 | 0.946 |
| Na | 0.003 | 0.008 | 0.009 | 0.002 | 0.01 | 0.006 | 0.018 | 0.005 | 0.01 |
| Total | 4.005 | 4.02 | 4.015 | 4.074 | 4.037 | 4.024 | 4.034 | 4.028 | 4.036 |
| Mg# | 86.56 | 81.90 | 79.56 | 73.01 | 78.33 | 80.94 | 72.47 | 78.05 | 71.91 |
| Wo | 47.86 | 49.06 | 49.56 | 49.83 | 49.49 | 48.69 | 48.65 | 48.84 | 49.32 |
| En | 45.14 | 41.72 | 40.14 | 36.63 | 39.57 | 41.53 | 37.21 | 39.93 | 36.44 |
| Fs | 7.01 | 9.22 | 10.31 | 13.54 | 10.95 | 9.78 | 14.14 | 11.23 | 14.23 |

#### 1.5.2.2.2. Amphibole

Amphibole phenocrysts in the basalts and basaltic andesite have high CaO contents (11.3-12.8 wt. %; Table 1.8) and thus are calcic amphiboles (Leake 1978). According to Leake et al. (1978) $Al^{(IV)}$ versus $(Na+K)_A$ amphibole classification diagram (Fig. 1.12), amphiboles from basalts are plotted in the pargasite, pargasitic hornblende and edenitic hornblende field, whereas those from basaltic andesite are plotted in the pargasite field.. The ankaramite rocks contain groundmass amphiboles with edenitic (Na+K, 0.51-0.53; Si, >6.5) composition. The Mg# of amphibole in basaltic rocks is higher (lamprophyre ranges from 61 to 72, ankaramite from 73 to 74) compared to those in basaltic andesites (61-71) (Fig. 1.18). Amphiboles in lamprophyres exhibit higher content of $Al_2O_3$ (13.6-16.0 wt. %, average, 14.6 wt. %) and CaO (10.0-13.2 wt. %, average, 12.5 wt. %) than those of basaltic andesite $Al_2O_3$ 12.3~13.1 wt. %, average, 12.0 wt. %; CaO 11.4-11.6 wt. %, average, 11.5 wt. %).

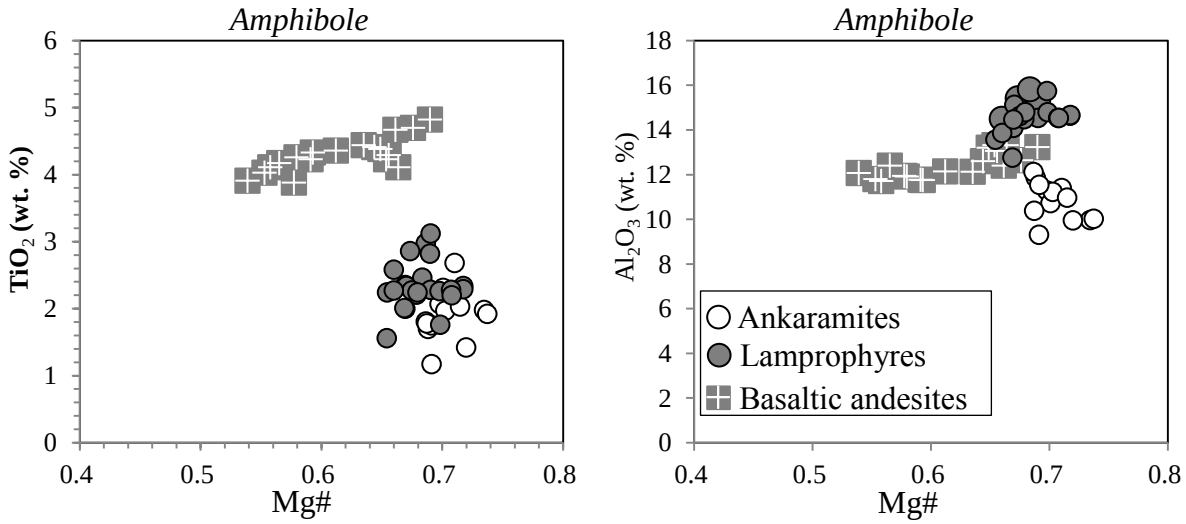


**Figure 1.18:** Major element chemistry of amphibole from basaltic rocks of Chukotka.

However, those in ankaramite show CaO ~11.2 wt. % and lower in $Al_2O_3$ ~10 wt. %. The $TiO_2$ concentration of amphiboles in basaltic andesites ranges from 4.12 to 4.74 wt. %, lamprophyres from 0.36-3.1 wt. % and ankaramite from 2.04-2.24 wt. %. Some of the amphibole phenocryts in basaltic andesite are characterized by oscillatory zoing (Fig. 1.19).

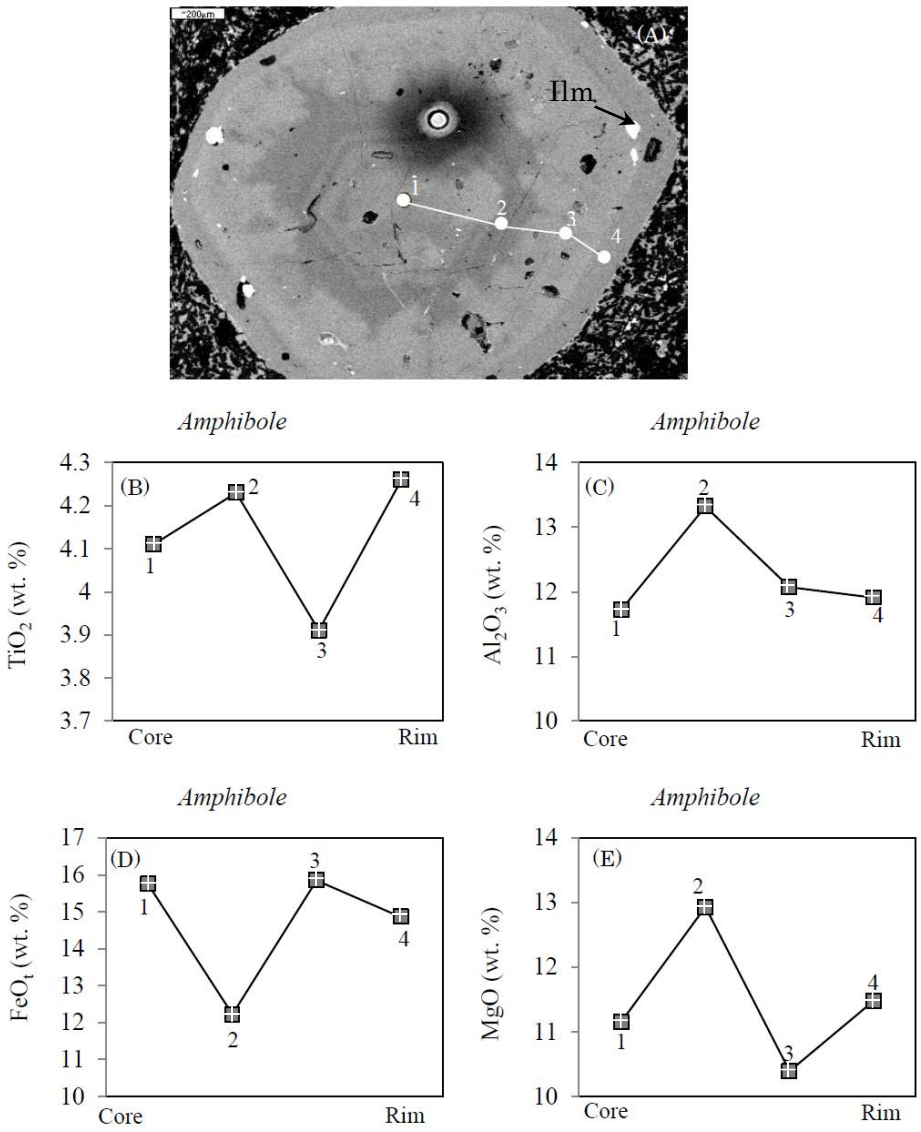


**Figure 1.19:** (A) BSE image of basaltic andesite with euhedral amphibole phenocryst showing oscillatoryzoning. White filled circles indicate analyses point. The white circle is a damge due to LA-ICP-MS analyses. (B-E) Compositional variations ($TiO_2$, $Al_2O_3$, FeO, and MgO) from core to rim traverse for a oscillatory zoning of amphibole phenocryst of basaltic andesite (Hb7, Sample #55; Table 1.8). Ilm, Ilmenite.

**Table 1.8:** Representative electron-microprobe analyses of hornblende phenocrysts and microphenocrysts in basaltic rocks of Chukotka, NE Russia

| Rock | Basaltic andesites | | | | | | | | | | | | | | | | | |
|---|---|---|---|---|---|---|---|---|---|---|---|---|---|---|---|---|---|---|
| Sample | #55 | | | | | | | | | | | #56 | | | | | | |
| Mineral | Hb1 | | Hb7 | | | | Hb8 | | Hb10 | | | Hb1 | | Hb2 | Hb3 | | | |
| Position | core | rim | core | rim1 | rim2 | rim3 | core | rim | core | rim1 | rim2 | core | rim | core | core | rim1 | rim2 | |
| $SiO_2$ | 42.35 | 41.82 | 42.74 | 41.92 | 42.6 | 42.16 | 42.35 | 42.42 | 42.82 | 42.65 | 42.49 | 43.34 | 42.25 | 42.7 | 42.64 | 42.4 | 42.57 | |
| $TiO_2$ | 4.03 | 4.23 | 4.11 | 4.23 | 3.91 | 4.26 | 4.41 | 4.38 | 4.33 | 4.11 | 4.29 | 3.88 | 4.7 | 4.67 | 4.44 | 4.36 | 4.82 | |
| $Al_2O_3$ | 11.8 | 11.77 | 11.72 | 13.32 | 12.07 | 11.91 | 12.6 | 13.21 | 11.75 | 13.32 | 13.06 | 11.94 | 12.65 | 12.4 | 12.13 | 12.14 | 13.24 | |
| $Cr_2O_3$ | 0.06 | 0.11 | 0.02 | 0.09 | 0.03 | 0.06 | 0.03 | 0.08 | 0.13 | 0.11 | 0.13 | 0.13 | 0.15 | 0.21 | 0.09 | 0.16 | 0.28 | |
| FeO | 15.89 | 14.26 | 15.75 | 12.22 | 15.85 | 14.86 | 12.64 | 12.42 | 14.5 | 12.06 | 12.26 | 15.24 | 11.21 | 12 | 12.74 | 13.73 | 10.98 | |
| MnO | | | | | | | | | | | | | | 0.18 | 0.16 | 0.1 | 0.05 | |
| MgO | 11.04 | 11.57 | 11.15 | 12.93 | 10.39 | 11.48 | 12.84 | 12.87 | 11.85 | 13.36 | 13.11 | 11.69 | 13.12 | 13.16 | 12.45 | 12.15 | 13.71 | |
| CaO | 11.11 | 11.14 | 11.39 | 11.7 | 10.63 | 11.33 | 11.21 | 11.76 | 11.48 | 11.48 | 11.51 | 11.3 | 11.76 | 11.69 | 11.43 | 11.41 | 11.81 | |
| $Na_2O$ | 2.84 | 2.7 | 2.81 | 2.71 | 3.12 | 2.8 | 2.84 | 2.74 | 2.79 | 2.81 | 2.77 | 2.81 | 2.78 | 2.85 | 2.6 | 2.77 | 2.82 | |
| $K_2O$ | 1.08 | 1.09 | 1.11 | 1.01 | 1.13 | 1.06 | 0.9 | 0.99 | 1.08 | 1.02 | 0.94 | 0.96 | 1.02 | 0.99 | 1.09 | 0.99 | 1.01 | |
| Total | 100.20 | 98.69 | 100.80 | 100.13 | 99.73 | 99.92 | 99.82 | 100.87 | 100.73 | 100.92 | 100.56 | 101.29 | 99.64 | 100.85 | 99.77 | 100.21 | 101.29 | |
| Cations (O=23) | | | | | | | | | | | | | | | | | | |
| Si | 6.213 | 6.191 | 6.229 | 6.058 | 6.268 | 6.179 | 6.138 | 6.085 | 6.212 | 6.099 | 6.105 | 6.255 | 6.112 | 6.126 | 6.195 | 6.163 | 6.051 | |
| Ti | 0.444 | 0.471 | 0.45 | 0.46 | 0.433 | 0.47 | 0.48 | 0.473 | 0.472 | 0.441 | 0.464 | 0.421 | 0.511 | 0.504 | 0.485 | 0.476 | 0.515 | |
| Al | 2.04 | 2.053 | 2.013 | 2.269 | 2.093 | 2.058 | 2.153 | 2.234 | 2.008 | 2.245 | 2.211 | 2.03 | 2.157 | 2.097 | 2.077 | 2.08 | 2.218 | |
| $Cr^{3+}$ | 0.007 | 0.013 | 0.002 | 0.01 | 0.004 | 0.007 | 0.003 | 0.009 | 0.014 | 0.013 | 0.014 | 0.015 | 0.018 | 0.024 | 0.01 | 0.018 | 0.032 | |
| $Fe^{2+}$ | 1.950 | 1.765 | 1.919 | 1.476 | 1.949 | 1.821 | 1.533 | 1.489 | 1.758 | 1.442 | 1.473 | 1.839 | 1.356 | 1.44 | 1.548 | 1.669 | 1.306 | |
| Mn | | | | | | | | | | | | | | 0.022 | 0.02 | 0.012 | 0.006 | |
| Mg | 2.414 | 2.553 | 2.422 | 2.785 | 2.278 | 2.509 | 2.773 | 2.752 | 2.563 | 2.848 | 2.808 | 2.514 | 2.829 | 2.814 | 2.696 | 2.633 | 2.905 | |
| Na | 0.808 | 0.775 | 0.793 | 0.759 | 0.89 | 0.795 | 0.797 | 0.762 | 0.786 | 0.78 | 0.772 | 1.747 | 1.822 | 1.798 | 1.779 | 1.778 | 1.798 | |
| Ca | 1.746 | 1.767 | 1.779 | 1.811 | 1.676 | 1.779 | 1.741 | 1.807 | 1.784 | 1.759 | 1.772 | 0.785 | 0.78 | 0.791 | 0.731 | 0.781 | 0.777 | |
| K | 0.202 | 0.207 | 0.206 | 0.186 | 0.213 | 0.199 | 0.166 | 0.18 | 0.199 | 0.185 | 0.172 | 0.177 | 0.188 | 0.181 | 0.201 | 0.184 | 0.182 | |
| Total | 15.82 | 15.79 | 15.81 | 15.81 | 15.80 | 15.82 | 15.78 | 15.79 | 15.79 | 15.81 | 15.79 | 15.78 | 15.77 | 15.79 | 15.74 | 15.79 | 15.79 | |
| Mg# | 55.32 | 59.12 | 55.79 | 65.36 | 53.89 | 57.94 | 64.39 | 64.89 | 59.31 | 66.38 | 65.59 | 57.75 | 67.59 | 66.14 | 63.52 | 61.20 | 68.98 | |

*Total Fe as FeO; Mg#= 100×Mg (Mg+$Fe^{2+}$).

**Table 1.8:** (*Continued*)

| Rock | Ankaramites | | | | | | | | | | | | |
|---|---|---|---|---|---|---|---|---|---|---|---|---|---|
| Sample | #69 | | | | | #70 | | | | #71 | | | |
| Mineral | Hb1 gm | Hb2 gm | Hb3 gm | Hb4 gm | Hb5 gm | Hb1 gm | Hb2 gm | Hb3 gm | Hb4 gm | Hb1 gm | Hb2 gm | Hb4 gm | Hb5 gm |
| $SiO_2$ | 43.67 | 44.34 | 42.9 | 44.84 | 46.11 | 45.37 | 43.76 | 44.61 | 43.65 | 44.58 | 45.67 | 44.5 | 46.08 |
| $TiO_2$ | 1.7 | 2.07 | 1.81 | 2.31 | 1.75 | 1.98 | 2.68 | 1.78 | 1.97 | 1.17 | 1.92 | 2.03 | 1.42 |
| $Al_2O_3$ | 11.86 | 11.29 | 12.12 | 10.73 | 9.31 | 9.97 | 11.4 | 10.38 | 11.23 | 11.54 | 10.02 | 10.97 | 9.95 |
| $Cr_2O_3$ | | 0.11 | 0.06 | 0.03 | 0.05 | 0.04 | | 0.02 | 0.12 | 0.14 | 0.04 | 0.05 | 0.07 |
| FeO | 12.07 | 11.71 | 12.02 | 11.84 | 12.23 | 10.53 | 11.09 | 11.93 | 11.35 | 11.61 | 10.26 | 10.99 | 11.14 |
| MnO | 0.49 | 0.35 | 0.43 | 0.45 | 0.56 | 0.5 | 0.33 | 0.49 | 0.39 | 0.48 | 0.44 | 0.43 | 0.43 |
| MgO | 14.96 | 15.18 | 14.78 | 15.58 | 15.38 | 16.36 | 15.26 | 14.72 | 15.05 | 14.59 | 16.17 | 15.46 | 16.05 |
| CaO | 11.15 | 11.49 | 11.24 | 11.37 | 11.38 | 10.39 | 11.25 | 11.02 | 11.17 | 11.67 | 10.96 | 11.2 | 10.79 |
| $Na_2O$ | 2.98 | 3.1 | 3.15 | 2.97 | 2.84 | 3.04 | 3.01 | 2.83 | 2.97 | 2.72 | 3.09 | 3.05 | 3.01 |
| $K_2O$ | 0.8 | 0.81 | 0.8 | 0.82 | 0.64 | 0.61 | 0.71 | 0.74 | 0.82 | 0.84 | 0.66 | 0.74 | 0.63 |
| Total | 99.68 | 100.45 | 99.31 | 100.94 | 100.25 | 98.79 | 99.49 | 98.52 | 98.72 | 99.34 | 99.23 | 99.42 | 99.57 |
| Cations (O=23) | | | | | | | | | | | | | |
| Si | 6.317 | 6.357 | 6.241 | 6.395 | 6.614 | 6.543 | 6.313 | 6.509 | 6.359 | 6.448 | 6.557 | 6.416 | 6.606 |
| Ti | 0.185 | 0.224 | 0.198 | 0.248 | 0.189 | 0.214 | 0.291 | 0.195 | 0.216 | 0.127 | 0.208 | 0.22 | 0.153 |
| Al | 2.022 | 1.908 | 2.079 | 1.804 | 1.574 | 1.695 | 1.939 | 1.785 | 1.927 | 1.967 | 1.695 | 1.864 | 1.681 |
| $Cr^{3+}$ | | 0.012 | 0.007 | 0.003 | 0.006 | 0.004 | | 0.002 | 0.014 | 0.016 | 0.004 | 0.006 | 0.008 |
| $Fe^{2+}$ | 1.46 | 1.404 | 1.463 | 1.413 | 1.468 | 1.271 | 1.338 | 1.456 | 1.383 | 1.404 | 1.232 | 1.325 | 1.335 |
| Mn | 0.06 | 0.043 | 0.053 | 0.055 | 0.068 | 0.061 | 0.04 | 0.061 | 0.048 | 0.059 | 0.053 | 0.052 | 0.052 |
| Mg | 3.227 | 3.245 | 3.206 | 3.311 | 3.288 | 3.518 | 3.281 | 3.2 | 3.269 | 3.145 | 3.46 | 3.323 | 3.43 |
| Na | 1.728 | 1.765 | 1.752 | 1.738 | 1.748 | 1.605 | 1.739 | 1.723 | 1.744 | 1.809 | 1.686 | 1.73 | 1.657 |
| Ca | 0.835 | 0.861 | 0.888 | 0.822 | 0.79 | 0.851 | 0.842 | 0.8 | 0.838 | 0.764 | 0.86 | 0.853 | 0.835 |
| K | 0.147 | 0.147 | 0.148 | 0.149 | 0.117 | 0.112 | 0.13 | 0.137 | 0.152 | 0.155 | 0.121 | 0.135 | 0.115 |
| Total | 15.98 | 15.97 | 16.04 | 15.94 | 15.86 | 15.87 | 15.91 | 15.87 | 15.95 | 15.89 | 15.88 | 15.92 | 15.87 |
| Mg# | 68.85 | 69.80 | 68.67 | 70.09 | 69.13 | 73.46 | 71.03 | 68.73 | 70.27 | 69.14 | 73.74 | 71.49 | 71.98 |

**Table 1.8:** (*Continued*)

| Rock | Lamprophyres | | | | | | | | | | | | | | | | | |
|---|---|---|---|---|---|---|---|---|---|---|---|---|---|---|---|---|---|---|
| Sample | #59 | | | | #74 | | | | | | | #77 | | | | | | |
| Minera | Hb1 | Hb4 | Hb5 | Hb7 | Hb1 | Hb2 | | Hb5 | Hb6 | Hb7 | Hb10 | Hb1 | Hb2 | | Hb4 | | | |
| Positio | core | core | core | core | core | core | rim | core | core | core | core | core | core | rim | core | rim1 | rim2 | |
| $SiO_2$ | 37.72 | 39.94 | 39.72 | 41.51 | 40.21 | 39.6 | 40.44 | 39.98 | 39.68 | 39.38 | 40.14 | 40.27 | 40.93 | 40.56 | 41.16 | 41.4 | 42.7 | |
| $TiO_2$ | 2.98 | 2.82 | 3.12 | 2.58 | 2.28 | 1.76 | 2.34 | 2.29 | 2. 34 | 2.26 | 2.28 | 2.21 | 2.27 | 2.24 | 2.2 | 2 | 2.01 | |
| $Al_2O_3$ | 15.24 | 15.25 | 15.32 | 14.49 | 14.54 | 14.79 | 14.64 | 14.66 | 15.12 | 15.74 | 14.54 | 14.48 | 14.62 | 14.79 | 14.54 | 14.47 | 12.76 | |
| $Cr_2O_3$ | 0.03 | 0.1 | 0.05 | 0.02 | | 0.1 | | | | 0.04 | | | | 0.12 | 0.01 | 0 | 0.04 | |
| FeO | 10.42 | 11.01 | 10.92 | 12.43 | 10.72 | 12.27 | 9.97 | 9.86 | 11.3 | 10.36 | 10.23 | 11.56 | 11.96 | 11.6 | 10.77 | 11.96 | 12.19 | |
| MnO | 0.17 | 0.06 | 0.17 | 0.28 | 0.03 | 0.09 | 0.14 | 0.09 | 0.16 | 0.15 | 0.07 | 0.11 | 0.06 | 0.06 | 0.16 | 0.16 | 0.15 | |
| MgO | 12.8 | 13.75 | 13.67 | 13.54 | 13.41 | 15.95 | 14.22 | 14.07 | 12.89 | 13.43 | 13.89 | 13.71 | 13.94 | 13.81 | 14.66 | 13.6 | 13.82 | |
| CaO | 12.12 | 12.69 | 12.65 | 12.62 | 12.54 | 9.77 | 12.73 | 12.61 | 12.68 | 12.79 | 12.6 | 12.65 | 12.84 | 12.72 | 12.98 | 13.03 | 13.05 | |
| $Na_2O$ | 2.8 | 2.88 | 3.11 | 2.99 | 2.7 | 2.41 | 2.65 | 2.67 | 2.81 | 2.77 | 2.65 | 2.55 | 2.58 | 2.89 | 2.82 | 2.64 | 2.28 | |
| $K_2O$ | 0.82 | 0.72 | 0.75 | 0.77 | 0.96 | 0.92 | 1 | 1.06 | 1.02 | 1.05 | 1.04 | 1.07 | 1.05 | 1.08 | 1.12 | 0.91 | 1.02 | |
| Total | 95.1 | 99.22 | 99.48 | 101.23 | 97.39 | 97.66 | 98.13 | 97.29 | 98 | 97.97 | 97.44 | 98.61 | 100.25 | 99.87 | 100.42 | 100.17 | 100.02 | |
| Cations (O=23) | | | | | | | | | | | | | | | | | | |
| Si | 5.743 | 5.822 | 5.783 | 5.957 | 5.96 | 5.853 | 5.932 | 5.918 | 5.873 | 5.81 | 5.939 | 5.923 | 5.925 | 5.896 | 5.928 | 5.992 | 6.184 | |
| Ti | 0.341 | 0.309 | 0.342 | 0.278 | 0.254 | 0.196 | 0.258 | 0.255 | 0.26 | 0.251 | 0.254 | 0.245 | 0.247 | 0.245 | 0.238 | 0.218 | 0.219 | |
| Al | 2.735 | 2.621 | 2.628 | 2.451 | 2.54 | 2.577 | 2.531 | 2.557 | 2.638 | 2.736 | 2.535 | 2.511 | 2.494 | 2.533 | 2.468 | 2.469 | 2.178 | |
| $Cr^{3+}$ | 0.004 | 0.012 | 0.006 | 0.002 | | 0.012 | | | | 0.005 | | | | 0.014 | 0.001 | 0 | 0.005 | |
| $Fe^{2+}$ | 1.327 | 1.342 | 1.329 | 1.492 | 1.328 | 1.517 | 1.224 | 1.221 | 1.399 | 1.278 | 1.266 | 1.422 | 1.449 | 1.41 | 1.298 | 1.448 | 1.477 | |
| Mn | 0.022 | 0.008 | 0.021 | 0.034 | 0.003 | 0.011 | 0.017 | 0.011 | 0.02 | 0.019 | 0.009 | 0.014 | 0.007 | 0.008 | 0.019 | 0.02 | 0.019 | |
| Mg | 2.905 | 2.986 | 2.966 | 2.896 | 2.963 | 3.513 | 3.109 | 3.103 | 2.845 | 2.954 | 3.063 | 3.005 | 3.008 | 2.991 | 3.147 | 2.933 | 2.983 | |
| Na | 1.977 | 1.981 | 1.973 | 1.94 | 1.991 | 1.548 | 2.002 | 2 | 2.012 | 2.021 | 1.997 | 1.994 | 1.992 | 1.982 | 2.003 | 2.02 | 2.025 | |
| Ca | 0.827 | 0.814 | 0.879 | 0.833 | 0.777 | 0.691 | 0.754 | 0.767 | 0.806 | 0.792 | 0.759 | 0.728 | 0.723 | 0.815 | 0.787 | 0.741 | 0.64 | |
| K | 0.159 | 0.133 | 0.139 | 0.142 | 0.181 | 0.173 | 0.187 | 0.2 | 0.193 | 0.198 | 0.196 | 0.201 | 0.195 | 0.2 | 0.205 | 0.168 | 0.189 | |
| Total | 16.04 | 16.028 | 16.066 | 16.025 | 15.997 | 16.091 | 16.014 | 16.032 | 16.046 | 16.064 | 16.018 | 16.043 | 16.04 | 16.094 | 16.094 | 16.009 | 15.919 | |
| Mg# | 68.64 | 68.99 | 69.06 | 66.00 | 69.05 | 69.84 | 71.75 | 71.76 | 67.04 | 69.80 | 70.76 | 67.88 | 67.49 | 67.96 | 70.80 | 66.95 | 66.88 | |

#### 1.5.2.2.3. Plagioclase

Plagioclase feldspar and minor k-feldspar occur in most of studied volcanic rocks. The k-feldspar is orthoclase (mainly in Sample #69, #70, #74 and #77), whereas plagioclase has composition of $An_{1.4\text{-}13.7}Ab_{80.9\text{-}98.3}Or_{0.2\text{-}6.6}$ in basaltic rocks (except Sample #74 which has higher $An_{65.2\text{-}73.6}$ contents) and $An_{56\text{-}85}Ab_{14\text{-}69}Or_{0.6\text{-}5}$ in hornblende basaltic andesite (Fig. 1.20). Plagioclase in basaltic rocks may mostly be the product of albitization (secondary alteration).

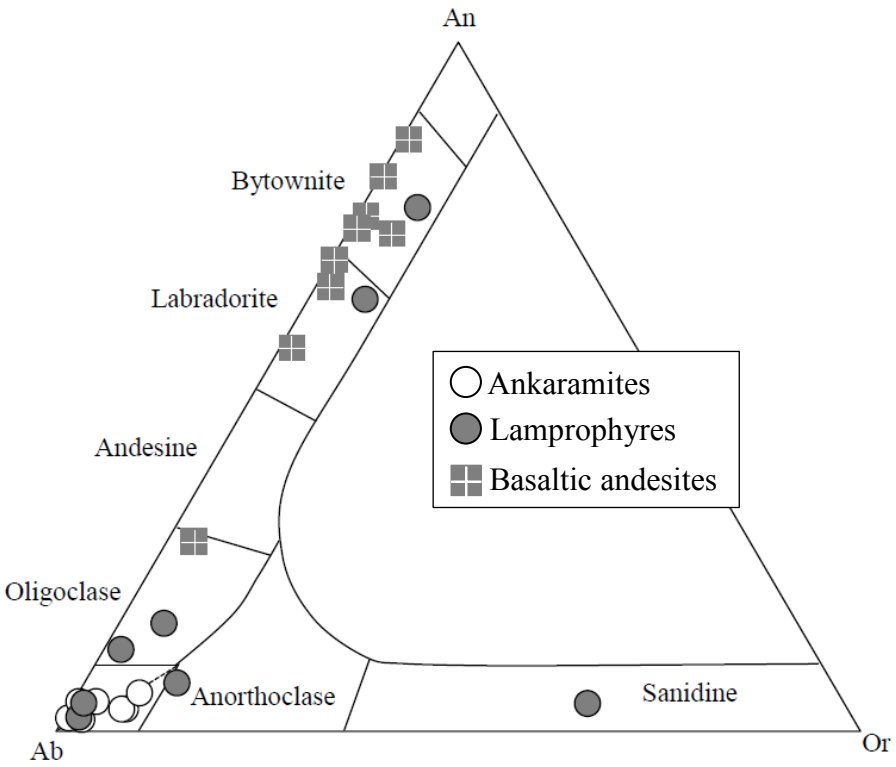


**Figure 1.20:** An-Ab-Or triangular diagram showing the compositions of plagioclase from basaltic rocks of Chukotka. An, Anorthite; Ab, Albite; Or, Orthoclase.

#### 1.5.2.2.4. Biotite

*Biotites* in the basaltic andesite (Sample #56) have a compositional range of Mg# (0.51-0.53; Table 1.6) and the alumina saturation index (ASI= Al/Ca+Na+K) ranges from 0.42 to 1.95. All these biotites are not primary magmatic and in the ternary FeO* (=$FeO_{total}$+MnO)-10$TiO_2$-MgO discrimination diagram (Fig. not shown) they plot in the re-equilibriated biotite field, suggesting their chemical compositions are likely influenced by late-magmatic hyrdrothermal fluid (Nachit et al., 2005).

#### 1.5.2.2.5. Opaque minerals

Opaque minerals from the pyroxene-phyric basalt are predominantly iron-sulphide minerals. Lamprophyres includes both Ti-bearing (0.3<$TiO_2$<19.5 wt. %) and Ti-free magnetite. Ti- magnetite also contains minor $Cr_2O_3$ (0.03-0.16 wt. %) and $Al_2O_3$ (0.21-4.44 wt. %).

### 1.5.2.3. Trace elements in clinopyroxene and amphibole

Representative, clinopyroxene and amphibole trace element compositions of the studied samples are reported in Tables 1.9 1.10 and 1.11, although amphiboles from OIB-type gabbro are not analyzed.

#### 1.5.2.3.1. Clinopyroxene in gabbroic rocks

Clinopyroxenes in IAB-type gabbroic rocks are characterized by enrichment in LREE ($(Ce/Yb)_N$ =1.69-2.62; where N refers to primitive mantle normalization) and MREE ($(Eu/Yb)_N$=2.8-3.3) relative to HREE as compared

to those in OIB-type gabbro (~1.69 and 2.1 respectively). No significant Eu anomaly was observed for clinopyroxenes from both IAB-type and OIB-type gabbroic rocks (Eu/Eu*=0.97-1 and 0.91-0.96 respectively). Clinopyroxenes of IAB-type gabbros have higher $(La/Nb)_N$ than clinopyroxenes from OIB-type gabbros. As a result, the primitive-mantle normalized trace element patterns of the clinopyroxenes from IAB-type gabbros are distinctive in their deep negative Nb anomalies (Fig. 1.21A). The concentration of LILE (Cs, Rb, Ba) in clinopyroxens of OIB-type gabbroic rocks are higher than those in IAB-type gabbros, but significant depletion of Sr is detected in the former.

#### 1.5.2.3.2. Clinopyroxene in basaltic rocks

Basalts show trace element compositions of clinopyroxene characterized by negative anomalies of HFSE (Nb, Ta, Zr) and LILE (Ba, Rb). In addition, these phenocrysts exhibit variable concentrations of Cs, Th and U (Fig. 1.21C). The negative anomalies of the aforementioned incompatible trace elements also exhibited in clinopyroxenes from basaltic andesite, but the concentrations are higher than those in basalts. The primitive mantle-normalized REE patterns (Fig. 1.21D) of clinopyroxenes in both basalt and basaltic andesite samples are characterized by similar depletion in LREE $(La/Sm)_N$=0.19-0.34; 0.22-0.26 respectively) relative to MREE. However, clinopyroxene in basaltic andesite is characterized by HREE enrichment ($(Eu/Yb)_N$=0.75-0.79) relative to MREE and display slight negative Eu anomalies (Eu/Eu*(=EuN/$\sqrt{\mathrm{SmN} \times \mathrm{GdN}}$)). This REE signature is significantly different from that of the clinopyroxenes in basaltic rocks. In basalts, clinopyroxene contains high

Cr contents (up to 1181 ppm in pyroxene-phyric basalt, 3347 ppm in ankaramite and 435 ppm in lamprophyre) and Ni (up to 131 ppm in pyroxene phyric basalt, 124 ppm in ankaramite and 38 ppm in lamprophyre). These values drop to less than 200 ppm of Cr and 20 ppm of Ni in basaltic andesite (Table 1.9).

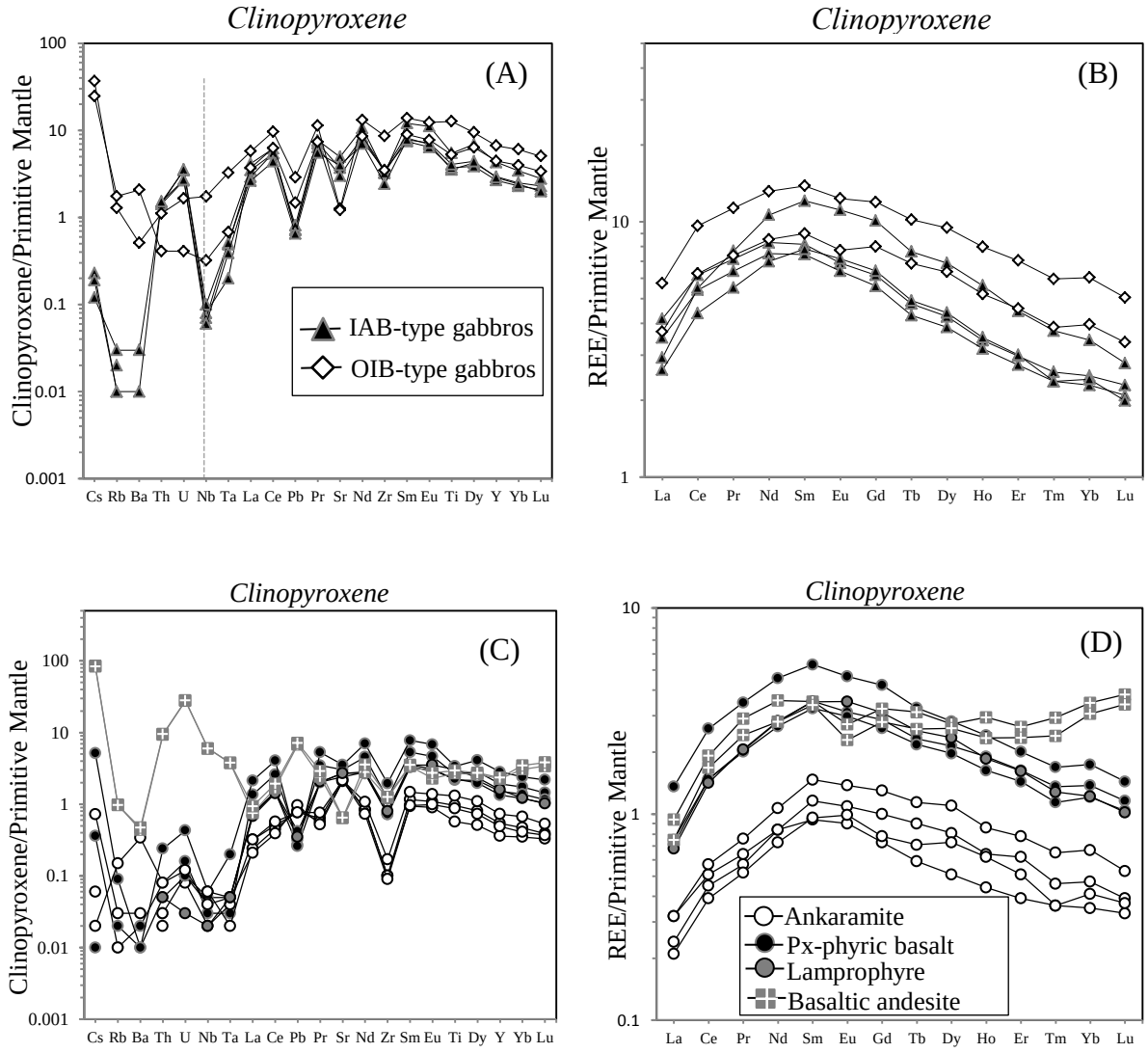


**Figure 1.21**: Primitive mantle normalized multi-element (A) and REE (B) patterns for the clinopyroxenes from the gabbroic rocks of Ckukotka. Mantle–normalization values are from McDonough and Sun (1995). (C) and REE (D) patterns for the clinopyroxenes from the basaltic rocks of Ckukotka. Mantle–normalization values are from McDonough and Sun (1995).

**Table 1.9:** Trace element analyses (ppm) of clinopyroxenes from gabbroic rocks of Chukotka, NE Russia.

| Rock type | IAB-type gabbros | | | | OIB-type gabbros | |
|---|---|---|---|---|---|---|
| Sample | #60 | | #57 | | #84 | |
| Mineral | Cpx1 | Cpx2 | Cpx1 | Cpx2 | Cpx1 | Cpx2 |
| Determined by LA-ICP-MS | | | | | | |
| Sc | 116.0 | 110.1 | 71.1 | 76.9 | 148.5 | 90.0 |
| Ti | 4261 | 4497 | 6593 | 4897 | 15298 | 6335 |
| V | 253 | 247 | 381 | 285 | 797 | 459 |
| Cr | 2.8 | 2.8 | n.d. | 0.6 | 11.8 | 4.4 |
| Co | 34.7 | 33.6 | 32.7 | 33.4 | 60.6 | 52.3 |
| Ni | 29 | 26 | 11 | 14 | 35 | 19 |
| Rb | 0.008 | 0.010 | 0.018 | 0.005 | 0.769 | 1.047 |
| Sr | 73.4 | 59.6 | 98.6 | 79.2 | 25.1 | 24.1 |
| Y | 12.6 | 11.5 | 18.5 | 12.4 | 28.7 | 19.1 |
| Zr | 34.5 | 36.6 | 34.0 | 25.5 | 90.3 | 36.6 |
| Nb | 0.05 | 0.05 | 0.07 | 0.04 | 1.15 | 0.21 |
| Cs | 0.005 | n.d. | 0.002 | 0.004 | 0.773 | 0.517 |
| Ba | 0.03 | 0.01 | 0.20 | 0.05 | 3.35 | 13.67 |
| La | 2.70 | 2.27 | 1.90 | 1.70 | 3.72 | 2.40 |
| CE | 10.37 | 9.05 | 9.23 | 7.33 | 16.15 | 10.51 |
| Pr | 1.81 | 1.63 | 1.95 | 1.40 | 2.87 | 1.87 |
| Nd | 10.36 | 9.39 | 13.30 | 8.74 | 16.43 | 10.65 |
| Sm | 3.31 | 3.03 | 4.90 | 3.17 | 5.61 | 3.65 |
| Eu | 1.06 | 0.99 | 1.71 | 1.10 | 1.90 | 1.19 |
| Gd | 3.36 | 3.04 | 5.48 | 3.49 | 6.49 | 4.35 |
| Tb | 0.47 | 0.43 | 0.76 | 0.49 | 1.01 | 0.68 |
| Dy | 2.87 | 2.60 | 4.64 | 2.96 | 6.37 | 4.28 |
| Ho | 0.51 | 0.47 | 0.84 | 0.52 | 1.19 | 0.78 |
| Er | 1.31 | 1.20 | 1.96 | 1.32 | 3.08 | 2.00 |
| Tm | 0.18 | 0.16 | 0.25 | 0.16 | 0.41 | 0.26 |
| Yb | 1.10 | 1.01 | 1.52 | 1.07 | 2.66 | 1.75 |
| Lu | 0.16 | 0.14 | 0.19 | 0.14 | 0.34 | 0.23 |
| Hf | 1.66 | 1.67 | 1.97 | 1.54 | 3.91 | 1.66 |
| Ta | 0.01 | 0.02 | 0.02 | 0.01 | 0.12 | 0.03 |
| Pb | 0.11 | 0.11 | 0.12 | 0.10 | 0.43 | 0.22 |
| Th | 0.120 | 0.114 | 0.11 | 0.12 | 0.09 | 0.03 |
| U | 0.069 | 0.053 | 0.071 | 0.054 | 0.033 | 0.008 |

Abbreviations: Cpx, clinopyroxene; n.d. not detected.

**Table 1.10:** Trace element analyses (ppm) of clinopyroxenes from basaltic rocks of Chukotka, NE Russia.

| Rock | Ankaramite | | | Pyroxene-phyic basalt | | | | Lamprophyre | | Basaltic andesite |
|---|---|---|---|---|---|---|---|---|---|---|
| Sample | #69 | | | #67 | | | | #77 | | #55 |
| Mineral | Cpx1 | Cpx2 | | Cpx1 | | Cpx3 | | Cpx1 | | Cpx2 |
| | core | core | rim | core | rim | core | rim | core | rim | core |
| Determined by LA-ICP-MS | | | | | | | | | | |
| Sc | 91.4 | 87.0 | 100.6 | 98.3 | 126.0 | 117.7 | 125.9 | 173.0 | 123.7 | 32.6 |
| Ti | 1156 | 1048 | 1251 | 3154 | 4079 | 2706 | 2351 | 3671 | 4044 | 3258 |
| V | 119 | 110 | 133 | 293 | 355 | 250 | 205 | 269 | 346 | 305 |
| Cr | 2767 | 3077 | 3348 | 15 | 545 | 736 | 1096 | 435 | 20 | 188 |
| Co | 33.6 | 35.0 | 35.2 | 44.2 | 43.9 | 44.2 | 43.5 | 33.6 | 37.9 | 38.4 |
| Ni | 121 | 125 | 114 | 74 | 86 | 107 | 114 | 54 | 22 | 18 |
| Rb | 0.003 | 0.001 | 0.007 | 0.005 | 0.015 | 0.001 | 0.003 | n.d. | 0.016 | 0.587 |
| Sr | 41.5 | 42.8 | 42.8 | 60.54 | 70.5 | 54.4 | 42.5 | 53.4 | 54.3 | 12.7 |
| Y | 2.33 | 2.10 | 3.35 | 8.27 | 12.12 | 5.76 | 4.83 | 6.82 | 10.34 | 9.76 |
| Zr | 1.08 | 0.91 | 1.79 | 12.50 | 20.49 | 7.55 | 5.50 | 8.35 | 13.71 | 12.92 |
| Nb | 0.04 | 0.04 | 0.05 | 0.02 | 0.04 | 0.02 | 0.02 | 0.01 | 0.02 | 3.94 |
| Cs | n.d. | 0.001 | 0.005 | 0.008 | n.d. | 0.000 | 0.001 | n.d. | 0.098 | 1.785 |
| Ba | 0.03 | 0.01 | 0.14 | 0.14 | 0.04 | 0.00 | 0.01 | 0.01 | 0.13 | 2.90 |
| La | 0.15 | 0.13 | 1.04 | 0.88 | 1.39 | 0.49 | 0.32 | 0.44 | 0.67 | 0.49 |
| Ce | 0.75 | 0.66 | 3.11 | 4.35 | 6.79 | 2.48 | 1.78 | 2.38 | 3.40 | 2.81 |
| Pr | 0.14 | 0.13 | 0.43 | 0.88 | 1.35 | 0.51 | 0.38 | 0.52 | 0.73 | 0.61 |
| Nd | 1.05 | 0.91 | 2.09 | 5.71 | 8.72 | 3.34 | 2.47 | 3.54 | 5.01 | 3.51 |
| Sm | 0.47 | 0.39 | 0.66 | 2.16 | 3.14 | 1.32 | 1.02 | 1.42 | 2.00 | 1.38 |
| Eu | 0.17 | 0.15 | 0.25 | 0.72 | 1.05 | 0.46 | 0.37 | 0.54 | 0.75 | 0.35 |
| Gd | 0.55 | 0.43 | 0.80 | 2.30 | 3.38 | 1.42 | 1.14 | 1.69 | 2.37 | 1.52 |
| Tb | 0.09 | 0.07 | 0.11 | 0.32 | 0.46 | 0.22 | 0.17 | 0.25 | 0.37 | 0.26 |
| Dy | 0.55 | 0.49 | 0.76 | 1.90 | 2.76 | 1.32 | 1.09 | 1.58 | 2.40 | 1.76 |
| Ho | 0.10 | 0.09 | 0.14 | 0.36 | 0.50 | 0.24 | 0.18 | 0.28 | 0.43 | 0.35 |
| Er | 0.27 | 0.22 | 0.37 | 0.88 | 1.31 | 0.63 | 0.51 | 0.71 | 1.13 | 1.03 |
| Tm | 0.03 | 0.02 | 0.05 | 0.12 | 0.18 | 0.08 | 0.07 | 0.09 | 0.15 | 0.16 |
| Yb | 0.21 | 0.18 | 0.28 | 0.77 | 1.06 | 0.53 | 0.44 | 0.54 | 0.92 | 1.35 |
| Lu | 0.03 | 0.02 | 0.04 | 0.10 | 0.15 | 0.07 | 0.06 | 0.07 | 0.12 | 0.23 |
| Hf | 0.06 | 0.06 | 0.11 | 0.64 | 1.14 | 0.41 | 0.33 | 0.49 | 0.71 | 0.51 |
| Ta | 0.00 | 0.00 | n.d. | 0.00 | 0.01 | 0.00 | 0.00 | 0.00 | 0.00 | 0.14 |
| Pb | 0.12 | 0.14 | 0.07 | 0.05 | 0.04 | 0.06 | 0.04 | 0.05 | 0.08 | 1.02 |
| Th | 0.00 | 0.00 | 0.16 | 0.01 | 0.02 | 0.00 | n.d. | 0.00 | 0.01 | 0.75 |
| U | n.d. | 0.000 | 0.047 | 0.003 | 0.009 | 0.002 | 0.000 | 0.001 | 0.007 | 0.553 |

Abbreviations: Cpx, clinopyroxene; n.d. not detected.

#### 1.5.2.3.3. Amphiboles in gabbroic rocks

In the spider diagram (Fig. 1.22A), amphiboles from IAB-type gabbros exhibit negative anomalies for Th, U, Pb, Zr and enrichment in LILE (Ba and Sr). In the primitive mantle-normalized REE patterns (Fig. 1.22B) they are characterized by LREE enrichment relative to HREE ($(La/Yb)_N$=1.4-1.8). REE patterns do not show Eu anomaly (Eu/Eu*=1.04-1.11).

#### 1.5.2.3.4. Amphiboles in basaltic rocks

The trace element characteristics of amphibole further emphasize the existence of two types among basaltic rocks in the Chukotka area. The primitive mantle-normalized REE pattern (Fig. 1.22D) of amphiboles from both basalts and basaltic andesite are convex-upward shaped with lower LREE ($La_N/Sm_N$; 0.22-0.24, 0.48-0.53 respectively) and HREE. This shape is typical of deep cumulates from basaltic melts (Irving and Frey, 1984). Amphiboles from basaltic andesite have higher HFSE (Nb, Ta) and total REE contents as compared to those in basalts. Moreover, these phenocrysts show a remarkable negative Eu anomaly (Eu/Eu*= 0.51-0.71) in the primitive mantle–normalized REE pattern. Amphiboles of basalts are highly enriched in Sr, but slight negative anomaly is detected for those from basaltic andesite. The incompatible element pattern of amphiboles from both basalts and basaltic andesites (Fig. 1.22C) reveals a strong depletion in Th, U and Zr relative to the neighbouring elements. However, the concentrations of the aforementioned elements are still higher in amphiboles from basaltic andesite. The Ni and Cr contents of amphiboles are very low; 55-78 ppm and 3.9-79 ppm in basalt (Sample #77) and 36-39 ppm and 125-319 ppm in basaltic andesite (Sample #55), respectively (Table 1.11).

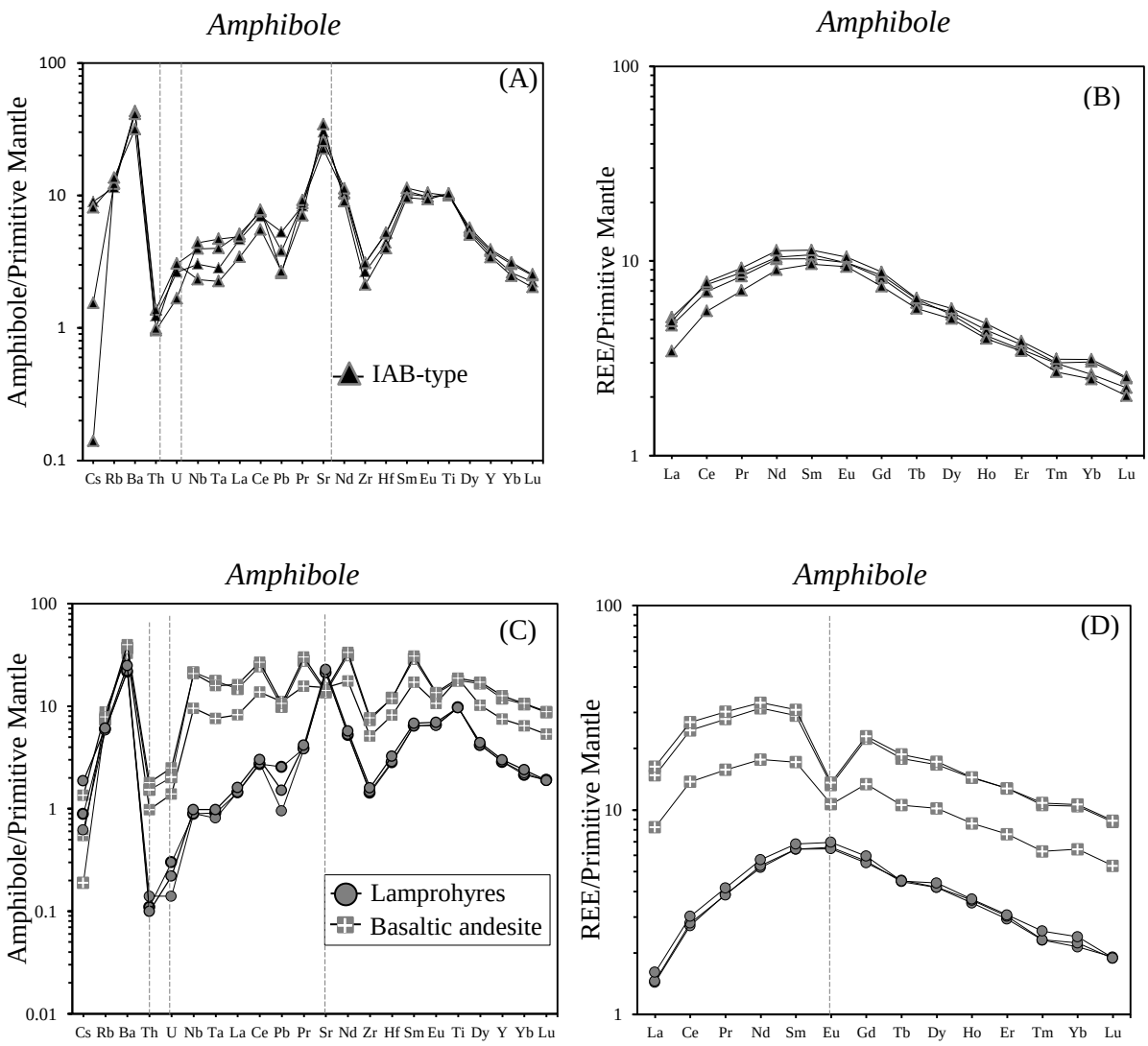


**Figure 1.22**: Primitive mantle normalized multi-element (A, C) and REE (B, D) patterns for the amphiboles from the gabbroic (A, B) and basaltic (C, D) rocks of Ckukotka. Mantle–normalization values are from McDonough and Sun (1995).

**Table 1.11:** Trace element composition of amphiboles in the IAB-type gabbros and basalts of Chukotka, NE Russia.

| Rock type | IAB-type gabbros | | | | Lamprophyre | | | Basaltic andesite | | |
|---|---|---|---|---|---|---|---|---|---|---|
| Sample | #57 | | #60 | | #77 | | | #55 | | |
| Mineral | Hb1 | Hb2 | Hb1 | Hb2 | Hb1 | Hb2 | | Hb1 | Hb2 | |
| | | | | | Core | Core | Rim | Core | Core | Rim |
| Determined by LA-ICP-MS | | | | | | | | | | |
| Sc | 76.5 | 67.6 | 110.3 | 111.5 | 160.0 | 148.4 | 148.0 | 83.6 | 84.5 | 99.4 |
| Ti | 12023 | 12498 | 11944 | 12292 | 11714 | 11736 | 11671 | 22453 | 21469 | 22629 |
| V | 467 | 509 | 501 | 478 | 608 | 638 | 641 | 1514 | 870 | 1329 |
| Cr | 13.1 | 0.5 | 1.9 | 4.8 | 78.9 | 10.2 | 3.8 | 318.6 | 125.3 | 303.5 |
| Co | 60.2 | 62.2 | 58.4 | 64.2 | 61.9 | 63.3 | 63.6 | 51.7 | 52.4 | 52.3 |
| Ni | 45.5 | 39.3 | 51.5 | 64.5 | 78.0 | 52.2 | 54.7 | 35.5 | 35.6 | 38.8 |
| Rb | 7.3 | 8.2 | 6.9 | 7.4 | 3.6 | 3.5 | 3.7 | 5.3 | 4.5 | 4.7 |
| Sr | 515 | 685 | 598 | 447 | 424 | 423 | 453 | 302 | 271 | 284 |
| Y | 16.8 | 14.7 | 15.4 | 16.3 | 12.3 | 12.4 | 12.9 | 32.2 | 51.2 | 54.4 |
| Zr | 32.5 | 22.3 | 27.9 | 32.5 | 15.0 | 15.5 | 16.8 | 53.8 | 77.3 | 81.2 |
| Nb | 2.9 | 1.5 | 2.0 | 2.6 | 0.6 | 0.6 | 0.6 | 6.3 | 14.1 | 13.8 |
| Cs | 0.032 | 0.003 | 0.189 | 0.170 | 0.019 | 0.013 | 0.039 | 0.028 | 0.004 | 0.012 |
| Ba | 272 | 208 | 288 | 285 | 143 | 147 | 165 | 217 | 244 | 263 |
| La | 3.18 | 2.22 | 3.02 | 3.33 | 0.93 | 0.95 | 1.04 | 5.34 | 9.58 | 10.56 |
| Ce | 13.04 | 9.24 | 11.64 | 12.67 | 4.55 | 4.70 | 5.06 | 23.02 | 41.07 | 45.06 |
| Pr | 2.34 | 1.79 | 2.12 | 2.22 | 0.98 | 0.98 | 1.06 | 4.00 | 7.07 | 7.68 |
| Nd | 14.11 | 11.25 | 12.77 | 13.06 | 6.55 | 6.71 | 7.15 | 22.07 | 39.37 | 41.87 |
| Sm | 4.61 | 3.91 | 4.18 | 4.38 | 2.61 | 2.62 | 2.77 | 6.96 | 11.76 | 12.55 |
| Eu | 1.61 | 1.44 | 1.51 | 1.50 | 1.01 | 1.00 | 1.07 | 1.64 | 2.04 | 2.10 |
| Gd | 4.77 | 4.02 | 4.60 | 4.45 | 3.06 | 3.00 | 3.24 | 7.28 | 12.13 | 12.50 |
| Tb | 0.64 | 0.56 | 0.63 | 0.60 | 0.44 | 0.45 | 0.45 | 1.05 | 1.77 | 1.85 |
| Dy | 3.83 | 3.40 | 3.58 | 3.68 | 2.81 | 2.82 | 2.97 | 6.87 | 11.24 | 11.61 |
| Ho | 0.71 | 0.59 | 0.62 | 0.65 | 0.52 | 0.54 | 0.55 | 1.28 | 2.14 | 2.15 |
| Er | 1.69 | 1.51 | 1.53 | 1.63 | 1.28 | 1.32 | 1.34 | 3.34 | 5.59 | 5.59 |
| Tm | 0.21 | 0.18 | 0.20 | 0.20 | 0.16 | 0.16 | 0.17 | 0.43 | 0.72 | 0.74 |
| Yb | 1.37 | 1.09 | 1.15 | 1.34 | 0.94 | 0.99 | 1.06 | 2.84 | 4.61 | 4.70 |
| Lu | 0.17 | 0.14 | 0.15 | 0.17 | 0.13 | 0.13 | 0.13 | 0.36 | 0.59 | 0.60 |
| Hf | 1.48 | 1.13 | 1.24 | 1.47 | 0.80 | 0.82 | 0.92 | 2.31 | 3.43 | 3.38 |
| Ta | 0.17 | 0.08 | 0.10 | 0.15 | 0.03 | 0.03 | 0.04 | 0.28 | 0.65 | 0.59 |
| Pb | 0.39 | 0.40 | 0.79 | 0.57 | 0.38 | 0.14 | 0.23 | 1.66 | 1.48 | 1.60 |
| Th | 0.077 | 0.079 | 0.098 | 0.110 | 0.009 | 0.011 | 0.008 | 0.079 | 0.123 | 0.144 |
| U | 0.033 | 0.061 | 0.053 | 0.061 | 0.006 | 0.003 | 0.004 | 0.028 | 0.041 | 0.050 |

## 1.6. DISCUSSION

### 1.6.1. Parental magma

The trace element composition of parental melts in equilibrium with clinoyroxens from the studied samples have been calculated using clinopyroxene/melt partition coefficients after Hart and Dunn, (1993), Adam and Green, (2006), and Tiepolo (1999). On the primitive mantle normalized trace element diagram (Fig. 1.23), the calculated melt from clinopyroxene in IAB-type gabbros exhibits a marked enrichment of Th, U and LREE over HREE ($(La/Yb)_N$) average is 10.24) and depletion of HFSE (Nb, Ta, Zr). These geochemical features are a characteristic of subduction zone magmatism (Pearce and Peate, 1995) or crustal contamination (Rudnick and Gao, 2003). Given that these magmas have not signifificantly contaminated by crustal materials as discussed below, the negative Nb-Ta anomalies may be reflect the primary feature mantle source that was previously metasomatized by a subduction related component (Pearce et al., 2005). The general trace element patterns of calculated melt are similar to basalts in terms of strong depletion of HFSE, but higher contents of overall trace elements for the former. These similarities of trace element patterns between calculated melts for IAB-type gabbros and bulk rock composition of basalts may suggest that they are genetically related but the relatively higher concentration of the calculated melt suggesting that it was slightly more evolved. This interpretation is consistent with the absence of olivine in the IAB-type gabbros, indicating the evolved nature of the parental melt. On the other hand, we do not observe negative anomalies of HFSE in calculated melt in equilibrium with clinopyroxene in OIB-type gabbros, suggesting that OIB-type gabbros are not genetically related to IAB-type

gabbros, basalts and basaltic andesites.

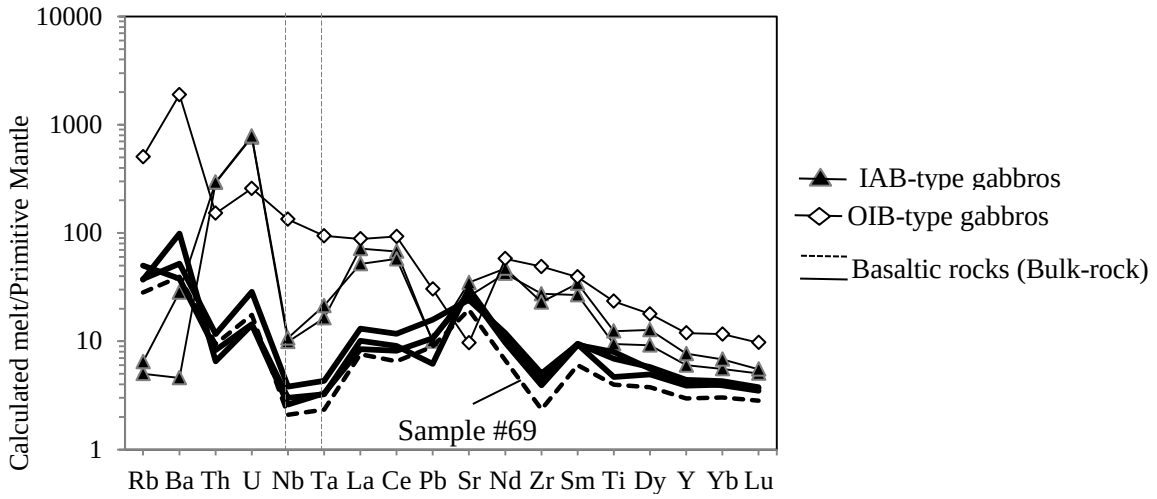


**Figure 1.23**: Primitive mantle normalized multi-element patterns for the calculated liquid in equilibrium with clinopyroxene compared with volcanic rock trace element composition. Normalization factors for the calculated liquid are after Hart and Dunn (1993), Tiepolo (1999), and Adam and Green (2006). The bulk-rock composition of basalts also plotted for comparison. Mantle-normalization values are from McDonough and Sun (1995). CL, calculated liquid.

Ankaramites of Chukotka (Sample #69 and #71) have Mg# 63-65, Cr-contents 466-530 ppm, and Ni-contents of 67-81ppm. They are also characterized by very low REE abundance with a strong depletion of HFSE. They include high-Mg clinopyroxene (Mg# ≤93), although olivine is absent. Moreover, they are characterized by high $CaO/Al_2O_3$ ~1.04, which are common features of primitive or parental arc-ankaramite (Della-Pasqua and Varne, 1997). Hence, these features make them a likely candidate for a near-primary mantle melt. High MgO, high CaO lavas and melt inclusions akin to ankaramites have been reported from many active island-arc systems (Barsdell and Berry, 1990; Della-Pasqua and Varne, 1997; Schiano et al., 2000). Several

experimental modelling has revealed that melting of MORB-sourced upper mantle peridotite cannot produce primitive ankaramite (Schiano et al., 2000; Kogisio and Hirschmann 2001). Della-Pasqua and Varne (1997) and Green et al. (2004) suggested that ankaramites can be formed by melting of $CO_2$ metasomatized mantle, or by fusion of clinopyroxenites or wehrlites with in the mantle or at the base of the crust (Barsdell and Berry, 1990; Schiano et al., 2000; Kogisio and Hirschmann 2001). Therefore, the petrological and geochemical constraints suggest that the Chukotka ankaramite magma was probably formed by hydrous melting of the clinopyroxene-rich source as evidenced by the occurrence of amphibole.

### 1.6.2. Fractional crystallization

Primary basaltic magma resulting from partial melting of mantle peridotite source must have Mg# in the range of 68-75 (Green, 1976; Hanson and Langmuir, 1978). The studied basaltic and gabbroic rocks display different evolutionary trends, suggesting that they followed different paths of fractional crystallization or accumulation. A negative correlation between MgO and $FeO^*$ for the basalts and IAB-type gabbros suggests no fractionation of olivine, this interpretation is supported by the absence of this mineral in these rocks. The positive correlation between CaO and MgO in the OIB-type gabbros (Fig. 1.7) suggests fractionation of clinopyroxene. Furthermore, the positive correlations of Cr against MgO for the studied samples suggest the role of clinopyroxene fractionation. The lack of negative Eu anomalies and the progressive increase in $Al_2O_3$ with decreasing MgO for basalts and gabbros suggests an absence of significant plagioclase fractionation (Fig. 1.7B). However, slight negative Eu anomalies indicate fractionation of plagioclase in the basaltic andesite. This interpretation is

supported by the presence of marked negative Eu anomalies exhibited by hornblende phenocrysts in basaltic andesite (Fig. 1.22D). Moreover, IAB-type gabbroic and basaltic rocks do not have obvious Eu anomalies in the primitive mantle–normalized REE diagram (Fig. 1.22), suggesting that plagioclase were not important fractionating phase for IAB-type gabbroic and basaltic rocks of Chukotka. Most of the studied samples (except OIB-type gabbros) show trends of decreasing Dy/Yb with differentiation index ($SiO_2$) (Fig. 1.24A), this is interpreted as significant amphibole fractionation (Davidson et al. 2007; Smith, 2014), because amphibole incorporates preferentially MREE compared to HREE (Tiepolo et al. 2007).

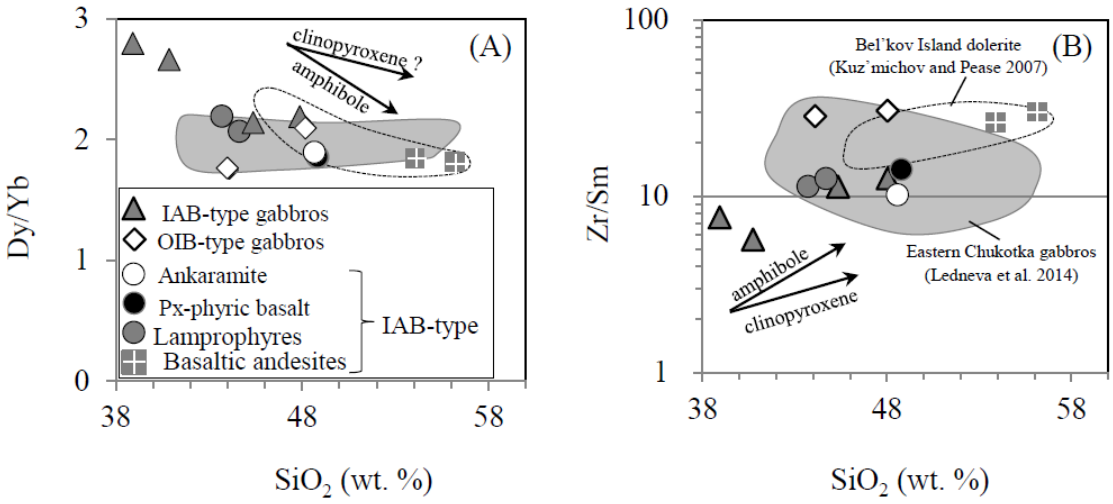


**Figure 1.24:** (A, B) Plots of $SiO_2$ (wt. %) vs. Dy/Yb and Zr/Sm. Variation of Dy/Yb and Zr/Sm primarily attributed to amphibole fractionation. However, clinopyroxene fractionation may also exert an influence on these ratios. Fractionation trends for amphibole are after Davidson et al. (2007). The geochemical data of Bel'kov Island dolerite (Siberian LIP; after Kuz'michov and Pease, 2007) and eastern Chukotka gabbros (Ledneva et al. 2014) also shown for comparison.

However, this interpretation is arguing against the absence of saucer-shaped REE patterns in the studied basaltic rocks (Fig. 1.9), which would be expected due to amphibole fractionation that observed in some arc lavas (e.g. Jolly et al., 2002; Figueroa et al., 2009).

As shown, in Fig. 1.9B, the REE patterns of the basaltic andesite is slightly concave-upward shaped, a feature classically attributed to amphibole fractionation (Green and Pearson, 1985) and confirmed by the presence of amphibole phenocrysts in these rocks. In addition, variation of Zr/Sm ratio is also often attributed primarily to amphibole fractionation (Fig. 1.24B). However, augite fractionation (Thirlwall et al., 1994) and magnetite fractionation (Tribuzio et al., 1999) may also exert an influence on the Zr/Sm ratios.

### 1.6.3. Crustal contamination

When continental basaltic magmas rise from their sources in the mantle through the continental crust, they often experience contamination (Watson, 1982; Arndt and Chrisensen, 1992; Hawkesworth et al., 1984; 1992; Mahoney, 1988; Carlson, 1991; Hergt et al., 1991). HFSE ratios are important indicators of crustal contamination in an open magma system. As shown in Fig. 1.31A IAB-type gabbroic and basaltic rocks (excepting OIB-type gabbros) are characterized by $(Th/Ta)_N$ and $(La/Nb)_N$ ratios >1, suggesting that the significant contribution of crustal material in their genesis (Neal et al., 2002). However, these rocks have obvious negative Zr-Hf anomalies in the primitive mantle-normalized trace element diagram (Fig. 1.9), arguing against significant crustal contamination because minor crustal contamination will increase the Zr-Hf contents due to the enrichment of

these elements in crustal material (Wedepohl, 1995). In addition, the Nb/La ratios for IAB-type gabbroic and basaltic rocks remain constant irrespective of $SiO_2$ content (Fig. 1.25), contradicting to the trend that would expect for crustal contamination. Thus, the observed negative Zr-Hf anomalies may suggest that they originated from a mantle source metasomatized by slab derived fluid because Zr and Hf are immobile in fluid-dominated subduction processes (Münker et al., 2004). On the other hand, the depletion of Zr and Hf by amphibole fractionation is likely (Hollings and Kerrich, 2000), which is consistent with the presence of abundant amphibole crystals in these rocks. The involvement of crustal material for OIB-type gabbros is not supported by (1) relatively enrichment in Nb and Ta with Nb/La ratios of 0.99-1.43, and (2) its high $TiO_2$ and FeO* contents. Trace element ratios such as Th/Yb, Nb/Yb and Ta/Yb can be used as geochemical indicator mainly for understanding the nature of crustal inputs during magma genesis manifested in terms of subduction, crustal contamination and crustal recycling (Pearce and Peate, 1995; Pearce, 2008). In the Th/Yb vs Nb/Yb diagram (Fig. 1.32B) (Pearce, 2008) the IAB-type gabbros and basaltic rocks show a characteristic feature of arc setting with a prominent signature of slab dehydration and mantle enrichment, which in turn indicate the important role of subduction zone fluids enriched in Th in their petrogenesis. The IAB-type gabbros and basaltic rocks plot above MORB-OIB field in Fig. 1.31B, (except for OIB-type gabbroic samples that plot close or in the mantle array field), suggesting that their magma had an input from enriched subducted material (Pearce, 2008). The above lines of evidence suggest that crustal contamination was not important during the magma evolution.

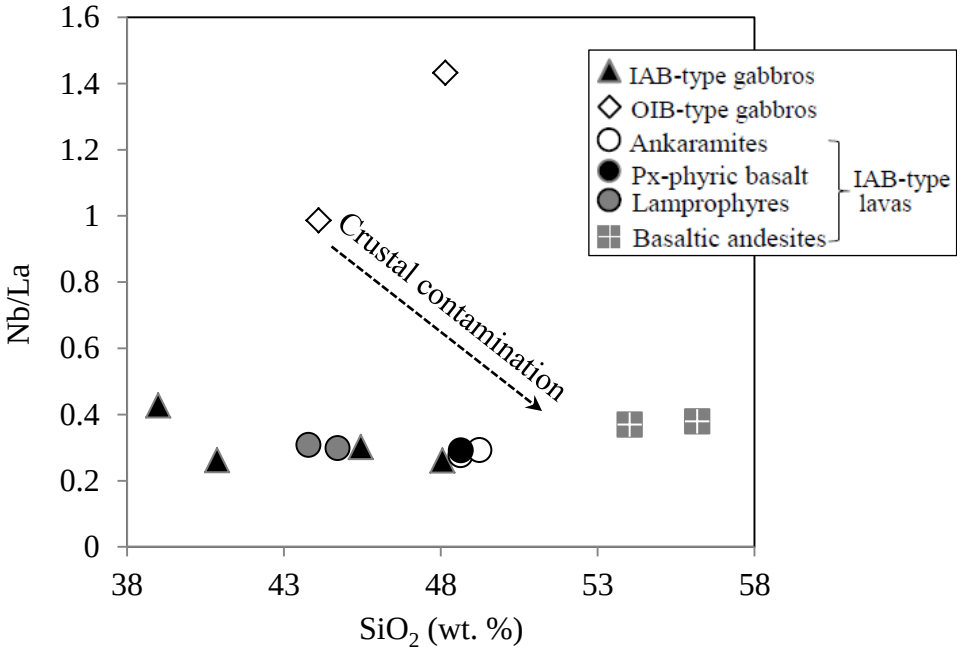


**Figure 1.25:** $SiO_2$ (wt. %) vs. Nb/La diagram showing the crustal contamination.

### 1.6.4. Nature of mantle source

The incompatible element patterns defined by negative anomalies at Nb, Ta and Ti are characteristic features of HFSE depleted rocks generated by subduction zone magmatic processes. The depletion of HFSE, mainly Nb–Ta relative to LILE can be ascribed to three processes: (1) addition of LILE-enriched, Nb–Ta poor fluid released from the subducted slab to the mantle wedge, (2) the preferential retention of Nb–Ta in amphibole and rutile relative to the other phases in the subducted slab or mantle source, and (3) contamination of mantle-derived magma by crustal components (Rollinson 1993; Weyer et al., 2003; Wilson, 2007). Moreover, the depletion in HFSEs may have been caused by previous melt extraction in a back-arc basin (Woodhead et al., 1993; 1998; Elliott et al., 1997) or in arc settings (Grove et al., 2002). The absence of negative spike at Nb and Ta in the OIB-

type gabbroic rocks precludes the major role of crustal contamination and/or subduction-related magmatic sources in their origin. The nature of the mantle source rocks can further be constrained by the trace element ratios such as Nb/Yb, Zr/Yb, and Th/Yb (Pearce and Peate, 1995). In the Nb/Yb vs. Th/Yb relationship (Fig. 1.32B), where our IAB-type gabbroic and basaltic rocks (except OIB-type gabbros) plot above the MORB-OIB array (Pearce and Peate, 1995), suggesting a subduction component in their source regions because fluid/melt released from a subducted slab is known to result in high Th and low Nb in the upper mantle wedge (Pearce et al. 1995). The Zr/Yb vs Nb/Yb diagram (Pearce and Peate, 1995) can be used to define a mantle array (Fig. 1.26A). Data points plotted above the upper boundary of the array can be interpreted as Zr derived from the subducted slab, accumulated zircon, or have undergone crustal contamination (Pearce and Peate, 1995). The studied basalts and gabbroic rocks of Chukotka plot within the mantle array (except basaltic andesite samples that falls above the upper boundary of array); hence we interpreted that slab-derived fluid, not melt, contributed to the magma source. The Nb/Y vs. Zr/Y diagram (Fitton et al., 1997) can be used to distinguish MORB-source mantle from more enriched source; arc magmas derived from depleted MORB-source plot below the lower boundary of the 'Iceland array', whereas those derived from more enriched sources plot with in the Iceland array (Fig. 1.26B). All the studied basaltic and gabbroic rocks of Chukotka (except basaltic andesite samples) fall within the Iceland array, suggesting that they are derived from enriched MORB-source mantle that was affected by subduction zone processes as mentioned above.

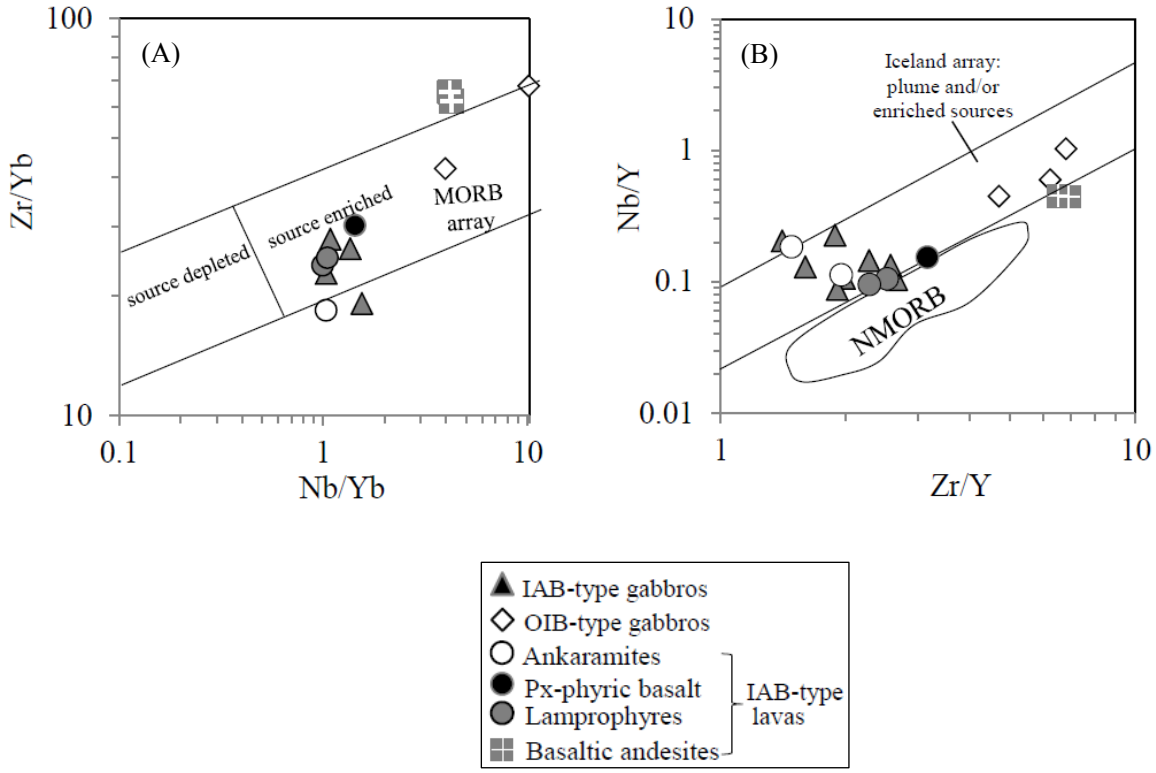


**Figure 1.26**: (A) Nb/Yb vs. Zr/Yb after Pearce and Peate (1995) and (B) Zr/Y vs. Nb/Y after Fitton et al. (1997) showing separation of MORB-source and enriched, plume-like mantle sources

The enrichment of LILEs and depletion of HFSEs of the Chukotka IAB-type gabbroic and basaltic rocks may reflect the metasomatism of mantle sources by the influx of slab-drived fluids; because crustal contamination possibility is excluded as discussed above (see Section 1.6.3). The metasomatism characteristics of mantle source for the basaltic and gabbroic rocks of Chukotka can be examined using a plot of $(Ta/La)_{PM}$ vs. $(Hf/Sm)_{PM}$ (LaFlèche et al., 1998) and Th/Zr vs. Nb/Zr (Kepezhinskas et al. (1997). As shown in the Fig. 1.27A, the data points of IAB-type gabbros and basalts plot into fluid-related metasomatism. Similarly, the Th/Zr vs. Nb/Zr diagram (Fig. 1.27B) also shows that the matle source for IAB-type gabbros and basaltic was metasomatizd by fluids, whereas for OIB-type gabbros was probably related to melt enrichment.

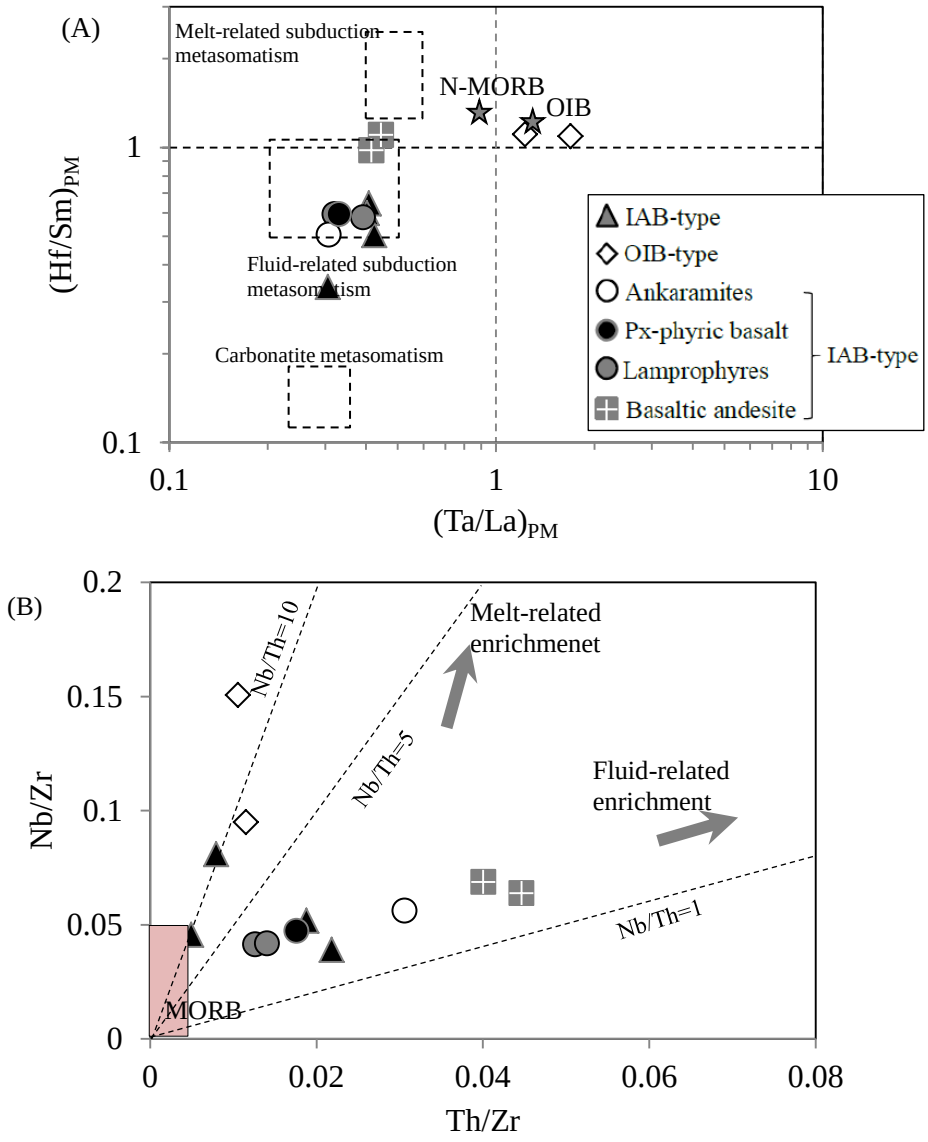


**Figure 1.27:** (A) $(Ta/La)_N$ vs. $(Hf/Sm)_N$ diagram (LaFlèche et al., 1998). Subscript N denotes the primitive mantle-normalized. Primitive mantle-normalizing values from (McDonough and Sun, 1995). (B) Th/Zr vs. Nb/Zr diagram (after Kepezhinskas et al. (1997) for the gabbroic and basaltic rocks of Chukotka, NE Russia.

This interpretation is also supported by the multiple formations of hydrous minerals, such as amphibole, in IAB-type gabbros, which implies that magmas of the Chukotka IAB-type gabbroic and basaltic rocks were drived from a "wet" source. The basaltic andesite samples exhibit the ratios of Th/Ce>0.1, indicating minor

contributions from melting of pelagic sediment of the subducted oceanic lithosphere (Hawkesworth et al., 1997). HFSE and HREE have not been mobilized from the slab to mantle wedge. Therefore, we suggest that the IAB-type gabbroic and basaltic rocks (except OIB-type gabbros) were derived from a mantle source strongly modified by fluids released by subducted slab, although minor contribution of sediment melt in basaltic andesite cannot be ruled out.

### 1.6.5. Mantle melting conditions

Trace element data (mainly rare-earth element compositions) can provide important constraints in understanding the mantle melting conditions because their relative abundances in mantle derived melts are strongly dependent on the degree of partial melting and the nature of aluminous phases (spinel or garnet) in the mantle source (Lassiter et al., 1995; Aldanmaz et al., 2000; Reichow et al., 2005; He et al., 2010). HREE especially Yb has high garnet/melt partition coefficient ($D_{garnet/melt}$=6.6) and is compatible in garnet, whereas La (LREE) and Sm has low garnet/melt partition coefficients ($D_{garnet/melt}$= 0.0016 and 0.25 respectively) and are less compatible (Johnson, 1994; Green, 2006). Sm and Yb have similar partition coefficients during partial melting of spinel lherzolite mantle source, thus the Sm/Yb ratio does not change during the partial melting, whereas, it may decrease La/Sm ratios and Sm contents of the melts (Aldanmaz et al., 2000). On the other hand, partial melting of garnet lherzolite mantle source with residual garnet will produce a more steep-slope trend on a Sm/Yb versus La/Sm (Fig. 1.28).

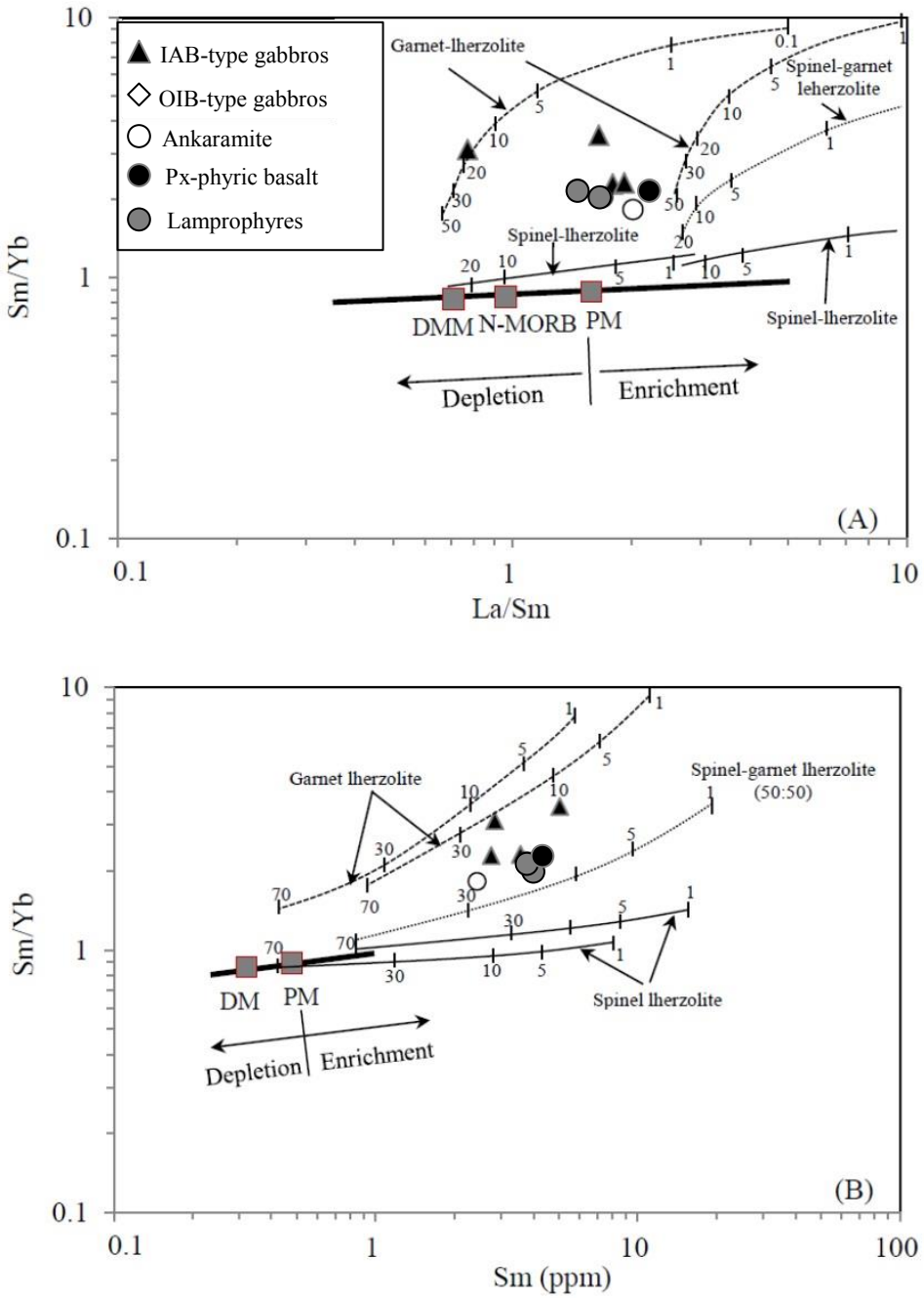


**Figure 1.28**: Plots of Sm/Yb vs. La/Sm (A) and Sm/Yb vs. Sm (B) for the IAB-type gabbroic and basaltic rocks of Chukotka, NE Russia (After Zhao and Zhou, 2007). Mantle array (heavy line) defined by depleted MORB mantle (DMM, McKenzie and O'Nions, 1991) and primitive mantle (PM, Sun and McDonough, 1989). Melting curves for spinel lherzolite ($Ol_{53}$+$Opx_{27}$+$Cpx_{17}$+$Sp_{11}$) and garnet peridotite ($Ol_{60}$+$Opx_{20}$+$Cpx_{10}$+$Gt_{10}$) with both DMM and PM compositions are after Aldanmaz et al. (2000). Numbers along lines represent the degree of the partial melting.

IAB-type gabbroic and basaltic rocks have Sm/Yb ratios higher than the spinel+garnet lherzolite melting curve, but lower than the garnet lherzolite melting. We excluded the composition of the OIB-type gabbros and basaltic andesites because they are relatively fractionated rocks. Thus, the composition of the mantle source and degree of partial melting that produced the parental magma of these rocks, indicate that IAB-type gabbroic and basaltic melts were generated at about 10-30% partial melting of garnet lherzolite.

In the Tb/Yb versus La/Yb diagram (Fig. 1.29), a high level of MREE/HREE enrichment of the IAB-type gabbros and basaltic rocks can be attributed to large amout of (2-7%) of residual garnet in their source.

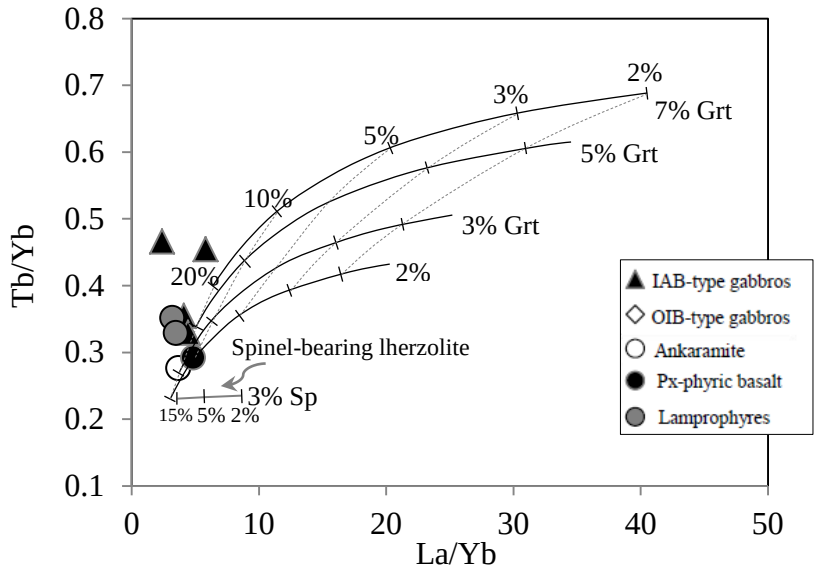


**Figure 1.29:** Tb/Yb versus La/Yb for the basaltic and gabbroic rocks of Chukotka (after Wei et al., 2014) and non-modal bach melting (Shaw, 1970) of a lherzolite mantle source showing the role of garnet and spinel in the melting region.

According to Stolper and Newman (1994) the increasing amounts of slab-derived fluid in the mantle wedge would lower the solidus and resulting in higher degree of melting. The IAB-type gabbros and basalts

demonstrating highest percent of melts in the Sm/Yb versus La/Sm diagram (Fig. 1.28), consistent with the fluid dominated mantle sources.

### 1.6.6. Pressure and Temperature constraints

The physical conditions of crystallizations such as pressure and temperature estimate can be obtained based on compositions of phases with in the gabbro. Equilibrium pressure was estimated using classical Al content in hornblende geobarometers (Hammarstrom and Zen 1986; Hollister et al. 1987; Johnson and Rutherford 1989; Blundy and Holland 1990), because the Al content in amphiboles is a sensitive indicator of pressure and temperature condition of crystallization. Calculated pressures show a range of 6.6-9.8 kbar within IAB-type gabbros but range as low as 1.0-1.9 kbar for OIB-type gabbros when applying the Hammarstrom and Zen (1986), Hollister et al. (1987) and Blundy and Holland (1990) methods. The obtained pressure for amphibole crystallization in IAB-type gabbros (average 7.4 kbar) and OIB-type gabbros (average 1.3 kbar) indicating an intrusion depth of about 24 km and 4.3 km respectively. The geobarometer of Johnson and Rutherford (1989) gave a pressure estimate lower by about 2 kbar for amphibole in IAB-type gabros, whereas about 0.2 kbar for amphibole in OIB-type gabbros. Application of Al in hornblende geobarometer (Schmidt 1992) for amphiboles from basaltic rocks yield different pressure estimates: 6.5-7.8 kbar for basaltic andesite, 7.4-10.0 kbar for lamprophyre, and generally lower for groundmass amphiboles from ankaramite and pyroxene pyric basalt (4.5-6.6 kbar). However, pressure estimates may be affected by ion substitutions in hornblende, oxygen fugacity and

fluid composition. Hornblende Al content will also vary as a function of temperature (Spear 1981; Hammarstrom and Zen 1986; Holland and Blundy 1994; Anderson and Smith 1995). On the other hand, the Ti/Al ratios in the IAB-type gabbros clinopyroxenes are lower than those in the OIB-type gabbros. These may suggest that the clinopyroxenes from IAB-type gabbros have higher pressure of crystallization than those from OIB-type gabbros.

Moreover, qualitative estimate can be also obtained from the ratio of $Al^{(IV)}/Al^{(VI)}$ in amphibole, as proposed by (Fleet and Barnett, 1978). The amphiboles in the basaltic and gabbroic rocks of Chukotka plot in the low-pressure Ca-amphibole field on the $Al^{(IV)}$ vs. $Al^{(VI)}$ diagram (Fig. 1.30). Fleet and Barnett (1978) have proposed that the $Al^{(IV)}/Al^{(VI)}=2$ ratio correspondes to about 5kbar pressureof Rease (1974), however, these preesure estimates are generally lower than those estimated by quantitative methods.

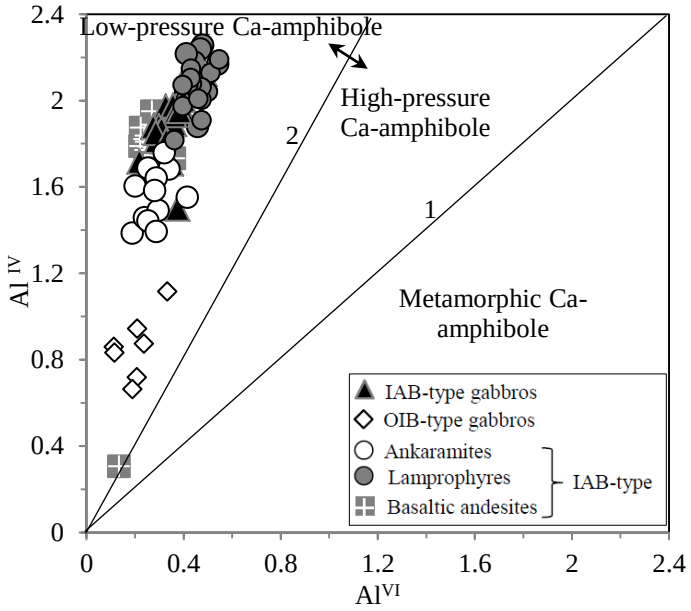


**Figure 1.30:** $Al^{(IV)}$ versues $Al^{(VI)}$ diagram for amphiboles from the gabbroic anad basaltic rocks of Chukotka, NE Russsia. Ratios and fields are from Fleet and Barnett, 1978).

Equilibration temperatures for amphiboles were calculated using the amphibole geothermobarometer of Ridolfi et al. (2010). Results show temperature values that range from 940-1006℃for basaltic andesites, 900-1080℃ for basaltic rocks, 930-1001℃ for IAB-type gabbros and 720-800℃ for OIB-type gabbros. Ridolfi et al. (2010) reported uncertainities of ±22℃ for the amphibole geothermometer. These temperature estimates are generally lower than the crystallization temperature of a normal basaltic magma (>1200 ℃) (Lee et al., 2009).

### 1.6.7. Evaluation of tectonic setting

The $Al_Z/TiO_2$ ratios (where $Al_Z$ indicates the percentage of tetrahedral sites occupied by Al) in clinopyroxene are an effective indicators for discriminating the tectonomagmatic affiliations of gabbros (Loucks, 1990). Clinopyroxenes from subduction-related yield an $Al_z/TiO_2$ ratio that is twice as steep that of reft-related magams, mainly because that the former form under high water and oxygen fugacity condition (Loucks, 1990). Clinopyroxene of IAB-type gabbros and basalts are clearly follow the trend defined by volcanic rocks and cumulates from island arc magmas (Loucks, 1990; Himmelberg and Loney, 1995; Krause et al., 2007), whereas those of OIB-type gabbros follow rift cumulate trend (Fig. 1.31A). The relationship between anorthite (An) content of plagioclase and Mg-number (Mg#) of clinopyroxene (Fig. 1.31C; Ishiwatari et al., 1990) also indicate an island arc basalt affinity for the IAB-type gabbroic and basaltic rocks (Except lamprophyre which is plotted in the MORB field). In terms of 2Nb-Zr/4-Y variations (Fig. 1.31D), all the IAB-type gabbroic and basaltic rocks (except for OIB-type gabbros and basaltic andesites) exhibit an affinity for volcanic arc basalts (VAB), which supports an arc-related tectonic environment for their generation in the former.

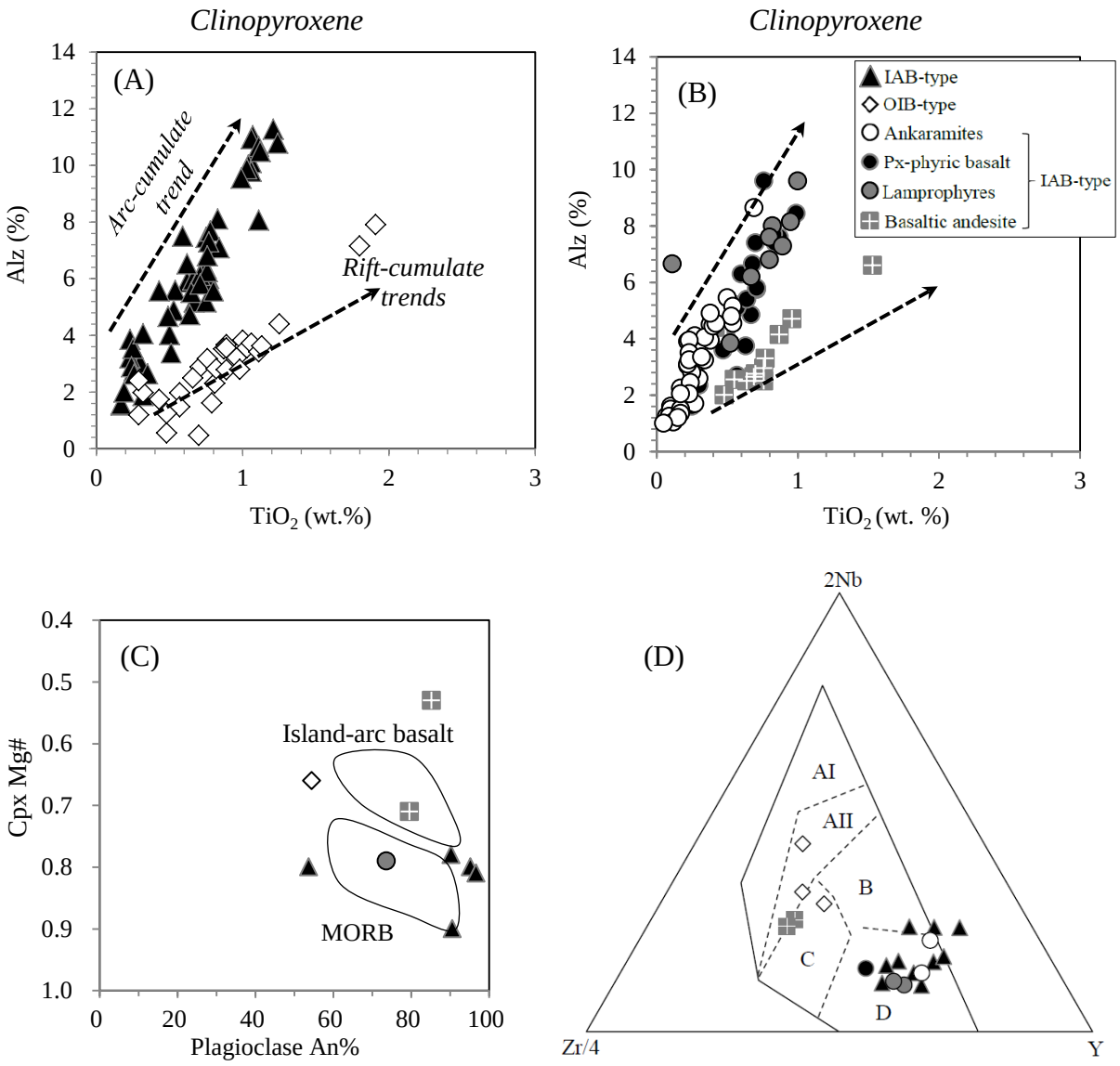


**Figure 1.31:** (A) and (B) Alz (percentage of tetrahedral sites occupied by Al) vs. $TiO_2$ in clinopyroxene (Loucks, 1990) from gabbroic and basaltic rocks respectively. (C) Relationship between anorthite (An) content of plagioclase and Mg-number (=Mg/Fe+Mg)) of coexisting clinopyroxene in the mafic rocks of Chukotka. The fields for island arc basalts (IAB) and mid-ocean ridge basalts (MORB) are from Ishiwatari et al. (1990). (D) 2Nb-Zr/4-Y tectonic environment discrimination diagram for the studied mafic rocks of Chukotka (after Meschede, 1986). AI + AII: within-plate basalt; B: MORB; D: N-MORB; C + D: magma series at destructive plate margins.

Moreover, in the $(La/Nb)_N$ vs $(Th/Ta)_N$ diagram, the studied basaltic rocks and IAB-type gabbros (except OIB-type gabbros) have trace element compositions similar to island-arc basalts, particularly similar to the eastern volcanic front lava of Kamchatka arc (Churikova et al., 2001), also suggesting subduction related environment (Fig. 1.32A).

### 1.6.8. COMPARISON WITH THE NORIL'SK BASALTS OF THE SIBERIAN LIP

#### 1.6.8.1. Hydrous nature

Most Siberian trap basalts are known to have erupted during a very short time interval at the Permian-Triassic boundary (252-250 Ma) (Kamo et al., 2003; Reichow et al., 2009). Based on the U-Pb and $^{40}Ar/^{39}Ar$ geochronologic data, however, Ivanov et al. (2013) shown that the Siberian LIP magmatism had two pulses at the Permo-Triassic boundary and in the Middle Triassic. Siberian LIP represents one of the largest Phanerozoic continental LIPs with an area and volume of about $7\times10^6$ $km^2$ and $4\times10^6$ $km^3$, respectively (Masaitis, 1983; Ivanov, 2007). It makes up of volumetrically dominant low-Ti tholeiitic rocks with subordinate amount of rocks with acidic, intermediate and ultrabasic alkaline composition (Lightfoot et al., 1993; Wooden et al., 1993; Fedorenko et al., 1996; Reichow et al., 2005; Ivanov, 2007; Krivolutskaya and Rudakova, 2009). Geochemical studies of volcanic and gabbroic rocks from several localities of the broad region of Siberian LIP have been documented. Among such regions are classical Nori'sk lava sequence (Sharma et al., 1991; Lightfoot et al., 1993; Wooden et al., 1993; Fedorenko et al., 1996; Walker et al., 1997; Al'mukhamedov et al., 2004), Putorana plateau (Sharma et al., 1991; Basu et al., 1998; Ryabchikov et al., 2001; Al'mukhamedov et al., 2004),

Maymecha-Kotuy area (Arndt et al., 1995; Basu et al., 1995; Fedorenko and Czamanske, 1997; Fedorenko et al., 2000; Al'mukhamedov et al., 2004), Tunguska Syncline (DePaolo and Wasserburg 1979) and the west Siberian basin (Medvedev et al., 2003; Reichow et al., 2005).

In general, magmatic activity within the Siberian LIP divided into three stages (Wooden et al., 1993; Al'mukhamedov et al., 1999). The early rift stage dominated by variably differentiated subalkaline volcanic rocks ranging from high-Fe mantle melt (ferropicrites) like other LIPs (e.g. Parana-Etendeka, Tuff et al., 2005; Ethiopia, Desta et al., 2014) to evolved silica saturated basalts and basaltic andesites and characterized by variable trace element abundances similar to ocean island basalts. In general, the rift stage volcanic deposits reach a maximum thickness of 1 km below Nadezhdinsky suite of Noril'sk region (Al'mukhamedov et al., 2004). The main plateau stage, defined by voluminous extrusion of low-Ti tholeiitic flood basalts above the Nadezhdinsky suite reaching a maximal thickness of ~2.5 km (e.g. Al'mukhamedov et al., 2004) and show very uniform major and trace element composition (Reichow et al., 2005). The final stage is dominated by alkaline magmatism such as meimechite (Fedorenko and Czamanske, 1997; Arndt et al., 1998; Elkins-Tanton et al., 2007).

Moreover, the occurrences of Siberian LIP in the Arctic region were reported in the Taimyr Peninsula, in the islands of Kara Sea (Vernikovsky, et al., 2003; Dobretsov, et al., 2008) and in the New Siberian Islands (Kuz'michov and Pease, 2007). Gabbros and associated lavas from the eastern Chukotka in the Kolyuchinskaya Bay area show geochemical feature similar to intra-plate basalts and in general some tholeiitic basalts of Siberian

LIP (Ledneva et al., 2011). Recently, Ledneva et al. (2014) also reported gabbroic rocks with intraplate type geochemistry from southwest of Kolyuchinskaya Bay (these rocks are analogous to our OIB-type gabbros and some of them were sampled from the same localities i.e. S5 and S6 in Fig. 1.2).

A number of different models have been proposed to explain the origin of Siberian LIP (For a detailed review, see Ivanov, 2007). In general, the plume model is suggested for the origin of Siberian LIP on the basis of major, trace and radiogenic isotope data (e.g. Sharma et al., 1992; Arndt et al., 1993; Wooden et al., 1993; Saunders et al., 2005, Reichow et al., 2005, 2009). However, the plume model has been criticized by Czamanske et al. (1998) on the basis of uplift/subsidence history. Recently, an alternative subduction related model or "wet" mantle source is suggested by Ivanov (2007) for the Siberian LIP considering the following points: (1) the tectonic position of Siberian LIP in a back-arc setting of Permian subduction system in the Mongolian-Okhotsk belt, (2) the majority of low-Ti basalts show island-arc basalt type trace element patterns, and (3) the presence of primary mica in volcanic rocks. The presence of hydrous minerals is reported from several localities of Siberian LIP: amphibole and biotite in Noril'sk I intrusion (Renne 1995), biotite in meimechite from Maymecha-Kotuy region (Fedorenko and Czamanske 1997); biotite in the olivine gabbro from west Siberian basin (Reichow et al., 2002); biotite in dolerite sills of Angara-Taseevskaya (Ivanov 2007); amphibole and biotite in the dolerite of New Siberian Islands (Kuz'michov and Pease 2007). However, it is important to note that amphibole is rarely a phenocryst in arc basalts (Davidson et al., 2007) and their scarcity can be attributed to its instability at low pressures (e.g. Rutherford and Devine, 1988; Romick et al., 1992). Ivanov and Litasov (2014) have shown that

the influence of the subduction related deep water cycle on the Siberian LIP on the basis of experimental data and numerical calculations. The above lines of evidence support the hydrous nature of the Siberian LIP.

The hydrous nature of the IAB-type gabbroic and basaltic rocks of Chukotka is evident from its high Ca content of clinopyroxene and crystallization of abundant magmatic amphibole. High water-pressure ($P_{H2O}$) conditions in the magma are suggested by the occurrence of Ca-rich clinopyroxene (Johannes, 1978). High $P_{H2O}$ could also cause plagioclase to be Ca-rich (Johannes, 1978), which is consistent with the presence of An-rich plagioclase crystals from IAB-type gabbros (Fig. 1.31C). In addition, Arculus and Wills (1980) described that hydrous basaltic melts crystallize more Ca-rich (anorthitic) plagioclase than anhydrous melts.

#### 1.6.8.2. HFSE depletion

Basalts of the Nadezhdinsky suite belong to a particular sub-type of the low-Ti rock series (Fedorenko et al., 1996), which is characterized by pronounced negative anomalies of HFSE (e.g. Nb, Ti) compared to the rest of volcanic suites of Siberian traps and are attributed to crustal contamination (e.g., Arndt et al., 1993; Wooden et al., 1993) or melting of the lithospheric mantle (Lightfoot et al., 1993; Hawkesworth et al., 1995). Multi-element diagrams for the Triassic basalts and gabbros of Chukotka are compared with averaged data for the Siberian LIP from the Noril'sk region (Fig. 1.9). Trace element patterns for the basalts and IAB-type gabbros resemble to the low-Ti Nadezdinsky suite of Noril'sk region in terms of depletion in HFSE (i.e. Nb, Ta, Zr, P), which may suggest similar condition of formation. However, our samples show a more pronounced HFSE depletion and

higher $(La/Nb)_N$ ratios (Figs. 1.9 and 1.32A, respectively) which are remarkably similar with the eastern volcanic front basalts of the Kamchatka arc (Churikova et al., 2001). The degree of HFSE depletion in our samples is lower compared to intra-oceanic convergent margin lavas (i.e. Mariana arc, Tamura et al., 2014). It is important to mention that the major continental LIPs, e.g. Siberian LIP (Wooden et al., 1993; Krivolutskaya and Rudakova, 2009), Central Atlantic magmatic province (Callegaro et al., 2013), and Karoo LIP (Luttinen et al., 2010) are characterized by elevated $(La/Nb)_N$ ratios similar to island-arc basalts (Fig. 1.32).

Such arc-like features of continental LIPs have been attributed to a sudden reactivation of dormant arc or backarc sources trapped under continental-plate sources (Puffer, 2001). The island-arc basalt like trace element pattern of the low-Ti basalts of Siberian LIP have been usually attributed to the signature of lithospheric contamination (e.g. Lightfoot et al., 1993; Reichow et al., 2005).

On the other hand, Puffer (2001) discussed the geochemical similarity between low-Ti Siberian LIP and island-arc basalts in terms of depletion of HFSE and enrichment of LILE, which indicates their mantle source, is similar to mantle wedge of active continental margins.

OIB-type gabbros have $(La/Nb)_N$ between 0.7 and 1.0 and $(Th/Ta)_N$ between 0.5 and 0.8 (Fig. 1.32) similar to typical plume related LIPs, e.g. Ethiopian LIP (Beccaluva et al., 2009; Desta et al., 2014) and Hawaiian-Emperor Chain basalts (Huang et al., 2005), which can be interpreted as insignificant contribution of continental material in their source. Similarly, in terms of Th/Yb vs. Nb/Yb relations (Fig. 1.32B) (Pearce, 2008) OIB-type gabbroic samples like typical plume related LIPs e.g. Ethiopian LIP (Beccaluva et al., 2009; Desta et al., 2014)

and Etendeka magmatism (Gibson et al., 2000) and Hawaiian-Emperor Chain basalts (Huang et al., 2005) plot close to or with in the oceanic mantle array, which may indicate no influence of lithospheric component in their genesis.

However, the Nadezhdinsky suit (Siberian LIP) (Wooden et al., 1993), Central Atlantic magmatic province (Callegaro et al., 2013), Karoo LIP (Luttinen et al., 2010) clearly displaced from the oceanic mantle array field to higher Th/Yb ratios (Fig. 1.32B), which can be explained by crustal contamination or subduction zone enrichment (Pearce and Peate, 1995). In the case of IAB-type gabbros and basaltic rocks of Chukotka, the displacement of data above the mantle array is attributed to enrichment by fluids. Ivanov et al. (2008) and Ivanov and Litasov (2014) discussed the similarity of the calculated initial melt compositions of the southeastern Siberian flood basalt province (Angara-Taseevskaya dolerite sills) with the initial melt compositions of the modern arc of Eastern Kamchatka (Portnyagin et al., 2007) in terms of trace elements, suggesting a similar subduction-related processes are responsible for their origin. Ivanov and Litasov (2014) concluded that the Siberian LIP is formed in a far back-arc region of the Mongolia-Okhotsk subduction system and the influence of subduction in the trace element budget of flood basalts reduces away from subduction zone (e.g. presence of rocks with OIB signature such as meimechite from the northernmost Maymecha–Kotuy region). However, meimechite and picritic lavas are not known in Chukotka like that of Siberian LIP.

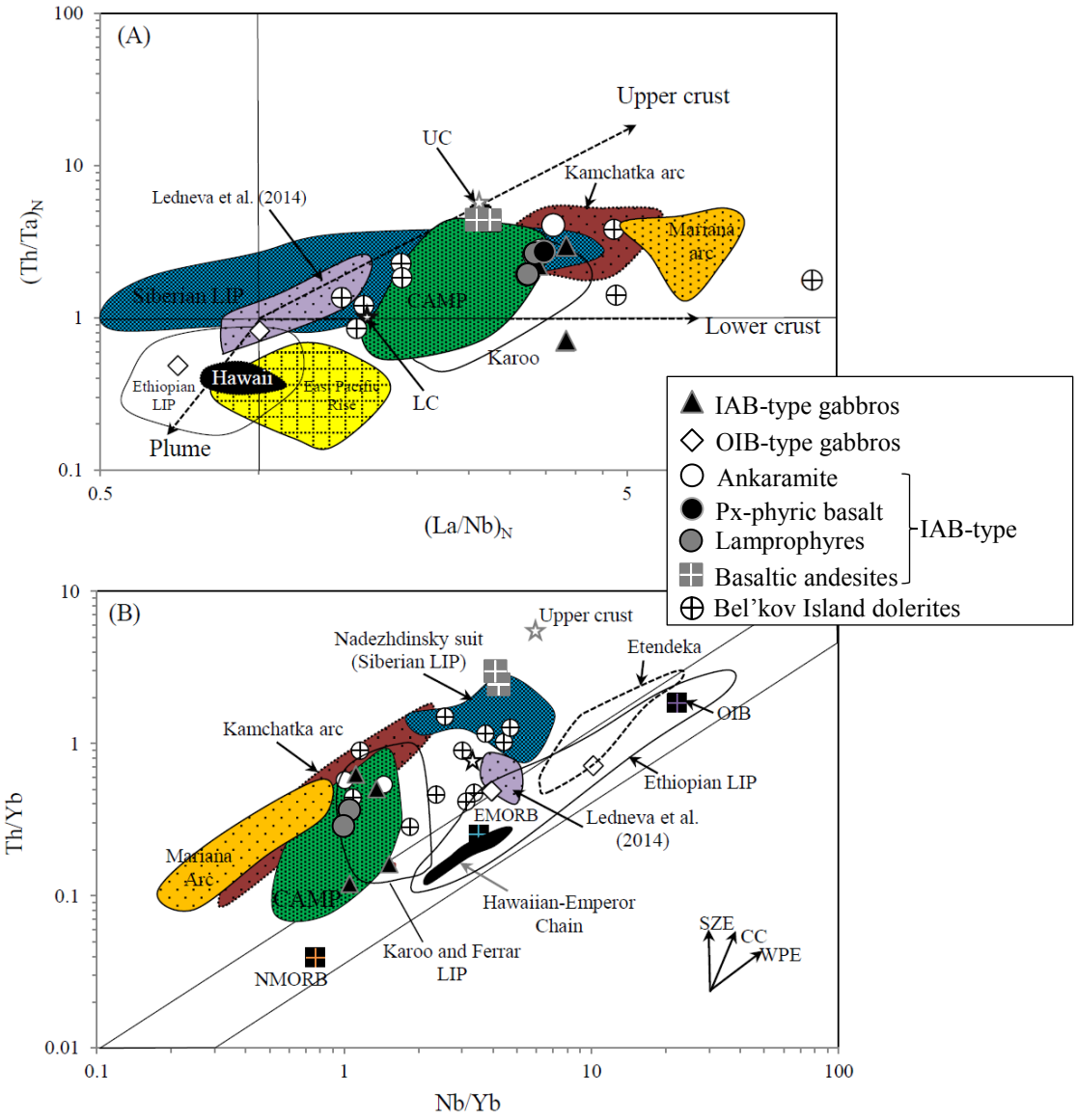


**Figure 1.32:** (A) $(La/Nb)_N$ vs. $(Th/Ta)_N$ (after Neal et al., 2002), where N denotes normalized toprimitivemantle (McDonough and Sun, 1995) and (B) Nb/Yb vs. Th/Yb diagram discriminating rocks enriched by input from subduction componenet, crustal contamination, and deep crustal recycling (modified after Pearce, 2008). SZE: subduction zone enrichment, CC: continental contamination, WPE: within-plate enrichment. The field of Siberian LIP is from Wooden et al. (1993) and Krivolutskaya et al. (2009); Bel'kov Island, Kuz'michov and Pease (2007); Central Atlantic magmatic province (CAMP), Callegaro et al. (2013); Ethiopian LIP, Beccaluva et al. (2009) and Desta et al., 2014; Etendeka, Gibson et al. (2000); Karoo LIP, Luttinen et al. (2010); Kamchatka arc, Churikova et al. (2001); Mariana arc, Tamura et al. (2014); East Pacific Rise, Turner et al. (2011); Hawaiian-Emperor Chain, Huang et al. (2005) are shown for comparison. Upper crust (UC) and lower crustal (LC) values are from Rudnick and Gao, (2003). NMORB, EMORB and OIB are from Sun and McDonough (1989).

The vast distribution of the Paleozoic accretionary complexes in Mongolia with oceanic sediments, oceanic plateau fragments with a trace of forearc magmatism evidences for a long term, wide scale operation of the subduction system (Erdenesaihan et al., 2013).

In summary, the Triassic mafic rocks of Chukotka may represent the eastern margin of Siberian LIP based on the following points: (1) the presence of both OIB and IAB-like (i.e. depletion of HFSE) mafic rocks throughout Chukotka like that of Siberian LIP, (2) the hydrous nature of Siberian magma to crystallize hydrous minerals, (3) plat formal field occurrence of the studied rocks and (4) the geochemical and petrological similarity between the IAB-type gabbros of Chukotka and the Bel'kov Island dolerites suggests that the eastern Chukotka was closer to the Siberian margin during Triassic and later tectonically rifted and moved to the current position.

## 1.7. CONCLUSIONS

IAB-type gabbroic suite is genetically related to the associated basaltic rocks and represents the slowly cooled, tabular-shaped intrusion of mafic magma. Mineral and bulk rock chemical characteristics of IAB-type gabbroic rocks and basalts are compatible with magmas from subduction zone geotectonic setting, whereas OIB-type gabbros show within plate magma characteristics. Geochemical data suggest partial melting of the subduction-modified, metasomatized enriched mantle wedge of garnet lherzolite to produce the parental melt of the IAB-type gabbroic and basaltic rocks of Chukotka. The parental magma of the IAB-type gabbroic and basaltic rocks formed by about 10-30% partial melting of garnet lherzolite. The near-primary nature of the ankaramite of

Chukotka reflected on its high Mg# (63-65), Cr contents (466-530 ppm), Ni-contents (67-81 ppm) and occurrenc of high-Mg clinopyroxene phenocrysts (Mg# ≤93). The geochemical similarity of the studied IAB-type gabbroic and basaltic rocks of Chukotka with Bel'kov dolerite and low-Ti Nadezhdinsky suit (Noril'sk region) in terms of the presence of dominant hydrous minerals and negative HFSE anomalies, it is possible that the eastern Chukotka was placed closer to the Siberian LIP in Triassic, and the Triassic mafic magmatism in Chukotka represents a marginal part of the Siberian LIP.

## 1.8. REFERENCES


Adam, J., and Green, T. (2006) Trace element partitioning between mica- and amphibole-bearing garnet lherzolite and hydrous basanitic melt: 1. Experimental results and the investigation of controls on partitioning behaviour. *Contributions to Mineralogy and Petrology*, 152, 1-17.

Aldanmaz, E., Pearce, J.A., Thirlwall, M.F., and Mitchell, J.G. (2000) Petrogenetic evolution of late Cenozoic, post-collision volcanism in western Anatolia, Turkey. *Journal of Volcanology Geothermal Researc*h, 102, 67–95.

Al'Mukhamedov, A.I., Medvedev, A.Ya., and Kirda, N.P. (1999) Comparitive analysis of geodynamic settings of the Permo–Triassic magmatism in East Siberia and West Siberia. *Russian Geology and Geophysics*, 40 (No. 11), 1550– 1561.

Al'mukhamedov, A.I., Medvedev, A.Ya., and Zolotukhin, V.V. (2004) Chemical evolution of the Permian–Triassic basalts of the Siberian platform in space and time. *Petrology*, 12, 297–311.

Amato, J.M., Toro, J., Miller, E.L., Gehrels, G.E., Farmer, G.L. Gottlieb, E.S. and Till, A.B. (2009) Late Proterozoic-Paleozoic evolution of the Arctic Alaska-Chukotka terrane based on U-Pb igneous and detrital zircon ages: Implications for Neoproterozoic paleogeographic reconstructions. *GSA Bulletin*, 121(9/10), 1219–1235.

Anderson, J.L., and Smith, D.R. (1995) The effects of temperature and $fO_2$ on the Al-in-hornblende barometer. *American Mineralogist*, 80, 549–559.

Arculus, R.J., and Wills, K.J.A. (1980) The petrology of plutonic blocks and inclusions from the Lesser Antilles island arc. *Journal of Petrology*, 21, 743–799.

Arndt, N., Chauvel, C., Czamanske, G., and Fedorenko, V. (1998) Two mantle sources, two plumbing systems: tholeiitic and alkaline magmatism of the Maymecha River basin, Siberian flood volcanic province. *Contributions to Mineralogy and Petrology*, 133, 297-313.

Arndt, N., Lehnert, K., and Vasil'ev, Y. (1995) Meimechites: highly magnesian lithosphere-contaminated alkaline magmas from deep subcontinental mantle. *Lithos*, 34, 41–59.

Arndt, N.T., Czamanske, G.K., Wooden, J.L., and Fedorenko, V.A. (1993) Mantle and crustal contributions to continental flood volcanism. *Tectonophysics*, 223, 39–52.

Arndt, N.T., and Christensen, U.R. (1992) The role of lithospheric mantle in continental flood volcanism: thermal and geochemical constraints. *Journal of Geophysical Research*, 97, 10967–10981.

Bardsell, M., and Berry, R.F. (1990) Origin and evolution of primitive island arc ankaramites from Western Epi, Vanuatu. *Journal of Petrology*, 31, 747–777.

Basu, A.R., Hannigan, R.E., and Jacobsen, S.B. (1998) Melting of the Siberian mantle plume. *Geophysical Research Letters*, 25, 2209–2212.

Basu, A.R., Poreda, R.J., Renne, P.R., Teichmann, F., Vasiliev, Yu.R., Sobolev, N.V., and Turrin, B.D. (1995) High-$^{3}$He plume origin and temporal-spatial evolution of the Siberian flood basalts. *Science*, 269, 822–825.

Beccaluva, L., Bianchini, G., Natali, C. and Siena, F. (2009) Continental flood basalts and mantle plumes: a case

study of the northern Ethiopian Plateau. *Journal of Petrology*, 50, 1377–1403.

Blundy, J.D., and Holland, T.J.B. (1990) Calcic amphibole equilibria and a new amphibole-plagioclase geothermometer. *Contributions to Mineralogy and Petrology*, 104:208–224

Callegaro S., Marzoli A., Bertrand H., Chiaradia M., Reisberg L., Meyzen C., Bellieni G., Weems R. E., and Merle R. (2013) Upper and lower crust recycling in the source of CAMP basaltic dykes from southeastern North America. *Earth and Planetary Science Letters*, 376, 186–199.

Carlson, R.W. (1991) Physical and chemical evidence on the cause and source characteristics of flood-basalt volcanism. Australian Journal of Earth Science, 38, 525–544.

Churikova, T., Dorendorf, F., and Worner, G. (2001) Sources and fluids in the mantle wedge below Kamchatka, evidence from across-arc geochemical variation. *Journal of Petrology*, 42, 1567–1593.

Czamanske, G.K., Gurevich, A.B., Fedorenko, V., and Simonov, O. (1998) Demise of the Siberian plume: paleogeographic and paleotectonic reconstruction from the prevolcanic and volcanic records, North-Central Siberia. *International Geology Review*, 40, 95–115.

Davidson J, Turner S, Handley H, Macpherson C, and Dosseto A (2007) Amphibole "sponge" in arc crust? *Geology*, 35(9):787–790.

DePaolo, D.J., and Wasserburg, G.J. (1979) Neodymium isotopes in flood basalts from the Siberian Platform and inferences about their mantle sources. *Proceedings of the National Academy of Science of the United States of America*, 76**,** 3056–3060.

Degtyaryov, V.S. (1975) Petrochemical peculiarities of the Amguema-Anyui diabase formation of the Chukotka fold region. In Shatalov, E.T. (ed.). Magmatism of North East Asia, part 2. Magadan book publisher, Magadan, 160–175 (in Russian).

Della-Pasqua F., and Varne, R. (1997) Primitive ankaramitic magmas in volcanic arcs: a melt-inclusion approach. *Canadian Mineralogist*, 35,291–312.

Desta, M.T., Ayalew, D., Ishiwatari, A., Arai, S., and Tamura, A. (2014) Ferropicrite from the Lalibela area in the Ethiopian large igneous province. *Journal of Mineralogical and Petrological Science*s, 109, 191–207.

Dobretsov, N.L., Kirdyashkin, A.A., Kirdyashkin, A.G., Vernikovsky, V.A., and Gladkov, I.N. (2008) Modeling of thermochemical plumes and implications for the origin of the Siberian Traps. *Lithos*, 100, 66–92.

Elkins-Tanton, L.T., Draper, D.S., Agee, C.B., Jewell, J., Thorpe, A., and Hess, P.C. (2007) The last lavas erupted during the main phase of the Siberian flood volcanic province. Results from experimental petrology. *Contributions to Mineralogy and Petrology*, 153, 191–209.

Elliott, T., Plank, T., Zindler, A., White, W., and Bourdon, B. (1997) Element transport from slab to volcanic front at the Mariana arc. *Journal of Geophysical Research*, 102(B7):14991–15019.

Erdenesaihan, G., Ishiwatari, A., Orolmaa, D., Arai, S., and Tamura, A. (2013) Middle Paleozoic greenstons of the Hangay region, central Mongolia: Remnants of an accreted oceanic plateau and forearc magmatism. *Journal of Mineralogical and Petrological Sciences*, 108, 303–325.

Fedorenko, V., Czamanske, G., Zen'ko, T., Budanh, J., and Siems, D. (2000) Field and geochemical studies of

the melilite bearing Arydzhangsky suite, and an overall perspective on the Siberian alkaline-ultramafic flood-volcanic rocks. *International Geology Review*, 42, 769–804.

Fedorenko, V.A., and Czamanske, G.K. (1997) Results of new field and geochemical studies of the volcanic and intrusive rocks of the Maymecha–Kotuy area, Siberian flood-basalt province. *International Geological Review*, 39, 479–531.

Fedorenko, V.I., Lightfoot, P.C., Naldrett, A.J., Czamanske, G.K., Hawkesworth, C.J., Wooden, J.L., and Ebel, D.S. (1996) Petrogenesis of the flood-basalt sequence at Noril'sk, North Central Siberia. *International Geology Review*, 38, 99–135.

Figueroa, O., Deruelle, B., and Demaiffe, D. (2009) Genesis of adakite-like lavas of Licancabur volcano (Chile-Bolivia, Central Andes). *Comptes Rendus Geosci*, 341:310–318.

Fitton, J. G., Saunders, A. D., Norry, M. J., Hardarson, B. S., and Taylor, R. N. (1997) Thermal and chemical structure of the Iceland plume. *Earth and Planetary Science Letters*, 153, 197–208.

Fleet, M.E., Barnett, R.L. (1978) $Al^{(IV)}/Al^{(VI)}$ partitioning in calciferous amphiboles from the mine, Sudbury, Ontario. *Canadian Mineralogist* ,16, 527 532.

Gel'man, M. L. (1963) Triassic diabase association in the Anyui fold zone (Chukotka). *Geologiya i Geofizika*, 2, 127–134 (in Russian).

Gibson S. A., Thompson R. N., and Dickin A. P. (2000) Ferropicrites: Geochemical evidence for Fe-rich streaks in upwelling mantle plumes. *Earth and Planetary Science Letters*, 174, 355–374.

Grantz, A., Clark, D.L., Phillips, R.L., and Srivastava, S.P. (1998) Phanerozoic stratigraphy of Northwind Ridge, magnetic anomalies in the Canada basin, and geometry and timing of rifting in the Amerasia basin, Arctic Ocean. *Geological Society of America Bulletin*, 110, 801–820.

Green, D. H., Schmidt, M.W. & Hibberson, W. O. (2004) Island-arc ankaramites: Primitive melts from fluxed refractory lherzolitic mantle. *Journal of Petrology*, 45, 391–403.

Green, N.L. (2006) Influence of slab thermal structure on basalt source regions andmelting conditions: REE and HFSE constraints form the Garibaldi volcanic belt, northern Cascadia subduction system. *Lithos*, 87, 23–49.

Green, D.H. (1976) Experimental testing of "equilibrium" partial melting of peridotite under water-saturated, high-pressure conditions. Canadian Mineralogist, 14, 255–268.

Green, T. H. and Pearson, N. J. (1985) Experimental determination of REE partition coefficients between amphibole and basaltic to andesitic liquids at high pressure. *Geochimica et Cosmochimica Acta*, 49, 1465-1468.

Grove, T.L., Parman, S.W., Bowring, S.A., Price, R.C., and Baker, M.B. (2002) The role of an $H_2O$-rich fluid component in the generation of primitive basaltic andesites and andesites form the Mt. Shasta region, N. California. *Contributions to Mineralogy and Petrology*, 142, 375–396.

Hammarstrom, J.M., and Zen, E. (1986) Aluminum in hornblende: an empirical igneous geobarometer. *American Mineralogist*, 71, 1297–1313.

Hanson, G.N., and Langmuir, C.H. (1978) Modeling of major elements in mantle–melts systems using trace

element approaches. Geochimica et Cosmochimica Acta, 42, 725–742.

Hart, S.R., and Dunn, T. (1993) Experimental cpx/melt partitioning of 24 trace elements. *Contributions to Mineralogy and Petrology*, 113, 1–8.

Hawkesworth, C.J., Gallagher, K., Kelley, S., Mantovani, M.S.M., Peate, D.W., Regelous, M., and Rogers, N.W. (1992) Paraná magmatism and the opening of the South Atlantic. In: Storey, B.C., Alabaster, A., Pankhurst, R.J. (Eds.), Magmatism and the Causes of Continental Break-up: Geological Society of London Special Publication, 68, 221–240.

Hawkesworth, C.J., Lightfoot, P.C., Fedorenko, V.A., Blake, S., Naldrett, A.J., Doherty, W. and Gorbachev, N.S. (1995) Magma differentiation and mineralisation in the Siberian continental flood basalts. *Lithos*, 34, 61–88.

Hawkesworth, C.J., Rogers, N.W., Vancalsteren, P.W.C. (1984). Mantle enrichment processes. *Nature*, 311, 331–335.

Hawkesworth, C.J., Turner, S.P., McDermott, F., Peate, D.W., and van Calsteren, P. (1997) U-Th isotopes in arc magmas: implecations for element transfer from the subducted crust. Science, 276, 551–555.

He, Y.H., Zhao, G.Z., Sun, M., Han, Y. (2010) Petrogenesis and tectonic setting of volcanic rocks in the Xiaoshan and Waifangshan areas along the southern margin of the North China Craton: constraints from bulk-rock geochemistry and Sr-Nd isotopic composition. *Lithos*, 114, 186–199.

Hergt, J., Peate, D., and Hawkesworth, C.J. (1991) The petrogenesis of Mesozoic Gondwana low-Ti flood basalts. *Earth and Planetary Science Letters*, 105, 134–148.

Himmelberg, R.G., and Loney, R.A. (1995) Characteristics and perogenesis of Alaskan-type ultramafic–ultramafic intrusions, southeastern Alaska. *US Geological Survey Professional Paper*, 1564, 1–47.

Holland, T., and Blundy, J. (1994) Non-ideal interactions in calcic amphiboles and their bearing on amphibole-plagioclase thermometry. *Contributions to Mineralogy and Petrology*, 116, 433–447.

Hollings, P., and Kerrich, R. (2000) An Archean arc basalt-Nb-enriched basalt-adakite association: the 2.7Ga confederation assemblage of the Birch-Uchi greenstone belt, Superior Province. *Contributions to Mineralogy and Petrology*, 139, 208–226.

Hollister, L.S., Griddom, G.C., Peters, EK, Stowel, H.H., and Sisson, V.B. (1987) Confirmation of the empirical correlation of Al in hornblende with pressure of solidification of calc-alkaline plutons. *American Mineralogist*, 72, 231–239.

Huang, S., Regelous, M., Thordarson, T., and Frey, F.A. (2005) Petrogenesis of lavas from Detroit Seamount: Geochemical differences between Emperor Chain and Hawaiian volcanoes. *Geochemistry, Geophysics and Geosystems*, 6, Q01L06, doi:10.1029/2004GC000756.

Irvine, T.N., and Baragar, W.R.A. (1971) A guide to the chemical classification of the common volcanic rocks. *Canadian Journal of Earth Science*s, 8, 523–548.

Irving, A.J., and Frey, FA. (1984) Trace element abundances in megacrysts and their host basalts; constraints on partition coefficients and megacryst genesis. *Geochimica et Cosmochimica Acta*, 48, 1201–122l.

Ishida, H., Morishita, T., Arai, S., and Shirasaka, M. (2004) Simultaneous in-situ multi-element analysis of

minerals on thin section using LA-ICP-MS. Sci. Rep. Kanazawa Univ. 48, 31–42.

Ivanov, A.I., and Litasov, K.D. (2014) The deep water cycle and flood basalt volcanism. *International Geology Review*, 56, 1–14.

Ivanov, A.V. (2007) Evaluation of different models for the origin of the Siberian traps. In: Foulger, G.R., Jurdy, D.M. (Eds.), The Origin of Melting Anomalies: Plates, Plumes and Planetary Processes. *Geological Society of America Special Paper*, 430, p. 669– 691.

Ivanov, A.V., Demonterova, E.I., Rasskazov, S.V., and Yasnygina, T.A. (2008) Low-Ti melts from the Southeastern Siberian Traps large igneous province: Evidence for a water-rich mantle source? *Journal of Earth System Science*, 117, 1–21.

Ivanov, A.V., He, H., Yan, L., Ryabov, V.V., Shevko, A.Y., Palesskii, S.V., and Nikolaeva, I.V. (2013) Siberian Traps large igneous province: Evidence for two flood basalt pulses around the Permo-Triassic boundary and in the Middle Triassic, and contemporaneous granitic magmatism. *Earth-Science Reviews*, 122, 58–76.

Ivanov, O. N., and Milov, A. P. (1975) The diabase association in the Chukchi fold system and its relation to the basic magmatism in the northern portion of the Pacific Mobile Belt (in Russian), in Magmatism of North East Asia, part 2, edited by E. T. Shatalov, pp. 155 – 159, Magadan Publ. House, Magadan, Russia.

Johannes, W. (1978) Melting of plagioclase in the system Ab-An-$H_2O$- and Qz-Ab-An-$H_2O$ at $PH_2O$=5 kbars an equilibrium problem. *Contributions to Mineralogy and Petrology*, 66, 295–303.

Johnson, K.T.M. (1994) Experimental cpx/ and garnet/melt partitioning of REE and other trace elements at high

pressures; petrogenetic implications. *Mineralogical Magazine*, 58, 454–455.

Johnson, M.C., and Rutherford, M.J. (1989) Experimental caliberation of the aluminum-in-hornblende geobarometer with application to Long Valley caldera (California) volcanic rocks. *Geology*, 17, 837–841.

Jolly, W.T., Lidiak, E.G., Dickin, A.P., and Way, T-W (2002) Recycling in the Puerto Rican mantle wedge, Greater Antilles island arc. *The Island Arc*, 11:10–24.

Kamo, S.L., Czamanske, G.K., Amelin, Yu., Fedorenko, V.A., Davis, D.W., and Trofimov, V.R. (2003) Rapid eruption of Siberian flood volcanic rocks and evidence for coincidence with the Permian–Triassic boundary and mass extinction at 251 Ma. *Earth and Planetary Science Letters*, 214, 75–91.

Kepezhinskas, P., McDermott, F., Defant, M., Hochstaedter, A., Drummond, M.S., Hawdesworth, C.J., Koloskov, A., Maury, R.C., Bellon, H., (1997) Trace element and Sr–Nd–Pb isotopic constraints on a three-component model of Kamchatka Arc petrogenesis. *Geochim. Cosmochim. Acta*, 61, 577–600.

Kogiso,T. and Hirschmann, M. M. (2001) Experimental study of clinopyroxenite partial melting and the origin of ultra-calcic melt inclusions. *Contributions to Mineralogy and Petrology*, 142, 347–360.

Krause, J., Brugmann, G.E., and Pushkarev, E.V. (2007) Accessory and rock forming minerals monitoring the evolution of zoned mafic–ultramafic complexes in the Central Ural Mountains. *Lithos*, 95, 19–42.

Krivolutskaya, N.A., and Rudakova, A.V. (2009) Structure and Geochemical characteristics of trap rocks from the Noril'sk trough, northwestern Siberian craton. *Geochemistry International*, 47, 635-656.

Kuz'michov, A.B., and Pease, V.L. (2007) Siberian trap magmatism on the New Siberian Islands: constraints for

Arctic Mesozoic plate tectonic reconstructions. *Journal of Geological Society*, 164, 959–968.

LaFlèche, M.R., Camire, G., Jenner, G.A. (1998) Geochemistry of post-Acadian, Carboniferous continental intraplate basalts from the Maritimes Basin, Magdalen islands, Quebec, Canada. *Chemical Geology*, 148, 115–136.

Lassiter, J.C., DePaolo, D.J., and Mahoney, J.J. (1995) Geochemistry of the Wrangellia Flood Basalt Province: implications for the role of continental and oceanic lithosphere in Flood Basalt Genesis. *Journal of Petrology*, 36, 983-1009.

Lawver, L.A., Grantz, A., and Gahagan, L.M. (2002) Plate kinematic evolution of the present Arctic region since the Ordovician. In: Miller, E.L., Grantz, A. & Klemperer, S.L. (eds) Tectonic Evolution of the Bering Shelf–Chukchi Sea–Arctic Margin and Adjacent Landmasses. *Geological Society of America, Special Papers*, 360, 333–358.

Leake, B.E. (1978) Nomenclature of amphiboles. *American Mineralogist*, 63, 1023–1052.

Ledneva, G.V., Bazylev, B.A., Layer, P.W., Ishiwatari, A., Sokolov, S.D., Kononkova, N.N., Tikhomirov, P.L., and Novikova, M.S. (2014) Intra-plate gabbroic rocks of Permo-Triassic to Early-Middle Triassic dike-and sill province of Chukotka (Russia). *International Conference on Arctic Margins* VI, 115–156.

Ledneva, G.V., Sokolov, S.D., and Pease, V.L. (2011) Permo-Triassic hypabyssal mafic intrusions and associated tholeiitic basalts of the Kolyuchinskaya Bay, Chukotka (NE Russia): Links to the Siberian LIP. *Journal of Asian Earth Sciences*, 40, 737–745.

Lee, C.-T.A., Luffi, P., Plank, T., Dalton, H., and Leeman, W.P. (2009) Constraints on the depths and temperatures of basaltic magma generation on Earth and other terrestrial planets using new thermobarometers for mafic magmas. *Earth and Planetary Science Letters*, 279, 20–33.

Lightfoot, P.C., Hawkesworth, C.J., Hergt, J., Naldrett, A.J., Gorbachev, N.S., Fedorenko, V.A., and Doherty, W. (1993) Remobilisation of the continental lithosphere by a mantle plume: major-, trace-element, and Sr-, Nd-, and Pb-isotope evidence from picritic and tholeiitic lavas of the Noril'sk district, Siberian Trap, Russia. *Contributions to Mineralogy and Petrology*, 114, 171– 188.

Loucks, R.R. (1990) Discrimination of ophiolitic from nonophiolitic ultramafic-mafic allochthons in orogenic belts by the Al/Ti ratio in clinopyroxene. *Geology*, 18, 346–349.

Luttinen, A.V., Leat, P.T., and Furnes, H. (2010) Björnnutane and Sembberget basalt lavas and the geochemical provinciality of Karoo magmatism in the western Dronning Maud Land, Antarctica. *Journal of Volcanology and Geothermal Research*, 198, 1–18.

Mahoney, J.J. (1988) Deccan Traps. In: Macdougall, J.D. (Ed.). Continental Flood Basalts. Kluwer, Dordrecht, pp. 151–194.

Masaitis, V.L. (1983) Permian and Triassic volcanism of Siberia. *Zapiski VMO, part CXII, issue,* 4:412–425 (in Russian).

McDonough, W.F., and S.-s. Sun. (1995) The composition of the Earth. *Chemical Geology*, 120, 223-253.

McKenzie, D., and O'Nions, R.K. (1991) Partial melt distribution from inversion of rare earth element

concentrations. *Journal of Petrology*, 32, 1021–1091.

Medvedev, A.Ya., Al'mukhamedov, A.I., and Kirda, N,P. (2003) Geochemistry of Permo-Triassic volcanic rocks of West Siberia. *Geologiya i Geofizika*, 44, 86–100.

Meschede, M. (1986) A method of discriminating between different types of mid-ocean ridge basalts and continental tholeiites with the Nb–Zr–Y diagram. *Chemical Geology*, 56, 207–218.

Miller, E.L., Toro, J., Gehrels, G., Amato, J.M., Prokopiev, A., Tuchkova, M.I., Akinin, V.V., Dumitru, T.A., Moore, T.E., and Cecile, M.P. (2006) New insights into Arctic paleogeography and tectonics from U–Pb detrital zircon geochronology. *Tectonics*, 25, 1–19.

Miyashiro, A. (1974). Volcanic rock series in island-arcs and active continental margins. *American Journal of Science*, 274, 321–355.

Moore, T.E., Wallace, W.K., Bird, K.J., Karl, S.M., Mull, C.G., and Dillon J.T. (1994) Geology of northern Alaska. In: Plafker, G., Berg H.C. (Eds.), The Geology of North America, Geological Society of America, vol. G-1. *The Geology of Alaska*, pp. 49– 140.

Morimoto, N., Fabries, J., Ferguson, A.K., Ginzburg, I.V., Ross, M., Seifert, F.A., Zussman, J., Aoki, K. and Gottardi, D., (1988) Nomenclature of pyroxenes. *American Mineralogist*, 62, 53–62.

Münker, C., Worner, G., Yogodzinski, G., and Churikova, T. (2004) Behaviour of high field strength elements in subduction zones: constraints from Kamchatka–Aleutian arc lavas. *Earth and Planetary Science Letters*, 224, 275–293.

Nachit, H., Ibhi, A., Abia, E.H., and Ohoud, M.B. (2005) Discrimination between primary magmatic biotites, re-equilibrated biotites and neoformed biotities. *Comptes Rendus Geoscience*, 337, 1415–1420.

Natal'in, B.A., Amato, J.M., Toro, J., and Wright, J.E. (1999) Paleozoic rocks of northern Chukotka Peninsula, Russian Far East: implication for the tectonics of the Arctic region. *Tectonics*, 18, 977–1003.

Neal, C.R., Mahoney, J.J., and Chazey III, W.J. (2002) Petrogenesis of Kerguelen Plateau and Broken Ridge LIP: Results from ODP Leg 183. *Journal of Petrology*, 43, 1177–1205.

Nokleberg, W. J., Parfenov, L. M., Monger, J. W. H., Norton, I. O., Khanchuk, A. I., Stone, D. B., Scholl, D. W., and Fujita, K. (1998) Phanerozoic Tectonic Evolution the Circum-North Pacific, U.S. Geological Survey, Open-File Report 98–754.

Parfenov, L. M. (1984) Continental Margins and Island Arcs in the Mesozoides of Northeastern Asia, Novosibirsk: Nauka, (in Russian).

Parfenov, L. M., Natapov, L. M., Sokolov, S. D., and Tsukanov, N. V. (1993) Terranes analysis and accretion in northeast Asia. *The Islands Arc*, 2, 35–54.

Pearce, J.A. (1996) A user's guide to basalt discrimination diagrams. In: Trace Element Geochemistry of Volcanic Rocks: Applications for Massive Sulphide Exploration. Short Course Notes, vol. 12. *Geological Association Canadian*, pp. 79–113.

Pearce, J.A. (2008) Geochemical fingerprinting of oceanic basalts with applications to ophiolite classification and the search for Archaean oceanic crust. *Lithos*, 100, 14-48.

Pearce, J.A., Baker, P.E., Harvey, P.K., and Luff, I.W. (1995) Geochemical evidence for subduction fluxes, mantle melting and fractional crystallization beneath the South Sandwich island arc. *Journal of Petrology*, 36, 1073– 1109.

Pearce, J.A., Stern, J.R., Bloomer, S.H., Fryer, P. (2005) Geochemical mapping of the Mariana arc–basin system: implications for the nature and distribution of subduction components. *Geochemistry, Geophysics, Geosystems 6, Q07006*. http://dx.doi.org/10.1029/2004GC000895.

Pearce, J.A., and Norry, M.J. (1979) Petrogenetic implications of Ti, Zr, Y and Nb variations in volcanic rocks. *Contributions to Mineralogy and Petrology*, 69, 33–47.

Pearce, J.A., and Peate, D.W. (1995) Tectonic implications of the composition of volcanic arc lavas. *Annual Review of Earth and Planetary Sciences*, 23, 251–285.

Portnyagin, M., Hoernle, K., Plechov, P., Mironov, N., and Khubunaya, S. (2007) Constraints on mantle melting and composition and nature of slab components in volcanic arcs from volatiles ($H_2O$, S, Cl, F) and trace elements in melt inclusions from the Kamchatka Arc. *Earth and Planetary Science Letters*, 255, 53–69.

Puffer, J.H. (2001) Contrasting high filed strength element content of continental flood basalts from plume versus reactivated-arc sources. *Geology*, 29, 675–678.

P'yankov, A. Y. (1981) Gosudarstvennaya geologicheskaya karta SSSR (National Geological map of USSR), 1:200,000 scale, Anyui-Chaun series, Sheet R-60 – XXI, XXII, MinGeo Russ., Magadan.

Rease, P. (1974) Al and Ti contents of hornblende, indicators of pressure and temperature of regional

metamorphism. *Contributions to Mineralogy and Petrology*, 45, 231 236.

Reichow, M.K., Pringle, M.S., Al'Mukhamedov, A.I., Allen, M.B., Andreichev, V.L., Buslov, M.M., Davies, C.E., Fedoseev, G.S., Fitton, J.G., Inger, S., Medvedev, A.Y., Mitchell, C., Puchkov, V.N., Safonova, I.Y., Scott, R.A., and Saunders, A.D. (2009). The timing and extent of the eruption of the Siberian Traps large igneous province: implications for the end-Permian environmental crisis. *Earth and Planetary Science Letters*, 277, 9–20.

Reichow, M.K., Saunders, A.D., White, R.V., Al'Mukhamedov, A.I., and Medvedev, A.Y. (2005). Geochemistry and petrogenesis of basalts from the West Siberian Basin: an extension of the PermoeTriassic Siberian Traps, Russia. *Lithos*, 79, 425–452.

Reichow, M.K., Saunders, A.D., White, R.V., Pringle, M.S., Al'mukhamedov, A.I., Medvedev, A.I., and Kirda, N.P. (2002). $^{40}Ar/^{39}Ar$ dates from the West Siberian Basin: Siberian flood basalt province doubled. *Science*, 296, 1846–1849.

Renne, P.R. (1995) Excess $^{40}Ar$ in biotite and hornblende from the Norilsk 1 intrusion, Siberia: implication for the age of Siberian Traps. *Earth and Planetary Science Letters*, 131, 165–176.

Ridolfi, F, Renzulli, A, Puerini, and M. (2010) Stability and chemical equilibrium of amphibole in calcalkaline magmas: an overview, new thermobarometric formulations and application to subduction-related volcanoes. *Contributions to Mineralogy and Petrology*, 160(1), 45–66.

Rollinson, H.R. (1993) Using geochemical data: evaluation, presentation, interpretation. Wiley 325p.

Romick, J. D., Kay, S. M. and Kay, R. W. (1992) The influence of amphibole fractionation on the evolution of calc-alkaline andesite and dacite tephra from the Central Aleutians, Alaska. *Contributions to Mineralogy and Petrology*, 112, 101-118

Rudnick, R. L. and Gao, S. (2003) Composition of the continental crust. In: Rudnick, R. L. (ed.) The Crust. Amsterdam: Elsevier, pp. 1–70.

Rudnick, R.L. (1995) Making continental crust. *Nature*, 378, 571–578.

Rutherford, M. J., and Devine, J. (1988) The May 18, 1980, eruption of Mount St. Helens 3. Stability and chemistry of amphibole in the magma chamber. *Journal of Geophysical Research*, 93(B10), 11949-11959.

Ryabchikov, I.D., Ntaflos, Th., Büchl, A., and Solovova, I.P. (2001) Subalkaline picrobasalts and plateau basalts from Putorana Plateau (Siberian CFB province). 1. Mineral compositions and geochemistry of major and trace elements. *Geokhimiya*, 5, 467–483.

Saunders, A.D., England, R.W., Reichow, M.K., and White, R.V. (2005) A mantle plume origin for the Siberian Traps: Uplift and extension in the West Siberian Basin. *Lithos*, 79, 407– 424.

Schiano, P., Eiler, J. M., Hutcheon, I. D. and Stolper, E. M. (2000) Primitive CaO-rich, silica-undersaturated melts in island arcs: evidence for the involvement of clinopyroxene-rich lithologies in the petrogenesis of arc magmas. *Geochemistry, Geophysics, Geosystems* 1, paper number 1999G000032.

Schmidt, M.W. (1992) Amphibole composition in tonalities as a function of pressure: An experimental calibration of the Al-in-hornblende barometer. *Contributions to Mineralogy and Petrology*, 110, 304–310.

Seslavinsky, K.B. (1979) The South Anyui Suture (Western Chukotka). *Doklady Akademii Nauk SSSR*, 249, 1181–1185 (in Russian).

Sharma, M., Basu, A. R., and Nesterenko, G. V., (1992) Temporal Sr-, Nd-, and Pb-isotopic variations in the Siberian flood basalts: Implications for the plume-source characteristics. *Earth and Planetary Science Letters*, 113, 365–381.

Sharma, M., Basu, A.R., and Nesterenko, G.V. (1991) Temporal Sr, Nd-, and Pb-isotopic variations in the Siberian flood basalts: Implications for the plume-source characteristics. *Earth and Planetary Science Letters*, 113, 365–381.

Shaw, D. M. (1970) Trace element fractionation during anatexis. *Geochimica et Cosmochimica Acta*, v. 34, n. 2, p. 237–243, http://dx.doi.org/10.1016/0016-7037(70)90009-8.

Smith, D.J. (2014) Clinopyroxene precursors to amphibole sponge in arc crust. Nature Communications, DOI: 10.1038/ncomms5329.

Sokolov, S.D., Bondarenko, G.Ye., Morozov, O.L., Shekhovtsov, V.A., Glotov, S.P., Ganelin, A.V., and Kravchenko-Berezhnoy, I.R. (2002) The South Anyui Suture, NE Arctic Russia: facts and problems to solve. In: Miller, E.L., Grantz, A., Klemperer, S.L. (Eds.), Tectonic Evolution of the Bering Shelf–Chukchi Sea–Arctic Margin and Adjacent Landmasses. *Geological Society of America, Special Paper*, 360, pp. 209–224.

Sokolov, S.D., Ledneva, G.V. and Pease, V.L. (2009) New data on the age and genesis of igneous rocks in the

Kolyuchinskaya Guba (Eastern Chukotka). Transactions (Doklady) of the Russian Academy of Sciences/Earth Science Section, 425A (3), 384–388.

Spear, F.S. (1981) An experimental study of hornblende stability and compositional variability in amphibolite. *American Journal of Science*, 281, 697–734.

Stolper, E., and Newman, S. (1994) The role of water in the petrogenesis of Mariana trough magmas. *Earth and Planetary Science Letters*, 121, 293– 325.

Sun, S.-s., and McDonough, W.F. (1989) Chemical and isotopic systematics of oceanic basalts: implications for mantle composition and processes. In: Saunders, A.D., Norry, M.J. (Eds.), Magmatism in the Ocean Basins. *Geological Society Special Publication*, No. 42, pp. 313–345.

Tamura, Y., Ishizuka, O., Stern, R. J., Nichols, A. R. L., Kawabata, H., Hirahara, Y., Chang, Q., Miyazaki, T., Kimura, J.-I., Embley, R. W., and Tatsumi, Y. (2014) Mission immiscible: distinct subduction components generate two primary magmas at Pagan volcano, Mariana arc. *Journal of Petrology*, 55, 63–101.

Taylor, S.R., and McLennan, S.M. (1995) The geochemical evolution of the continental crust. *Review of Geophysics*, 33, 241–265.

Thirlwall, M. F., Smith, T. E., Graham, A. M., Theodorou, N., Hollings, P., Davidson, J. P. and Arculus, R. J. (1994). High field strength anomalies in arc lavas: source or process? *Journal of Petrology*, 35, 819–838.

Tiepolo, M. (1999) Determinazione sperimentale dei coefficient di distribuzione solido/liquido in anfiboli di mantello: ruolo del controllo cristallochimico. PhD Thesis, Università di Pavia.

Tiepolo, M., Oberti, R., Zanetti, A., Vannucci, R., and Foley, S. (2007) Tracee element partitioning between Amphibole and Silicate Melt. *Reviews in Mineralogy and Geochemistry*, 67, 417–452.

Tikhomirov, P.L., Kalinina, E.A., Moriguti, T., Makishima, A., Kobayashi, K., Cherepanova, I.Yu., and Nakamura, E. (2012) The Cretaceous Okhotsk–Chukotka Volcanic Belt (NE Russia): Geology, geochronology, magma output rates, and implications on the genesis of silicic LIPs. *Journal of Volcanology and Geothermal Researc*h, 221, 14–32.

Til'man, S.M. and Sosunov, G.M. (1960) Some peculiarities of evolution of the Chukotka geosynclines in the Early Triassic. *Doklady Akademii Nauk SSSR*, 130(4), 834-837 (in Russian).

Tribuzio, R., Tiepolo, M., Vannucci, R. and Bottazzi, P. (1999) Trace element distribution within olivine-bearing gabbros from the Northern Apennine ophiolites (Italy): evidence for post-cumulus crystallization in MOR-type gabbroic rocks. *Contributions to Mineralogy and Petrology*, 134, 123–133.

Tuchkova, M.I., Sokolov, S. and Kravchenko-Berezhnoy, and I.R. (2009) Provenance analysis and tectonic setting of the Triassic clastic deposits in Western Chukotka, Northeast Russia. *Stephan Mueller Special Publication Series*, 4, 177–200.

Tuff, J., Takahasi, E., and Gibson, S.A. (2005) Experimental constraints on the role of garnet pyroxenite in the genesis of high-Fe mantle plume derived melts. *Journal of Petrology*, 46, 2023–2058.

Turner, S., Beier, C., Niu, Y., and Cook, C. (2011) U‐Th‐Ra disequilibria and the extent of off‐axis volcanism across the East Pacific Rise at 9°30′N, 10°30′N, and 11°20′N. *Geochemistry Geophysics*

*Geosystems*, 12, Q0AC12, doi:10.1029/2010GC003403.

Vatrushkina, E.V. and Tuchkova M.I. (2014) Peculiarities of lithology and geochemistry of the Raucha Formation (upper Jurassic, western Chukotka). Bulletin MOIP. *Geology Branch*, 89(1), 59–74 (in Russian).

Vernikovsky, V.A., Pease V.L., Vernikovskaya A.E., Romanov A.P., Gee D. and Travin, A.V. (2003) First report of early Triassic A-type granite and syenite intrusions from Taimyr: product of the northern Eurasian superplume? *Lithos*, 66(1–2), 23–36.

Walker, R.J., Morgan, J.W., Beary, E.S., Smoliar, M. I., Czamanske, G.K., and Horan, M. F. (1997) Application of $^{190}$Pt-$^{186}$Os isotope system to geochemistry and cosmochemistry. *Geochimica et Cosmochimica Acta*, 61, 4799–4807.

Watson, E.B. (1982) Basalt contamination by continental crust: some experiments and models. *Contributions to Mineralogy and Petrology*, 80, 73–87.

Wedepohl, K.H. (1995) The composition of the continental crust. *Geochimica et Cosmochimica Acta*, 59, 1217–1232.

Wei, X., Xu, Y.G., Feng, Y.X, and Zhao, J.X. (2014) Plume-lithosphere interaction in the generation of the Tarim large igneous province, NW China: geochronological and geochemical constraints. American Journal of Science, 314, 314-356.

Weyer, S., Munker, C., and Mezger, K. (2003) Nb/Ta, Zr/Hf and REE in the depleted mantle: implications for the differentiation history of the crust-mantle system. *Earth and Planetary Science Letters*, 205, 309–324.

Wilson, M. (2007) Igneous petrogenesis. *Springer*, 466 pp.

Winchester, J.A., and Floyd, P.A. (1977) Geochemical discrimination of different magma series and their differentiation products using immobile elements. *Chemical Geology*, 20, 325–343.

Wooden, J. L., Czamanske G. K., Bouse R. M., King B.-S. W., Knight R. J., and Siems D. F. (1993) Isotopic and trace-element constraints on mantle and crustal contributions to Siberian continental flood basalts, Noril'sk area, Siberia. *Geochimica et Cosmochimica Acta*, 57, 3677–3704.

Woodhead, J.D., Eggins, S., and Gamble, J. (1993) High field strength and transition element systematics in island arc and back-arc basin basalts: evidence for a multiphase melts extraction and a depleted mantle wedge. *Earth and Planetary Science Letters*, 144, 491–504.

Woodhead, J.D., Eggins, S.M., and Johnson, R.W. (1998) Magma genesis in the New Britain Island arc: further insights into melting and mass transfer processes. *Journal of Petrology*, 39, 1641–1668.

Zhao, J.H., and Zhou, M.F. (2007) Geochemistry of Neoproterozoic mafic intrusions in the Panzhihua district (Sichuan Province, SW China): Implications for subductionrelated metasomatism in the upper mantle. *Precambrian Research*, 152, 27–47.

# CAPTER 2

# Ferropicrite from the Lalibela area in the Ethiopian large igneous province

Minyahl Teferi DESTA[*], Dereje AYALEW[**], Akira ISHIWATARI [***],

Shoji ARAI [****] and Akihiro TAMURA [****]

[*]*Department of Earth Science, Graduate School of Science, Tohoku University, Aoba, Sendai 980-8578, Japan*

[**]*School of Earth Sciences, Addis Ababa University, P.O.Box 1176, Addis Ababa, Ethiopia*

[***]*Center for Northeast Asian Studies, Tohoku University, Kawauchi 41 Aoba-ku, Sendai 980-8576, Japan*

[****] *Department of Earth Sciences, Faculty of Science, Kanazawa University, Kanazawa 920-1192, Japan*

## 2.1 ABSTRACT

Ferropicrite (FeO*=14.0 wt. % and MgO=13.9 wt. %) and picritic ferrobasalt (FeO*=14.7 wt. % and MgO=10.8 wt. %) lava flows are found near Lalibela in the Oligocene (~30 Ma) Ethiopian large igneous province (LIP) in association with ultratitaniferous transitional basalt and picrites of the second high-Ti (HT2) series. The dominant phenocryst in the studied samples is Mg-rich olivine (up to $Fo_{88.9}$) with high CaO contents (to 0.42

wt. %) without any kink band structure, indicating that the olivines are crystallized from a magnesian melt. Spinel microphenocrysts and inclusions in olivine are characterized by extremely high Cr# (79-84), moderate Mg# (18-51), moderate $Fe^{3+}$# (11-39) and high $TiO_2$ (3.6-14.8 wt. %). The clinopyroxene phenocrysts are Mg#=74-88, $TiO_2$=0.84-1.82 wt. %, and $Al_2O_3$= 1.2-3.2 wt. % in the cores. The REE contents of clinopyroxenes display enrichment in LREE ($La_N/Yb_N$=1.2-1.9) and MREE ($Eu_N/Yb_N$=3.3-4.3) relative to HREE. Relative depletion of HFSE (e.g. Nb and Zr) is also observed. In general, these trace element characteristics of clinopyroxene are similar to those of the HT2 basalts. Some of the clinopyroxene crystals show strong reverse zoning with abrupt increase in Cr, Ni and Mg# from core to rim, which may be resulted from reaction of melt with mantle peridotite during magma ascent. Bulk rock chemistry of the studied samples exhibits very low $Al_2O_3/TiO_2$ (1.8-2.2) and high Zr/Y (8.2-10.2) ratios. These may indicate the important role for garnet during melting and that the lavas were formed by a small degree of partial melting which apparently contradicts to the high Cr# of spinel. In view of low Cr/Al ratio of the bulk rock, the high Cr# of spinel suggests very high temperature of the magma (and the mantle plume). The origin of these ferropicrite and picritic ferrobasalt could be attributed to high pressure partial melting of peridotite-eclogite (pyroxenite) mixture that possibly incorporated recycled oceanic crust components.

**Keywords**: Ferropicrite, Cr-spinel, large igneous province, Oligocene, Lalibela, eclogitic source

## 2.2. INTRODUCTION

Ferropicrites are subalkaline or mildly alkaline primitive rocks that were reported for the first time from the Paleoproterozoic Pechenga volcanic belt of the Kola Peninsula by Hanski and Smolkin (1989), who defined ferropicrite as an MgO rich volcanic rock with FeO* higher than 14 wt. %. Ferropicrites may have similar MgO contents to komatiites (~19 wt. %) but significantly higher $TiO_2$ contents (>1 wt. %) like meimechite (Le Bas, 2000). The geochemical characteristics of ferropicrites and meimechites indicates their derivation by lower degree of partial melting at higher pressure as compared to common continental flood basalt picrites that originate as more homogenized and voluminous melting at lower pressures (Gibson, 2002). For the last two decades, a number of ferropicritic whole-rock compositions have been reported from the Precambrian volcanic belts e.g. Slave and Superior Provinces (Goldstein and Francis, 2008; Francis et al., 1999) and from the Phanerozoic continental flood basalt provinces (CFB) (Siberian Traps, Karoo, Paraná-Etendeka, North Atlantic, Emeishan; Wooden et al., 1993; Gibson et al., 2000; Riley et al., 2005; Zhang et al., 2006). Ichiyama et al. (2006) reported ferropicritic; highly magnesian olivine cumulates from a Permian accreted oceanic plateau, southwestern Japan.

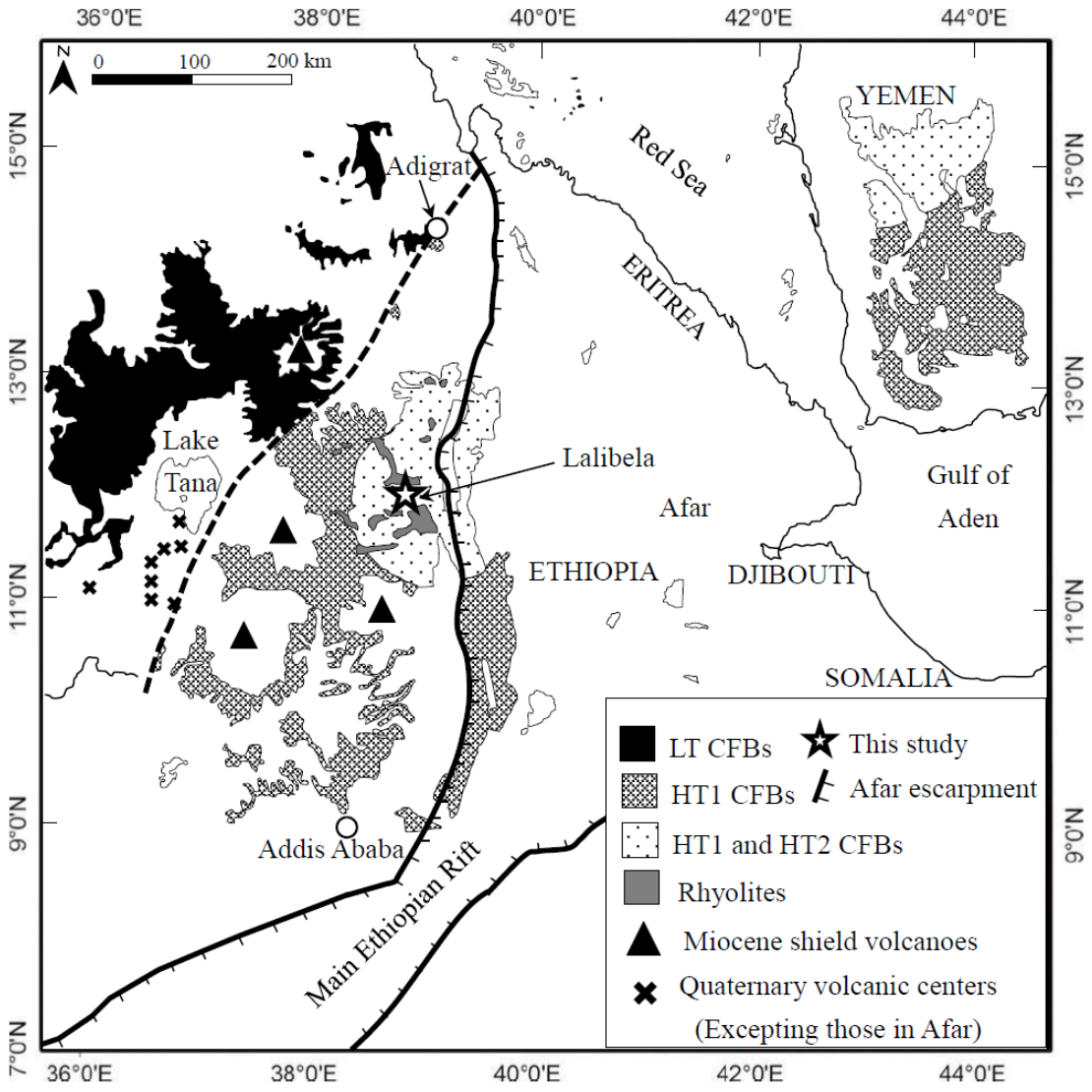


**Figure 2.1:** Sketch map of the Ethiopian large igneous province (LIP) including the Yemen conjugate margin, modified after Beccaluva et al. (2009) and Natali et al. (2011). Oligocene (~30 Ma) volcanic rocks: LT, Low-Ti tholeiitic basalts; HT1, High-Ti tholeiitic basalts; HT2, very High-Ti transitional basalts and picrites. Location of ferropicrite from the Dilb road section reported in this study is indicated by star. Miocene to Quaternary volcanic rocks in the Main Ethiopian Rift (MER), are not shown. CFB: Continental flood basalt.

Recently, several petrogenetic models are provided for the origin of ferropicrite. Gibson (2002) describes the significance of recycled oceanic crust as a "re-fertilizer" of peridotite in the starting mantle plume head. Ichiyama et al. (2006) and Tuff et al. (2005) also suggested analogous models with recycled eclogitic or

pyroxenitic mantle source, respectively. On the basis of silicate liquid immiscibility study, Jakobsen et al. (2005) interpreted that ferropicrites could also form by mixing of evolved, immiscible Fe-rich liquid with picritic mantle melts. More recently, Sobolev et al. (2007) described that iron-rich source regions in the mantle can be produced by pyroxenite veining. Generally, ferropicrites are attributed to anomalously hot mantle sources and mantle plumes (Hanski and Smolkin, 1995; Goldstein and Francis, 2008).

Picritic lavas from Ethiopian LIP are representative of the second high-Ti (HT2) series, as described by Pik et al. (1998) and Beccaluva et al. (2009) and are overlain by rhyolitic ignimbrite of 30 Ma age (Hofmann et al., 1997). In previous literatures the occurrence of Fe-rich picrite in Ethiopian large igneous province (LIP) has been unrecognized.

In this study, we report the results of the mineral chemistry and whole rock geochemistry of ferropicrite (Sample 1) and picritic ferrobasalt (Samples 2 and 3) rocks from the eastern part of Ethiopian large igneous province in order to obtain insight into the characteristics of their mantle source. Ferropicrite and picritic ferrobasalt samples were obtained from the Dilb road section of the Lalibela area, eastern portion of Ethiopian LIP (Fig. 2.1).

## 2.3. GEOLOGICAL SETTING

The Oligocene Ethiopian LIP represents one of the youngest, best exposed sequences of mafic and felsic volcanic rocks, associated with incipient lithospheric breakup (extensional tectonics) and plume impingement

(Marty et al., 1996). It is dissected by the Main Ethiopian Rift (MER)-Red Sea-Gulf of Aden rift system (with the Afar R-R-R-triple junction), which indicates the close association of magmatism and lithospheric extension and hence satisfy the plume theory. In addition, the tectonomagmatic and geophysical studies shows that the existence of deep mantle plume (Ritsema et al., 1999; Courtillot et al., 2003). The present remnants of Ethiopian flood volcanism cover an area of at least $6\times10^6$ $km^2$ and have a total volume of about ~$3.5\times10^5$ $km^3$ (Mohr & Zanettin, 1988). Rochette et al. (1998) estimated as the original volume reached up to $10^6$ $km^3$. This voluminous basaltic magmatism was emplaced in a rather short time interval ~30±1 Ma (Hofmann et al., 1997) and successively followed by a number of huge shield volcanoes (Piccirillo et al., 1979). These shield volcanoes are a conspicuous feature of the Ethiopian LIP and distinguish it from other LIPs, such as Deccan and Karoo (Kieffer et al., 2004) and Siberia. The ferropicrite and picritic ferrobasalt of this study is considered as a part of the main flood basalt volcanism (~30 Ma). Ayalew et al. (2002) and Ayalew and Ishiwatari (2011) described the presence of significant volume of rhyolite (up to 20 %) with a maximum thickness of ca. 500 m mostly on the upper part of the Ethiopian continental flood basalt sequence. The final phase of volcanism (i.e. Pliocene to present) mostly concentrated along the Main Ethiopian Rift and Afar region. However, volumetrically small volcanic rocks as old as 45-40 Ma are found in southern and south-western Ethiopia (George et al., 1998). All the Ethiopian plateau rocks rest either directly over the Neoprotrozoic crystalline basement or over the Mesozoic sedimentary sequences. According to Pik et al. (1998) and Beccaluva et al. (2009), the Northern Ethiopian plateau basalts are classified into three magma types based on their $TiO_2$ content (Fig.2.1): Low-Ti tholeiites

(LT) distributed in the northwestern areas; the first high-Ti lavas (HT1) in the eastern areas and ultratitaniferous transitional basalt and picrites of the second high-Ti (HT2) series, which are concentrated in the Lalibela area close to the Afar depression. The lava piles in the Lalibela area reaches up to ~1800 m thick, consisting of basaltic and picritic units capped by rhyolitic ignimbrite. The HT2 picrites are geographically localized in the high-Ti sub-province and the ferropicrite and picritic ferrobasalt rocks occur associated with HT2 basalt and picrite series. Ferropicrites constitute volumetrically minor parts of Ethiopian LIP and they typically form thin flows at or near the base of thick lava piles in the Lalibela area.

**2.4. ANALYTICAL METHODS**

The major element analysis of the constituent minerals of these samples was determined by electron probe micro analyser (EPMA) using energy dispersive X-ray spectrometer Oxford Link ISIS equipped on the JEOL JSM-5410 Scanning electron microscope (SEM) at the Earth Science department laboratory of Tohoku University, Japan. The operating conditions were at 15 kV acceleration voltage and a beam current of 1 nA. A number of natural standards were applied for calibration, and the data were corrected with ZAF quantitative procedure. Major and some trace elements for the whole-rock analyses (such as V, Cr, Ni, Rb, Sr, Ba, Y, Zr, Nb) were carried out by X-ray fluorescence spectrometer (XRF-RIX 2100) at the aforementioned department, Tohoku University. Three glass beads were prepared by using fusion procedure, which consists of heating a 1:5 mixture of sample and flux ($Li_2B_4O_7$) at ~1050 ℃. The Loss on Ignition (LOI) is determined by weighing a 1

gram of rock powder before and after ignition at 750 ℃ for 6 hours. Trace element concentrations of clinopyroxene in ferropicrite and picritic ferrobasalts were determined by a laser ablation (193 nm ArF excimer: MicroLas GeoLas Q-plus)-inductively coupled plasma spectrometer Agilent 7500S (LA-ICP-MS) at Kanazawa University (Ishida et al., 2004). The analysis was conducted by ablating spot of 50-60 μm in diameter at laser power of 8 J/cm$^2$. NIST SRM 612 glass was used as a standard. The trace element concentration of NIST SRM 612 was selected from Pearce et al. (1997). $^{29}$Si was used as internal standard for pyroxene, with concentration of $SiO_2$ determined by EPMA.

**Table 2.1:** Whole rock chemistry of the ferropicrite and picritic ferrobasalts from the Lalibela area, Ethiopian LIP.

| Rock | Ferropicrite | Picritic ferrobasalts | |
|---|---|---|---|
| Sample | 1 | 2 | 3 |
| Major elements (wt. %) | | | |
| $SiO_2$ | 45.82 | 43.04 | 44.03 |
| $TiO_2$ | 3.84 | 4.74 | 5.04 |
| $Al_2O_3$ | 8.58 | 8.65 | 9.23 |
| FeO* | 14.00 | 14.50 | 14.70 |
| CaO | 10.00 | 9.87 | 10.63 |
| MgO | 13.92 | 10.05 | 10.81 |
| MnO | 0.18 | 0.18 | 0.18 |
| $K_2O$ | 0.76 | 0.90 | 0.76 |
| $Na_2O$ | 1.82 | 1.89 | 2.02 |
| $P_2O_5$ | 0.35 | 0.62 | 0.58 |
| Total | 99.27 | 94.44 | 97.98 |
| LOI | -0.01 | 1.58 | 0.10 |
| Mg# | 63.9 | 55.3 | 56.7 |
| Trace elements (ppm) | | | |
| V | 407 | 463 | 490 |
| Cr | 195 | 40.8 | 18.2 |
| Ni | 501 | 389 | 356 |
| Rb | 16.1 | 20.3 | 9.6 |
| Sr | 415 | 503 | 567 |
| Ba | 210 | 268 | 282 |
| Y | 34.4 | 38.9 | 37.2 |
| Zr | 283 | 359 | 378 |
| Nb | 23.6 | 31.0 | 31.9 |

*Total iron as FeO. Mg# (=Mg/Mg+ $Fe_{Total}$)$\times$100; LOI = Loss on ignition.

## 2.5. WHOLE ROCK CHEMISTRY

### 2.5.1. Major and trace elements

Table 2.1 shows whole-rock analyses of the ferropicrite and picritic ferrobasalt from the Lalibela area. The studied samples are characterized by high $TiO_2$ (3.8-5.1 wt. %) and FeO* (total Fe as FeO) (14.0-14.7 wt. %) (Fig. 2.2). The FeO* content is within the range of ferropicrites of other LIPs (Superior Province, Pechenga, Siberia, Paraná-Etendeka and Japan). The Fe/Mn ratios of the bulk rock range from 78 to 82, which is higher than those reported for the Ethiopian picritic lava (70-76; Rogers et al., 2010). The Ni/Cr ratio is also high (0.4 in ferropicrite). The MgO content ranges from 10.5 to 13.8 wt. % and Sample 1 satisfies the definition of picrite (> 12 wt. % MgO) (Le Bas, 2000). A general decrease of Ni (500 to 350 ppm) with decreasing Mg# (64 to 56) implies removal of olivine through evolution from ferropicritic to ferro-basaltic composition. They show enrichment of high field strength elements (HFSE), e.g. $P_2O_5$ (0.35-0.64 wt. %), Nb (24-32 ppm), Y (34-39 ppm) and $TiO_2$ (3.8-5.1 wt. %) and their increase with decreasing MgO (Figs. 2.2 and 2.3). They are further characterized by very high V (407-490 ppm) content. The content of Zr (283-378 ppm) in the Ethiopian ferropicrite is very high and is comparable to that of Siberian ferropicrite, but the latter is characterized by higher Nb/Y ratio. Figure 2.4 shows the variations of $Al_2O_3/TiO_2$ with respect to Zr/Y ratios for the ferropicrite and picritic ferrobasalt. In comparison with other ferropicrites (Superior Province, Pechenga, Paraná-Etendeka and Japan) the Ethiopian ferropicrite and picritic ferrobasalt exhibit low $Al_2O_3/TiO_2$ ratio close to Siberian ferropicrite (~2.2) and are similar to HT2 basalt and picrite (Beccaluva et al., 2009).

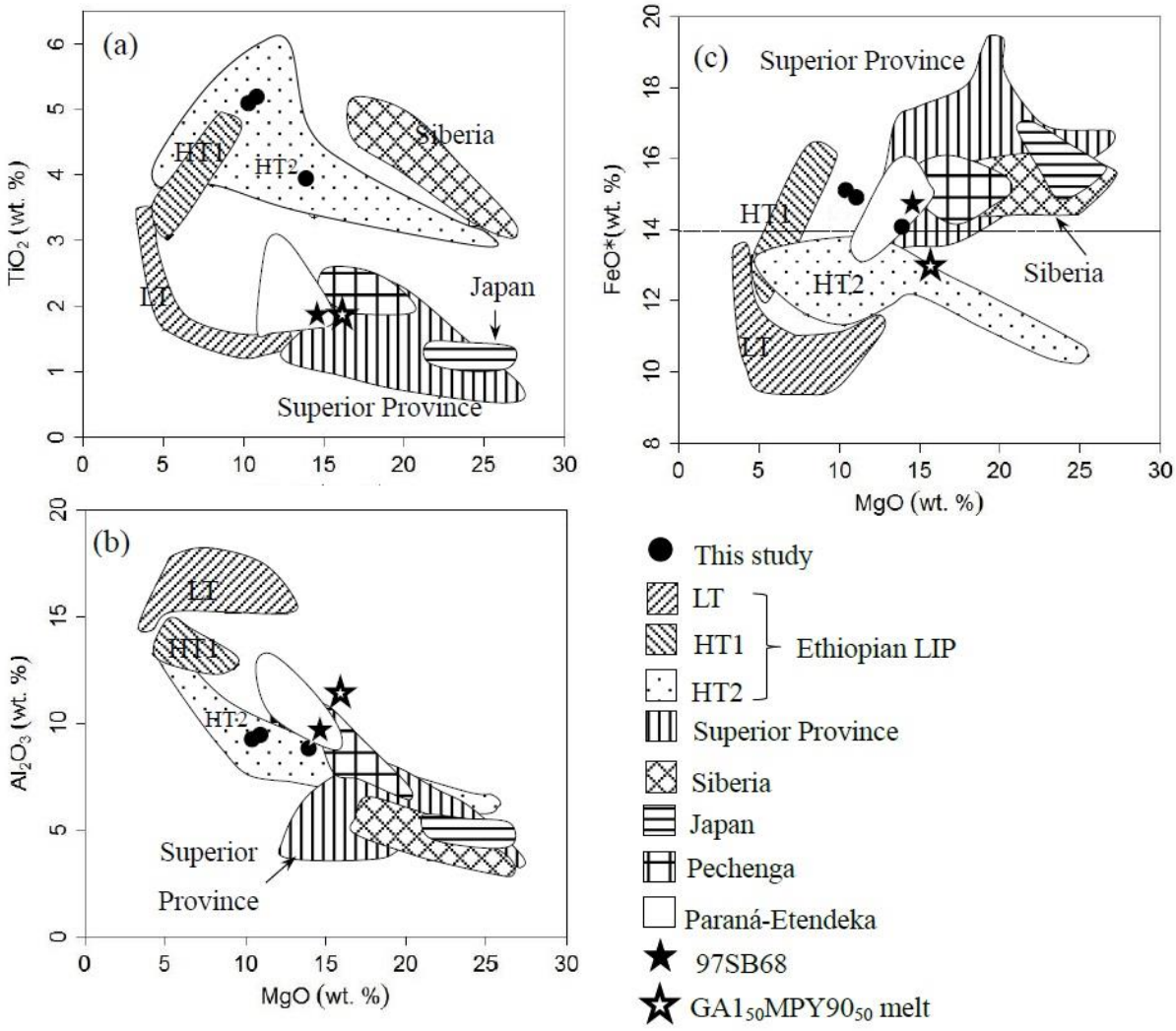


**Figure 2.2:** Major element variations with respect to MgO of the ferropicrite and picritic ferrobasalt rocks. For comparison, Ethiopian LIP (LT, low-Ti basalt; HT1, high-Ti 1 basalt; HT2, high-Ti 2 basalt and picrite; Beccaluva et al., 2009), ferropicrites from Superior Province (Goldstein and Francis, 2008), Pechenga (Hanski and Smolkin, 1995), Siberia (Arndt et al., 1995), Paraná-Etendeka (Gibson et al., 2000), Japan (Ichiyama et al., 2006), the composition of a picritic melt produced from $GA1_{50}MPY90_{50}$ at 3.5 GPa (Yaxley & Green, 1998) and 97SB68 starting composition of Tuff et al. (2005) experiment.

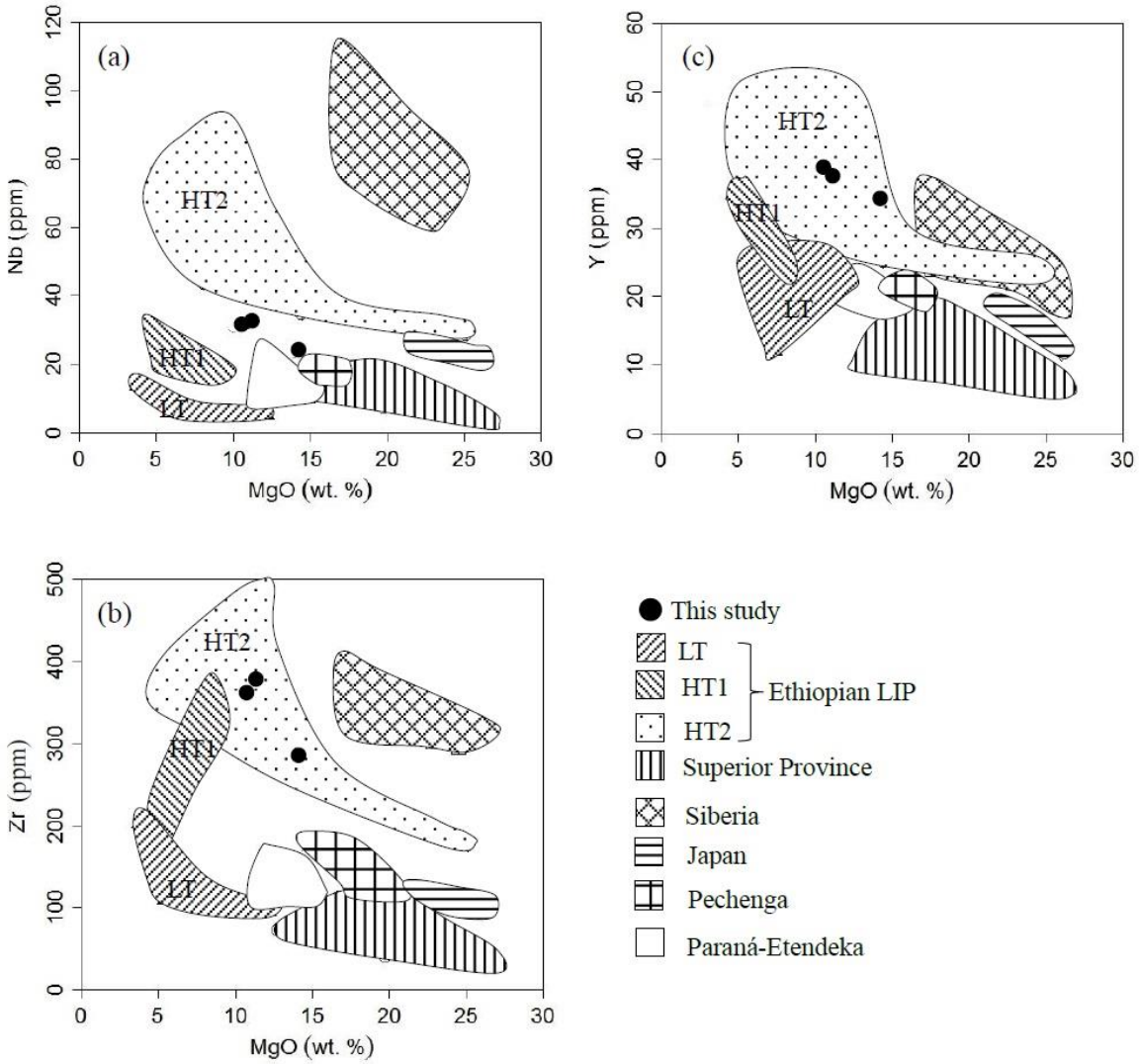


**Figure 2.3:** Trace element variation with respect to MgO of Ethiopian ferropicrite and picritic ferrobasalt. Symbols and data sources are as in figure 2.2.

According to the Pik et al. (1998) classification of the Ethiopian LIP based on Ti/Y ratio, the studied samples falls in the HT1 compositional field (not shown). The high FeO* content of these samples are similar to the first high-Ti basalts (HT1) of Adigrat area (Beccaluva et al., 2009). However, the latter is characterized by lower MgO (< 10 wt. %), $CaO/Al_2O_3$ (~ 0.5) and Ni (≤ 110 ppm), supporting HT2 affiliation of our samples.

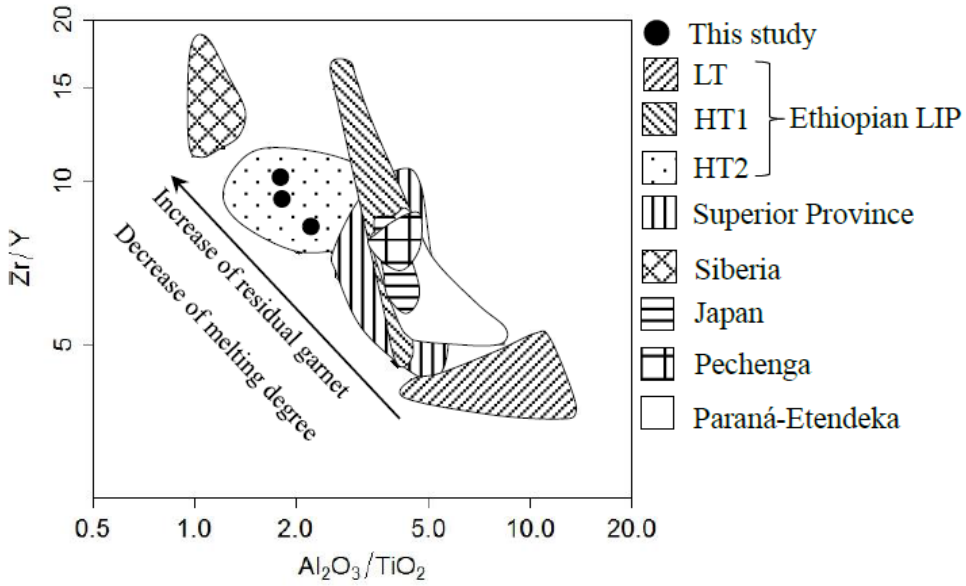


**Figure 2.4:** Bulk-rock $Al_2O_3/TiO_2$ vs Zr/Y plot for the Ethiopian ferropicrite and picritic ferrobasalt. Data sources are as in fig. 2.2. The arrow assumes a single peridotitic source.

## 2.6. PETROGRAPHY AND MINERAL CHEMISTRY

### 2.6.1. Petrography

Ferropicrite and picritic ferrobasalts examined in this study shows porphyritic texture with phenocryst phases of olivine (15-30 vol. %) and augitic clinopyroxene (10-25 vol. %) (Fig.2.5). Minor plagioclase microphenocrysts occur in one of the studied samples. Chrome-spinels are included in olivine and rarely occur as microphenocrysts set in the groundmass, which comprises a mixture of plagioclase, clinopyroxene, and ilmenite. Olivine phenocrysts typically show hexagonal euhedral shape (Fig. 2.5a, b) with irregular cracks and slight iddingsite alteration along the cracks. Some of the faces on olivine crystal are curved and embayed. Smaller olivines (~2 mm) are generally rounded and exhibit a rim of distinctive red tarnish of iddingsite formed by

oxidation of olivine. Some olivine crystals are completely replaced by iddingsite. Deformed, kink-banded crystals are absent. Clinopyroxenes occur as euhedral, elongated pinkish phenocrysts (<4 mm) which are partially embayed and resorbed (Fig. 2.5c and d). In places, olivine and clinopyroxene occur together as glomerocrysts up to 7 mm in size in which olivines appear to be interstitial between clinopyroxenes. Ilmenites (up to 0.2 mm) are also included in some clinopyroxene phynocrysts. Representative compositions of the main mineral phases are shown in Tables 2.2-2.5.

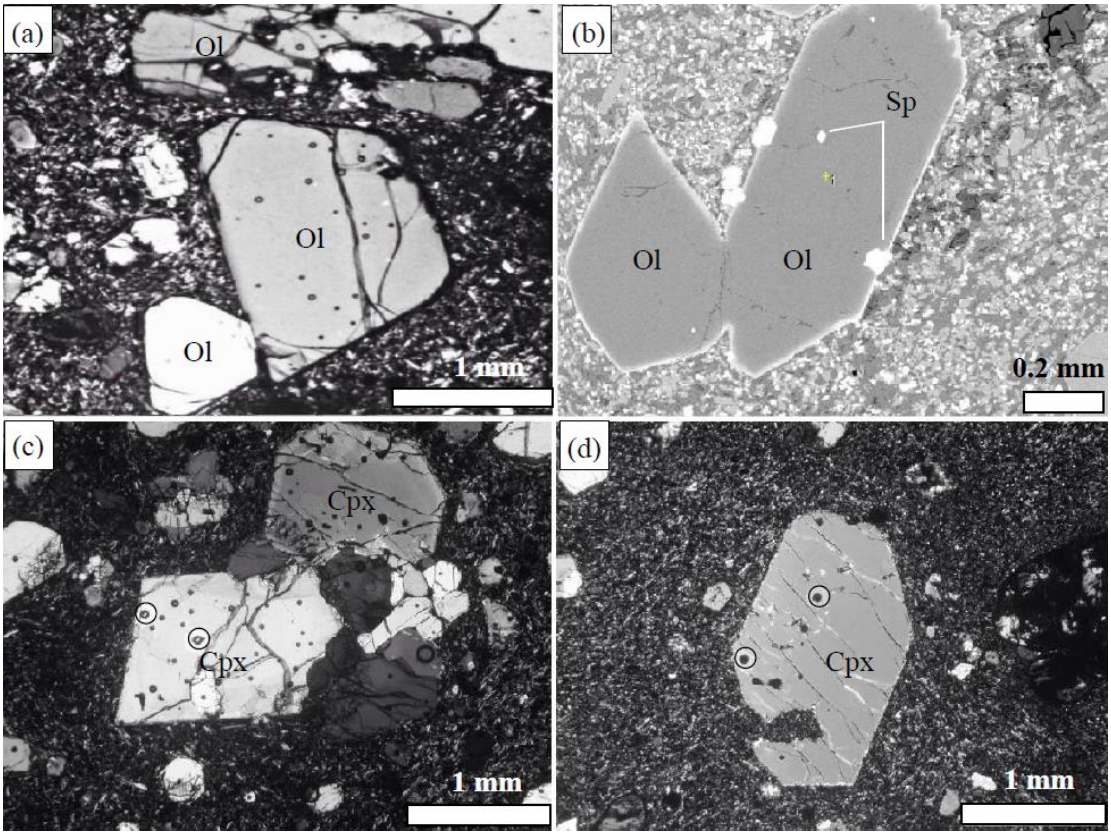


**Figure 2.5:** Photomicrographs of Ethiopian ferropicrite and picritic ferrobasalt. (a) Crossed polarized light showing porphyritic texture with abundant magnesian olivine phenocrysts. (b) Back-scattered electron images of olivine phenocrysts and spinel inclusions. Subhedral to euhedral olivine phenocrysts are set in a microcrystalline groundmass. (c) Crossed polarized light images of clinopyroxene with reverse zoning, Cpx3 of Sample 1 and (d) that with resorbed texture, Cpx1 of Sample 2. Small circles in the clinopyroxene phenocrysts show ICP-MS analytical points (Table 2.5). Ol, olivine; Cpx, clinopyroxene; Sp, spinel.

**Table 2.2:** Representative analyses of olivine phenocrysts in ferropicrite and picritic ferrobasalt rocks from Lalibela area, Ethiopian LIP

| Sample | Ferropicrite | | | | | | | | Picritic ferrobasalt 1 | | | | | | |
|---|---|---|---|---|---|---|---|---|---|---|---|---|---|---|---|
| Mineral | Ol1 | Ol2 | | Ol3 | | Ol4 | Ol5 | Ol6 | Ol1 | Ol3 | | Ol4 | | Ol5 | |
| | Core | core | Rim | core | rim | core | core | core | Core | core | rim | core | rim | core | rim |
| $SiO_2$ | 39.03 | 41.68 | 40.00 | 40.94 | 39.08 | 40.48 | 40.03 | 41.80 | 41.17 | 42.12 | 40.73 | 41.01 | 40.44 | 40.44 | 41.08 |
| FeO* | 19.48 | 12.39 | 16.33 | 11.41 | 18.59 | 11.19 | 17.27 | 10.82 | 14.80 | 10.63 | 11.91 | 10.52 | 12.75 | 13.19 | 13.83 |
| MnO | 0.24 | 0.16 | 0.26 | 0.20 | 0.30 | 0.18 | 0.14 | 0.18 | 0.16 | 0.18 | 0.18 | 0.14 | 0.22 | 0.19 | 0.14 |
| MgO | 39.35 | 46.96 | 42.32 | 46.55 | 40.28 | 46.00 | 42.09 | 48.24 | 45.17 | 48.00 | 46.19 | 47.18 | 44.90 | 44.86 | 45.33 |
| CaO | 0.29 | 0.34 | 0.32 | 0.42 | 0.34 | 0.37 | 0.29 | 0.32 | 0.37 | 0.31 | 0.31 | 0.28 | 0.31 | 0.30 | 0.30 |
| NiO | 0.27 | 0.22 | 0.25 | 0.25 | 0.39 | 0.27 | 0.26 | 0.11 | 0.34 | 0.30 | 0.44 | 0.30 | 0.30 | 0.25 | 0.40 |
| Total | 98.66 | 101.75 | 99.48 | 99.77 | 98.98 | 98.49 | 100.08 | 101.47 | 102.01 | 101.54 | 99.76 | 99.43 | 98.92 | 99.23 | 101.08 |
| Cations (O=4) | | | | | | | | | | | | | | | |
| Si | 1.016 | 1.015 | 1.016 | 1.014 | 1.012 | 1.015 | 1.015 | 1.013 | 1.011 | 1.018 | 1.011 | 1.014 | 1.016 | 1.015 | 1.014 |
| $Fe^{2+}$ | 0.424 | 0.252 | 0.347 | 0.236 | 0.403 | 0.235 | 0.366 | 0.219 | 0.304 | 0.215 | 0.247 | 0.218 | 0.268 | 0.277 | 0.286 |
| Mn | 0.005 | 0.003 | 0.006 | 0.004 | 0.007 | 0.004 | 0.003 | 0.004 | 0.003 | 0.004 | 0.004 | 0.003 | 0.005 | 0.004 | 0.003 |
| Mg | 1.526 | 1.704 | 1.602 | 1.718 | 1.554 | 1.719 | 1.590 | 1.743 | 1.654 | 1.730 | 1.709 | 1.738 | 1.682 | 1.678 | 1.668 |
| Ca | 0.008 | 0.009 | 0.009 | 0.011 | 0.009 | 0.010 | 0.008 | 0.008 | 0.010 | 0.008 | 0.008 | 0.007 | 0.008 | 0.008 | 0.008 |
| Total | 2.984 | 2.986 | 2.984 | 2.983 | 2.985 | 2.983 | 2.982 | 2.987 | 2.982 | 2.981 | 2.989 | 2.980 | 2.979 | 2.986 | 2.986 |
| Fo | 77.73 | 86.57 | 81.61 | 87.23 | 78.79 | 87.38 | 80.84 | 88.28 | 83.91 | 88.42 | 86.83 | 88.41 | 85.69 | 85.31 | 84.91 |

*Total Fe as FeO.

**Table 2.2:** Continued

| Sample | Picritic ferrobasalt 2 | | | | | |
|---|---|---|---|---|---|---|
| Mineral | Ol2 | Ol3 | | Ol5 | Ol6 | |
| | Core | Core | Rim | Core | Core | Rim |
| $SiO_2$ | 40.04 | 40.51 | 40.96 | 39.92 | 39.29 | 40.97 |
| FeO* | 14.40 | 14.69 | 14.52 | 13.23 | 16.48 | 17.26 |
| MnO | 0.11 | 0.23 | 0.24 | 0.19 | 0.23 | 0.24 |
| MgO | 43.74 | 43.82 | 44.32 | 43.59 | 40.87 | 42.70 |
| CaO | 0.40 | 0.37 | 0.36 | 0.33 | 0.37 | 0.36 |
| NiO | 0.31 | 0.29 | 0.45 | 0.29 | 0.28 | 0.21 |
| Total | 99.00 | 99.91 | 100.85 | 97.55 | 97.52 | 101.74 |
| Cations (O=4) | | | | | | |
| Si | 1.014 | 1.018 | 1.017 | 1.020 | 1.020 | 1.019 |
| $Fe^{2+}$ | 0.305 | 0.309 | 0.301 | 0.283 | 0.358 | 0.359 |
| Mn | n.d. | 0.005 | 0.005 | 0.004 | 0.005 | 0.005 |
| Mg | 1.651 | 1.641 | 1.640 | 1.659 | 1.582 | 1.583 |
| Ca | 0.011 | 0.010 | 0.010 | 0.009 | 0.010 | 0.010 |
| Total | 2.981 | 2.983 | 2.983 | 2.980 | 2.980 | 2.981 |
| Fo | 83.84 | 83.53 | 83.84 | 84.88 | 80.91 | 80.91 |

### 2.6.2. Mineral chemistry

#### 2.6.2.1. Olivine

Olivine phynocrysts in the studied samples are homogenous and show a narrow compositional range ($Fo_{78-88}$), which corresponds to the previously reported values from HT2 basalts and picrites ($Fo_{77-90}$, Beccaluva et al., 2009). The Fo content of olivines from the Ethiopian ferropicrite and picritic ferrobasalt fall within the range of those in Archean and Phanerozoic ferropicrites ($Fo_{83-84}$ in Pechenga complex, Hanski and Smolkin, 1995; $Fo_{85-88}$ in Emeishan/Lijiang, Zhang et al., 2006). Generally, the largest olivines are the most magneisan, whereas smaller crystals are relatively Fe-rich. NiO in the Fo-rich olivine cores reaches 0.3 wt. % (Fig. 2.6).

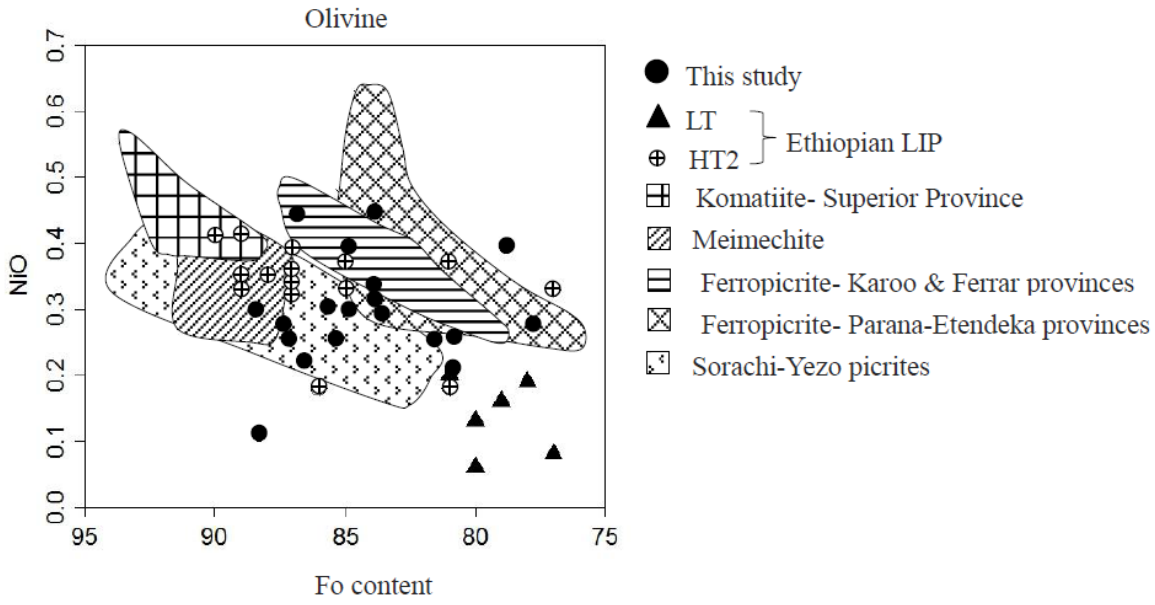


**Figure 2.6:** Fo content vs NiO (wt. %) for olivines in ferropicrite and picritic ferrobasalt rocks from Ethiopian LIP. Those of the komatiites from Superior Province (Arndt et al., 1977); meimechite from Siberian traps (Elkins-Tanton et al., 2007), ferropicrites from Karoo & Ferrar provinces (Heinonen and Luttinen, 2008), Paraná-Etendeka provinces (Gibson et al., 2000) and picrites from Sorachi-Yezo (Ichiyama et al., 2012). The composition of olivines from the LT (low-Ti) and HT2 (high-Ti 2 basalt and picrites) of Ethiopian LIP (Beccaluva et al., 2009) are also shown for comparison.

The CaO contents range from 0.28 to 0.42 wt. %, indicating that they are not mantle xenocrysts (Simkin and Smith, 1970; Gurenko et al., 1996; Thompson and Gibson, 2000; Kawabata et al., 2011) and MnO contents vary between 0.14 and 0.24 wt. %.

#### 2.6.2.2. Cr-spinel

The Cr-spinels are characterized by extremely high Cr# (100Cr/ (Cr+Al)) (up to 84), moderate Mg# (100Mg/ ($Mg+Fe^{2+}$)) (18-51) and moderate $Fe^{3+}$# (100$Fe^{3+}$/ ($Cr+Al+Fe^{3+}$)) (11-39) (Table 2.3). The $Cr_2O_3$ content varies from 14 to 49 wt. %. The $TiO_2$ contents of Cr-spinels are very high (3.6-14.8 wt. %) as compared to Cr-spinels in meimechite and depleted ferropicrites from Vestfjella (Heinonen and Luttinen, 2010). The Cr# of Cr-spinels from these ferropicrite and picritic ferrobasalt is as high as those in boninite and is distinctly higher than Cr-spinels in abyssal peridotites (Dick and Bullen, 1984), MORB (Sigurdsson and Schilling, 1976), picritic basalts (e.g. West Greenland; Larsen and Pedersen, 2000, Emeishan; Kamenetsky et al., 2012, Iceland; Sigurdsson et al., 2000, Sorachi-Yezo; Ichiyama et al., 2012) and ferropicrites from Pechenga (Hanski, 1992) and accreted oceanic plateau in Japan (Mino-Tamba belt; Ichiyama et al., 2006), (Figs. 2.7a and b). Figure 2.8 shows the relationship between Cr-spinel and bulk rock in their Cr/Al ratios of the studied samples and other related rocks. The high Cr/Al of the Cr-spinels and very low Cr/Al of the host rock is unique feature of the studied Ethiopian ferropicritic rocks.

**Table 2.3:** Representative analyses of spinel inclusions in olivine phenocrysts.

| Sample | Ferropicrite | | Picritic ferrobasalt 1 | | | | Picritic ferrobasalt 2 | |
|---|---|---|---|---|---|---|---|---|
| Mineral | Spl1(ol1) | Spl4(ol3) | Spl1(ol1) | Spl2(ol3) | Spl3(ol4) | Spl5 gm | Spl2 (ol2) | Spl5 (ol5) |
| $TiO_2$ | 14.81 | 9.60 | 6.22 | 3.81 | 3.60 | 3.75 | 7.08 | 5.99 |
| $Al_2O_3$ | 8.02 | 5.52 | 5.85 | 6.85 | 6.44 | 5.90 | 6.12 | 4.74 |
| $Cr_2O_3$ | 13.97 | 38.50 | 37.38 | 48.93 | 47.31 | 43.21 | 34.44 | 37.85 |
| FeO* | 51.77 | 32.61 | 39.39 | 30.74 | 30.62 | 39.50 | 39.07 | 43.86 |
| MnO | 0.34 | 0.24 | 0.16 | 0.19 | 0.17 | 0.32 | 0.16 | 0.26 |
| MgO | 5.80 | 9.47 | 9.18 | 7.79 | 11.08 | 3.74 | 8.27 | 4.86 |
| Total | 94.71 | 95.94 | 98.18 | 98.31 | 99.22 | 96.42 | 95.14 | 97.56 |
| Cations (O=4) | | | | | | | | |
| Ti | 0.398 | 0.253 | 0.160 | 0.099 | 0.090 | 0.102 | 0.188 | 0.161 |
| Al | 0.338 | 0.228 | 0.235 | 0.278 | 0.253 | 0.252 | 0.255 | 0.199 |
| Cr | 0.395 | 1.065 | 1.009 | 1.332 | 1.247 | 1.238 | 0.962 | 1.067 |
| $Fe^{3+}$ | 0.470 | 0.202 | 0.437 | 0.192 | 0.319 | 0.306 | 0.407 | 0.413 |
| $Fe^{2+}$ | 1.079 | 0.752 | 0.688 | 0.693 | 0.535 | 0.890 | 0.748 | 0.894 |
| Mn | 0.010 | 0.007 | 0.005 | 0.006 | 0.005 | 0.010 | 0.005 | 0.008 |
| Mg | 0.309 | 0.494 | 0.467 | 0.400 | 0.551 | 0.202 | 0.436 | 0.258 |
| Total | 2.999 | 3.001 | 3.001 | 3.000 | 3.000 | 3.000 | 3.001 | 3.000 |
| Cr# | 53.89 | 82.39 | 81.08 | 82.73 | 83.13 | 83.09 | 79.06 | 84.27 |
| Mg# | 22.28 | 39.65 | 40.44 | 36.59 | 50.74 | 18.49 | 36.81 | 22.40 |
| $Fe^{3+}$# | 39.06 | 13.54 | 25.97 | 10.66 | 17.54 | 17.05 | 25.05 | 24.60 |

*Total Fe as FeO; Cr#=100Cr/(Cr+Al); Mg#=100Mg/(Mg+$Fe^{2+}$); $Fe^{3+}$#=100$Fe^{3+}$/(Cr+Al+$Fe^{3+}$).

Abbreviations: n.d. not detected; Spl, spinel; Ol, olivine; Gm, groundmass.

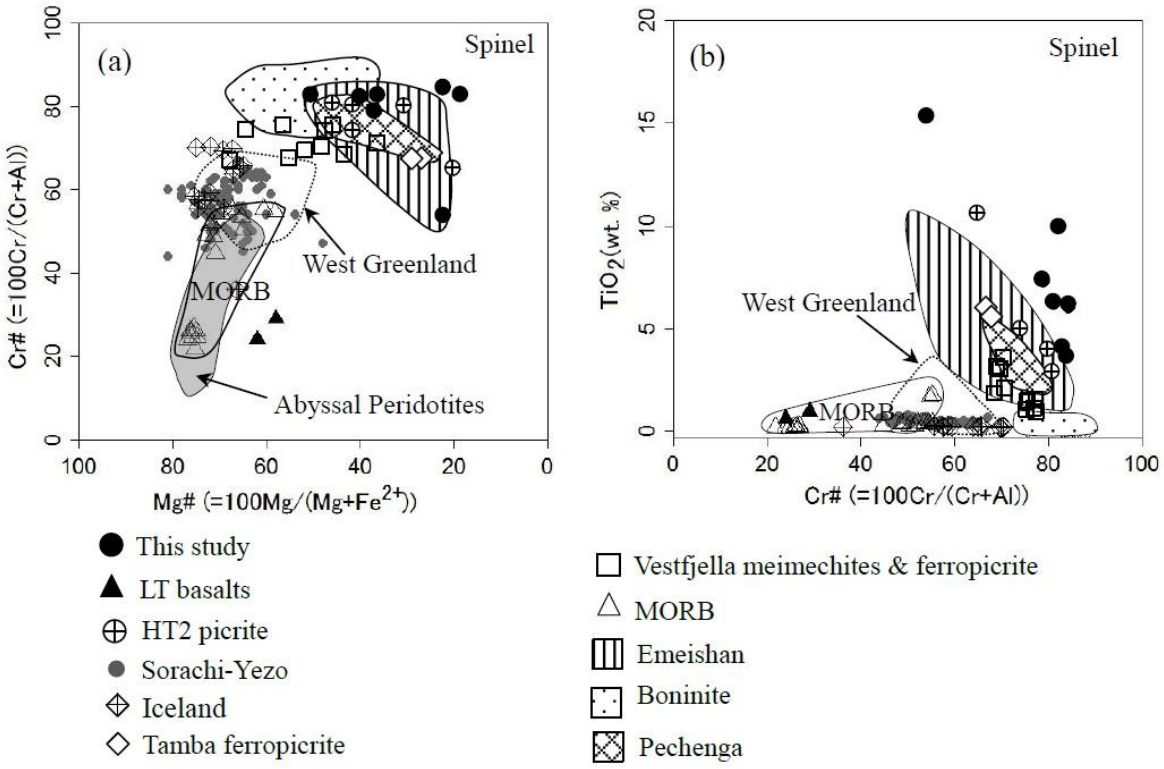


**Figure 2.7:** Cr-spinel composition of the Ethiopian ferropicrite and low-Ti basalt and HT2 picrites (Beccaluva et al., 2009). Those of the picrites from Sorachi-Yezo (Ichiyama et al., 2012), Iceland (Sigurdsson et al., 2000), Tamba belt (Ichiyama et al., 2006), Emeishan (Kamenetsky et al., 2012), West Greenland (Larsen and Pedersen, 2000), Vestfjella meimechites and ferropicrite (Heinonen and Luttinen, 2010) and the ferropicrites from Pechenga (Hanski, 1992). The composition of MORB (Sigurdsson and Schilling, 1976), abyssal peridotites (Dick and Bullen, 1984) and boninite are also taken for comparison.

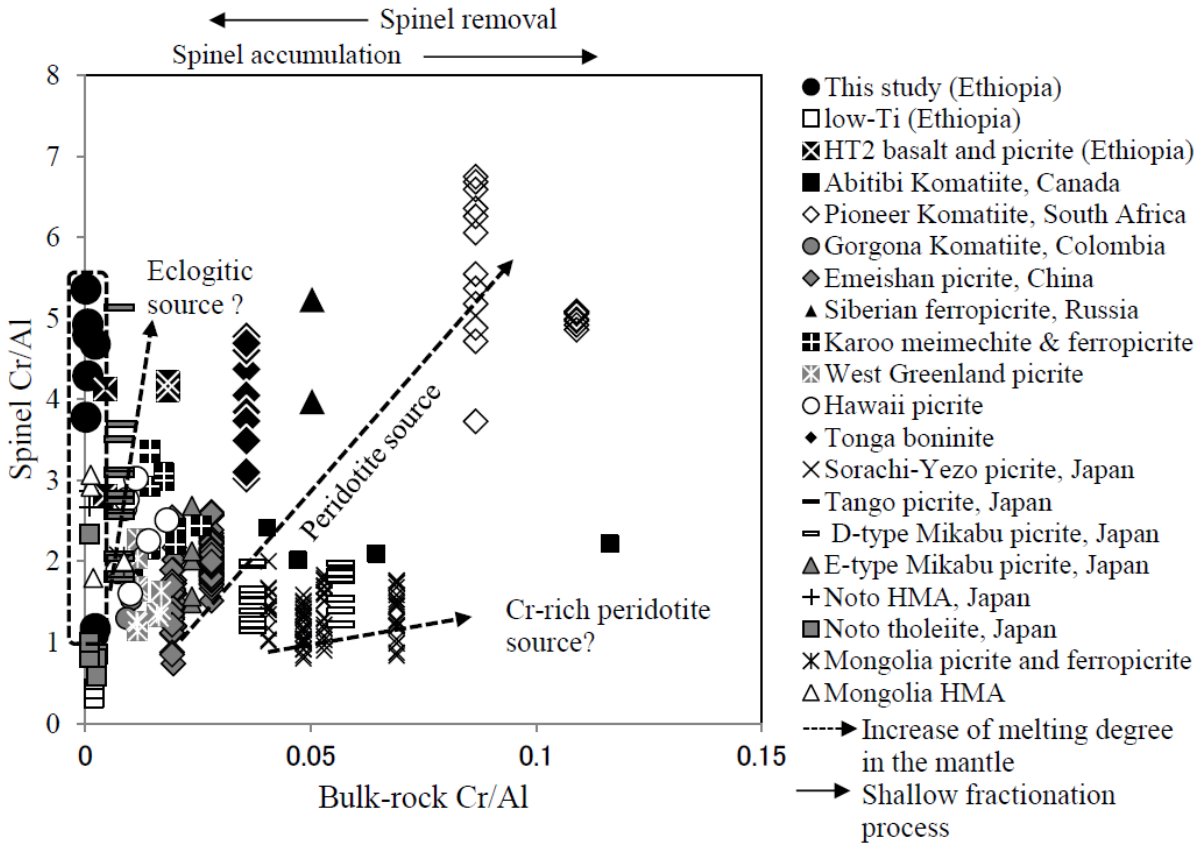


**Figure 2.8:** Bulk rock Cr/Al vs Spinel Cr/Al ratios for the Ethiopian ferropicrite and picritic ferrobasalts. Dashed arrows indicate the possible eclogitic and peridotitic sources. Data sources: Ethiopian LIP low-Ti and HT2 suits (Beccaluva et al., 2009); Abitibi komatiite (Barnes, 1985); Pioneer komatiite (Stiegler et al., 2012); Gorgona komatiite (Dietrich et al., 1981); Emeishan picrites (Kamenetsky et al., 2012); Siberian ferropicrite (Arndt et al., 1995); Karoo meimechite and ferropicrite (Heinonen and Luttinen, 2008, 2010); West Greenland picrite (Larsen and Pedersen, 2000); Hawaii picrite (Wilkinson and Hensel 1988); Tonga boninite (Sobolev and Danyushevsky, 1994); Sorachi-Yezo picrite (Ichiyama et al., 2012); Tango picrite (Ishiwatari and Imasaka, 2002); depleted (D-type) and enriched (E-type) picrites from Mikabu belt (Ichiyama et al., 2014); high magnesian andesite (HMA) and tholeiite lava Noto Peninsula (López and Ishiwatari, 2002); Mongolian high magnesian andesite and picrite (Erdenesaihan et al., 2013).

### 2.6.2.3. Clinopyroxene

Clinopyroxene phenocrysts are Mg#=74-88, $TiO_2$=0.84-1.82 wt. %, and $Al_2O_3$= 1.2-3.2 wt. % in the cores. Clinopyroxenes are Mg-rich augite ($Wo_{43-46}En_{41-48}Fs_{7-15}$; Fig 2.9) in composition. They commonly show normal zoning and it gives a trend of increasing Fe, Al, and Ti concentrations and decreasing Mg#, Si and Cr from core to rim (Fig. 2.10).

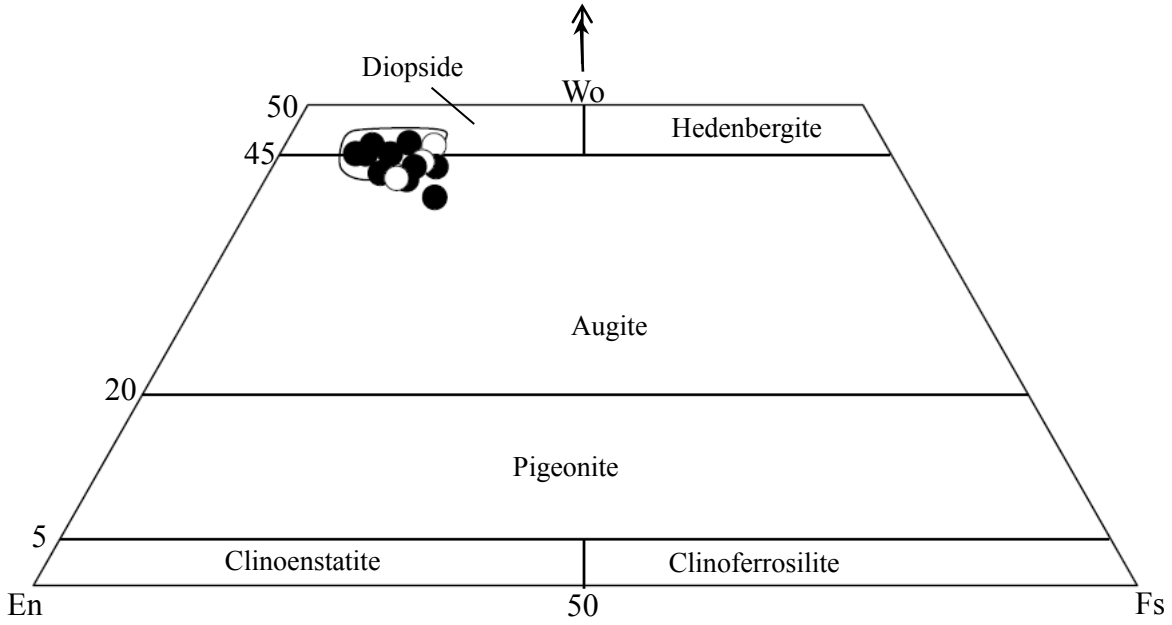


**Figure 2.9:** Pyroxene quadrilateral diagram showing the composition of pyroxene (after Morimoto et al., 1988) from the ferropicrite and picritic ferrobasalts in the Lalibela area. The circlualr area displays the composition of clinopyroxene in the picrite of Ethiopian LIP (Beccaluva et al. 2009).

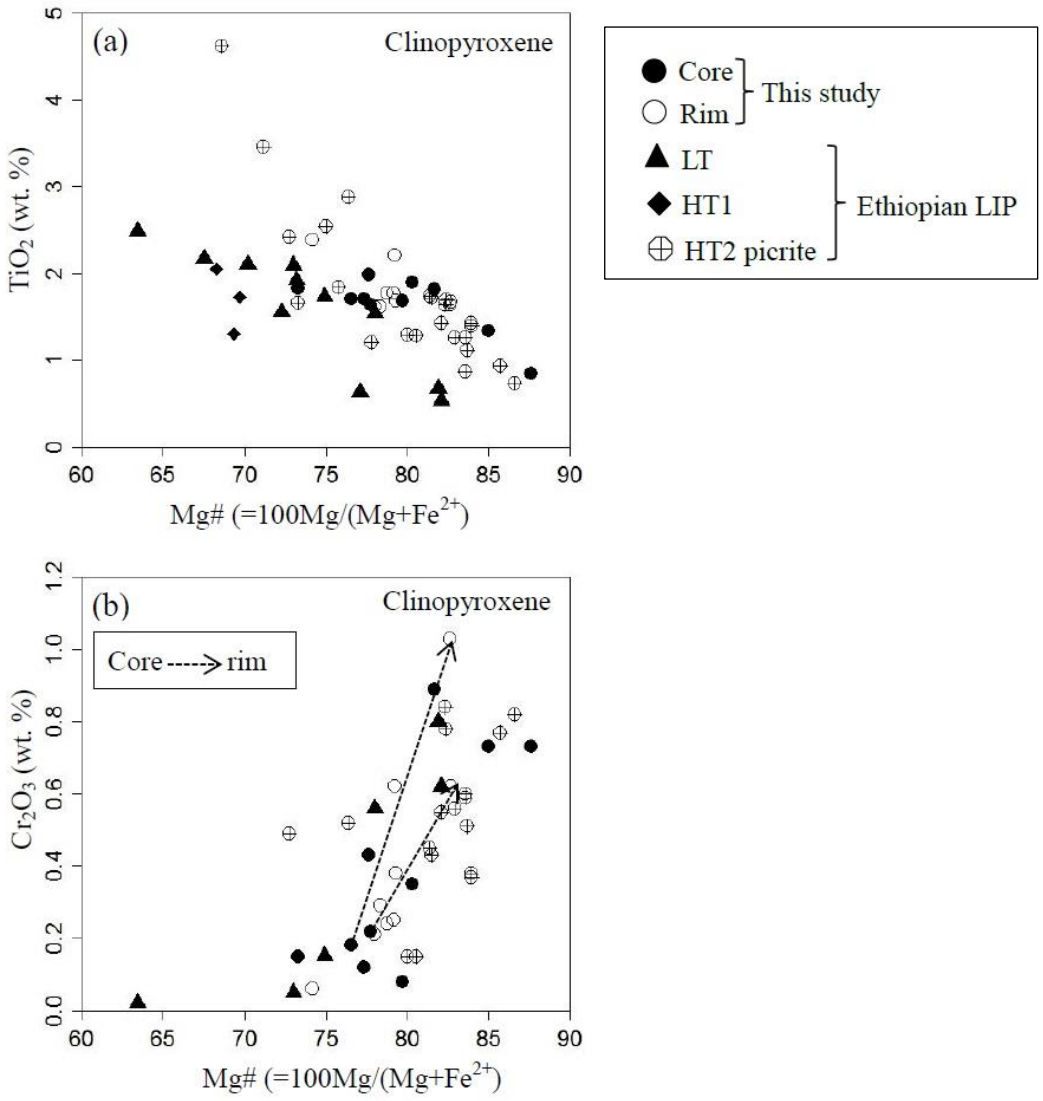


**Figure 2.10:** Plots of Mg# versus $TiO_2$ (a) and $Cr_2O_3$ (b) for the ferropicrite and picritic ferrobasalt of Ethiopian LIP. For comparison, clinopyroxenes from the high-Ti 2 picrite (Beccaluva et al., 2009) are also plotted. Dashed arrow represents the core to rim reverse zoning trend within a single crystal.

**Table 2.4:** Representative, analyses of clinopyroxene phenocrysts and microphynocrysts of ferropicrite and picritic ferrobasalt rocks from Ethiopian LIP.

| Sample | 1 Ferropicrite | | | | 2 Picritic ferrobasalt | | | | | 3 Picritic ferrobasalt | | | | | |
|---|---|---|---|---|---|---|---|---|---|---|---|---|---|---|---|
| Mineral | Cpx1 | | Cpx3 | | Cpx1 | | Cpx1gm | Cpx3 | | Cpx1 | | Cpx2 | | Cpx3 | |
| | Core | Rim | Core | Rim | Core | Rim | Core | Core | Rim | core | rim | core | rim | core | rim |
| SiO2 | 53.87 | 50.45 | 50.74 | 52.46 | 51.78 | 50.62 | 49.55 | 53.5 | 51.78 | 51.25 | 48.90 | 50.59 | 50.47 | 50.81 | 48.08 |
| $TiO_2$ | 0.84 | 1.68 | 1.64 | 1.67 | 1.70 | 1.77 | 1.83 | 1.08 | 1.80 | 1.34 | 2.21 | 1.82 | 1.77 | 1.68 | 2.39 |
| $Al_2O_3$ | 1.25 | 2.50 | 2.71 | 2.74 | 2.55 | 2.62 | 2.82 | 1.22 | 2.76 | 1.75 | 3.49 | 3.21 | 3.18 | 2.98 | 4.14 |
| $Cr_2O_3$ | 0.73 | 0.38 | 0.22 | 0.62 | 0.12 | 0.25 | 0.15 | 0.67 | 0.20 | 0.73 | 0.62 | 0.89 | 0.24 | 0.08 | 0.06 |
| FeO* | 4.37 | 7.13 | 7.65 | 6.02 | 7.97 | 7.08 | 9.24 | 4.83 | 8.05 | 5.03 | 6.80 | 6.23 | 7.16 | 6.96 | 8.39 |
| MnO | 0.16 | 0.20 | 0.07 | 0.14 | 0.16 | 0.13 | n.d. | n.d. | n.d. | 0.15 | 0.17 | 0.09 | 0.13 | 0.21 | 0.14 |
| MgO | 17.36 | 15.33 | 15.02 | 16.15 | 15.26 | 15.12 | 14.21 | 16.96 | 15.33 | 15.97 | 14.54 | 15.57 | 14.91 | 15.35 | 13.53 |
| CaO | 22.48 | 20.96 | 20.61 | 21.67 | 21.43 | 21.26 | 20.93 | 22.6 | 20.73 | 21.79 | 21.46 | 21.42 | 21.38 | 21.26 | 21.06 |
| Total | 101.06 | 98.63 | 98.66 | 101.47 | 100.97 | 98.85 | 98.73 | 100.86 | 100.65 | 98.01 | 98.19 | 99.82 | 99.24 | 99.33 | 97.79 |
| Cations (O=6) | | | | | | | | | | | | | | | |
| Si | 1.949 | 1.895 | 1.904 | 1.902 | 1.903 | 1.896 | 1.878 | 1.944 | 1.904 | 1.922 | 1.851 | 1.873 | 1.884 | 1.893 | 1.837 |
| Ti | 0.023 | 0.047 | 0.046 | 0.046 | 0.047 | 0.050 | 0.052 | 0.030 | 0.050 | 0.038 | 0.063 | 0.051 | 0.050 | 0.047 | 0.069 |
| Al | 0.053 | 0.111 | 0.120 | 0.117 | 0.111 | 0.116 | 0.126 | 0.052 | 0.120 | 0.077 | 0.156 | 0.140 | 0.140 | 0.131 | 0.187 |
| Cr | 0.021 | 0.011 | 0.007 | 0.018 | 0.003 | 0.007 | 0.004 | 0.019 | 0.006 | 0.022 | 0.018 | 0.026 | 0.007 | 0.002 | 0.002 |
| $Fe^{2+}$ | 0.132 | 0.224 | 0.240 | 0.182 | 0.245 | 0.222 | 0.293 | 0.147 | 0.248 | 0.158 | 0.215 | 0.193 | 0.224 | 0.217 | 0.268 |
| Mn | 0.005 | 0.006 | 0.002 | 0.004 | 0.005 | 0.004 | n.d. | n.d. | n.d. | 0.005 | 0.005 | 0.003 | 0.004 | 0.007 | 0.004 |
| Mg | 0.936 | 0.859 | 0.840 | 0.873 | 0.836 | 0.844 | 0.803 | 0.919 | 0.840 | 0.893 | 0.821 | 0.859 | 0.830 | 0.852 | 0.771 |
| Ca | 0.871 | 0.844 | 0.828 | 0.842 | 0.844 | 0.853 | 0.850 | 0.880 | 0.817 | 0.876 | 0.870 | 0.850 | 0.855 | 0.848 | 0.862 |
| Total | 3.990 | 3.997 | 3.985 | 3.984 | 3.994 | 3.992 | 4.006 | 3.991 | 3.985 | 3.991 | 3.999 | 3.992 | 3.994 | 3.997 | 4.000 |
| Wo | 44.9 | 43.8 | 43.4 | 44.4 | 43.8 | 44.5 | 43.7 | 45.2 | 42.9 | 45.5 | 45.7 | 44.7 | 44.8 | 44.2 | 45.4 |
| En | 48.3 | 44.6 | 44.0 | 46.0 | 43.4 | 44.0 | 41.3 | 47.2 | 44.1 | 46.4 | 43.0 | 45.2 | 43.5 | 44.4 | 40.5 |
| Fs | 6.8 | 11.6 | 12.6 | 9.6 | 12.7 | 11.6 | 15.1 | 7.5 | 13.0 | 8.2 | 11.3 | 10.1 | 11.7 | 11.3 | 14.1 |
| Mg# | 87.63 | 79.31 | 77.78 | 82.71 | 77.34 | 79.2 | 74.33 | 86.22 | 77.25 | 84.98 | 79.22 | 81.67 | 78.78 | 79.72 | 74.19 |

*Total Fe as FeO; Mg#=100Mg/(Mg+$Fe^{2+}$).

Abbreviations: Cpx, clinopyroxene; Wo, wollastonite; En, enstatite; Fs, ferrosilite; gm, groundmass; n.d., not detected.

However, some of the studied clinopyroxene crystals are very rich in Cr (up to 6240 ppm) and display very strong reverse zoning with significant increase of compatible elements (such as Cr and Ni; Tables 2.4 and 2.5) and decreasing REEs from core to rim. This unusual, significant reverse zoning provides insight in to the origin of these lavas (see Section 2.79). The trace element composition of clinopyroxenes of ferropicrite and picritic ferrobasalt rocks resembles those of HT2 basalt (Beccaluva et al., 2009), but they are enriched in total REE contents than those of iron-poor picrites. The REE contents of clinopyroxenes display enrichment in LREE ($La_N/Yb_N$=1.2-1.9) and MREE ($Eu_N/Yb_N$=3.3-4.3) relative to HREE. The primitive mantle-normalized pattern (Fig. 2.10) of clinopyroxene is characterized by low contents of Pb, Zr and LILE (e.g. Ba, Rb, Sr) relative to the neighboring elements, which is consistent with the low $D_{LILE}^{Cpx/liq}$ (Tuff and Gibson, 2007). Slight depletion of HFSE (e.g. Nb and Ta) is also observed relative to LREE (La and Ce). There is no significant negative Eu anomaly (Eu/Eu*=0.95-1).

#### 2.6.2.4. Plagioclase

Plagioclase microphenocrysts have labradorite composition ($An_{62}Ab_{36}Or_2$) while plagioclase in groundmass is andesine ($An_{41}Ab_{54}Or_4$), consistent with its late crystallization. The opaque minerals in the groundmass are mainly ilmenite.

**Table 2.5:** Representative trace element analyses (LA-ICP-MS; values in ppm) of clinopyroxenes from ferropicrite and picritic ferrobasalt rocks from Lalibela area, Ethiopian LIP

| Sample | 1 Ferropicrite | | 2 Picritic ferrobasalt | | | | 3 Picritic ferrobasalt | | | |
|---|---|---|---|---|---|---|---|---|---|---|
| Mineral | Cpx3 | | Cpx1 | | Cpx2 | | Cpx1 | | Cpx2 | |
| | Core | Rim | Core | Rim | Core | Rim | Core | Rim | Core | Rim |
| Sc | 64.3 | 62.2 | 64.2 | 66.1 | 81.1 | 73.1 | 68.4 | 68.4 | 58.9 | 61.1 |
| Ti | 7480 | 7840 | 10050 | 10010 | 11140 | 10600 | 8580 | 8690 | 7110 | 9750 |
| V | 449 | 313 | 471 | 419 | 391 | 402 | 247 | 252 | 202 | 314 |
| Cr | 886 | 4240 | 809 | 2040 | 2550 | 2440 | 6240 | 5850 | 2120 | 2320 |
| Co | 52.6 | 44.9 | 49.0 | 49.3 | 47.4 | 48.4 | 39.2 | 39.1 | 41.7 | 42.0 |
| Ni | 262 | 358 | 255 | 305 | 300 | 295 | 374 | 347 | 375 | 364 |
| Rb | 0.004 | 0.043 | 0.02 | 0.1 | 0.01 | 0.01 | 0.01 | 0.001 | 0.004 | 0.01 |
| Sr | 49.9 | 46.9 | 73.5 | 70.0 | 68.3 | 65.7 | 58.6 | 62.1 | 56.1 | 77.7 |
| Y | 14.6 | 11.2 | 18.0 | 15.5 | 14.2 | 16.8 | 11.0 | 11.3 | 10.6 | 14.1 |
| Zr | 35.0 | 25.7 | 62.4 | 54.4 | 53.5 | 60.7 | 30.2 | 31.8 | 24.0 | 45.9 |
| Nb | 0.1 | 0.2 | 0.3 | 0.3 | 0.3 | 0.3 | 0.2 | 0.2 | 0.1 | 0.2 |
| Cs | n.d. | 0.002 | n.d. | 0.010 | n.d. | 0.0003 | n.d. | 0.002 | n.d. | n.d. |
| Ba | 0.02 | 0.64 | 0.23 | 0.33 | 0.03 | 0.05 | 0.02 | 0.03 | 0.01 | 0.02 |
| La | 2.2 | 1.4 | 3.3 | 2.8 | 2.7 | 2.8 | 2.1 | 2.3 | 1.6 | 2.6 |
| Ce | 10.7 | 7.2 | 15.9 | 13.7 | 12.6 | 13.5 | 9.3 | 10.4 | 7.6 | 12.8 |
| Pr | 2.1 | 1.4 | 2.9 | 2.6 | 2.4 | 2.5 | 1.7 | 1.9 | 1.5 | 2.4 |
| Nd | 12.2 | 8.3 | 17.5 | 15.0 | 13.9 | 15.0 | 10.0 | 11.0 | 8.8 | 13.9 |
| Sm | 4.0 | 2.8 | 5.5 | 4.8 | 4.6 | 5.1 | 3.3 | 3.6 | 3.0 | 4.5 |
| Eu | 1.3 | 0.9 | 1.8 | 1.6 | 1.5 | 1.6 | 1.1 | 1.2 | 1.0 | 1.5 |
| Gd | 4.3 | 3.1 | 5.7 | 4.9 | 4.6 | 5.2 | 3.5 | 3.8 | 3.3 | 4.5 |
| Tb | 0.6 | 0.5 | 0.8 | 0.7 | 0.6 | 0.7 | 0.5 | 0.6 | 0.5 | 0.7 |
| Dy | 3.6 | 2.7 | 4.5 | 3.9 | 3.6 | 4.0 | 2.9 | 3.1 | 2.7 | 3.7 |
| Ho | 0.6 | 0.5 | 0.8 | 0.7 | 0.6 | 0.7 | 0.5 | 0.5 | 0.4 | 0.6 |
| Er | 1.5 | 1.1 | 1.8 | 1.5 | 1.4 | 1.6 | 1.2 | 1.2 | 1.1 | 1.5 |
| Tm | 0.2 | 0.1 | 0.2 | 0.2 | 0.2 | 0.2 | 0.1 | 0.2 | 0.1 | 0.2 |
| Yb | 1.1 | 0.8 | 1.3 | 1.0 | 0.9 | 1.1 | 0.8 | 0.9 | 0.8 | 1.0 |
| Lu | 0.1 | 0.1 | 0.2 | 0.1 | 0.1 | 0.1 | 0.1 | 0.1 | 0.1 | 0.1 |
| Hf | 1.7 | 1.2 | 2.8 | 2.4 | 2.6 | 2.8 | 1.7 | 1.7 | 1.2 | 2.2 |
| Ta | 0.02 | 0.02 | 0.05 | 0.04 | 0.04 | 0.04 | 0.03 | 0.03 | 0.01 | 0.04 |
| Pb | 0.05 | 0.05 | 0.1 | 0.06 | 0.04 | 0.03 | 0.05 | 0.05 | 0.05 | 0.04 |
| Th | 0.01 | 0.01 | 0.03 | 0.02 | 0.03 | 0.02 | 0.02 | 0.02 | 0.01 | 0.02 |
| U | 0.003 | 0.003 | 0.007 | 0.004 | 0.004 | 0.003 | 0.002 | 0.006 | 0.002 | 0.005 |

Abbreviations: cpx, clinopyroxene; n.d. not detected.

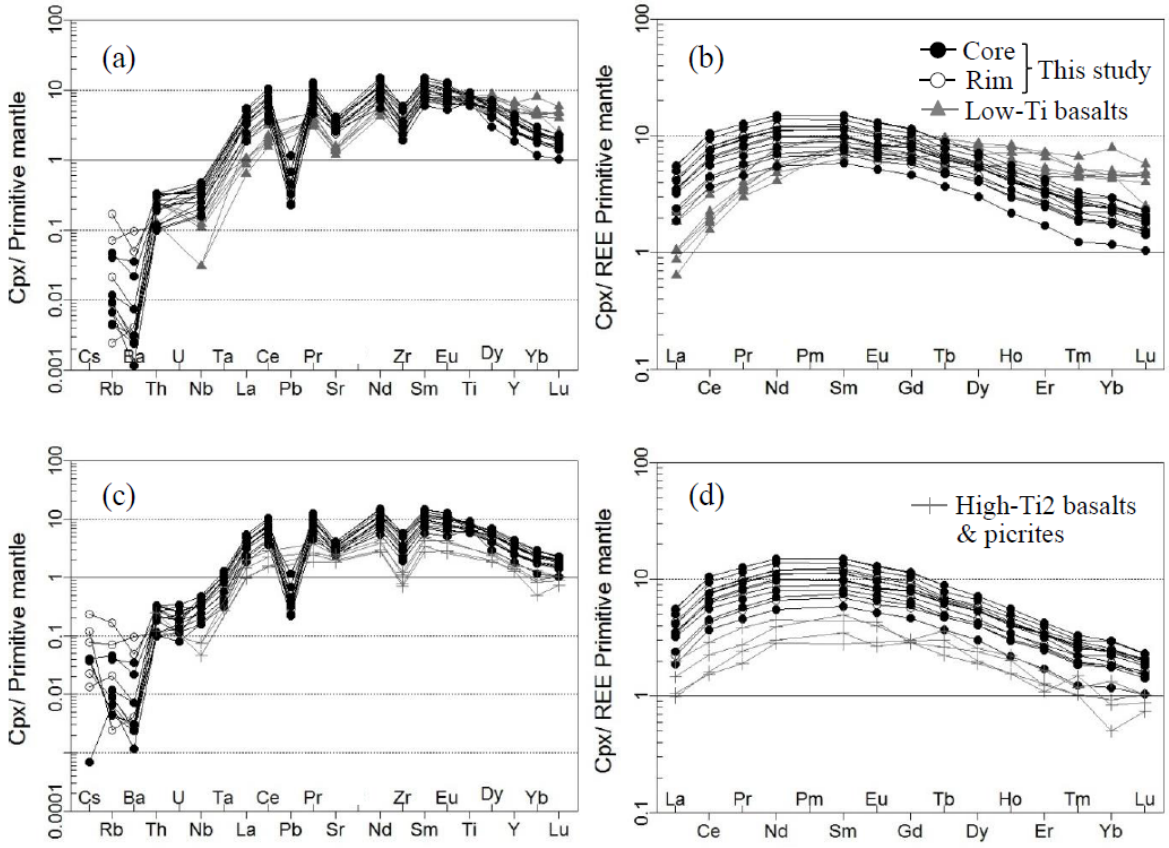


**Figure 2.11:** Primitive-mantle-normalized REE and trace element patterns for clinopyroxenes of ferropicrite and picritic ferrobasalt rocks from Lalibela area, Ethiopian LIP. Normalizing values are from McDonough and Sun (1995). For comparison, clinopyroxene compositions from low-Ti (a-b) and High-Ti 2 basalt and picrites (c-d) of Ethiopian LIP are also plotted after Beccaluva et al. (2009).

## 2.7. DISCUSSION

### 2.7.1. Olivine Fo and NiO showing primitive mantle-derived melt

Primitive rocks that are associated with continental flood basalt LIPs are scarce, but their presence provides important information on the parental sources of these voluminous mantle derived magma. The most MgO-rich olivine that we analyzed is $Fo_{88.9}$ (Table 2.2), which is higher than those of Paraná-Etendeka ferropicrite $Fo_{85}$

(Gibson et al., 2000) and slightly lower than those of anhydrous fertile lherzolite ($Fo_{90}$) (e.g. Ishiwatari, 1985). They are only slightly less forsteritic than the most magnesian olivine from HT2 picrites ($Fo_{90}$) of Ethiopia (Beccaluva et al., 2009) and picrites from Karoo ($Fo_{90}$, Cox and Jamieson, 1974). More magnesian olivines from Hokkaido, Japan ($Fo_{94}$, Ichiyama et al., 2012) and West Greenland ($Fo_{92}$, Pedersen, 1985) may represent higher potential temperature in the mantle. The magnesian and high NiO (up to 0.3 wt. %) characteristics of olivine (Fig. 2.6) support the primitive, mantle-derived nature of the Ethiopian ferropicrite.

### 2.7.2. Primary bulk-rock nature of the melt

To assess the hypothetical primary melt compositions for the Ethiopian ferropicrite, we have tested a modeling program (PRIMELT2) (Herzberg and Asimow, 2008); however the outcome is unreliable due to the possible pyroxenite source component suggested by PRIMELT2 model. We thus focused on the modeling of primary melts on the basis of olivine-liquid equilibrium (Putirka, 2008). The analyzed samples are characterized by primitive olivine (> $Fo_{78}$; Table 2.2). The most Mg-rich olivine compositions ($Fo_{88}$ in ferropicrite and $Fo_{88-85}$ in picritic ferrobasalts) correspond to olivine that would crystallize from mantle derived melts. Assuming a $K_D(Fe\text{-}Mg)^{ol\text{-}liq}$ of 0.32 (Putirka, 2005), $Fo_{85-88}$ would have been in equilibrium with a liquid with Mg# 64-71 and 15-19 wt.% MgO. These observations indicate that the Ethiopian ferropicrite (Mg# 64), 14 wt. % MgO and 14 wt. % FeO*; Table 2.1 is likely to represent true Fe-rich mantle melt. Therefore, the high FeO* content of Ethiopian ferropicrite is not an accumulation effect.

### 2.7.3. Temperature estimates

Gibson (2002) suggested that the ferropicritic liquid is generated by the partial melting of basalt plus peridotite mixture at >1450 ℃ and >4.5 GPa. The experimental result of Tuff et al. (2005) confirmed that a ferropicrite melts 100 % at 5 GPa and 1650 ℃, which is similar to the solidus (5 GPa and 1625 ℃) of silica-undersaturated garnet pyroxenite studied by Kogiso et al. (2003). These temperature are higher than the ambient upper mantle ($T_p$ ~1280–1475 ℃; McKenzie and Bickle, 1988) and supports the derivation of ferropicrites from high temperature magma (and the plume). However, the available thermodynamic models are only compatible with peridotite sources (e.g. Herzberg and Asimow, 2008) and may not be applicable to estimate the physical conditions (pressure, mantle potential temperature) for pyroxene-rich sources. Considering the compositional similarity between the Ethiopian ferropicrite and 97SB68 in terms of MgO, FeO* and $Al_2O_3$ (Fig. 2.2), the melting condition of our ferropicrite may be close to that of the melting experiment conducted by Tuff et al. (2005) as noted above.

Application of olivine-spinel geothermometer (Fabriès, 1979) to the ferropicrite and picritic ferrobasalt rocks results in temperatures as high as 1090 ℃ for the most chromian spinel. This may represent closure temperature of Fe-Mg exchange between spinel inclusion and host olivine during cooling of the magma, and hence gives the lower limit of the magmatic temperature estimate.

In addition, the Cr content of spinel may provide a clue for the temperature of the magma from which it crystallized. The Cr content of the melt in equilibrium with spinel (Cr solubility) increases with increasing

temperature (Barnes, 1986). Effect of oxygen fugacity also matters, but co-existing ilmenite and absence of magnetite suggest low oxygen fugacity. The high Cr/Al spinel would have been expected to crystallize from the magma having high Cr/Al ratio, or the magmatic temperature was very high, and these in turn may indicate high degrees of melting, however, the bulk rock data of our samples shows very low content of Cr. Thus, it is likely that the observed high Cr/Al ratio of spinel is due to high magmatic temperature.

### 2.7.4. High degree melting of the source mantle?

Cr-spinel is one of the liquidus phases in basaltic magma and its chemical variation may have significant inferences about the degree of melting and source regions of magma (Dick and Bullen, 1984; Arai, 1994). The Cr-spinel of Ethiopian ferropicrite is significantly higher in Cr# (average 78.7) than those of MORB, Emeishan high-Ti picrite (Kamenetsky et al., 2012), Pechenga ferropicrite (Hanski, 1992) and comparable to those of boninite (Fig. 2.7). The $TiO_2$ content of Cr-spinel is also very high (Fig. 2.7b), which is consistent with the high Ti characteristics of bulk rock chemistry of the studied samples. Moreover, the $TiO_2$ content of spinel is equal to or higher than those of LIP lavas (Kamenetsky et al., 2001). The high Cr/Al ratio of spinels from the Ethiopian ferropicrite and picritic ferrobasalts (Fig. 2.8) might indicate high degree of melting, but the bulk rock Cr/Al ratio is very low and is not proportional to that of spinel. Thus we propose very low Cr/Al of the source material (see Section 2.75). Removal of spinel in the early stage of magma evolution is another possibility (Fig. 2.8), but is unlikely in view of the very primitive nature of the magma. However, this interpretation apparently contradicts to the suggested small degree of partial melting (of peridotite source) on the basis of low $Al_2O_3/TiO_2$ and high

Zr/Y ratios of bulk rock compositions (Fig. 2.4).

### 2.7.5. Cr/Al relationship between spinel and bulk rock: indicator of source lithology

Figure 2.8 shows the relationship between the bulk-rock Cr/Al and spinel Cr/Al ratios of the Ethiopian ferropicrite in comparison with mafic-ultramafic rocks of other igneous provinces. Based on this, the Cr/Al ratio of spinels of Ethiopian ferropicrite is similar to those of Archean komatiite (Stiegler et al., 2012), Siberian ferropicrite (Arndt et al., 1995), and boninite (Sobolev and Danyushevsky, 1994), although the bulk-rock Cr/Al ratio (<0.005) is significantly lower than those mentioned above.

The observed very low bulk-rock Cr/Al ratios in the Ethiopian ferropicrite and picritic ferrobasalts might be attributed to the removal of Cr-spinel in the early stage of magma evolution. However, primitive nature of the studied samples does not support extensive early stage crystal fractionation. On the other hand, Sorachi-Yezo picrites (Ichiyama et al., 2012), Mikabu D-type picrites (Ichiyama et al., 2014) and Abitibi komatiite (Barnes, 1985) shows high bulk rock Cr/Al but low spinel Cr/Al ratios, which might indicate the accumulation of spinel in the magma (Fig. 2.8). However, occurrence of high Fo olivines in these rocks is compatible with high degree melting of peridotitic mantle rather than olivine accumulation process in shallow magma chamber. Thus, bulk rock Cr/Al ratio of the primitive magmas may be mainly controlled by lithology of the source material in the mantle. For example, if the source is eclogite (or pyroxenite), bulk rock Cr/Al ratios of magma may not exceed 0.01, but if the source is peridotite, Cr/Al of the magma may be as high as 0.1 (Fig. 2.8). The very low Cr/Al ratio of the Ethiopian ferropicrite together with the others of low bulk-rock Cr/Al (such as those of Noto tholeiite

and high magnesian andesite (HMA), López and Ishiwatari, 2002; Mongolia picrite and HMA, Erdenesaihan et al., 2013; Hawaii picrite, Wilkinson and Hensel, 1988) (Fig. 2.8) may suggest eclogitic source, which is supported by the lines of evidence as discussed later (see Section 2.7.8).

### 2.7.6. High-pressure melting of the source mantle

The increasing Zr/Y and decreasing $Al_2O_3/TiO_2$ ratios (Fig. 2.4) are generally attributed to increase of melting pressure or melt segregation depth and increasing stability of garnet in the residue (Walter, 1998). The Ethiopian ferropicrite and picritic ferrobasalts are characterized by higher Zr/Y and lower $Al_2O_3/TiO_2$ ratios than other ferropicritic rocks (e.g. Superior Province, Pechenga, Paraná-Etendeka and Mino-Tamba), indicating that their source region contained residual garnet and thus the partial melting took place in the garnet stability field. The low Al content in magmas such as ferropicrite (Tuff et al., 2005) and Al-depleted komatiites (Arndt et al., 2008; Robin-Popieul et al., 2012) is interpreted to indicate the presence of residual garnet in the mantle source. Compared to the Ethiopian ferropicrite, the ferropicrites of Siberia exhibit higher Zr/Y and lower $Al_2O_3/TiO_2$ ratios, suggesting higher melting pressure.

The high Ni content (501 ppm) along with the low $Al_2O_3$ (~9 wt. %) of Ethiopian ferropicrite may also indicate that garnet was a residual phase in its mantle source. This interpretation is consistent with the high pressure experimental result on the Paraná-Etendeka ferropicrite produced by Tuff et al. (2005).

In addition, REE patterns of clinopyroxene phenocrysts from the studied samples show distinct convex upward patterns in chondrite-normalized diagrams (Fig. 2.10) with $La_N/Yb_N$ (1.2-1.9) and $Eu_N/Yb_N$ (3.3-4.3),

resembling those reported HT2 basalt and picrites of Ethiopia (Beccaluva et al., 2009). Therefore, the strong HREE fractionation supports the presence of garnet in the mantle source region.

### 2.7.7. Bulk-rock high Fe/Mn and Ni/Cr ratios: a core-mantle issue?

High Fe/Mn ratios of basalts could be resulted from core-mantle interaction. However, on the basis of high Fe/Mn and unradiogenic $^{187}Os/^{188}Os$ content of the Ethiopian picrite, Roger et al. (2010) speculated that the entrapment of core material in the source of the Afar mantle plume is unlikely. Basaltic melts with high Fe/Mn (>60) ratio can be formed by partial melting of pyroxenite at the degree of melting less than 70 % (Kogiso and Hirschmann, 2001, Pertermann and Hirschmann, 2003, Kogiso et al., 2004) or of hydrous peridotite at the degree of melting greater than 50 % (Parman and Grove, 2004).

High fraction of clinopyroxene crystallization (> 30 %) could also produce a melt with high Fe/Mn ratio (Liu et al., 2008). In view of high MgO (> 10 wt. %) of the studied samples, such a high degree of crystallization is unrealistic. High Fe/Mn could be also resulted from the presence of residual garnet in the source (Herzberg, 2011), because $D_{Mn}^{Garnet/liquid}$ is ~7 at low melt fraction (Pertermann and Hirschmann, 2003). High Ni content (500 ppm) and high Ni/Cr ratio of the Ethiopian ferropicrite (Table 2.1) may also suggest contribution of Fe-Ni metal in its magma genesis, but to attribute this to the core-mantle reaction must be too speculative.

### 2.7.8. Eclogite vs. peridotite as the source for Ethiopian ferropicrite

The genesis of ferropicritic rocks have been considered to be associated with mantle plume (Gibson, 2002). Sobolev et al. (2007) suggested that ~2 % to 30 % of recycled crust is involved in the mantle melting to form MORBs, OIBs, continental basalts and komatiites. On the basis of phase relation and bulk rock composition of the Paraná-Etendeka ferropicrite, Tuff et al. (2005) speculated that ferropicrite primary melt is unlikely to have been derived from partial melt of normal peridotite and melting of garnet pyroxenite source may have been significant. The occurrence of garnet liquidus phase with clinopyroxene at pressure ≥ 6 GPa, leading Tuff et al. (2005) to propose garnet pyroxenite as mantle source for the Paraná- Etendeka ferropicrite. Ichiyama et al. (2006) have suggested that suitable ferropicrite sources include recycled ferrobasalts and Fe–Ti gabbros (that should have been eclogitized in the source mantle). It is evident that ferropicrite liquid cannot originate in direct partial melting of ambient depleted peridotite (Stone, 1995).

Jakobsen et al. (2005) suggested a mixing between the peridotite-derived picritic melts with evolved Fe-rich basalts or immiscible liquids could result in a ferropicritic composition. However, liquid immiscibility and subsequent mixing process is unlikely cause for the generation of Ethiopian ferropicritic melt because of two reasons: (1) immiscibility tends to fade away with increasing pressure (Charlier and Grove, 2012); (2) such mixing process would be expected to produce significant disequilibrium textures, which are not observed among studied rocks.

The bulk rock Cr/Al ratio (Fig. 2.8) may provide important clue about the source material. The extremely

low bulk rock Cr/Al ratio of Ethiopian ferropicrite and picritic ferrobasalt rocks evidence that they cannot be formed from the partial melting of only peridotite mantle source as the other mafic-ultramafic rocks (e.g. Sorachi-Yezo picrites, Japan; D-type Mikabu picrite, Japan; Pioneer komatiite, South Africa). Thus, we suggest that the significant contribution of recycled eclogitic material for the origin of Ethiopian ferropicrite and picritic ferrobasalts.

### 2.7.9. Reversely zoned clinopyroxene; reaction with peridotitic mantle

The origin of reversely zoned clinopyroxenes with resorbed texture has been attributed to magma mixing in many literatures (e.g. Wass, 1979; Simonetti et al., 1996). Kay (1978) suggested that the reversely zoned clinopyroxene may indicate reaction between a silicic melt and peridotite in the upper mantle. Reversely zoned clinopyroxenes have been also reported from Cenozoic basalts (Wang et al., 2007) and late Jurassic high-Mg adakaites of China (Gao et al., 2004), and suggested the presence of pyroxenite in the mantle source. Some of the analyzed clinopyroxene crystals of Ethiopian ferropicrite and picritic ferrobasalts exhibit unusually strong reverse zoning, which have a rim with distinctly high Mg#, Cr and Ni (Tables 2.4 and 2.5; Fig. 2.9). These zoning may indicate a significant increase of Mg#, Cr and Ni in the melt by assimilation of mantle peridotite (i.e. an olivine consuming reaction) or mixing with the peridotite-origin magma during magma ascent. Thus, the presence of these unusual reversely zoned clinopyroxene crystals may further proves the origin of Ethiopian ferropicrite and picritic ferrobasalt rocks from eclogitic source, and their reaction with the peridotitic mantle.

### 2.7.10. Experimental constraints for the source lithology

According to Yaxley & Green (1998), partial melting of relatively fusible eclogite inclusions produces $SiO_2$-rich melts that react with olivine in the host garnet peridotite and generate a secondary garnet pyroxenite source in upwelling mantle. Progressive melting of this "re-fertilized" source may yields silica-undersaturated, more mafic partial melt. Gibson (2002) suggested this "re-fertilized" source model to ferropicrite petrogenisis. Herzberg (2011) also discussed about the reaction between eclogite (pyroxenite)-origin melt and the host peridotite for the generation OIB.

Partial melting experiment of equal proportion of mixed basalt (GA1, in the form of coesite eclogite) and peridotite (MPY90) at 1500 ℃ and 3.5 GPa by Yaxley & Green (1998) and Yaxley (2000) yields a picritic melt that is close to Ethiopian ferropicrite composition. However, $GA1_{50}MPY90_{50}$ has slightly higher MgO (16.5 wt. %) and $Al_2O_3$ (11.7 wt. %), lower FeO* (12.50 wt. %) as compared with Ethiopian ferropicrite (13.92 wt. %, 8.58 wt. % and 14.00 wt. %, respectively) (Fig. 2.2 a-c). Tuff et al. (2005) proposed a source composition similar to a 75 % basalt and 25 % peridotite mixture at ≥5 GPa for the Paraná-Etendeka ferropicrite, but it is not supported by experimental data at this pressure. Likewise, we suggest that a higher pressure mixture of eclogite-peridotite ($GA1_{75}MPY90_{25}$) might be a plausible explanation to achieve the FeO* content similar with Ethiopian ferropicrite.

The high $TiO_2$ (>3 wt. %) content of the Ethiopian ferropicrite and picritic ferrobasalts may further support the important role of Ti-rich recycled oceanic crust (eclogite).

### 2.7.11. Hydrous mantle melting?

The significance of water for the origin of ferropicrite is poorly known. However, different suggestions are given in literatures, such as the parental melt have been hydrous (Hanski and Smolkin, 1995, Fiorentini et al., 2008; their interpretation is based on the presence of kaersutite and phlogopite) and anhydrous (Gibson, 2002).

Partial melting experiment at high pressures (5- 11 GPa) have been conducted on $H_2O$-saturated mantle peridotite (KLB-1) by Kawamoto and Holloway (1997). At about 7.5 GPa the partial melt have lower $SiO_2$, $TiO_2$, $Al_2O_3$, $Na_2O$ and significantly higher MgO (32 wt. %) than the Ethiopian ferropicrite, but similar FeO*. Thus, partial melt of $H_2O$ saturated peridotite unlikely to be the source of Ethiopian ferropicrite. Moreover, the absence of primary magmatic hydrous mineral phases as phenocrysts, in the groundmass or as inclusions from the studied Ethiopian ferropicrite precludes its derivation from hydrous magma source.

In summary, the presence of ferropicrite in Ethiopian LIP may provide additional evidence for the high temperature and high pressure mafic magmatism of Afar plume during Oligocene (~30 Ma) and thus it may further proves for the high eruption temperature in Phanerozoic time. The origin of these ferropicrite and picritic ferrobasalt rocks could be attributed to high pressure partial melting of mantle peridotite that possibly incorporated recycled components (eclogite or garnet pyroxenite).

### 2.7.12. CONCLUSIONS

The ferropicrite and picritic ferrobasalt from Lalibela area show high Zr/Y and low $Al_2O_3/TiO_2$ ratios indicating higher pressure melting or smaller degree of partial melting, which apparently contradicts to the high Cr# of spinel in these rocks. The major and trace element data of the Ethiopian ferropicrite is compatible with the eclogitic source that has possibly represents the recycled oceanic crust components in the upwelling Afar plume head. The occurrence of ferropicrite further supports the involvement of deep plume sources during Ethiopian LIP magmatism. In view of low Cr/Al ratio of the bulk rock, the high Cr# of spinel may be due to the very high temperature of the magma that originated in the eclogitic source. The occurrence of clinopyroxene crystals with extreme reverse zoning characteristics may further support the origin of Ethiopian ferropicrite and picritic ferrobasalts from eclogitic source at depths and their later interaction with the mantle peridotite.

### 2.7.13. REFERENCES


Arai, S. (1994) Characterization of spinel peridotites by olivine-spinel compositional relationships: review and interpretation. *Chemical Geology*, 113, 191-204.

Arndt, N.T., Naldrett, A.J. and Pyke, D.R. (1977) Komatiitic and Iron-rich tholeiitic lavas of Munro Township, Northeast Ontario. *Journal of Petrology*, 18, 319-369.

Arndt, N., Lehnert, K. and Vasil'ev, Y. (1995) Meimechites: highly magnesian alkaline magmas from the subcontinental lithosphere? *Lithos*, 34, 41–59.

Arndt, N.T., Lesher, C.M. and Barnes, S.J. (2008) Komatiite. Cambridge: Cambridge University Press, 467 p.

Ayalew, D., Barbey, P., Marty, B., Reisberg, L., Yirgu, G. and Pik, R. (2002) Source, genesis and timing of giant ignimbrite deposits associated with Ethiopian continental flood basalts. *Geochimica et Cosmochimica Acta*, 66, 1429-1448.

Ayalew, D. and Ishiwatari, A. (2011) Comparison of rhyolites from continental rift, continental arc and oceanic island arc: implication for the mechanism of silicic magma generation. *Island Arc,* 20, 78-93.

Barnes, S.J. (1985) The petrography and geochemistry of komatiite flows from the Abitibi Greenstone Belt and a model for their formation. *Lithos*, 18, 241-270.

Barnes, S.J. (1986) The distribution of chromium among orthopyroxene, spinel and silicate liquid at atmospheric pressure. *Geochim. Cosmochim. Acta*, 50, 1889-1909.

Beccaluva, L., Bianchini, G., Natali, C. and Siena, F. (2009) Continental flood basalts and mantle plumes: a case

study of the northern Ethiopian Plateau. *Journal of Petrology*, 50, 1377-1403.

Charlier, B. and Grove, T.L. (2012) Experiments on liquid immiscibility along tholeiitic liquid lines of descent. *Contributions to Mineralogy and Petrology*, 164, 27–44.

Courtillot, V., Davaille, A., Besse, J. and Stock, J.M. (2003) Three distinct types of hotspots in the Earth's mantle. *Earth and Planetary Science Letters*, 205, 295–308.

Cox, K.G. and Jamieson, B.G. (1974) The olivine-rich lavas of Nuanetsi: a study of polybaric magmatic evolution. *Journal of Petrology*, 15, 269-301.

Dick, H.J.B. and Bullen, T. (1984) Chromium spinel as a petrogenetic indicator in abyssal and alpine-type peridotites and spatially associated lavas. *Contributions to Mineralogy and Petrology*, 86, 54 – 76.

Dietrich, V.J., Gansser, A., Sommerauer, J. and Cameron, W.E. (1981) Palaeogene komatiites from Gorgona Island, East Pacific: A primary magma for ocean floor basalts? *Geochemical Journal*, 15, 141-161.

Elkins-Tanton, L.T., Draper, D.S., Agee, C.B., Jewell, J., Thorpe, R.I. and Hess, P.C. (2007) The last lavas erupted during the main phase of the Siberian flood volcanic province: results from experimental petrology. *Contributions to Mineralogy and Petrology*, 153, 191-209.

Erdenesaihan, G., Ishiwatari, A., Orolmaa, D., Arai, S. and Tamura, A. (2013) Middle Paleozoic greenstons of the Hangay region, central Mongolia: Remnants of an accreted oceanic plateau and forearc magmatism. *Journal of Mineralogical and Petrological Sciences*, 108, 303-325.

Fabriès, J. (1979) Spinel–olivine geothermometry in peridotites from ultramafic

complexes. *Contributions to Mineralogy and Petrology*, 69, 329–336.

Fiorentini, M.L., Beresford, S.W., Deloule, E., Hanski, E., Stone, W.E. and Pearson, N.J. (2008) The role of mantle-derived volatiles in the petrogenesis of Palaeoproterozoic ferropicrites in the Pechenga Greenstone Belt, northwestern Russia: Insights from in-situ microbeam and nanobeam analysis of hydromagmatic amphibole. *Earth and Planetary Science Letters*, 268, 2-14.

Francis, D., Ludden, J., Johnstone, R. and Davis, W. (1999) Picrite evidence for more Fe in Archean mantle reservoirs. *Earth and Planetary Science Letters*, 167, 197– 213.

Gao, S., Rudnick, R.L., Yuan, H.L., Liu, X.M., Liu, Y.S., Xu, W.L., Ling, W.L., Ayers J., Wang, X.C. and Wang, Q.H. (2004) Recycling lower continental crust in the North China craton. *Nature*, 432, 892–897.

George, R., Rogers, N. and Kelley, S. (1998). Earliest magmatism in Ethiopia: evidence for two mantle plumes in one flood basalt province. *Geology*, 26, 923-926.

Gibson, S.A., Thompson, R.N. and Dickin, A.P. (2000) Ferropicrites: geochemical evidence for Fe-rich streaks in upwelling mantle plumes. *Earth and Planetary Science Letters*, 174, 355-374.

Gibson, S.A. (2002) Major element heterogeneity in Archean to Recent mantle plume starting-heads. *Earth and Planetary Science Letters*, 195, 59–74.

Goldstein, S.B. and Francis, D.M. (2008) The Petrogenesis and mantle source of Archaean ferropicrites from the Western Superior Province, Ontario, Canada. *Journal of Petrology*, 49, 1729-1753.

Gurenko, A.A., Hansteen, T.H. and Schmincke, H.U. (1996) Evolution of parental magmas of Miocene shield

basalts of Gran Canaria (Canary Islands): constraints from crystal, melt and fluid inclusions in minerals. *Contributions to Mineralogy and Petrology*, 89, 422-435.

Hanski, E. (1992) Petrology of the Pechenga ferropicrites and co-genetic, Ni-bearing gabbro-wehrlite intrusions, Kola Peninsula Russia. *Bulletin of the geological Survey of Finland*, 367, 192 pp.

Hanski, E.J. and Smolkin, V.F. (1989) Pechenga ferropicrites and other early Proterozoic picrites in the eastern part of the Baltic Shield. *Precambrian Research*, 45, 63–82.

Hanski, E.J. and Smolkin, V.F. (1995) Iron- and LREE-enriched mantle source for early Proterozoic intraplate magmatism as exemplified by the Pechenga ferropicrites, Kola Peninsula, Russia. *Lithos*, 34, 107–125.

Heinonen, J.S. and Luttinen, A.V. (2008) Jurassic dikes of Vestfjella, Western Dronning Maud Land, Antarctica: geochemical tracing of ferropicrite sources. *Lithos*, 105, 347-364.

Heinonen, J.S. and Luttinin, A.V. (2010) Mineral chemical evidence for extremely magnesian subalkaline melts from the Antarctic extension of the Karoo large igneous province. *Contributions to Mineralogy and Petrology*, 99, 201-217.

Herzberg, C. and Asimow, P.D. (2008) Petrology of some oceanic island basalts: PRIMELT2.XLS software for primary magma calculation. *Geochemistry Geophysics Geosystems*, 8, doi:10.1029GC002057.

Herzberg, C. (2011) Identification of source lithology in the Hawaiian and Canary Islands: implications for origins. *Journal of Petrology*, 52, 113–146.

Hofmann, C., Courtillot, V., Feraud, G., Rochette, P., Yirgu, G., Ketefo, E. and Pik, R. (1997) Timing of the

Ethiopian flood basalt event and implications for plume birth and global change. *Nature*, 389, 838-841.

Ichiyama, Y., Ishiwatari, A., Hirahara, Y. and Shuto, K. (2006) Geochemical and isotopic constraints on the genesis of the Permian ferropicritic rocks from the Mino-Tamba belt, SW Japan. *Lithos*, 89, 47–65.

Ichiyama, Y., Ishiwatari, A., Kimura, J., Senda, R., Kawabata, H., Tatsumi, Y. (2012). Picrites in central Hokkaido: Evidence of extremely high temperature magmatism in the Late Jurassic ocean recorded in an accreted oceanic plateau. *Geology*, 40, 411-414.

Ichiyama, Y., Ishiwatari, A., Kimura, J-I., Senda, R. and Miyamoto, T. (2014) Jurassic plume-origin ophiolites in Japan: accreted fragments of oceanic plateaus. *Contributions to Mineralogy and Petrology,* (in press).

Ishida, H., Morishita, T., Arai, S. and Shirasaka, M. (2004) Simultaneous in-situ multi-element analysis of minerals on thin section using LA-ICP-MS. *Science Report of Kanazawa University,* 48, 31–42.

Ishiwatari, A. (1985) Igneous petrogenesis of the Yakuno ophiolite (Japan) in the context of the diversity of ophiolites. *Contributions to Mineralogy and Petrology*, 89, 155-167.

Ishiwatari, A., and Imasaka, M. (2002) Picritic basalt from the Miocene Yoka Formation in the Tango Peninsula, Kyoto Prefecture, south-western Japan. *The Journal of the Geological Society of Japan*, 108, 671-684. (In Japanese with English abstract).

Jakobsen, J.K., Veksler, I.V., Tegner, C., and Brooks, C.K. (2005) Immiscible iron- and silica-rich melts in basalt petrogenesis documented in Skaergaard intrusion. *Geology*, 33, 885-888.

Kamenetsky, V.S., Crawford, A.J. and Meffre, S. (2001) Factors controlling chemistry of magmatic spinel: an

empirical study of associated olivine, Cr-spinel and melt inclusions from primitive rocks. *Journal of Petrology*, 42, 655–671.

Kamenetsky, V.S., Chung, S., Kamenetsky, M.B., and Kuzmin, D.V. (2012) Picrites from the Emeishan large igneous province, SW China: a compositional continuum in primitive magmas and their respective mantle sources. *Journal of Petrology*, 53, 2095-2113.

Kawamoto, T. and Holloway, J.R. (1997) Melting temperature and partial melt chemistry of $H_2O$-saturated mantle peridotite to 11 Giga Pascals. *Science*, 276, 240–243.

Kawabata, H., Hanyu, T., Chang, Q., Kimura, J., Nichols, A.R.L. and Tatsumi, Y. (2011) The Petrology and Geochemistry of St. Helena Alkali Basalts: Evaluation of the Oceanic Crust-recycling Model for HIMU OIB. *Journal of Petrology*, 52, 791-838.

Kay, R.W. (1978) Aleutian magnesian andesites: melt from subducted Pacific Ocean crust. *Journal of Volcanology and Geothermal Research*, 4, 117-132.

Kieffer, B., Arndt, N., Lapierre, H., Bastien F., Bosch, D., Pecher, A., Yirgu, G., Ayalew, D., Weis, D., Jerram, D.A., Keller, F. and Meugniot, C. (2004) Flood and shield basalts from Ethiopia: magmas from the African superswell. *Journal of Petrology*, 45, 793–834.

Kogiso, T. and Hirschmann, M.M. (2001) Experimental study of clinopyroxenite partial melting and the origin of ultra-calcic melt inclusions. *Contributions to Mineralogy and Petrology*, 142, 347–360.

Kogiso, T., Hirschmann, M.M. and Frost, D.J. (2003) High pressure partial melting of garnet pyroxenite:

possible mafic lithologies in the source of ocean island basalts. *Earth and Planetary Science Letters,* 216, 603–617.

Kogiso T., Hirschmann M.M. and Pertermann, M. (2004) High-pressure partial melting of mafic lithologies in the mantle. *Journal of Petrology*, 45, 2407–2422.

Larsen, L.M. and Pedersen, A.K. (2000) Processes in high-Mg, high-T magmas: evidence from olivine, chromite and glass in Palaeogene picrites from West Greenland. *Journal of Petrology*, 41, 1071–1098.

Le Bas, M.J. (2000) IUGS reclassification of the high-Mg and picritic volcanic rocks. *Journal of Petrology*, 41, 1467–1470.

Liu, Y., Gao, S., Kelemen, P.B. and Xu, W. (2008) Recycled crust controls contrasting source compositions of Mesozoic and Cenozoic basalts in the North China Craton. *Geochimica et Cosmochimica Acta*, 72, 2349-2376.

López, J.C. and Ishiwatari, A. (2002) Petrogenesis of tholeiitic basalt, calc-alkaline basaltic andesite and high magnesian andesite lava succession of the Oligo-Miocene Anamizu Formation in northeastern Noto Peninsula, central Japan. *Journal of Mineralogical and Petrological Sciences*, 97, 85-113. (Errata in 98, 165 (2003)).

Marty, B., Pik, R. and Gezahegn, Y. (1996) Helium isotopic variations in Ethiopian plume lavas: nature of magmatic sources and limit on lower mantle contribution. *Earth and Planetary Science Letters*, 144, 223–237.

McDonough, W.F. and Sun, S.-s. (1995) The composition of the Earth. *Chemical Geology*, 120, 223-254.

McKenzie, D. and Bickle, M.J. (1988) The volume and composition of melt generated by extension of the lithosphere. *Journal of Petrology*, 29, 625–679.

Mohr, P. and Zanettin, B. (1988) The Ethiopian flood basalt province. In: MacDougall, J. D. (ed.) *Continental Flood Basalts*. Dordrecht: Kluwer, pp. 63-110.

Morimoto, N., Fabries, J., Ferguson, A.K., Ginzburg, I.V., Ross, M., Seifert, F.A., Zussman, J., Aoki, K. and Gottardi, D., (1988) Nomenclature of pyroxenes. *American Mineralogist*, 62, 53–62.

Natali, C., Beccaluva, L., Bianchini, G. and Siena, F. (2011) Rhyolites associated to Ethiopian CFB: Clues for initial rifting at Afar plume axis. *Earth and Planetary Science Letters*, 312, 59-68.

Parman, S.W. and Grove, T.L. (2004) Harzburgite melting with and without $H_2O$: experimental data and predictive modeling. *Journal of Geophysical Research*, 109 (B2). doi:10.1029/2003jb002566.

Pearce, N.J.G., Perkins, W.T., Westgate, J.A., Gorton, M.P., Jackson, S.E., Neal, C.R. and Chenery, S.P. (1997) A compilation of new and published major and trace element data for NIST SRM 610 and NIST SRM 612 glass reference materials. *Geostandard Newsletter*, 21, 115–144.

Pedersen, A.K. (1985) Reaction between picrite magma and continental crust: early Tertiary silicic basalts and magnesian andesites from Disko, West Greenland. *Bulltin Gronlands Geologiske Undersogelse*, 152, 126 pp.

Pertermann, M. and Hirschmann, M.M. (2003) Anhydrous partial melting experiments on MORB-like eclogite:

phase relations, phase compositions and mineral-melt partitioning of major elements at 2–3 GPa. *Journal of Petrology*, 44, 2173–2201.

Piccirillo, E.M., Justin Visentin, E., Zanettin, B., Joron, J.K. and Treuil, M. (1979) Geodynamic evolution from plateau to rift: Major and trace element geochemistry of the central eastern Ethiopian plateau volcanics. *Neues Jahrbuch für Geologie und Paläontologie*, 158, 139–179.

Pik, R., Deniel, C., Coulon, C., Yirgu, G., Hofmann, C. and Ayalew, D. (1998) The northwestern Ethiopian Plateau flood basalts: Classification and spatial distribution of magma types. *Journal of Volcanology and Geothermal Research*, 81, 91-111.

Putirka, K.D. (2005) Mantle potential temperatures at Hawaii, Iceland, and the mid-ocean ridge system, as inferred from olivine phenocrysts; evidence for thermally driven mantle plumes. *Geochemistry, Geophysics, Geosystems*, *6*, doi:10.1029/2005GC000915.

Putirka, K.D. (2008) *Thermometers and barometers for volcanic systems. Minerals, inclusions and volcanic processes.* In: Putirka, K.D., Tepley III, F.J. (Eds.), Reviews in Mineralogy and Geochemistry, 69. Mineralogical Society of America, pp. 61–120.

Riley, T.R., Leat, P.T., Curtis, M.L., Millar, I.L., Duncan, R.A. and Fazel, A. (2005) Early-middle Jurassic dolerite dykes from western Dronning Maud Land (Antarctica): identifying mantle sources in the Karoo large igneous province. *Journal of Petrology*, 46, 1489–1524.

Ritsema, J., Van Heijst, H.J. and Woodhouse, J.H. (1999) Complex shear wave velocity structure imaged

beneath Africa and Iceland. *Science*, 286, 1925-1928.

Robin-Popieul, C.C.M., Arndt, N.T., Chauvel, C., Byerly, G.R., Sobolev, A.V. and Wilson, A. (2012) A New Model for Barberton Komatiites: Deep Critical Melting with High Melt Retention. *Journal of Petrology*, 53, 2191-2229.

Rochette, P., Tamrat, E., Feraud, G., Pik, R., Courtillot, V., Ketefo, E., Coulon, C., Hoffmann, C., Vandamme, D. and Yirgu, G. (1998). Magnetostratigraphy of the Ethiopian traps. *Earth and Planetary Science Letters*, 164, 497-510.

Rogers, N.W., Davies, M.K., Parkinson, I.J. and Yirgu, G. (2010). Osmium isotopes and Fe/Mn ratios in Ti-rich picritic basalts from the Ethiopian flood basalt province. No evidence from core contribution to the Afar plume. *Earth Planetary Science Letters*, 296, 413-422.

Sigurdsson, H. and Schilling, J.G. (1976). Spinels in Mid-Atlantic Ridge basalts: chemistry and occurrence. *Earth and Planetary Science Letters*, 29, 7-20.

Sigurdsson, I.A., Steinthorsson, S. and Grönvold, K. (2000). Calcium-rich melt inclusions in Cr spinels from Borgarhraun, northern Iceland. *Earth and Planetary Science Letters*, 183, 15 – 26.

Simkin, T. and Smith, J.V. (1970). Minor-element distribution in olivine. *Journal of Geology,* 78, 304–325.

Simonetti, A., Shore, M., and Bell, K. (1996). Diopside phenocrysts from lavas, Napak Volcano, Eastern Uganda: Evidence for magma mixing. *Canadian Mineralogist*, 34, 411–421.

Sobolev, A.V. and Danyushevsky, L.V. (1994). Petrology and geochemistry of boninites from the north termination of the Tonga Trench: Constraints on the generation conditions of primary high-Ca boninite magmas. *Journal of Petrology*, 35, 1183-1211.

Sobolev, A.V., Hofmann, A.W., Kuzmin, D.V., Yaxley, G.M., Anderson, A.T., Arndt, N.T., Chung, S.-L, Garcia, M.O., Gurenko, A.A., Danyushevsky, L.V., Elliott, T., Frey, F.A., Kamenetsky, V.S., Kerr, A.C., Krivolutskaya, N.A., Matvienkov, V.V., Nikogosian, I.K., Rocholl, A., Sigurdsson, I., Suschevskaya, N.M. and Teklay, M. (2007). The amount of recycled crust in sources of mantle-derived melts. *Science*, 316, 412–417.

Stiegler, M.T., Cooper, M., Byerly, G.R. and Lowe, D.R. (2012). Geochemistry and petrology of komatiites of the Pioneer Ultramafic Complex of the 3.3 Ga Weltevreden Formation, Barberton greenstone belt, South Africa. *Precambrian Research*, 212-213, 1-12.

Stone, W.E., Crocket, J.H., Dickin, A.P. and Fleet, M.E. (1995). Origin of Archean ferropicrites: geochemical constraints from the Boston Creek Flow, Abitibi greenstone belt, Ontario, Canada. *Chemical Geology*, 121, 51–71.

Thompson, R.N. and Gibson, S.A. (2000). Transient high temperatures in mantle plume heads inferred from magnesian olivines in Phanerozoic picrites. *Nature*, 407, 502-506.

Tuff, J. and Gibson, S.A. (2007). Trace-element partitioning between garnet, clinopyroxene and Fe-rich picritic melts at 3 to 7 GPa. *Contributions to Mineralogy and Petrology*, 153, 369-387.

Tuff, J., Takahashi, E. and Gibson, S.A. (2005). Experimental constraints on the role of garnet pyroxenite in the genesis of high-Fe mantle plume derived melts. *Journal of Petrology*, 46, 2023–2058.

Walter, M.J. (1998). Melting of garnet peridotite and the origin of komatiite and depleted lithosphere. *Journal of Petrology*, 39, 29–60.

Wang, W., Xu, W., Wang, D., Ji, W., Yang, D. and Pei, F. (2007). Caiyuanzi Paleogene basalts and deep-derived xenocrysts in eastern Liaoning, China: constraints on nature and deep process of the Cenozoic lithospheric mantle. *Journal of Mineralogy and Petrology*, 27, 63–70.

Wass, S.Y. (1979). Multiple origins of clinopyroxene in alkalic basaltic rocks. *Lithos*, 12, 115–132.

Wilkinson, J.F.G. and Hensel, H.D. (1988). The petrology of some picrites from Mauna Loa and Kilauea volcanoes, Hawaii. *Contributions to Mineralogy and Petrology*, 98, 326-345.

Wooden, J.L., Czamanske, G.K., Fedorenko, V.A., Arndt, N.T., Chauvel, C., Bouse, R.M., King, W.B.S., Knight, R.J. and Siems, D.F. (1993). Isotopic and trace-element constraints on mantle and crustal contributions to Siberian continental flood basalts, Noril'sk area, Siberia. *Geochimica et Cosmochimica Acta*, 57, 3677–3704.

Yaxley, G.M. (2000). Experimental study of the phase and melting relations of homogeneous basalt + peridotite mixtures and implications for the petrogenesis of flood basalts. *Contributions to Mineralogy and Petrology*, 139, 326–338.

Yaxley, G.M. and Green, D.H. (1998). Reactions between eclogite and peridotite: mantle refertilisation by

subduction of oceanic crust. *Schweizerische mineralogische und petrographische Mitteilungen*, 78, 243–255.

Zhang, Z., Mahoney, J.J., Mao, J. and Wang, F. (2006). Geochemistry of picritic and associated basalt flows of the western Emeishan flood basalt province, China. *Journal of Petrology*, 47, 1997–2019.